

**DESIGN AND REAL-TIME EXPERIMENTAL EVALUATION  
OF A SEMIACTIVE SUSPENSION SYSTEM OF A FOUR-  
WHEELER WITH COST-EFFECTIVE MAGNETO-  
RHEOLOGICAL DAMPER**

Thesis

Submitted in partial fulfillment of the requirements for the degree of

**DOCTOR OF PHILOSOPHY**

by

**MOHIBB E HUSSAIN JAMADAR**



DEPARTMENT OF MECHANICAL ENGINEERING  
NATIONAL INSTITUTE OF TECHNOLOGY KARNATAKA,  
SURATHKAL, MANGALORE – 575025

October 2023



**DESIGN AND REAL-TIME EXPERIMENTAL  
EVALUATION OF A SEMIACTIVE SUSPENSION  
SYSTEM OF A FOUR-WHEELER WITH COST-  
EFFECTIVE MAGNETO-RHEOLOGICAL DAMPER**

Thesis

Submitted in partial fulfillment of the requirements for the degree of

**DOCTOR OF PHILOSOPHY**

by

**MOHIBB E HUSSAIN JAMADAR**

Under the guidance of

**Dr. Hemantha Kumar**

Professor

**Dr. Sharnappa Joladarashi**

Professor



DEPARTMENT OF MECHANICAL ENGINEERING  
NATIONAL INSTITUTE OF TECHNOLOGY KARNATAKA,  
SURATHKAL, MANGALORE – 575025

October 2023



## DECLARATION

I hereby *declare* that the Research Thesis entitled “**DESIGN AND REAL-TIME EXPERIMENTAL EVALUATION OF A SEMIACTIVE SUSPENSION SYSTEM OF A FOUR WHEELER WITH COST EFFECTIVE MAGNETO-RHEOLOGICAL DAMPER**” which is being submitted to the **National Institute of Technology Karnataka, Surathkal**, in partial fulfillment of the requirements for the award of the Degree of **Doctor of Philosophy** in **Department of Mechanical Engineering** is a *bonafide report of the research work carried out by me*. The material contained in this Research Thesis has not been submitted to any University or Institution for the award of any degree.

Register Number : 177154ME025

Name of the Research Scholar : **Mohibb e Hussain Jamadar**

Signature of the Research Scholar :



Department of Mechanical Engineering

Place : **NITK, Surathkal**

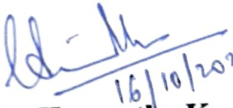
Date : 13/10/2023

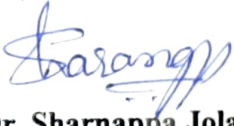


## CERTIFICATE

This is to *certify* that the Research Thesis entitled “**DESIGN AND REAL-TIME EXPERIMENTAL EVALUATION OF A SEMIACTIVE SUSPENSION SYSTEM OF A FOUR WHEELER WITH COST EFFECTIVE MAGNETO-RHEOLOGICAL DAMPER**” submitted by **Mr. Mohibb e Hussain Jamadar** (**Register Number: 177154ME025** as the record of the research work carried out by him, is *accepted as the Research Thesis submission* in partial fulfillment of the requirements for the award of the degree of **Doctor of Philosophy**.

### Research Guide(s)

  
16/10/2023  
**Dr. Hemantha Kumar**  
Professor

  
13/10/2023  
**Dr. Sharnappa Joladarashi**  
Professor

Department of Mechanical Engineering  
NITK, Surathkal

  
16/10/2023  
Chairman-DRPC

Department of Mechanical Engineering







## **Dedication**

*This thesis is dedicated to my Late father, my mother, sister and my wife without whose support this would not have been possible.*



## ACKNOWLEDGEMENTS

With a deep sense of gratitude, I wish to express my sincere thanks to my supervisor **Dr. Hemantha Kumar**, Professor, Department of Mechanical Engineering as well as my co-supervisor **Dr. Sharnappa Jodaladarshi**, Professor, Department of Mechanical Engineering, NITK, Surathkal, for their continuous guidance and support throughout my research work. I received instrumental, encouraging, excellent academic advice and constant motivation from them, which has helped me develop this thesis. Their constant encouragement, help and review of the entire work during the investigation were invaluable. I profoundly thank them.

I thank the Head of the Department, **Dr. Ravikiran Kadoli**, Professor, Department of Mechanical Engineering, for his encouragement and support. I take this opportunity to thank former Heads of the Department, **Dr. S. M. Kulkarni**, **Dr. Shrikantha S. Rao** and **Dr. Narendranath S.**, Department of Mechanical Engineering, for their help, continuous and timely suggestions.

I wish to thank all the Research Program Assessment Committee members, **Dr. M. R. Ramesh**, Associate Professor, Department of Mechanical Engineering and **Dr. A. S. Balu**, Associate Professor, Department of Civil Engineering, for their appreciation and valuable suggestions for this research work. I sincerely thank all the Department of Mechanical Engineering, NITK, Surathkal faculty members for their help, encouragement, and support through this research work.

I acknowledge and express gratitude for the funding support received from **IMPRINT** project No. **IMPRINT/2016/7330**, titled “Development of Cost Effective Magneto-Rheological (MR) Fluid Damper in Two wheelers and Four Wheelers Automobile to Improve Ride Comfort and Stability” under Ministry of Education (Formerly Ministry of Human Resource Development) and Ministry of Road Transport and Highways, Govt. of India.

I thank the technical support provided by **Mr. Raja Sekharan S. C., Mr. M. G. K. Sarvanan, and Mr. Amarnath G.**, the engineers of Rambal Ltd., Chennai, during the fabrication and testing of the MR dampers at Rambal Ltd..

My sincere thanks to all my colleagues **Dr. Gurubasavaraju T.M., Dr. Tak Radhe Shyam Saini, Dr. Rangaraj M Desai, Dr. Ravikumar, Dr. J. Vipin Allien, Dr. Pinjala Devikiran, Dr. Suhas Aralikatti, Dr. Ashok Kumar Kariganur, Dr. Puneet N. P., Dr. N. Suryarao and Mr. Abhinandan Hegale**, for their help and support to carry out this dissertation work. I am thankful to everybody who helped and encouraged me during this research work.

Finally, I would like to thank all my family members who have been a constant source of motivation and moral support to me throughout the completion of this research work.

**-Mohibb e Hussain Jamadar**

## **ABSTRACT**

The purpose of a damper in a vehicle suspension system is to isolate the vehicle body from disturbances arising from road undulations, generally referred to as ride comfort, while maintaining contact with the road at all times, generally referred to as road handling. Achieving good ride comfort and good road handling are the two conflicting criteria to be satisfied by an ideal vehicle suspension system. The viscous passive dampers, currently used in vehicle suspension systems, compromise a part of ride comfort to achieve partly good road handling in an attempt to satisfy these two criteria. A semi-active suspension system with Magneto Rheological (MR) dampers is one of the cost-effective methods to overcome the need for this compromise. The semi-active suspension system provides better control over energy dissipation by introducing a damper capable of achieving variable damping force during its operation. Although semi-active MR dampers are the cheapest option among the types of suspension systems (Passive, Active and Semiactive suspension systems), they are not the most affordable ones available in the automobile market. Hence, they can be found factory fitted only in some premium luxury cars. The work presented in this thesis attempts to develop and experimentally evaluate a cost-effective MR damper for application in a passenger vehicle while collaborating with a shock absorber manufacturer, Rambal Ltd., Chennai, India.

In the research work presented in this thesis a commercial MR damper is first characterized in the damper testing machine and fitted with two mathematical models, Equivalent Damping Model (EDM) and Magic Formula Model (MFM). The two mathematical models are compared for their accuracy and computational efficiency based on the simulation response of a Quarter Car Model (QCM) with a semiactive seat suspension system. The MFM was as accurate as the EDM while being computationally efficient.

Meanwhile, an MR damper was designed for application in the test vehicle, a passenger van, using a commercial MR fluid. The designed MR damper was fabricated at Rambal Ltd., Chennai. The fabricated MR damper was tested on the damper testing machine and also on the test vehicle. The results from the experiments on the damper

testing machine revealed that the fabricated damper delivered the desired MR effect. The experiments on the test vehicle revealed improved ride comfort and road handling with the developed MR damper. The cost evaluation of the developed MR damper revealed its cost-effectiveness compared to the commercially available MR dampers.

An attempt was made to further reduce the cost of the developed MR damper by designing a cost-effective MR fluid. The designing of MR fluid generally involves optimizing the composition of magnetic particles in the carrier fluid. The same was carried out in this study based on the simulation response of the full car model of the test vehicle subjected to the random road and the cost of synthesizing the MR fluid. The performance of the developed MR fluid was compared with the commercial MR fluid, MRF-132DG, on the rheometer, the damper testing machine and the test vehicle. The developed MR fluid yielded higher shear stress than the commercial MR fluid on the rheometer. Consequently, a higher damping force was achieved by the fabricated MR damper using the optimized MR fluid than the commercial MR fluid. The experiments conducted on the test vehicle with the developed MR fluid revealed its superior performance over the commercial MR fluid, indicated by higher ride comfort and road handling of the test vehicle compared to the ones achieved in previous experiments on the test vehicle. The optimized MR fluid was found to be more affordable than commercial MRF-132DG.

An acceleration-based control strategy is also proposed in this work to reduce the computational load and improve the overall reaction time of the semiactive suspension system. The performance and computational efficiency of the proposed control strategy were compared with an existing control strategy based on the experimental response and simulation time, respectively, of a Single Degree of Freedom (SDOF) system with an MR damper. The proposed control strategy was both effective and computationally efficient than the existing control strategy.

**Keywords:** *Magneto-Rheological damper, Equivalent damping, Magic Formula model, monotube MR damper, flow mode, MR damper optimization, Finite Elements Methods Magnetics, vehicle testing, MR fluid optimization, single degree of freedom system, acceleration-based semiactive control.*

# CONTENTS

<b>Acknowledgements .....</b>	<b>i</b>
<b>Abstract.....</b>	<b>iii</b>
<b>Contents .....</b>	<b>v</b>
<b>List of figures.....</b>	<b>xi</b>
<b>List of tables.....</b>	<b>xv</b>
<b>Abbreviations .....</b>	<b>xvii</b>
<b>1. INTRODUCTION.....</b>	<b>1</b>
1.1 WORKING PRINCIPLE OF AN AUTOMOBILE SUSPENSION SYSTEM....	1
1.2 DAMPERS.....	4
1.3 CLASSIFICATION OF DAMPERS BASED ON METHOD OF ENERGY DISSIPATION .....	7
1.3.1 Passive suspension system.....	9
1.3.2 Active suspension system .....	9
1.3.3 Semiactive suspension system .....	10
1.4 MAGNETO-RHEOLOGICAL FLUIDS.....	12
1.4.1 Shear mode.....	13
1.4.2 Flow mode .....	13
1.4.3 Squeeze mode .....	14
1.5 MR DAMPERS .....	15
1.6 SEMIACTIVE CURRENT CONTROL STRATEGIES.....	17
1.7 ORGANIZATION OF THESIS .....	19
<b>2. LITERATURE REVIEW AND RESEARCH METHODOLOGY .....</b>	<b>21</b>
2.1 INTRODUCTION .....	21

2.2	MAGNETO-RHEOLOGICAL FLUID (MR Fluid).....	21
2.3	MODELING OF MR DAMPERS .....	24
2.3.1	Quasistatic models .....	24
2.3.2	Dynamic parametric models .....	25
2.3.3	Dynamic non-parametric models.....	28
2.4	STRUCTURE OF MR DAMPERS AND THEIR OPTIMIZATION .....	30
2.4.1	Structure of MR damper piston.....	30
2.4.2	Optimization of MR dampers .....	33
2.5	SEMIACTIVE CONTROL STRATEGIES FOR VEHICLE SUSPENSION WITH MR DAMPERS .....	35
2.6	APPLICATION OF MR DAMPERS IN SUSPENSION OF PASSENGER VEHICLES .....	36
2.7	MOTIVATION .....	39
2.8	OBJECTIVES .....	40
2.9	SCOPE OF RESEARCH WORK.....	40
2.10	RESEARCH METHODOLOGY .....	41
2.10.1	Performance evaluation of a commercial MR damper .....	41
2.10.2	Design of MR damper for four-wheeler application.....	43
2.10.3	Real-time testing of MR damper on the test vehicle.....	43
2.10.4	Development of a cost-effective in-house MR fluid.....	43
2.10.5	Experimental evaluation and simulation of an acceleration-based control strategy .....	44
2.11	SUMMARY .....	44
<b>3.</b>	<b>EXPERIMENTAL EVALUATION AND MATHEMATICAL MODELLING OF COMMERCIAL MR DAMPER .....</b>	<b>45</b>
3.1	INTRODUCTION .....	45



3.2	METHODOLOGY FOR MR DAMPER MODEL SELECTION.....	45
3.3	EXPERIMENTAL EVALUATION OF COMMERCIAL MR DAMPER.....	46
3.3.1	The commercial MR damper .....	46
3.3.2	The damper testing machine .....	47
3.3.3	Discussion on results from experiments on RD-8041-1 in the damper testing machine .....	48
3.4	MATHEMATICAL MODELLING OF RD-8041-1 MR DAMPER.....	52
3.4.1	Equivalent damping model (EDM).....	52
3.4.2	Magic Formula Model (MFM) .....	55
3.5	SIMULATION OF A QUARTER CAR MODEL WITH SEAT SUSPENSION..	
	.....	57
3.5.1	The quarter car model with seat suspension .....	57
3.5.2	The control strategy .....	60
3.5.3	The road input.....	60
3.5.4	Discussion on results from the simulation of a quarter car model with a semiactive seat suspension system .....	61
3.6	SUMMARY .....	66
<b>4.</b>	<b>DESIGN AND EXPERIMENTAL EVALUATION OF A COST-EFFECTIVE MONOTUBE MR DAMPER FOR APPLICATION IN PASSENGER VAN.....</b>	<b>67</b>
4.1	INTRODUCTION .....	67
4.2	METHODOLOGY TO DESIGN MR DAMPER AND EVALUATE ITS PERFORMANCE.....	67
4.3	DESIGN OF MONOTUBE MR DAMPER .....	68
4.4	PERFORMANCE EVALUATION OF DEVELOPED MR DAMPER .....	80
4.4.1	Characterization of developed MR damper on damper testing machine ...	
	.....	80

4.4.2	Real-time testing of developed MR damper on the test vehicle .....	86
4.5	COST EVALUATION OF DEVELOPED MR DAMPER.....	92
4.6	RESULTS AND DISCUSSION .....	93
4.7	SUMMARY .....	95
<b>5.</b>	<b>DESIGN OF COST-EFFECTIVE MR FLUID AND ITS EXPERIMENTAL EVALUATION .....</b>	<b>97</b>
5.1	INTRODUCTION .....	97
5.2	METHODOLOGY TO DESIGN AND EVALUATE PERFORMANCE OF A COST-EFFECTIVE MR FLUID .....	97
5.3	SYNTHESIS AND CHARACTERIZATION OF MR FLUID SAMPLES.....	99
5.3.1	Synthesis of MR fluid samples .....	99
5.3.2	Rheological characterization of MR Fluid samples.....	100
5.4	DAMPING FORCE ESTIMATION OF DEVELOPED MR DAMPER WITH MR FLUID SAMPLES.....	107
5.5	OPTIMIZATION OF MAGNETIC PARTICLE COMPOSITION IN CARRIER FLUID.....	119
5.5.1	Simulation of full car model of the test vehicle.....	119
5.5.2	Cost estimation of MR fluid samples.....	126
5.5.3	Optimization of MR fluid composition.....	126
5.5.4	Performance evaluation of developed MR damper with optimized MR fluid .....	127
5.6	RESULTS AND DISCUSSIONS .....	133
5.6.1	Performance comparison of LMRF25 and MRF-132DG using Rheometer and damper testing machine .....	133
5.6.2	Performance evaluation of LMRF25 in the test vehicle and comparison with MRF-132DG.....	136
5.7	SUMMARY .....	139

<b>6. EXPERIMENTAL EVALUATION AND SIMULATION OF AN ACCELERATION-BASED CURRENT CONTROL STRATEGY .....</b>	<b>141</b>
6.1 INTRODUCTION .....	141
6.2 METHODOLOGY TO EVALUATE PERFORMANCE OF ASHC AND VSHC .....	142
6.3 EXPERIMENTAL EVALUATION OF ACCELERATION BASED SKYHOOK CONTROL IN THE SDOF SYSTEM.....	142
6.4 SIMULATION OF SDOF WITH ASHC AND VSHC .....	145
6.5 RESULTS AND DISCUSSION .....	148
6.6 SUMMARY .....	156
<b>7. SUMMARY AND CONCLUSIONS .....</b>	<b>157</b>
7.1 SUMMARY .....	157
7.1.1 Experimental evaluation and mathematical modelling of commercial MR damper .....	157
7.1.2 Design and experimental evaluation of a cost-effective monotube MR damper for application in passenger van .....	158
7.1.3 Design of cost-effective MR fluid and its experimental evaluation ....	158
7.1.4 Experimental evaluation and simulation of ASHC.....	159
7.2 CONCLUSIONS.....	160
7.3 SCOPE OF FUTURE WORK .....	162
<b>REFERENCES.....</b>	<b>163</b>
<b>APPENDIX.....</b>	<b>181</b>
<b>LIST OF PUBLICATIONS .....</b>	<b>199</b>
<b>BIODATA.....</b>	<b>201</b>



## LIST OF FIGURES

Figure 1.1 Solid axle suspension system (Reimpell et al., 2001) .....	2
Figure 1.2 McPherson strut suspension system (Jazar, 2014) .....	2
Figure 1.3 Double wishbone suspension system (Jazar, 2014) .....	3
Figure 1.4 Trailing arm suspension system (Dixon, 2009).....	4
Figure 1.5 Through rod damper .....	5
Figure 1.6 Twin tube damper.....	5
Figure 1.7 Single tube or Monotube damper .....	6
Figure 1.8 QCM.....	8
Figure 1.9 Half car model .....	8
Figure 1.10 Full car model (Nigwal et al., 2022).....	9
Figure 1.11 QCM with active suspension system.....	10
Figure 1.12 QCM with a semi-active suspension system .....	11
Figure 1.13 MR effect.....	12
Figure 1.14 Shear mode .....	13
Figure 1.15 Flow mode or valve mode .....	14
Figure 1.16 Squeeze mode.....	14
Figure 1.17 Monotube MR damper in flow mode .....	15
Figure 1.18 Monotube MR damper in shear mode .....	16
Figure 1.19 Schematic of skyhook control strategy.....	17
Figure 1.20 Schematic of ground hook control strategy.....	18
Figure 1.21 Schematic of a PID controller for MR dampers.....	18
Figure 2.1 (a) Particle size distribution of Large sized CIP – Sigma Aldrich – 44890 (b) Particle size distribution of Small sized CIP – Sigma Aldrich – C3518 (c) Magnetic moment vs Magnetic field strength curve of 44890 and C3518 (Acharya et al. 2019) .....	23
Figure 2.2 Bingham model (Wang and Liao, 2011) .....	25
Figure 2.3 Bour-Wen model (Wang and Liao, 2011).....	26
Figure 2.4 Polynomial model (Choi et al., 2001) .....	28
Figure 2.5 Neural network model of a MR damper (Chang and Roschke, 1998) .....	29

Figure 2.6 Block diagram of semiactive control with fuzzy controller (Schurter and Roschke, 2001b) .....	30
Figure 2.7 Steady state characteristic graph of a tire (Bakker et al. 1987) .....	30
Figure 2.8 Multicoil Seismic damper - LORD Corporation, USA (Goncalves et al. 2006) .....	31
Figure 2.9 Conventional multicoil design (Sassi et al., 2005) .....	32
Figure 2.10 Radial flux multicoil MR damper piston design (Sassi et al., 2005).....	32
Figure 2.11 Annular piston with axial and radial fluid flow path (Bai et al., 2013)....	33
Figure 2.12 MR damper on the front and rear axle of semitruck (Ahmadian and Simon, 2003) .....	37
Figure 2.13 ATV with commercial MR dampers (Kasprzyk et al., 2017) .....	38
Figure 2.14 Passenger car with MR damper (Du et al., 2020).....	39
Figure 2.15 Research methodology .....	42
Figure 3.1 Methodology for MR damper model selection .....	46
Figure 3.2 Commercial MR damper, RD-8041-1 .....	47
Figure 3.3 Experimental setup for MR damper characterization.....	49
Figure 3.4 FD diagram at (a) 0.05m/s (b) 0.1m/s (c) 0.15m/s (d) 0.2m/s.....	51
Figure 3.5 Characteristic graph of RD-8041-1 .....	52
Figure 3.6 Equivalent damping of RD-8041-1 .....	53
Figure 3.7 EDM curve fitting results .....	55
Figure 3.8 Curve fitting results of MFM .....	57
Figure 3.9 QCM with Seat suspension models (a) with passive damper (b) with MR damper.....	58
Figure 3.10 Random road profile of Medium road (R6) at 12 m/s.....	62
Figure 3.11 RMS of driver mass acceleration on road profile (a) R3 (b) R6 (c) R9 ...	63
Figure 3.12 Simulation time of QCMs with MR damper on road profile (a) R3 (b) R6 (c) R9 .....	65
Figure 4.1 Methodology to evaluate performance of MR damper developed for passenger van .....	68
Figure 4.2 Schematic of MR damper.....	69
Figure 4.3 Magnetic circuit of the piston.....	72

Figure 4.4 B-H curves of (a) AISI 1010 steel (MagWeb, 2021) (b) MRF-132DG (“LORD Corporation” 2019) .....	74
Figure 4.5 Field-dependent yield stress of MRF-132DG (“LORD Corporation”, 2019) .....	76
Figure 4.6 Dimensions of the MR damper piston.....	77
Figure 4.7 Simulation result of the magnetic circuit in FEMM.....	78
Figure 4.8 (a) CAD model of piston assembly (b) Exploded view of piston assembly (c) Fabricated parts of the piston assembly.....	80
Figure 4.9 Fully assembled monotube MR damper for the test vehicle .....	80
Figure 4.10 Damper testing machine from Rambal Ltd., Chennai.....	81
Figure 4.11 FD diagrams of developed MR damper at (a) 0.05m/s (b) 0.1m/s (c) 0.2m/s (d) 0.3m/s (e) 0.4 m/s.....	84
Figure 4.12 Characteristic graph of the developed MR damper.....	85
Figure 4.13 (a)The test vehicle (b) Rear suspension of the vehicle (right side) .....	86
Figure 4.14 Schematic of data flow during the experiment on the test vehicle.....	88
Figure 4.15 Schematic of the sharp speed bump .....	90
Figure 4.16 (a) Vehicle body acceleration measured at 10km/h (b) Vehicle body acceleration measured at 20km/h.....	91
Figure 4.17 (a) Wheel acceleration measured at 10km/h (b) Wheel acceleration measured at 20km/h.....	92
Figure 5.1 Methodology to design and evaluate performance of an MR fluid.....	98
Figure 5.2 Rheometer setup for MR fluid characterization .....	101
Figure 5.3 Rheological behavior of (a) LMRF5 (b) LMRF10 (c) LMRF15 (d) LMRF20 (e) LMRF25 .....	104
Figure 5.4 Rheological behavior of (a) SMRF5 (b) SMRF10 (c) SMRF15 (d) SMRF20 (e) SMRF25 .....	106
Figure 5.5 Theoretical characteristic graphs of developed MR damper with (a) LMRF5 (b) LMRF10 (c) LMRF15 (d) LMRF20 (e) LMRF25.....	111
Figure 5.6 Theoretical characteristic graphs of developed MR damper with (a) SMRF5 (b) SMRF10 (c) SMRF15 (d) SMRF20 (e) SMRF25.....	114
Figure 5.7 Full car model of the test vehicle (Nigwal et al., 2022) .....	120
Figure 5.8 Experimental setup to determine tire properties.....	123

Figure 5.9 Force-Displacement diagram of tire .....	124
Figure 5.10 FFT response of full car model simulation on the random road (a) LMRF samples (b) SMRF samples .....	125
Figure 5.11 Experimental characteristic graph of developed MR damper with LMRF25 .....	128
Figure 5.12 Experimental results of testing the vehicle over the sharp speed bump (a) Sprung mass acceleration at 10km/h (b) Sprung mass acceleration at 20km/h.....	129
Figure 5.13 Experimental results of testing the vehicle over the sharp speed bump (a) Unsprung mass acceleration at 10km/h (b) Unsprung mass acceleration at 20km/h	130
Figure 5.14 Satellite view of the random road test track at Rambal Ltd., Chennai (“Google Earth”, 2022).....	131
Figure 5.15 Experimental results of testing the vehicle over the random road test track (a) FFT of mass response at 10 km/h (b) FFT of sprung mass response at 20 km/h.	132
Figure 5.16 Experimental results of testing the vehicle over the random road test track (a) FFT of unsprung mass response at 10 km/h (b) FFT of unsprung mass response at 20 km/h .....	133
Figure 5.17 Comparison of experimental flow curves of LMRF25 and MRF-132DG .....	134
Figure 5.18 Comparison of experimental characteristic graphs with LMRF25 and MRF-132DG.....	135
Figure 5.19 Controllable damping forces of developed MR damper with LMRF25 and with MRF-132DG.....	136
Figure 6.1 Methodology to evaluate performance of ASHC and VSHC .....	142
Figure 6.2 Experimental setup of SDOF with MR damper .....	143
Figure 6.3 MFM fitting results for developed MR damper with LMRF25 .....	147
Figure 6.4 (a) Displacement of mass under positive step input (b) Acceleration of mass under positive step input (c) Displacement of mass under negative step input (d) Acceleration of mass under negative step input .....	150
Figure 6.5 (a) Displacement of mass under Sine-1 input (b) Acceleration of mass under Sine-1 input (c) Displacement of mass under Sine-2 input (d) Acceleration of mass under Sine-2 input.....	154
Figure 6.6 Reaction time of ASHC and VSHC .....	155



## LIST OF TABLES

Table 3.1 Equivalent damping coefficients of RD-8041-1 .....	53
Table 3.2 Coefficient values of EDM .....	54
Table 3.3 MFM coefficients for RD-8041-1.....	56
Table 3.4 Coefficients of QCM with seat suspension (Choi and Han, 2007).....	59
Table 3.5 Random road profiles as per ISO standards (Du et al., 2012) .....	61
Table 4.1 Dimensions of MR damper piston .....	77
Table 4.2 Peak acceleration of sprung mass .....	94
Table 4.3 Peak acceleration of unsprung mass .....	94
Table 5.1 Coefficients of Bingham model for LMRF samples .....	107
Table 5.2 Coefficients of Bingham model for SMRF samples.....	108
Table 5.3 MFM coefficients for MR damper with LMRF samples.....	114
Table 5.4 MFM coefficients for MR damper with SMRF samples.....	116
Table 5.5 MFM coefficients of LMRF samples .....	117
Table 5.6 MFM coefficients of SMRF samples.....	118
Table 5.7 Coefficient values of full car model of the test vehicle .....	122
Table 5.8 Peak FFT values of simulation response .....	125
Table 5.9 Cost of MR fluid samples .....	126
Table 5.10 Performance comparison of LMRF25 and MRF-132DG in the test vehicle .....	138
Table 5.11 Cost comparison of the LMRF25 and MRF-132DG.....	138
Table 6.1 MFM coefficients for the developed MR damper with LMRF25 .....	146
Table 6.2 Improvement in peak displacement and acceleration with ASHC .....	151
Table 6.3 Improvement in displacement and acceleration amplitude with ASHC....	152



## ABBREVIATIONS

ASHC	Acceleration based Skyhook Control
ATV	All-Terrain Vehicle
CIP	Carbonyl Iron Powder
DAQ	Data Acquisition system
DC	Direct Current
EDM	Equivalent Damping Model
ER	Electro-Rheological
FD	Force Displacement
FEM	Finite Element Methods
FEMM	Finite Element Methods Magnetics
FFT	Fast Fourier Transform
ISO	International Standard Organization
MFM	Magic Formula Model
MR	Magneto Rheological
MRD	Magneto-Rheological Device
PSD	Power Spectral Density
QCM	Quarter Car Model
RMS	Root Mean Square
RSM	Response Surface Methodology
SDOF	Single Degree of Freedom
VOD	Variable Orifice Damper
VSHC	Velocity-based Skyhook Control



# CHAPTER 1

## INTRODUCTION

The suspension system of an automobile is one of its integral parts for its functioning. The invention of motored vehicles has led to significant advancement in the automobile suspension technology. The automobile suspension system remains an active area of research even today and hence, it is also the field of research presented in this thesis. The purpose of an automobile suspension system is to provide ride comfort to the passengers by isolating the vehicle body from the road undulations and provide road handling by maintaining contact between the wheel and the road at all times during its operation. In general, an automobile suspension system comprises of an energy absorbing element, an energy dissipating element and the suspension linkages

### 1.1 WORKING PRINCIPLE OF AN AUTOMOBILE SUSPENSION SYSTEM

When a vehicle runs over a pothole or a bump the energy absorbing element i.e., the spring absorbs the energy of the wheel thereby isolating the passengers from this disturbance. This energy, if released, uncontrollably would cause discomfort for the passengers and could also cause the wheel to lose contact with the road, which is not desirable. Therefore, the energy dissipating element, the damper, dissipates this energy in a controlled manner. The suspension linkages connect the axle and the wheel assembly to the vehicle body ensuring there is a relative motion between the vehicle body and the wheel for the spring and the damper to operate.

A suspension system can be broadly classified as dependent and independent suspension system based on the linkages employed in the suspension system. The dependent suspension system are the ones where the vertical movement of one of the wheels on the axle affects the other wheel such as the rigid/solid rear axle of a bus or a truck where the dampers and the springs are directly connected to the vehicle body frame without any linkages as shown in Figure 1.1. The rear axle of some of the modern cars consist of dependent suspension systems due to its simple design and inexpensiveness.

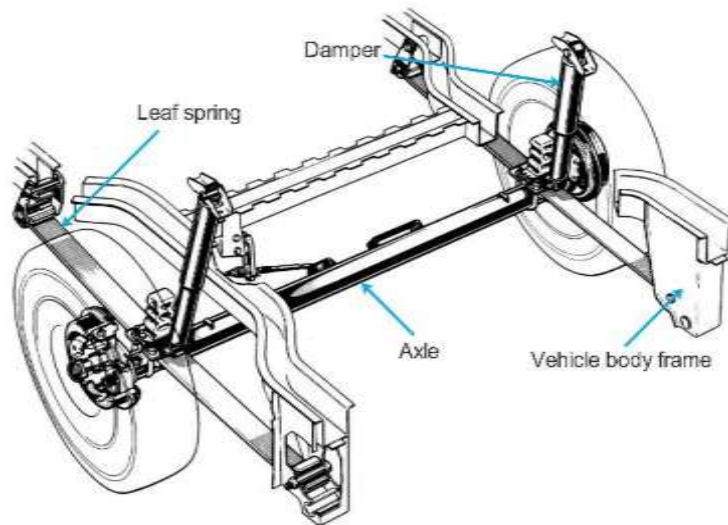


Figure 1.1 Solid axle suspension system (Reimpell et al., 2001)

In case of independent suspension systems, the movement of one wheel is independent of the other, hence the name independent suspension system. The independent suspension systems involve the McPherson strut, the double wishbone suspension and the trailing arm suspension.

The McPherson strut consists of a coil spring that is fit over a damper, as shown in Figure 1.2. One end of the damper is connected to the vehicle body and the other is connected to the wheel. The Lower-A arm connected between the vehicle body and the kingpin ensures both longitudinal and lateral movement of the wheel, hence, this is the of most widely used suspension system for the front wheel drive cars.

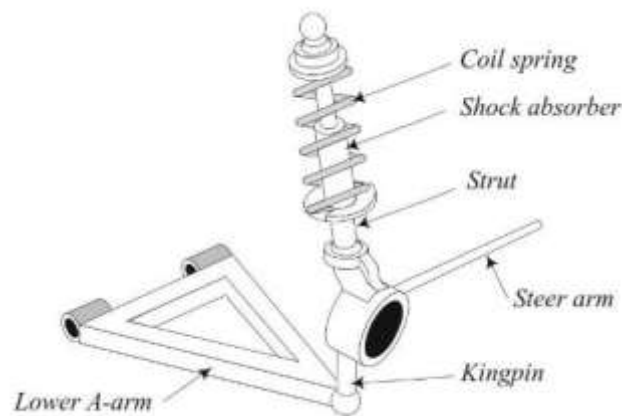


Figure 1.2 McPherson strut suspension system (Jazar, 2014)

The double wishbone suspension system consists of two arms connecting the wheel with the body, also known as A-arm, as shown in Figure 1.3. These two arms are shaped like the wishbone of a chicken, hence the name wishbone suspension system. One end of each arm is connected to the vehicle body and the other is connected to the wheel hub through a ball joint that also allows wheel steering. The spring and the damper are connected between the vehicle body and the lower arm. This is also one of the most widely used suspension system in the front wheel drive cars.

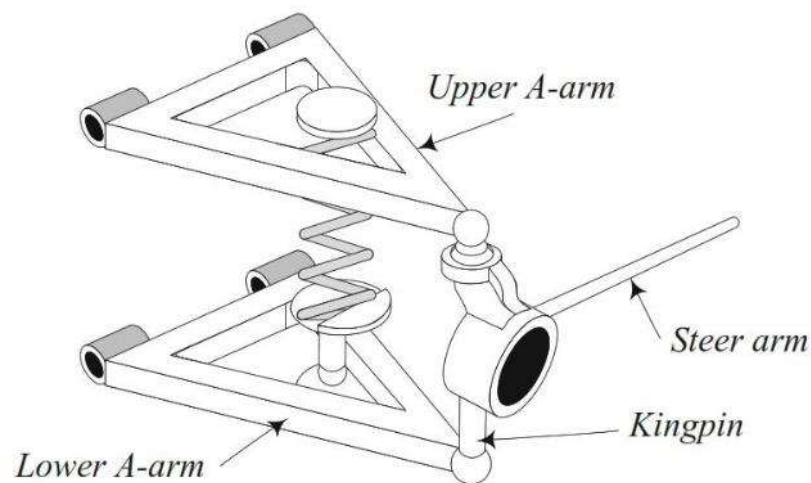


Figure 1.3 Double wishbone suspension system (Jazar, 2014)

The trailing arm suspension looks similar to the solid axle suspension system at the first glance, however, it's the trailing arms, shown in Figure 1.4, connected between the axle and the wheel hub that are the distinguishing feature. The spring and the damper are connected between these trailing arms and the vehicle body frame. The gap between the two trailing arms provided sufficient space for placing the fuel tank or a spare tire thereby allowing the car body floor plan to be completely flat. Hence, this kind of suspension is one of the most widely used rear suspension passenger cars.

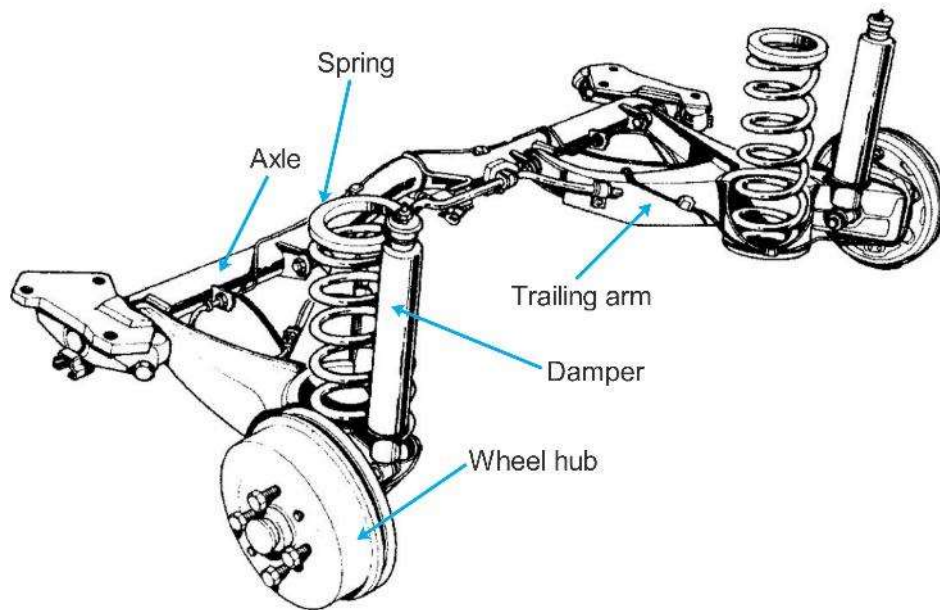


Figure 1.4 Trailing arm suspension system (Dixon, 2009)

## 1.2 DAMPERS

The early dampers employed the principle of Coulomb friction to dissipate the energy absorbed by the spring using solid elements such as rubber, inserted into leaf springs, and oiled leather found in Scissor and Snubber dampers (Dixon, 2007). These types of dampers soon went obsolete due to their tendency to lock up under small loads which would increase discomfort to the passengers. These friction type dampers were soon replaced by the fluid based dampers. One of the most successful and early fluid based damper was the rotary vane type damper. However, due to the requirement of lengthy seals and highly viscous hydraulic fluid, which increased their temperature sensitivity, the rotary type dampers were soon replaced by the telescopic dampers which are in use even today. The telescopic dampers are not only cost-effective to manufacture but also less critical about seal leakage and have better cooling apart from being easy to mount and install on the vehicle. Dixon (2007) classifies the telescopic dampers based on the method employed to accommodate the insertion volume of the piston rod as through-rod damper, double-tube damper and single-tube damper.

A through-rod damper, also known as a double-ended damper, consists of a piston connected to a piston rod that runs through both ends of a damper, as shown in Figure 1.5. The piston consists of orifices through which the fluid flows during damper



operation. The volume of the inserted part of piston rod is compensated by the volume of the piston rod going out of the cylinder at the same instant.

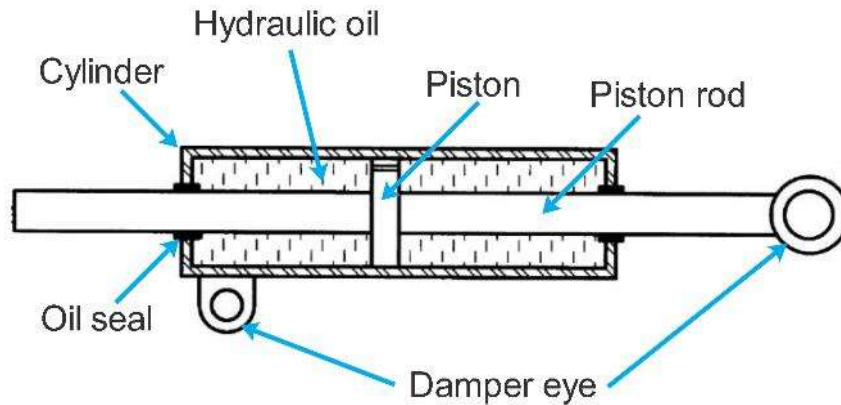


Figure 1.5 Through rod damper

It is an elegant solution to handle the issue of insertion volume compensation. However, it poses its own problems, such as increased pressure on the external seals at both ends, no provision for thermal expansion of the oil, and the protruding end may be inconvenient or dangerous during operation.

A double-tube or twin-tube damper, as the name suggests, consists of two concentric cylinders, as shown in Figure 1.6. The inner tube, also known as the pressure tube, houses the piston and the outer tube, also known as the reservoir tube, consists of some gas to accommodate the insertion volume of the piston rod.

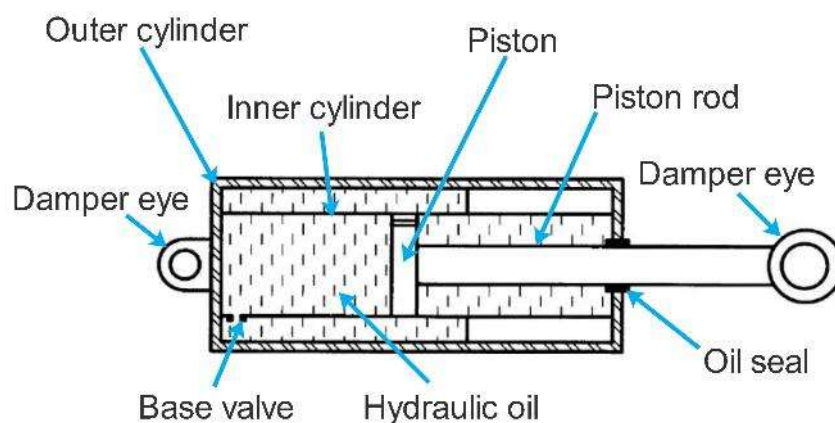


Figure 1.6 Twin tube damper

In this case, the orifices on the piston consist of shims that allow adjustments to the damping forces. The shims are flat discs that undergo circumferential bending to

allow fluid through the orifices on the piston under high pressure during the damper operation. The shim valves are the most common type of valves used in telescopic dampers due to their ease to setup accurately and yield consistent damping forces. The two concentric tubes are separated by a base valve which opens up when the pressure inside the pressure tube increases due to the piston rod entering the inner cylinder during operation. The volume of oil displaced by the base valve equals the volume of the piston rod entering the cylinder. The twin-tube damper solves the problem of a protruding piston rod, as seen in the double-ended damper case. However, it is always required to be installed in the upright position, i.e., the piston rod should always be connected to the vehicle body and the outer cylinder to the wheel to maintain fluid continuity between the inner and outer cylinders. This condition may limit its use where the installation space is a constraint.

The single-tube or monotube damper consists of a single tube, filled with hydraulic fluid housing the piston. The damping force can be adjusted using the valves on the piston. Pressurized gas accommodates the piston rod's insertion volume, which may mix with the hydraulic oil to become an emulsifier. Alternatively, another piston, known as the accumulator piston/floating piston, is used to separate the hydraulic oil and the pressurized gas, as shown in Figure 1.7.

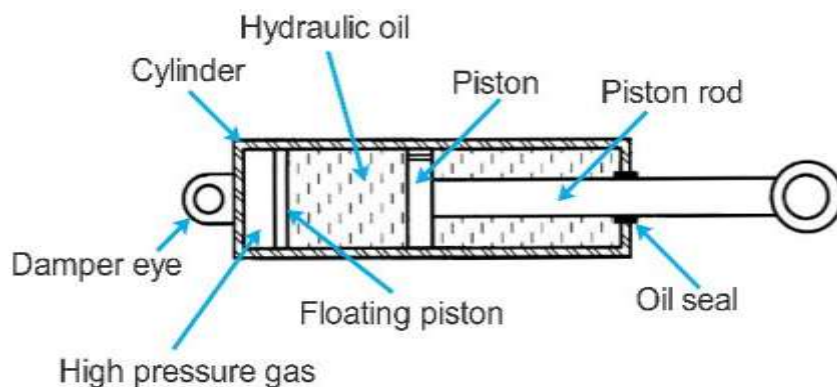


Figure 1.7 Single tube or Monotube damper

During operation, fluid movement through the orifices generates the required damping force, and the accumulator piston displacement occurs as per the volume of the piston rod entering the cylinder. The mono-tube damper is comparatively costlier and harder to manufacture due to high-pressure gas. However, unlike the twin-tube

damper, it is more compact and can be installed in any direction. Therefore, it is one of the most common types of telescopic damper that can be found on passenger vehicles even today.

### **1.3 CLASSIFICATION OF DAMPERS BASED ON METHOD OF ENERGY DISSIPATION**

A damper is an energy-dissipating device introduced in a vehicle suspension system to improve ride comfort and road handling. The ride comfort can be improved using a soft compliant damper, i.e., a damper with low damping force capacity. On the other hand, road handling can be improved using a hard damper, i.e., a damper with a high damping force capacity. Therefore, a damper tuned for ride comfort may not be best for road handling, and a damper tuned for road handling may not be best for ride comfort. Designing a damper for a vehicle suspension system is the art of satisfying these two conflicting criteria and based on the method employed to do so, the suspension system of modern vehicles can be classified as passive, active and semiactive suspension systems. All the types of suspension systems mentioned here can be explained using anyone of the mathematical models of four wheeler vehicles designed for evaluating the suspension performance. These models include the QCM, the half car model and the full car model.

A QCM represents  $1/4^{\text{th}}$  or a quarter of a car, i.e.,  $1/4^{\text{th}}$  the mass of the vehicle body, one spring, one damper and one wheel. The sprung mass represents a quarter of the vehicle body's mass, and the unsprung mass represents the mass of one of the wheels. The tire is represented in the QCM using a vertical spring and a damper as shown in Figure 1.8. The model assumes a single point contact between the tire and the road. The half car model, as the name itself suggests, represents half of the car and its components include a mass representing half the mass of vehicle body two springs and two dampers (front and rear), two unsprung masses representing the front and the rear axles along with wheels, as shown in Figure 1.9. The tires are represented using vertical spring and a dashpot system as done in case of QCM. The half car model is a four degree of freedom model; hence, it can be used to study the vertical motion of the two unsprung masses along with the heave and pitch motion of the sprung mass under various road inputs. A full car model is a seven degree of freedom system which

represents a complete four wheeler vehicle as shown in Figure 1.10. The vehicle body/sprung mass is represented with a rectangular slab with three degrees of motion. The four wheels can be represented by four separate unsprung masses in case of an independent suspension system, as shown in Figure 1.10, or the left and right side sprung masses can be combined to represent an axle with wheels in case of rigid axle suspension system. This model allows the user to study the vertical motion of each wheel along with heave, pitch and roll motion of the vehicle.

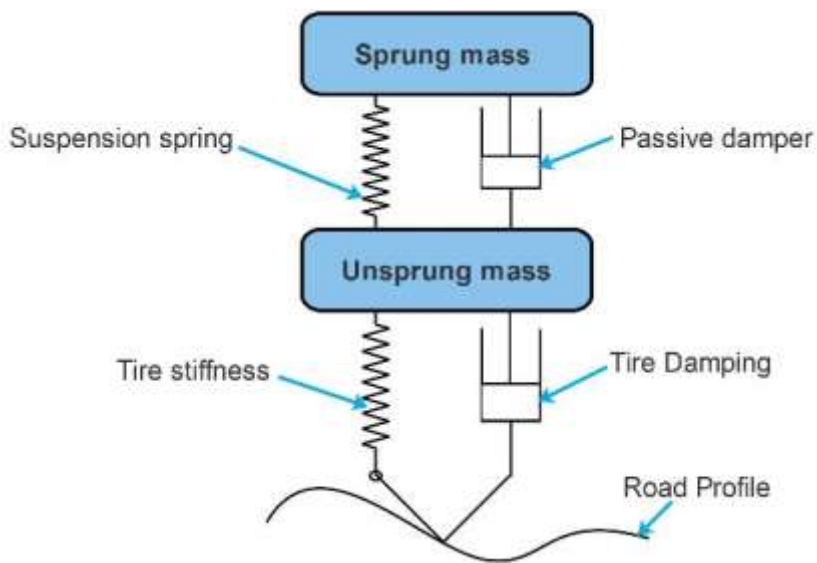


Figure 1.8 QCM

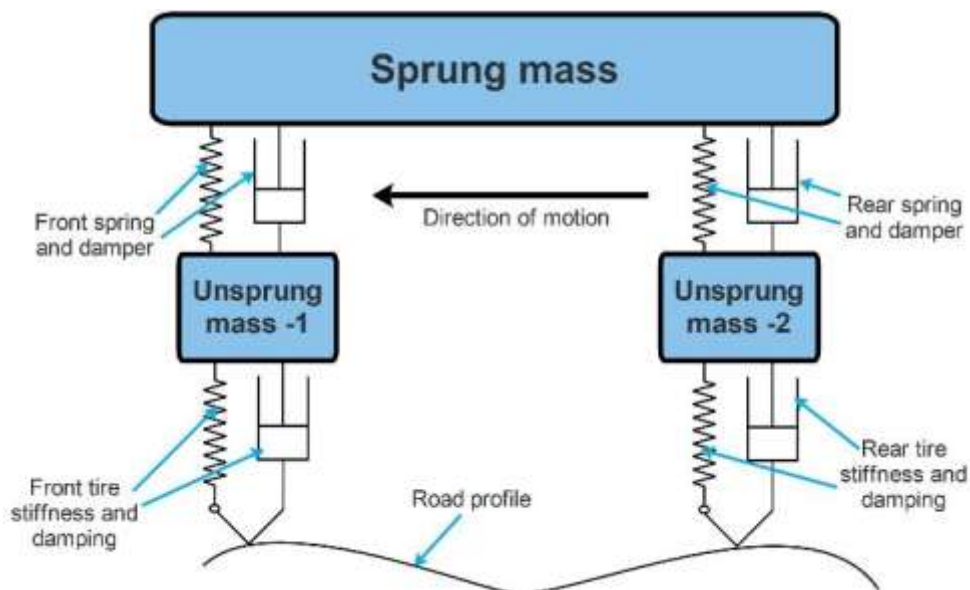


Figure 1.9 Half car model

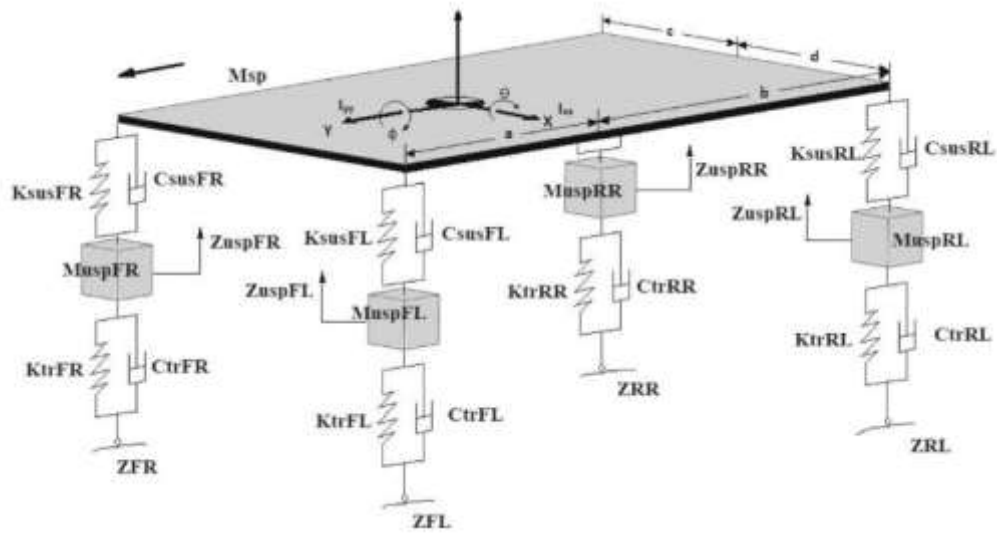


Figure 1.10 Full car model (Nigwal et al., 2022)

The passive, active and semiactive suspension systems have been explained in the following subsections using the QCM.

### 1.3.1 Passive suspension system

A passive suspension system is defined by the use of hydraulic dampers, which have been explained in the previous section in detail. As mentioned earlier, the passive dampers can be tuned for ride comfort or road handling. The passive dampers currently used on passenger vehicles are tuned to trade off some ride comfort for a small improvement in ride handling to achieve the compromise between the two conflicting criteria. In order to eliminate the need for this compromise, an active suspension system was invented. A schematic of a passive suspension system in the quarter car of the model vehicle can be seen in Figure 1.8.

### 1.3.2 Active suspension system

The most distinct feature of an active suspension system is the use of a hydraulic actuator instead of a damper. A passive damper dissipates the energy in the suspension system due to road undulations. In contrast, an actuator dynamically responds to the road profile by generating additional forces to induce relative motion between the vehicle body and the wheel (Sam et al., 2004). These additional forces are determined by a governing control law based on data received from the sensors onboard the vehicle.

The sensor data includes suspension variables such as the suspension displacement, wheel/body velocity and wheel/body acceleration. A schematic of an active suspension system in the QCM can be seen in Figure 1.11. The invention of active suspension was a huge leap in suspension systems. However, this system's high power requirement and cost limited its use exclusively in a few luxury vehicles. Hence, the concept of semi-active dampers came into existence.

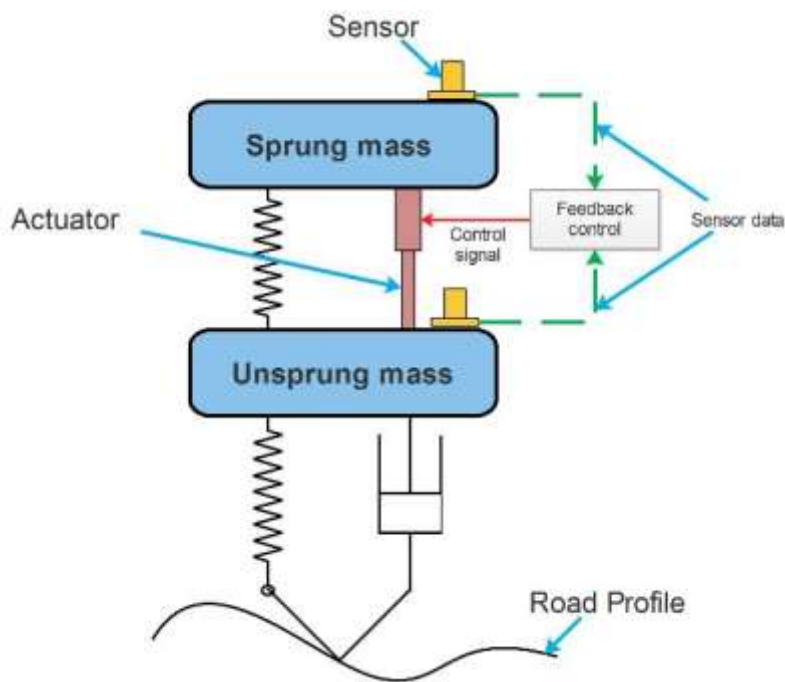


Figure 1.11 QCM with active suspension system

### 1.3.3 Semiactive suspension system

A semiactive system combines the energy dissipation function of a passive damper and the controllability of a hydraulic actuator resulting in a damper with controllable damping force. A controllable damper can vary its damping force readily during its operation on a moving vehicle in real time. A schematic of a semiactive suspension system in the QCM of a vehicle can be seen in Figure 1.12. The variability in damping force can be achieved either by varying the orifice size on the piston or by varying the viscosity of the hydraulic fluid. Those dampers that achieve variable damping by varying the size of the orifice are known as the Variable Orifice Dampers (VODs) and those dampers that achieve variable damping by varying the hydraulic fluid viscosity which can be done by employing a special class of fluid known as smart

fluids. Smart fluids can alter their rheological behavior in response to external stimuli such as electric fields and magnetic fields. The smart fluids responding to electric fields are termed as Electro-Rheological (ER) fluids and those that respond to the magnetic field are termed as Magneto-Rheological (MR) fluids. Among the VODs, ER fluid dampers and MR fluid dampers, VODs have the highest power requirement as these types of dampers require a solenoid or a similar device to operate. The ER and MR dampers consume comparatively low power and hence are preferred. Between the ER dampers and MR dampers, the ER dampers have a higher power requirement as the electric field necessary to achieve the variable damping requires a high voltage power source.

Further, a large amount of voltage is required to achieve a large variation in fluid viscosity. The MR fluid, on the other hand, requires only a fraction of the voltage required in the case of ER fluid to achieve the same amount of variability in fluid viscosity. Therefore, MR dampers are preferred over ER dampers, and the same is the focus of this study.

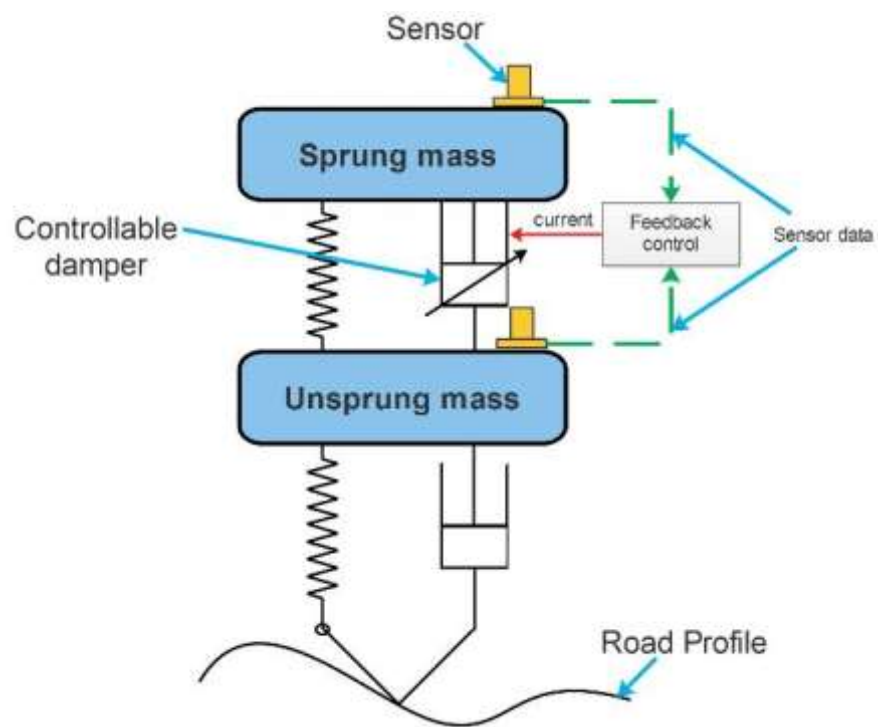


Figure 1.12 QCM with a semi-active suspension system

## 1.4 MAGNETO-RHEOLOGICAL FLUIDS

MR fluids are a class of fluids, known as smart fluids, that can change their rheological properties under the influence of a magnetic field. MR fluid can be defined as a suspension of micron-sized paramagnetic particles in a non-magnetic carrier fluid. The most commonly used paramagnetic particle for synthesis of MR fluid is the Carbonyl Iron Powder (CIP) obtained from the thermal decomposition of iron pentacarbonyl. Several carrier fluids have been employed for MR fluid synthesis. Some carrier fluids include hydraulic oils, silicone oils, mineral oils, paraffin oils, synthetic oils, silicone oils, hydrocarbon oils, silicon copolymers and water. Apart from the magnetic particles and the carrier fluid, the MR fluids comprise additives whose general objective is to prevent the rapid settling of the magnetic particles. However, some applications call for additives to improve durability, the operating temperature range, etc.

The MR fluids behave as a typical Newtonian fluid under normal conditions. However, under the influence of the magnetic field, the magnetic particles in the fluid align along the path of magnetic flux to form chain-like structures, as shown in Figure 1.13. These chain-like structures increase the resistance to fluid flow by transforming the MR fluid into a semi-solid, thus making the MR fluid behavior non-Newtonian. The strength of these chain-like structures in a particular MR fluid depends on the magnetic field strength.

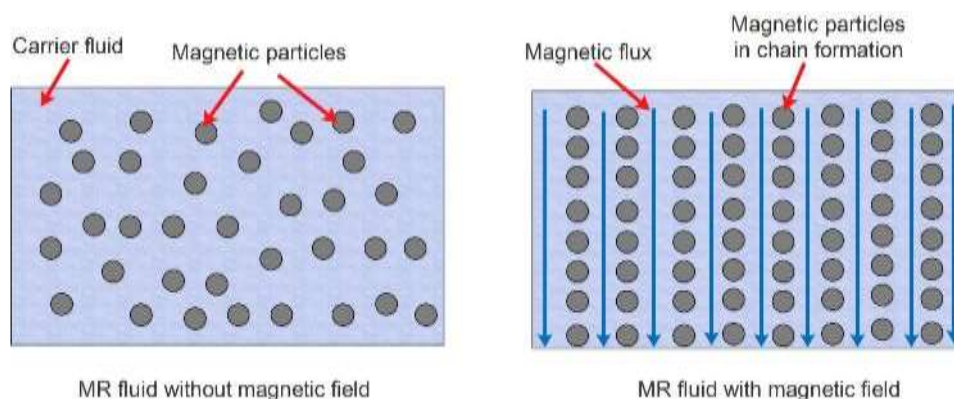


Figure 1.13 MR effect

Therefore, resistance to the flow of MR fluid can be varied by controlling the magnetic field strength. Therefore, the MR fluid is useful in numerous applications in



the field of engineering, such as MR dampers, MR brakes, MR clutches, MR mounts, prosthetic MR knees, MR-based polishing and many more. The MR fluids can be operated in three modes: shear, flow, and squeeze mode.

### 1.4.1 Shear mode

In shear mode, the fluid is sheared between two pole surfaces moving relative to each other, hence the name shear mode. The magnetic field is applied perpendicular to the direction of motion of pole surfaces in this mode, as shown in Figure 1.14.

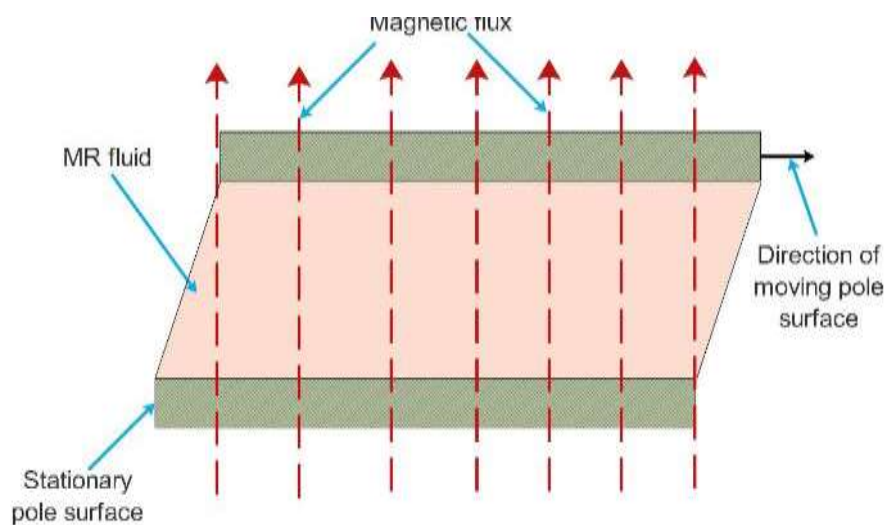


Figure 1.14 Shear mode

This mode of operation is commonly used in rotary devices such as MR clutches and MR brakes. Although it is the simplest operating mode to implement, it is the weakest as it requires a larger shear area to generate higher loads.

### 1.4.2 Flow mode

The MR fluid is said to be operated in flow mode when the fluid flows between two stationary pole surfaces due to pressure difference across, hence the name flow mode. The magnetic field is applied perpendicular to the direction of fluid flow, even in this case, as shown in Figure 1.15. This mode of operation is widely used in MR dampers and MR valves; hence it is also known as valve mode.

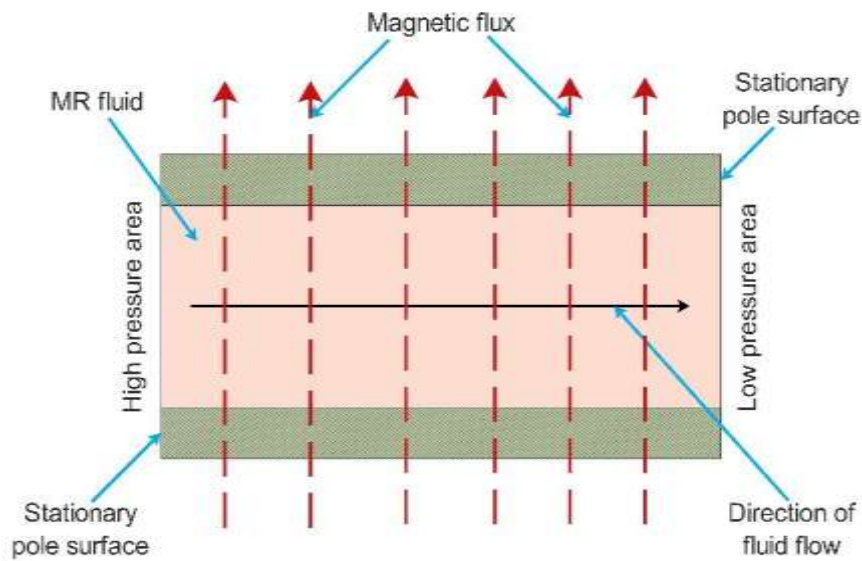


Figure 1.15 Flow mode or valve mode

### 1.4.3 Squeeze mode

This mode of operation is similar to the shear mode in the sense that it involves the pole surfaces being in motion relative to each other. However, its most distinctive feature is the direction of motion of the pole surfaces and the direction of the magnetic flux. As opposed to the perpendicular direction in the other two modes, this mode employs the magnetic field along the direction of the pole surface motion, as shown in Figure 1.16.

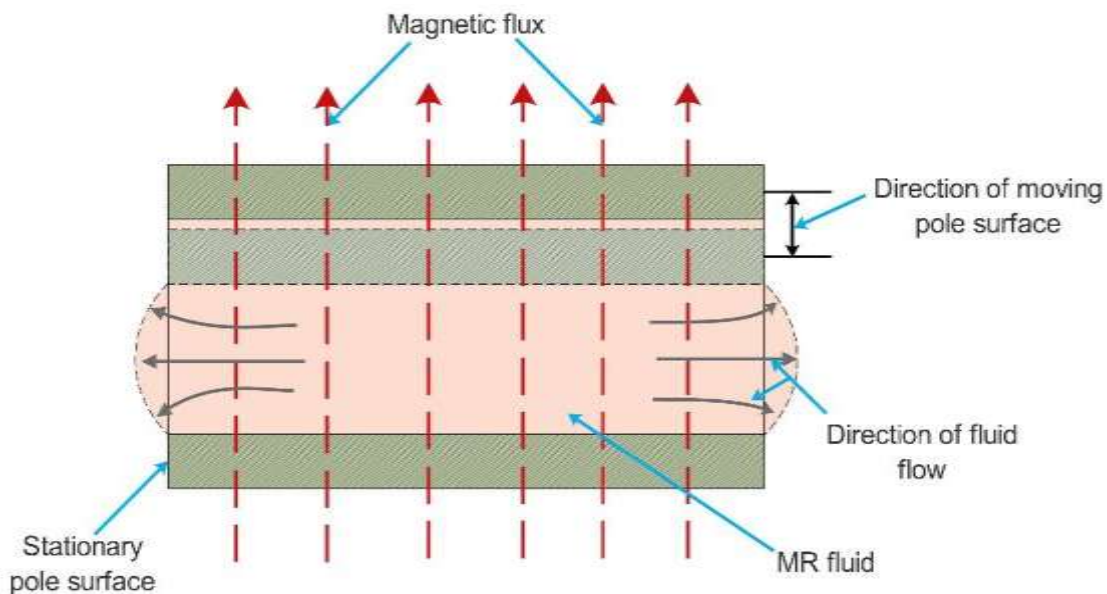


Figure 1.16 Squeeze mode

Therefore, this mode is implemented where large damping forces within small working spaces are a requirement, such as MR mounts. The study presented in this thesis focuses on MR dampers. Hence, the construction and working of a typical monotube MR damper have been described in the following section.

## 1.5 MR DAMPERS

As evident from the name, MR dampers are a class of hydraulic dampers that utilize a smart fluid, the MR fluid, instead of typical hydraulic oil. A typical monotube MR damper with a floating piston-type accumulator operating in flow mode is illustrated in Figure 1.17. The construction of an MR damper is similar to that of a passive damper. It consists of a piston with orifices sliding inside a cylinder filled with MR fluid. The piston comprises a core wound with copper wire to act as an electromagnetic coil, which generates the magnetic field required to activate the MR fluid flowing through the orifices or fluid flow gap and deliver a controllable damping force. The hollow piston rod carries the lead wires from the electromagnetic coil to the outside, where they can be connected to a power source.

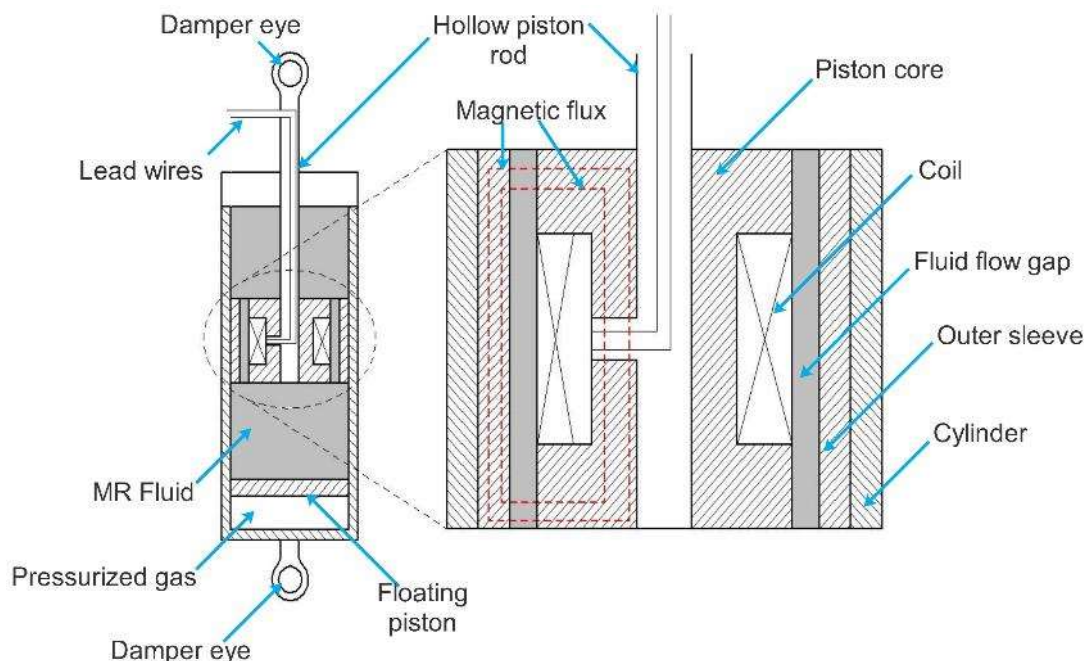


Figure 1.17 Monotube MR damper in flow mode

The narrow fluid flow gap between the piston core and the outer sleeve creates the pressure difference necessary to generate the viscous damping force when no

current is supplied, known as the off-state damping force. The magnetic circuit controls this pressure difference using the MR effect to deliver variable damping force. The magnetic flux is induced from the piston core, which then travels to the outer sleeve through the fluid flow gap via the pole near the piston rod, as shown in Figure 1.17. The magnetic circuit is complete when the magnetic flux travels back into the piston core at the pole away from the piston rod through the fluid flow gap.

The working principle of an MR damper operating in flow mode has been described in this section. It should be noted that a shear-mode MR damper would work similarly. However, the outer sleeve shown in Figure 1.17 would be absent in a shear mode MR damper. The fluid flow occurs between the piston core and the cylinder, as shown in Figure 1.18; as a result, the cylinder forms a part of the magnetic circuit.

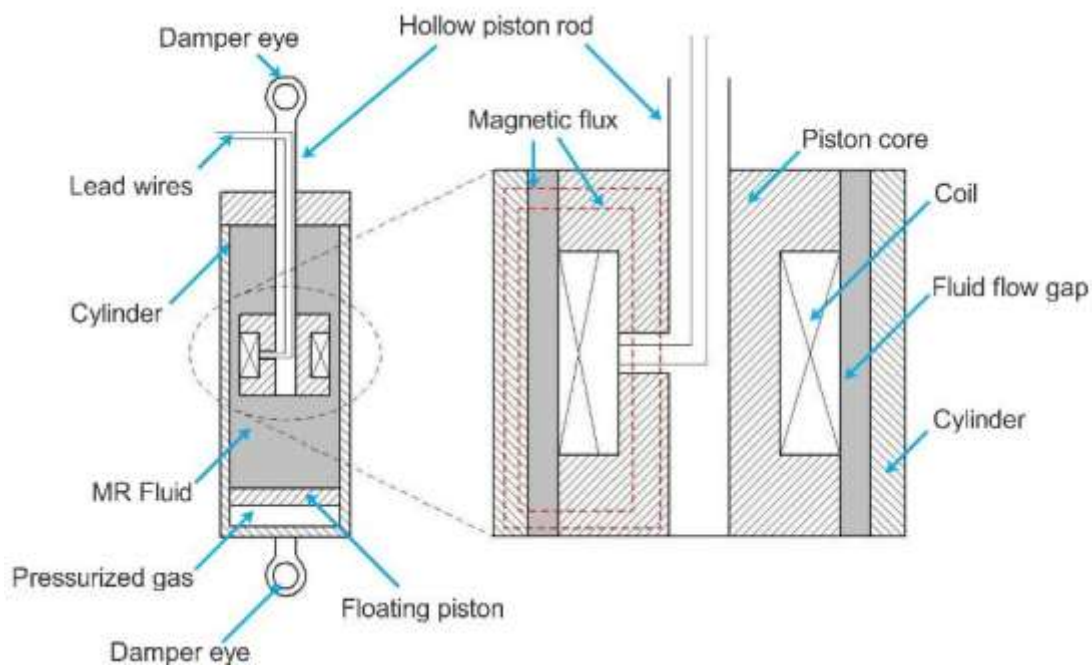


Figure 1.18 Monotube MR damper in shear mode

The other type of dampers, i.e., the twin tube and the double-ended hydraulic dampers, can also be converted into MR dampers in either flow mode or shear mode and their working principle would remain the same as described here.

## 1.6 SEMIACTIVE CURRENT CONTROL STRATEGIES

The current supplied to an MR damper in a semiactive suspension system is governed by a mathematical equation known as the control logic or control strategy. The decision of the magnitude and timing of the current supply to the MR damper is taken by the control strategy based on the suspension system data, such as the suspension displacement, vehicle body velocity, wheel velocity, vehicle body acceleration or wheel acceleration measured by the sensors onboard the vehicle. Skyhook control, Ground hook control, Proportional-Integral-Differential (PID) control, Linear Quadratic (LQ) control and Sliding Mode control (SMC) are some of the most widely used and notable control strategies (Choi and Han, 2012).

The skyhook control logic assumes an imaginary friction damper, with a damping coefficient of  $C_{sky}$ , connected between the sprung mass and the sky, hence the name skyhook control. This control strategy aims to improve the ride comfort of the vehicle independent of the wheel motion and the road profile. The control logic supplies current to the MR damper, to deliver the same damping force as the imaginary friction damper shown in Figure 1.19.

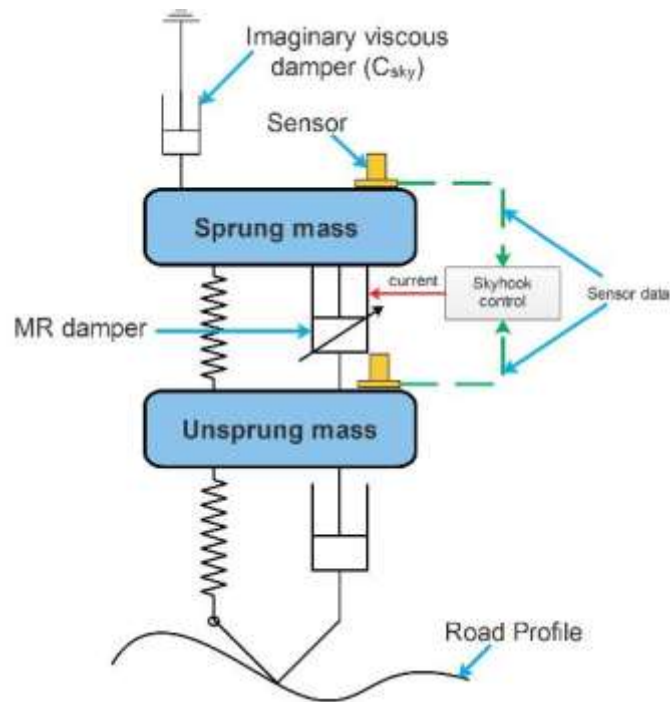


Figure 1.19 Schematic of skyhook control strategy

The ground hook control strategy works on the same principle as the skyhook control but with the difference that the imaginary friction damper with damping coefficient  $C_{ground}$  is assumed to connect the wheel with the ground, hence the name ground hook control. This control strategy aims to reduce the vertical vibration of the unsprung mass, thereby improving road handling independent of the sprung mass motion. The working of these two control logics has been depicted in Figure 1.20.

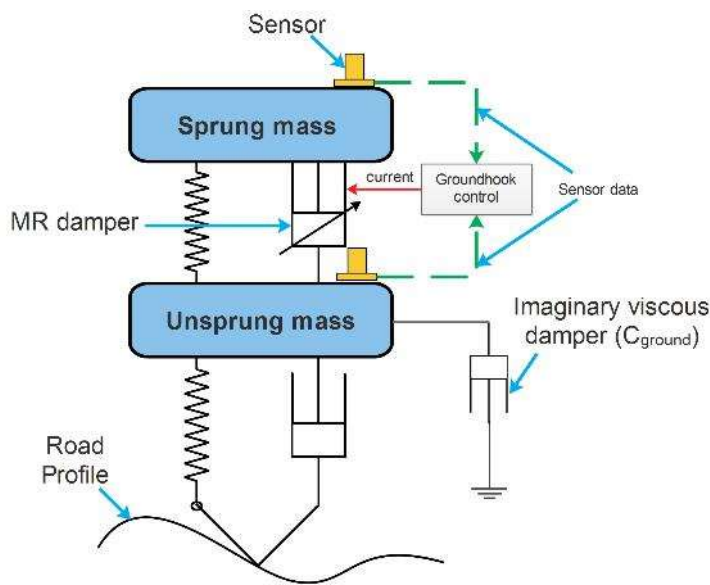


Figure 1.20 Schematic of ground hook control strategy

The PID control is well known for its ease of implementation in real time. A schematic of its implementation can be seen in Figure 1.21.

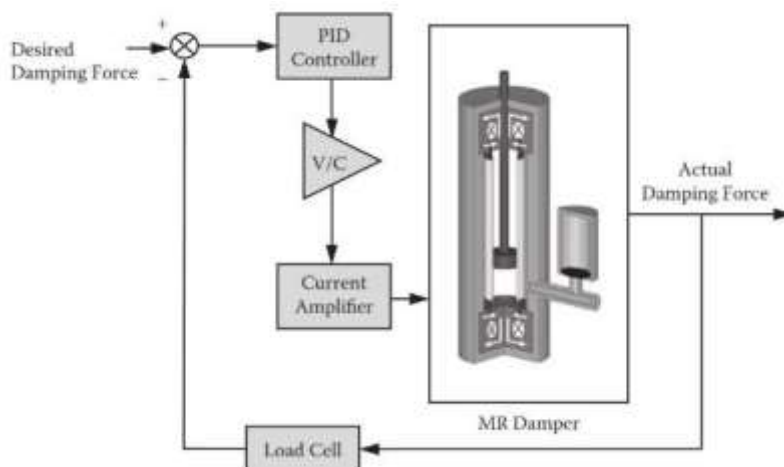


Figure 1.21 Schematic of a PID controller for MR dampers

The P controller by itself is an amplifier, the I part of the controlled eliminated the steady state error and the D controller is responsible for stability in the system. Determination of these control coefficients through an appropriate method would results in a superior performance of the controller.

The LQ control assumes the plant to be a linear system in the form of state space and the performance index is assumed to be a quadratic function of the control inputs and plant states. This leads to development of control laws that are linear which are easier to apply and analyze. The SMC is one of the oldest methods of control whose literature can be dated back to the days of Soviet Union. The salient feature of the SMC is its ability to exhibit robustness against the uncertainties of the system and external disturbances.

## **1.7 ORGANIZATION OF THESIS**

The thesis consists of seven chapters, and the summary of each chapter is as follows:

**Chapter 1** gives a brief history of the evolution of automotive dampers from dry friction type to modern controllable MR dampers. The reader is also introduced to the types of suspension systems, MR fluids, working of MR dampers and control strategies to improve automotive suspension.

**Chapter 2** provides a detailed literature review carried out for this thesis work. This chapter highlights the significant contributions made by researchers to designing, developing, and implementing MR dampers in automobiles. This chapter describes the objectives for carrying out the work based on the literature review. This chapter also contains the methodology used to accomplish these objectives.

**Chapter 3** discusses the characterization of a commercial MR damper. The MR damper is mathematically represented using the MFM. The performance of the MFM is compared against the EDM based on the simulation response of a semiactive seat suspension system while implementing the skyhook control strategy. The performance of the two damper models is also compared based on the simulation time of the seat suspension system.



**Chapter 4** discusses the design of a MR damper for application in the test vehicle, Force Motor's – Traveller. The critical dimensions of the piston are optimized to obtain the maximum possible controllable damping force. The magnetic circuit of the designed damper is simulated in the Finite Elements Methods Magnetics (FEMM) software. The MR damper with optimized dimensions is fabricated and evaluated on the damper testing machine. The MR damper is later installed on the test vehicle, which is run over a sharp speed bump while implementing the skyhook and ground hook control. The performance of the developed MR damper is compared against the stock passive damper. The cost of fabricating the developed MR damper is evaluated and compared against the commercial MR damper.

**Chapter 5** presents the development of a cost-effective MR fluid to further reduce the overall cost of the MR damper. The optimal composition of CIP in the silicone oil is obtained while considering the cost of the MR fluid. The performance of the in-house MR fluid is compared with commercial MR fluid, in the rheometer, in MR damper on the damper testing machine and the test vehicle subjected to the same tests discussed in chapter 4. The overall cost of developed MR damper with the optimized MR fluid is evaluated and compared with that of commercial MR fluid at the end of this chapter.

**Chapter 6** discusses the development of an acceleration-based skyhook control strategy. The proposed control strategy is compared against the conventional skyhook control based on the response of the experimental setup of a SDOF and its simulation time in MATLAB software.

**Chapter 7** draws significant conclusions from the work presented in this thesis and also presents the future scope of the work.



## CHAPTER 2

### LITERATURE REVIEW AND RESEARCH METHODOLOGY

#### 2.1 INTRODUCTION

The invention of MR fluid gave birth to a new area of research on controllable devices, especially MR dampers in automobile suspension systems. Therefore, it is imperative to look at some notable studies conducted towards designing an MR damper, mathematically modelling its damping behavior, optimization MR fluid for improving performance of MR damper and development of current control strategies to improve the performance of semi-active suspension systems.

#### 2.2 MAGNETO-RHEOLOGICAL FLUID (MR FLUID)

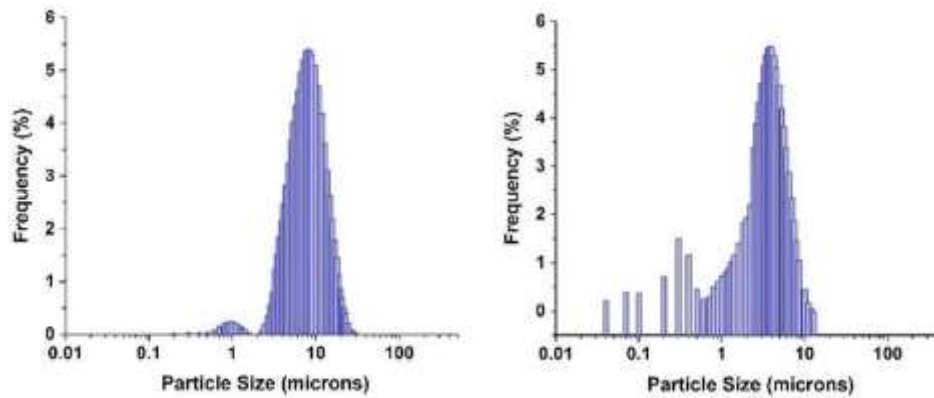
Rabinow (1948) first used MR fluid to develop a magnetic fluid clutch. Since then, extensive research has been done to improve these fluids (Ashtiani et al. 2015). Some notable studies include Shulman et al. (1986), who developed and patented a MR fluid whose performance was evaluated for application in MR suspension systems, Shulman et al. (1987) developed and studied the structural, physical and dynamic properties of MR suspensions and Kordonsky (1993) developed MR fluids exclusively for MR valves. The investigators from Lord Corporation, USA, Carlson and Weiss (1995) patented MR fluid with iron-alloy particles. Although the iron-alloy based MR fluids performed well, their high cost limited their applications.

Ginder et al. (1996) found that the rheology of MR fluid depends significantly on magnetic nonlinearity and saturation. Moreover, the maximum magneto-rheological performance was observed when magnetization saturated at higher fields. MR fluids' magnetostatics was modeled using numerical and analytical techniques. The effect of the saturation magnetization, particle size and volume fraction were studied by Genç and Phulé (2002). The study revealed that the dynamic yield stress increased with increased volume fraction of the magnetic particles. The MR fluid with smaller particles resulted in lower yield stress than those with large particles. It was suggested that this could be due to lower saturation magnetization in the presence of finer particles. Ierardi and Bombard (2009) optimized the yield stress and the off-state viscosity of the fluid

using a design of experiments approach, which was useful for viscosity optimization. Three types of CIP were utilized in this study as mixture components; coarse, medium and fine. The yield stress and the off-state viscosity were considered to be the mixture response. The approach employed in the study was useful for determining the optimal solution for minimum off-state viscosity only.

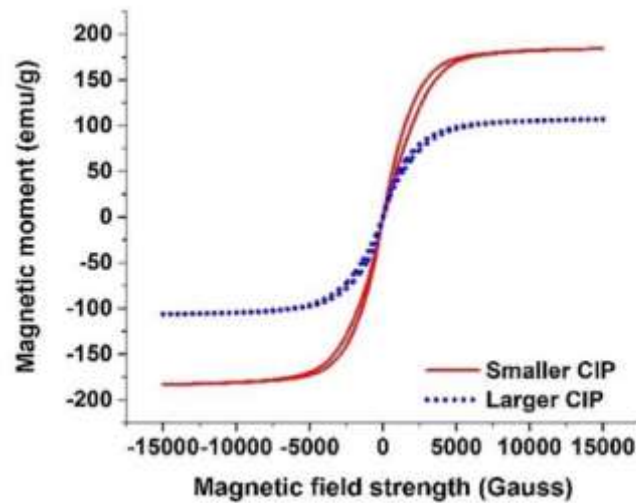
Sarkar and Hirani (2015) studied the effect of particle size on the rheology of MR fluid, and nine MR fluid samples were studied that consisted of small, large and mixed-sized CIP with three concentrations by volume. Increased volume fraction was found to work better with mixed-sized particles than small or large-sized particles at a higher shear rate. Chiriac and Stoian (2010) studied particle size distribution's effect on MR fluid performance. They found that the MR fluids with large-sized particles with narrow size distributions exhibited higher yield stress. Gurubasavaraju et al. (2017) determined the optimal volume fraction of iron particles in MR fluids. They optimized the dimensions of a shear mode MR damper using particle swarm optimization and response surface technique. The rheological characterization of the MR fluid samples revealed that the fluid gap influenced the shear stress at all magnetic field magnitudes. The study also revealed that the damping force of a shear mode damper is significantly affected by the current supplied and the fluid flow gap in the damper.

Mangal and Sharma (2017) considered the objectives to maximize the yield stress and minimize the off-state viscosity of MR fluids using analysis of variance and artificial neural network techniques. The study concluded that the MR fluid's yield stress mainly depends on the volume fraction of the magnetic particles and the viscosity of the carrier fluid. Acharya et al. (2019) employed a multi-objective genetic algorithm and analysis of variance to determine the optimal parameters of MR fluid and a monotube MR damper. The iron particles of two sizes were considered for the study, whose size distribution and magnetic properties can be seen in Figure 2.1. The study revealed that the MR fluid with larger-sized particles generates maximum damping force. However, a similar study was conducted by Acharya et al. (2021) to design MR fluid for brake application and optimize the geometrical parameters of the MR brake. It was found that the smaller-sized iron particles and low-viscosity silicone oil generated higher braking torques.



(a)

(b)



(c)

Figure 2.1 (a) Particle size distribution of Large sized CIP – Sigma Aldrich – 44890 (b) Particle size distribution of Small sized CIP – Sigma Aldrich – C3518 (c) Magnetic moment vs Magnetic field strength curve of 44890 and C3518 (Acharya et al. 2019)

Wang et al. (2019) studied the effect of the particle size, the weight fraction of particles and the viscosity of the carrier fluid on the performance of MR grease. A novel technique was used to prepare the grease, and four types of analysis were carried out to determine its performance. It was found that the viscosity of silicone oil and the weight fraction of the carrier fluid primarily affect the field-induced yield stress of the MR grease.

Pandian et al. (2022) studied the viscous behavior of MR fluids with silicone-based additives. The study revealed that MR fluids with higher particle loading are more suitable for automotive applications. It can be observed from the literature review that the performance index used to design the parameters of MR fluids is generally either the rheology data or the damping force/braking torque (in the case of dampers/brakes and clutches). Recently, TharehalliMata et al. (2022) used the simulated response of a three-wheeler vehicle to study the performance of MR fluids with flake-shaped particles. The study employed two models of MR damper based on the shear mode and the flow mode of operation of MR fluids. The damping forces predicted with the two models were modeled using a non-parametric polynomial model and used in simulating a three-wheeler semiactive suspension employing Proportional-Integral-Differential control. The performance of a semiactive suspension was compared with that of a passive suspension based on ride comfort and road handling.

### **2.3 MODELING OF MR DAMPERS**

Mathematical equations that govern the damping behavior of MR dampers are defined as MR damper models. These models are crucial in designing an MR damper, simulating the MR damper in a system and developing current control algorithms. As a result, it has been an area of interest for researchers working with semiactive devices. Wang and Liao (2011) and Rossi et al. (2018) classify the existing MR dampers models into quasistatic and dynamic models.

#### **2.3.1 Quasistatic models**

Quasistatic models use Bingham plastic model of MR fluid to describe the damping behavior of MR damper. Phillips (1969) developed a quintic equation with non-dimensional variables to determine the pressure gradient across a parallel plate duct. Wereley and Pang (1998) developed a similar model for parallel plate ducts but with a different set of non-dimensional variables. The Herschel-Bulkley model for MR fluid was also used to model the fluid flow through parallel plate ducts (Lee et al., 2002; Wang and Gordaninejad, 2000; Chooi and Oyadiji, 2008; Chooi and Oyadiji, 2009a; Chooi and Oyadiji, 2009b; Hong et al., 2008). The quasistatic models have not been sufficient for the intrinsic non-linear damping behavior of MR dampers; hence, their

use is limited only till the design stage of an MR damper. The dynamic models were introduced to overcome the limitations of quasistatic models.

### 2.3.2 Dynamic parametric models

The dynamic models can be further classified as parametric and non-parametric models. The parametric models use a collection of linear and/or nonlinear spring dampers and other physical elements to characterize the damping behavior of MR dampers. The parameters of these physical elements are identified by minimizing the error between the damper's experimental data and the model's simulated response (Wang and Liao, 2011; Rossi et al., 2018). A number of parametric models have been explored and validated in the past. The notable ones have been presented here.

Bingham-model-based dynamic models, as shown in Figure 2.2 employ a combination of a Coulomb friction element in parallel with the viscous dashpot to predict the damping force of a MR damper (Spencer et al., 1997). Piecewise variations of this models have also been presented in the past. The Bingham plastic models of MR dampers were soon outdated due to their inability to represent the dynamic behavior of the MR damper under small deformations and low shear rates (Occhiuzzi et al., 2003; Gamota and Filisko, 2010).

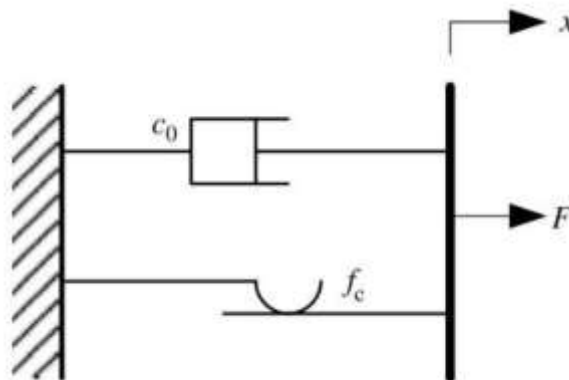


Figure 2.2 Bingham model (Wang and Liao, 2011)

The Biviscous models were introduced assuming that the MR fluid remains plastic in both pre-yield and post yield conditions (Wereley et al., 1998; Pang et al., 1998; Kamath et al., 1999). A number of variations of the biviscous models can be

found, one of which required nearly ten parameters to be identified to shape the predicted hysteresis curve of a MR damper (Snyder et al., 2001; Sims et al. 2004; Sims et al., 2000).

Viscoelastic–plastic models were developed by considering pre-yield and post-yield force components of the damping force. Wereley et al., 1999; Kamath and Wereley, 1997; Kamath and Werely 1997b). Li et al. (2000) improved the Viscoelastic–plastic model previously developed by considering the stiction effect from the piston seal. The stiffness–viscosity-elasto-slide models employs an elasto-slide element in the model, hence the name. it requires four set of parameters to represent the hysteresis curve (Hu and Wereley, 2008).

Bouc–Wen hysteresis operator-based models, as shown in Figure 2.3, presented their unique ability capture any hysteresis behavior, from the inelastic stress strain curve of materials to the damping behavior of MR damper, which has made them one of the most applied mathematical models in the field of MR damper (Spencer et al., 1997l; (Dominguez et al., 2004; Yang et al., 2004).

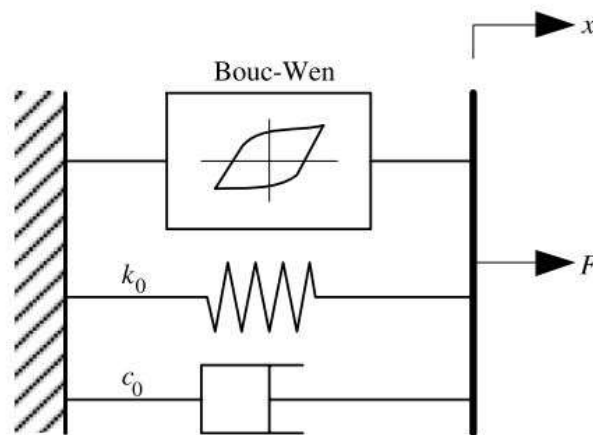


Figure 2.3 Bour-Wen model (Wang and Liao, 2011)

The variations in the Bouc-Wen models were observed in terms of its coefficient being represented as a function various parameters such as current , frequency or amplitude (Dominguez et al., 2006a; Dominguez et al., 2006b; Dominguez et al., 2008). The Dahl hysteresis based model was originally proposed to represent the strain

curve of a material, however, it takes a general form of the Bouc-Wen hysteresis model when applied to the MR dampers (Ikhouane and Dyke, 2007).

LuGre hysteresis operator-based models interpret the fluid in a damper as a set of interlocking bristles between two surfaces and the friction between these bristles is modelled by considering their bending forces along with relative velocity of the two surfaces and the viscous friction (Jiménez and Alvarez, 2002; Sakai et al., 2003; Terasawa et al., 2004). This model was later modified for application in MR fluid by considering the stiffness and damping coefficients which results in six current dependent coefficients (Jiménez and Álvarez-Icaza, 2005; Canudas-de-Wit et al., 1998; Lischinsky et al., 1999).

Kwok et al. (2006) presented a model based on the hyperbolic tangent based function whose simplicity made it computationally efficient than its predecessors. Sigmoid function-based models were developed to represent a particular hysteresis curve by knowing its various parameters such as the maximum force, maximum velocity, force intercept, velocity intercept, transition force, transition velocity and slope of the curve (Wang et al., 2003; Ma et al., 2007; Ma et al., 2002; Ma et al., 2006).

Equivalent models were proposed considering two spring elements, a viscous element and a coulomb friction element (Oh, 2004; Oh and Onoda, 2002). The resulting model contained a set of four current dependent variables to represent the MR damper behavior. The phase transition models were proposed by Wang and Kamath (2006) using the phase transition theory in which the shear rate is formulated in the form of a convex function of shear stress.

The parametric models, although successful, present their own challenges. The approach to identifying the model parameters through minimization of error between the experimental and simulated values could be divergent in case the model structure is flawed or the constraints imposed on the parameters are improper. It could also result in parameters such as negative mass or stiffness (Wang and Liao, 2011).

### 2.3.3 Dynamic non-parametric models

The non-parametric models consider analytical expressions that employ both experimental data and the physics of the MR damper to model its behavior. These models have been found to fulfill the shortcomings of parametric models.

The non parametric polynomial model, proposed by Choi et al. (2001), as shown in Figure 2.4, generalizes the hysteresis curve in two parts that is later represented by polynomials. Kim et al., 2008 applied this model to squeeze film dampers. Song et al. (2005) presented the multifunction model which was experimentally verified and its performance was compared with a parametric model and based on numerical efficiency, ability to represent force saturation and operating range accuracy. Song et al. (2005b) employed this model in simulating a single degree of freedom system with MR damper subjected to base excitation and Song et al. (2007) implemented this model into experimental evaluation of a seat suspension model with MR damper.

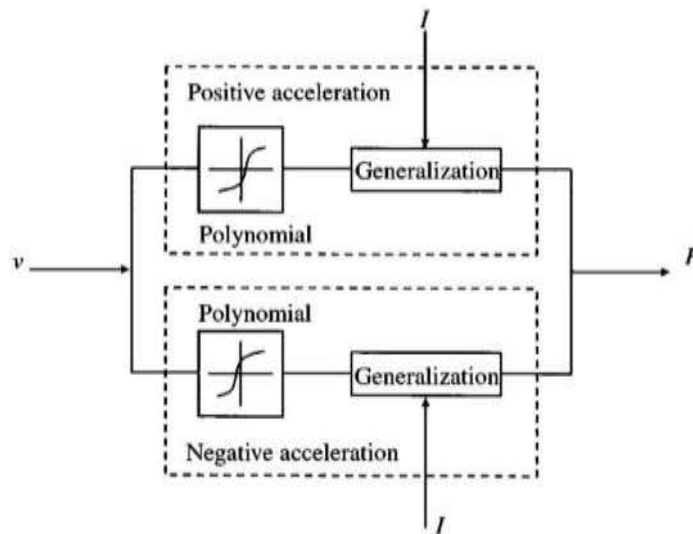


Figure 2.4 Polynomial model (Choi et al., 2001)

Jin et al., (2001) presented a black-box model predicts the MR damper behavior by considering a model as a sequence of functions that represent a method to predict the present output from previous observations. Jin et al. (2002) presented the ridgenet approach to model the MR damper using black-box model and Jin et al., (2005) implemented it for control of civil structures. Leva and Piroddi (2002) presented a NARX-based technique to model the MR damper behavior whereas Savaresi et al.



(2005) and Yijian et al. (2006) presented semi-physical and non-linear models based on black-box models for implementation in vehicle damper control.

Mori and Sano (2004) along with Koga and Sano (2006) took a data based approach to determine a way to predict the damping force of a MR damper at a given velocity and current input along with a way to find the current voltage that would generate the required damping force which led to development of the query-based model.

The neural network model, as depicted in Figure 2.5, is one of the MR damper models that can be classified as the intelligent models (Burton et al., 1996; Chang and Roschke, 1998). These models were implemented for the MR dampers due to their unique ability to be universal approximators (Kim and Roschke 1999). Considerable improvement of this model has taken place in the past (Cao et al. 2008; Chang and Zhou 2002; Du et al. 2006; Wang and Liao 2005; Wang et al. 2002).

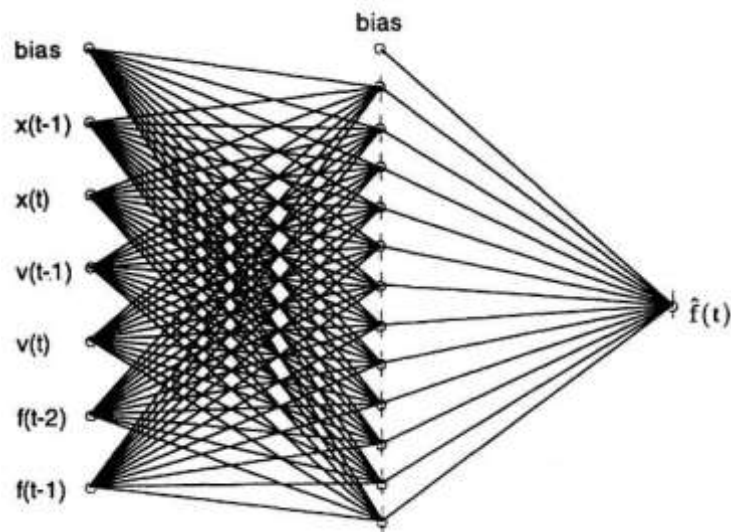


Figure 2.5 Neural network model of a MR damper (Chang and Roschke, 1998)

The fuzzy model is the other intelligent model, depicted in Figure 2.6, which is capable of quantifying and inducting the human experience in its laws of mapping. (Schurter and Roschke, 2000; Schurter and Roschke, 2001; Schurter and Roschke 2001b). The need to trade-off precision for the cost of fitting in case of traditional models is one of the reasons to choose the fuzzy models (Atray and Roschke, 2003; Atray and Roschke, 2004; Kim and Roschke, 2006; Kim and Roschke 2006b).

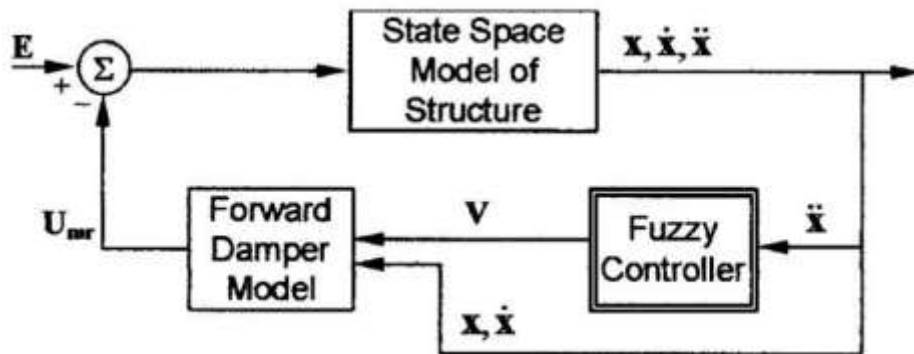


Figure 2.6 Block diagram of semiactive control with fuzzy controller (Schurter and Roschke, 2001b)

The MFM, developed by (Bakker et al. 1987) for representing the steady state characteristic tire behavior, has found its application in modelling the MR damper mainly due to the similarity between the steady state characteristic graph of tire, shown in Figure 2.7, and the characteristic graph of a MR damper.

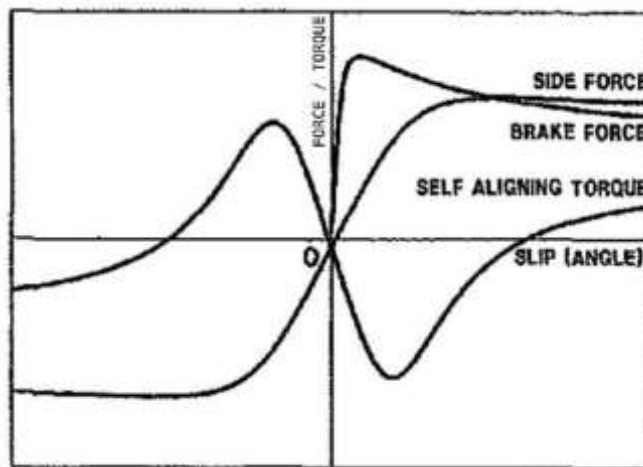


Figure 2.7 Steady state characteristic graph of a tire (Bakker et al. 1987)

## 2.4 STRUCTURE OF MR DAMPERS AND THEIR OPTIMIZATION

### 2.4.1 Structure of MR damper piston

The structure of a typical monotube, twin-tube and double-ended MR damper has been explained in detail in section 1.4 of Chapter 1 of this thesis. These MR dampers depict one of the earliest designs of MR dampers with a limited effective channel, i.e., the active region of the MR fluid in the fluid flow gap of the piston, which directly

affects the damping force. Therefore, increasing the length of the active region or the effective channel is one of the objectives in designing an MR damper which has given rise to several innovative piston designs, some notable ones have been discussed in this section.

The length of the effective channel could be increased using multiple coils instead of a single coil design (Hu et al., 2016; Lau and Wei, 2006; Yang et al., 2002); Zheng et al., 2014; Gavin et al., 2001; Wilson et al., 2013). The multi-coil design allowed a considerable increase in the damping force with the application of a small increase in current. The success of the multi-coil design led to the development of a three-coiled seismic MR damper by LORD Corporation, USA, as shown in Figure 2.8 (Goncalves, 2005).

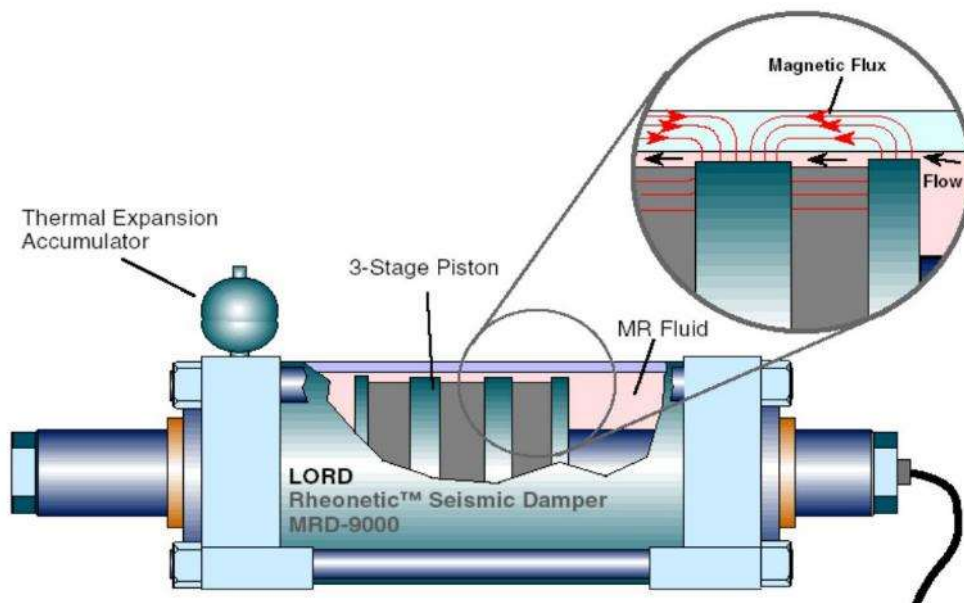


Figure 2.8 Multicoil Seismic damper - LORD Corporation, USA (Goncalves et al. 2006)

Sassi et al. (2005) presented an innovative piston design with multiple coils, which provided an effective channel length equal to the length of the piston itself. The increased effective channel length was achieved by making the coil axis perpendicular to the damper axis, as shown in Figures 2.9 and 2.10. This configuration would cause the magnetic flux to pass through the fluid flow gap radially along the entire length of the piston. Although this design presents a solution to increase the effective channel length, it does not solve the problem of reduced stroke of the damper that existed even

in the conventional multi-coil design. Moreover, the current requirement for the same amount of controllable damping force is higher in the case of the proposed design than the conventional multi-coil design.

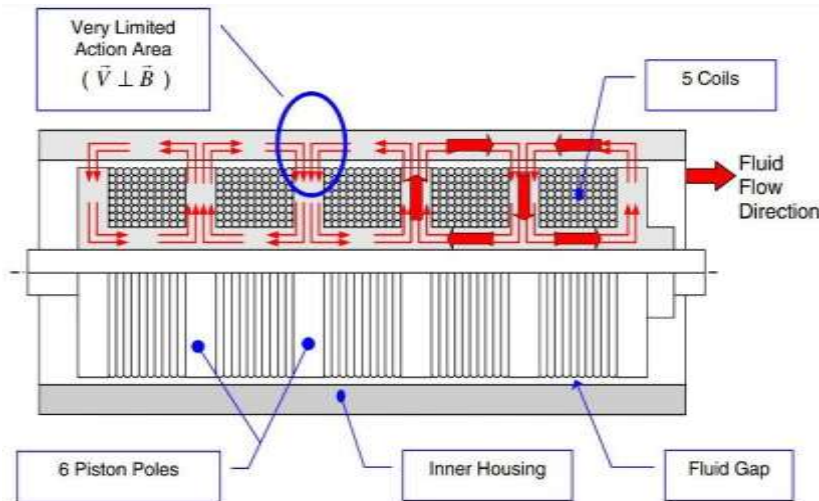


Figure 2.9 Conventional multicoil design (Sassi et al., 2005)

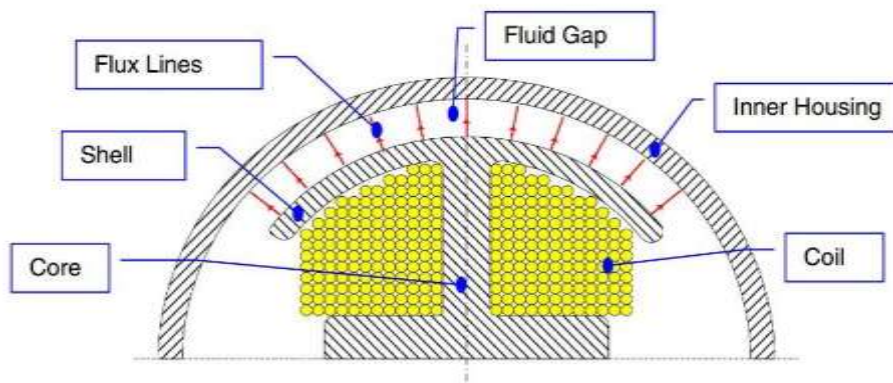


Figure 2.10 Radial flux multicoil MR damper piston design (Sassi et al., 2005)

Piston designs with single coaxial coils and multiple annular flow gaps have also been presented in the past (Bai et al., 2013). However, these designs could not increase effective channel length to cause any significant improvement in the dynamic range of the MR damper. Moreover, they require extensive optimization of the piston components. In the conventional annular design, the axially flowing fluid is unaffected by the magnetic flux, as seen in Figure 2.9. Hence, many studies were conducted to develop external MR valves to accommodate a radial flow of fluid (Ai et al., 2006; Nguyen et al., 2007; Nguyen et al., 2008; Aydar et al., 2010). However, Bai et al. (2013)

developed an annular radial duct MR damper featuring an integrated piston that allows axial and radial fluid flow through its annular fluid flow gap, as shown in Figure 2.11. The main advantage of the proposed design was the increased active region of the fluid flow gap without the need for multiple coils (coaxial or radial).

The piston designs with multiple coils and radial flow paths increase the effective channel length; however, the stroke and the off-state damping force of the MR damper, respectively, get affected. The conventional piston design suffers from demanding design requirements, increased piston head weight, reduced heat dissipation, inconvenient assembly, inflexible replacement and shorter damping channel. However, its efficiency in providing a high dynamic range, and a simple structure with relatively low cost in a compact and robust package have made it one of the most utilized designs in the suspension systems of passenger vehicles (Yuan et al., 2019; Zhu et al., 2012).

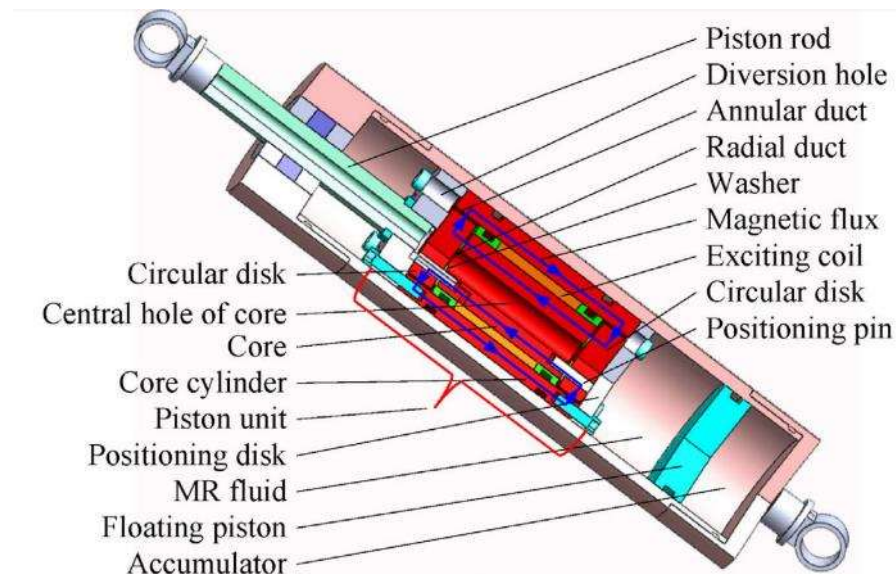


Figure 2.11 Annular piston with axial and radial fluid flow path (Bai et al., 2013)

## 2.4.2 Optimization of MR dampers

Generally, optimization of an MR damper involves determining the dimensions of the electromagnetic coil and fluid flow gap while meeting the user requirements. These requirements may include high dynamic range, high on-state force, low power consumption, low manufacturing cost and low time constant. It should also be ensured

that magnetic saturation does not occur in piston components and MR fluid. Researchers in the past have presented several ways to achieve this objective; a few notable ones reviewed by Rahman et al. (2017) have been presented in this subsection.

Gavin et al. (2001) optimized a multi-coil seismic MR damper to minimize the coil's time constant and electric power consumption. The damping force, the saturation flux density of the piston core material, maximum current, maximum voltage and overall piston dimensions were considered constraints. A Hessian of the objective function with respect to the design parameters was conducted to determine the manufacturing tolerances, and a sequential least squares method was employed to solve the constrained optimization problem.

Nguyen and Choi (2009) presented a general procedure to optimize MR valves. The objective of the optimization problem was to find the optimal geometric dimensions of flow ducts and coils to minimize the valve ratio, i.e., the ratio of field-dependent pressure drop to the viscous pressure drop, while considering the cylindrical volume of the valve as a constraint. The optimization is carried out via a golden-selection algorithm, and a local quadratic fitting technique is presented using the ANSYS parametric design language. The design procedure is used to optimize different valve configurations with the same specific volume, and the results are compared with the analytical ones. The same optimization procedure could be followed by considering the damping force, dynamic range or control energy, and the time constant as the objective functions (Nguyen and Choi, 2009; Nguyen et al., 2008).

Mangal and Kumar (2015) optimized the geometrical parameters of the MR damper using Finite Element Methods (FEM) coupled with the design of experiments through the Taguchi approach, considering the damping force as the objective function. Krishna et al. (2017) employed design of experiments and genetic algorithm approaches to determine the optimal dimensions of a twin-tube MR damper. Desai et al. (2019) designed a twin-tube MR damper for application in the semiactive suspension of a passenger van using the Taguchi analysis and the FEMM.

Gurubasavaraju et al. (2017b) evaluated the effectiveness of the magnetic and non-magnetic materials selected for the shear mode MR damper cylinder using FEM.

Further, the MR damper design was optimized to maximize the magnetic flux density and thereby improve the performance of the MR damper. The optimization was conducted by employing a screening technique and multi-objective genetic algorithm. The optimization results were then used to calculate the induced damping forces analytically.

Tak et al. (2019) designed a double-ended MR damper operating in flow mode for application in prosthetic knees using the constrained non-linear minimization techniques provided in the Optimization Toolbox<sup>®</sup> of MATLAB R2018b software. Saini et al. (2020) presented a novel method to optimize an MR brake to reduce the average computational time using an equivalent magnetic model, known for its computational efficiency and the finite element magnetostatic analysis, known for its accuracy. Particle swarm optimization method was employed by Saini et al. (2021) to obtain the optimal geometric dimensions of a double-ended MR damper and a vane-type rotary MR damper for application in the prosthetic knee.

## **2.5 SEMIACTIVE CONTROL STRATEGIES FOR VEHICLE SUSPENSION WITH MR DAMPERS**

The mathematical equations that govern the current supplied to the MR damper during its operation in a particular application are called control algorithms or control strategies. In the case of a semiactive vehicle suspension, the control strategies evaluate the displacements, velocity or accelerations of the vehicle body, wheel or damper piston for current supply.

Since Karnopp et al. (1974) introduced the skyhook control strategy, researchers in the field have put forth several control strategies to improve the ride comfort of a vehicle. Lv et al. (2021) classified the existing control strategies as classical, advanced, and intelligent control strategies. The classical control strategies are the ones that adjust the damping coefficient of the MR dampers. This included skyhook control, passive control and Discrete control (Karnopp et al., 1974; Savaresi and Spelta, 2007; Dyke et al., 1996)

The advance control strategies have been defined as the ones that depend on the dynamic model of a target system. Advanced control strategies include the optimal

control method, where a control problem is treated as an optimization problem (Sarkar and Hirani, 2015; Pohoryles and Duffour, 2015; Singh and Wereley, 2014). The other one is Antidromic control (Li and Li, 2004), where the control algorithm is MR damper model specific.

Intelligent control strategies are the ones that learn, adapt and make decisions inside a system (Zhang et al., 2010). This category includes the Fuzzy control method (Xu and Guo, 2006), Genetic Algorithm-based control (Zheng et al., 2014b) and Neural network-based control (Chandiramani and Motra, 2013; Yu et al., 2015).

Despite the control strategies mentioned here, skyhook control or its variations (Karnopp et al., 1974; Hong et al., 2002; Ahmadian and Simon, 2003; Song et al., 2008) have been found to be implementable by the suppliers or OEMs (Soliman and Kaldas, 2021) due to its simplicity, effectiveness and immunity from the reaction time of an MR damper (Strecker et al., 2015). Almost all control strategies studied, including the skyhook control strategy, are based on the velocity of sprung mass, unsprung mass or the damper piston, which requires using integrators and filters in the program before the evaluation of the control law itself. This conversion increases the computational load, which increases the reaction time of the control algorithm, thereby reducing the performance of the semiactive system. Consequently, the acceleration-based control algorithms have recently gained the interest of researchers due to their simplicity, reduced computational load and cost-effectiveness. Kopylov et al. (2020) proposed acceleration-based ground hook control of an electromagnetic regenerative tuned mass damper for vehicular application. The study showed that the proposed control improved the system's performance in the pre-resonant area. Negash et al. (2021) presented a mixed skyhook-acceleration-driven damper control using hardware-in-loop simulation. The control strategy proposed in this study outperformed the passive damper system at all frequency domains.

## **2.6 APPLICATION OF MR DAMPERS IN SUSPENSION OF PASSENGER VEHICLES**

The application of MR dampers to improve the ride comfort, handling and stability of a vehicle has been studied in a wide variety of studies (Marathe et al., 2011; Lam and Liao, 2003; Choi et al., 2003; Taghirad and Esmailzadeh, 1998; Morales et



al., 2018). Ahmadian and Simon (2003) developed and implemented the MR dampers in an 18-wheeler semi-truck, as shown in Figure 2.12. The test vehicle was run over a speed bump, and the acceleration was measured at various locations on the test vehicle. The ride comfort and road handling of the test vehicle with the passive and MR damper were compared to evaluate the performance of the semiactive suspension.

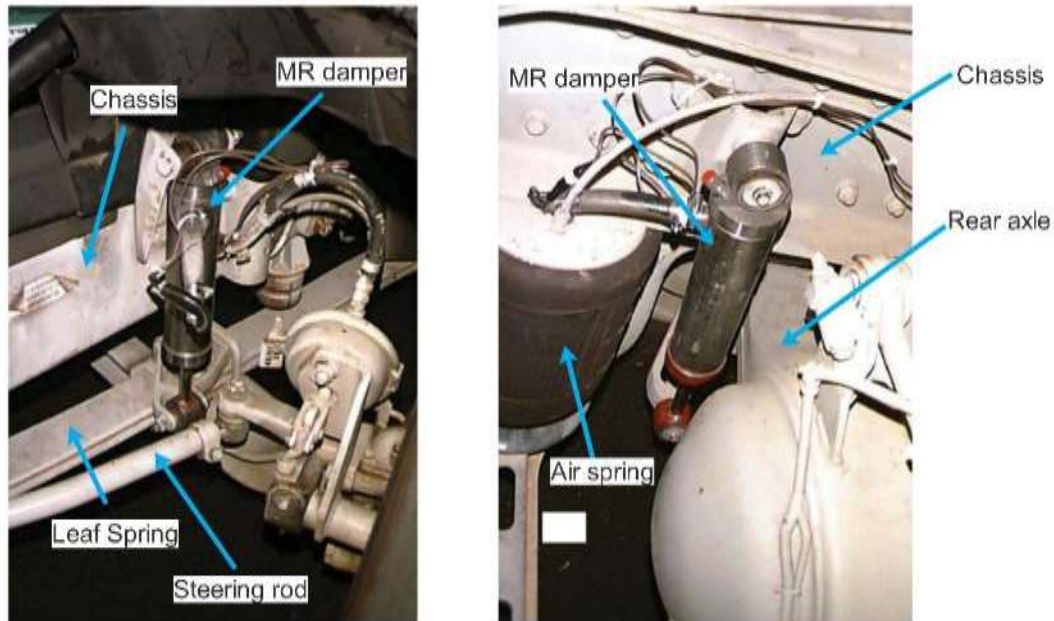


Figure 2.12 MR damper on the front and rear axle of semitruck (Ahmadian and Simon, 2003)

Ahmadian and Gravatt (2004) designed and tested the MR dampers for the front suspension of a two-wheeler. The MR dampers successfully reduced the suspension displacement and vehicle body acceleration during the experiments on the test vehicle.

The LORD Corporation, USA, developed MR dampers for seat suspension and industrial applications. These MR dampers have been retrofitted in the suspension of an All-Terrain Vehicle (ATV) to improve its suspension performance in terms of ride comfort and road handling, as shown in Figure 2.13 (Krauze and Kasprzyk, 2014; Kasprzyk et al., 2017; Krauze et al., 2018; Krauze et al., 2019). Several experiments were conducted on this ATV with commercial MR dampers over various terrains while implementing different semi-active control algorithms. The results from these experiments showed that the MR dampers significantly improved ride comfort and road handling capabilities.

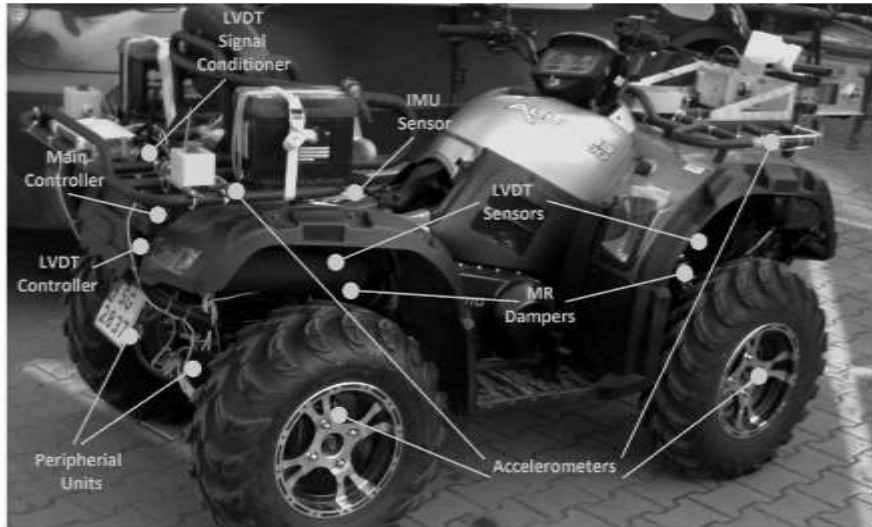


Figure 2.13 ATV with commercial MR dampers (Kasprzyk et al., 2017)

Zareh et al. (2015) attempted to develop a low-cost MR damper for a passenger car. The designed MR damper performed well in conjunction with the existing passive damper. Peng et al. (2017) installed MR dampers on a car and tested the car over a speed bump. The vehicle body acceleration improved as compared to the passive suspension. Makowski and Knap (2018) designed a twin-tube MR damper by replacing the bottom valve of a passive twin-tube damper with an electromagnetic coil and filling the damper with the commercial MR fluid, MTS-265, supplied by LORD Corporation. The developed MR damper was installed in the suspension of the test vehicle, Honker -2000 and conducted field tests on random roads and speed bumps. The suspension performance was observed to have improved by 21%.

Du et al. (2020) implemented MR dampers in a four-wheeler passenger car with an adaptive skyhook control that employs genetic algorithms, as shown in Figure 2.14. The test vehicle was subjected to a speed bump at three different speeds. The proposed control strategy improved the performance of the semiactive suspension compared to the conventional skyhook control and the passive suspension.

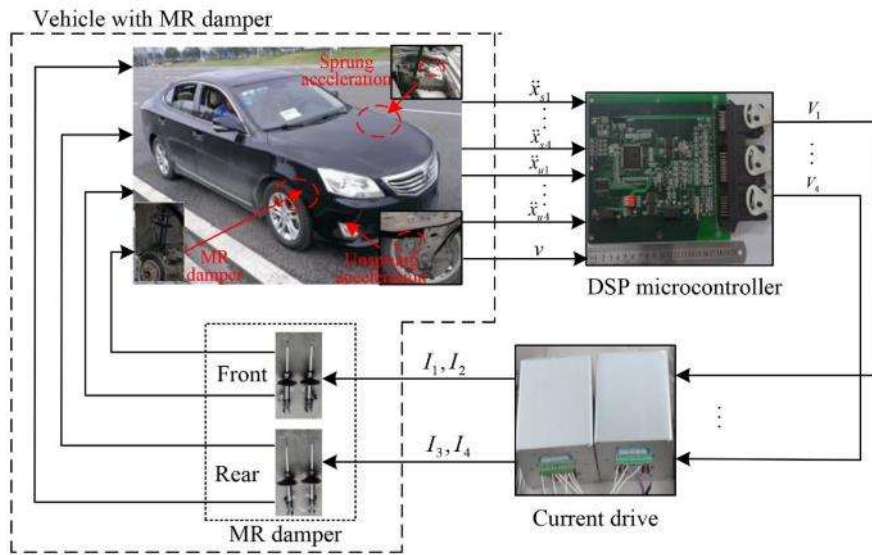


Figure 2.14 Passenger car with MR damper (Du et al., 2020)

## 2.7 MOTIVATION

A thorough literature review conducted during this study revealed the following gaps in the research.

- Most studies involving the implementation of MR dampers in the vehicle suspension system use them in conjunction with the passive damper, and very few studies attempt to replace the stock passive damper with an MR damper completely.
- Ample research has been conducted on developing MR damper pistons of different designs, control strategies, and implementing MR dampers on the vehicle suspension system. However, the development of a low-cost MR damper for a vehicle's semiactive suspension has seldom been explored.
- Many studies could also be found dedicated to optimizing the composition of magnetic particles of the MR fluid to match the performance of a commercial MR fluid. However, the fluid cost has not been considered as one of the variables in these optimization studies, which is crucial in developing a cost-effective MR damper.
- Almost all control strategies are developed based on the velocity of sprung mass, unsprung mass or the damper piston, which requires using integrators and filters in the program before evaluating the control law. This conversion

increases the computational load, which increases the reaction time of the control algorithm, reducing the performance of the semiactive system. The control strategies purely based on the acceleration of the system components have not been explored.

## **2.8 OBJECTIVES**

- 1) To design and develop an MR damper for application in a four-wheeler test vehicle
- 2) To develop an in-house MR fluid and compare it with commercial MR fluid
- 3) To evaluate and compare the performance of the developed MR damper on a test vehicle in real-time with commercial MR fluid and in-house MR fluid
- 4) To develop and evaluate the performance of an acceleration-based current control strategy

## **2.9 SCOPE OF RESEARCH WORK**

1. Experimental evaluation and characterization of a commercial MR damper in a damper testing machine under harmonic excitations. Development of a mathematical model for the commercial MR damper and its simulation in the seat suspension system of a quarter car model (QCM) subjected to random road excitations.
2. Design, optimization, fabrication and characterization of a monotube MR damper with a floating piston accumulator operating in flow mode. Experimental evaluation of the developed MR damper, with commercial MR fluid, through road tests on the test vehicle while implementing current control strategies in real-time. Cost evaluation of the developed MR damper with commercial MR fluid.
3. Synthesis and characterization of MR fluid samples with different volume fractions of magnetic particles on rotational plate Rheometer under different magnetic field strengths. Mathematical modeling of the developed MR damper to predict the damping force with the synthesized MR fluid samples. Optimization of the volume fraction of magnetic particles in MR fluid based on the simulation response of the full car model of the test vehicle with the developed MR damper model featuring synthesized MR fluid samples and the

cost of synthesizing the MR fluid samples. Performance evaluation of the cost-effective in-house MR fluid through experiments on the test vehicle featuring MR damper with in-house MR fluid.

4. Experimental evaluation and comparison of an acceleration-based control strategy with the existing control strategy based on the response of a single-degree-of-freedom (SDOF) system. Simulation of SDOF system with MR damper to evaluate and compare the response time of the proposed control strategy with the existing control strategy.

## **2.10 RESEARCH METHODOLOGY**

The study presented in this thesis aims to develop a cost-effective MR damper to replace the stock passive damper in the suspension system of the test vehicle, the Force Motor's – Traveller. The methodology employed at each stage of the study to achieve the set objectives has been depicted in Figure 2.15.

### **2.10.1 Performance evaluation of a commercial MR damper**

A commercial MR damper is first characterized on a damper testing machine by subjecting it to sinusoidal excitation with varying frequency. The damping behavior of the commercial MR damper is determined at different current values. The data obtained from the experiment on the damper testing machine is used to develop a mathematical model of the MR damper based on the Magic Formula Model (MFM), and an Equivalent Damping Model (EDM). As per the manufacturer's specification sheet, the commercial MR damper used in this study was built for the seat suspension system. Therefore, using the developed MFM, this MR damper is simulated on a quarter-car model with seat suspension in MATLAB. The on-off skyhook control is used to improve the ride comfort of the passenger in the simulation of a QCM with seat suspension. The performance of the MR damper models was evaluated through the seat suspension response and the simulation time of the model subjected to random roads.

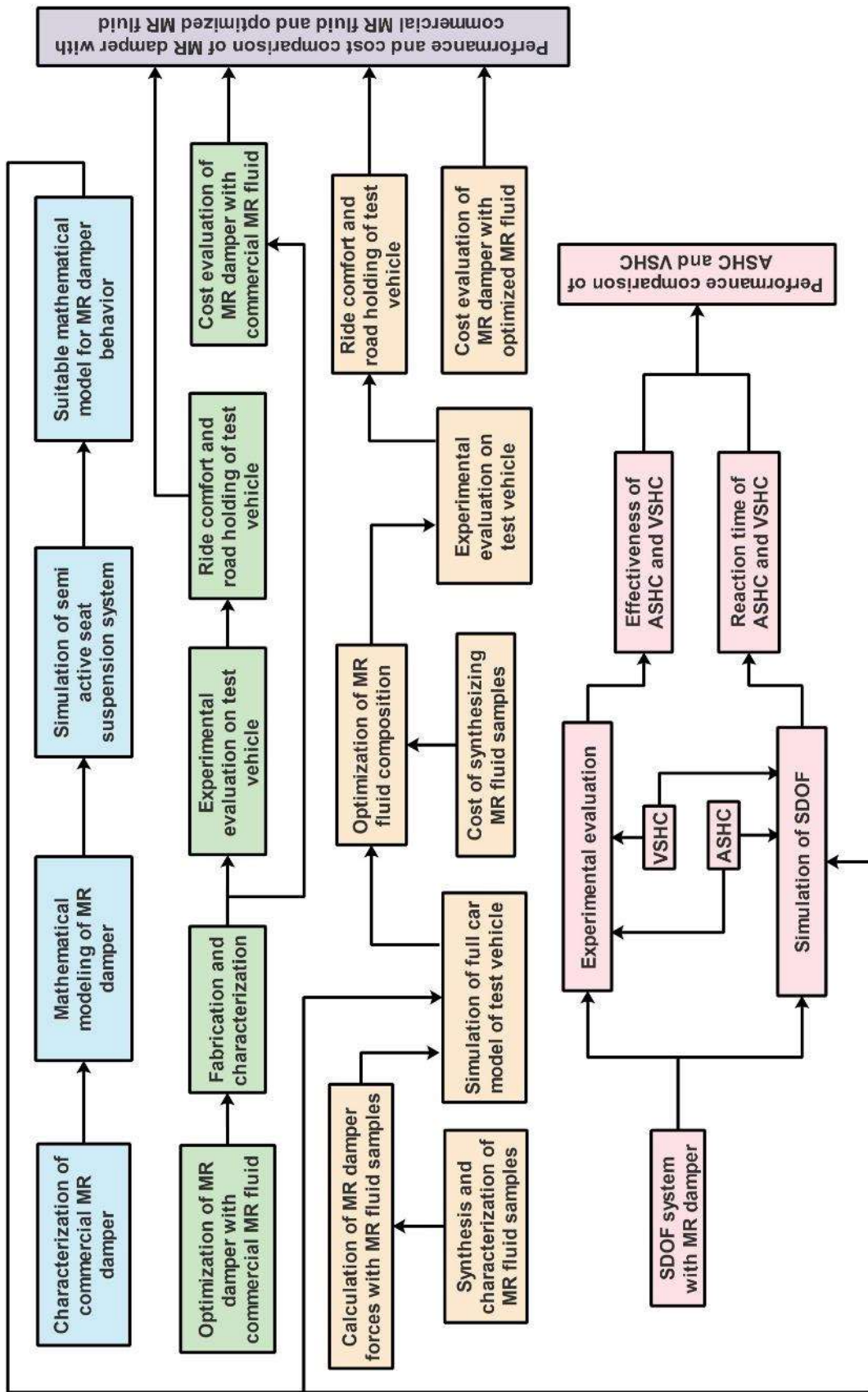


Figure 2.15 Research methodology

### **2.10.2 Design of MR damper for four-wheeler application**

Meanwhile, a monotube MR damper was designed for application in a passenger van. The design of an MR damper involves determining the dimensions of the piston to obtain the required damping force while ensuring that none of the piston components reaches its magnetic saturation, including the MR fluid in the flow gap. Achieving required damping forces and ensuring no magnetic saturation in piston components are two conflicting criteria that are solved using the `fmincon` algorithm from the optimization toolbox of MATLAB R2018b in this study. The optimized dimensions are validated in the FEMM software. The monotube MR damper, with the optimized piston dimensions, is fabricated and tested on the damper testing machine.

### **2.10.3 Real-time testing of MR damper on the test vehicle**

The real-time performance of the fabricated MR damper is evaluated by installing it on the test vehicle, Force Motor's Traveller, for which it was designed. The test vehicle is run over a sharp speed bump at different speeds while implementing on-off skyhook and ground hook control logic. The performance of the MR damper is compared against the stock passive damper by comparing the peak acceleration of the vehicle body and the wheel in each case. The cost of fabricating the MR damper is also evaluated and compared against the cost of the commercial MR damper.

### **2.10.4 Development of a cost-effective in-house MR fluid**

The in-house MR fluid consists of CIP as the magnetic particles, silicone oil as a carrier fluid and aluminum di-stearate as an additive. Designing an MR fluid involves determining the volume fraction of the magnetic particles in the carrier fluid to obtain the desired yield stress. Multiple samples of MR fluid with two sizes of CIP were synthesized and characterized in a rotational plate Rheometer. The developed MR damper with each sample fluid was simulated on a full car model of the test vehicle using the rheology data subjected to the random road. The Fast Fourier Transform (FFT) of full car model response was considered the performance index of each MR fluid sample. The cost of the CIP forms the major part of the cost of synthesizing an MR fluid. Therefore, the cost of synthesizing and FFT of the full car model response was also considered while designing the in-house MR fluid. The low cost of MR fluid

and the reduced response of the full car model of the test vehicle were the two conflicting criteria that were resolved using the Response surface optimization method. The rheological properties of the optimized in-house MR fluid are compared with that of the commercial MR fluid. The performance of the developed MR damper filled with in-house MR fluid is evaluated by installing it on the test vehicle. The test vehicle is again run over the sharp speed bump at different speeds while implementing the same two control strategies. The performance of the developed MR damper filled with in-house MR fluid is compared against the stock passive damper by comparing the peak acceleration of the vehicle body and the wheel in each case.

#### **2.10.5 Experimental evaluation and simulation of an acceleration-based control strategy**

A computationally efficient acceleration-based skyhook control strategy has been proposed whose effectiveness is experimentally evaluated on a SDOF system and compared against the conventional skyhook control strategy. The computational efficiency of the proposed control strategy is evaluated and compared with the conventional control strategy based on simulation time of the same SDOF system in MATLAB.

### **2.11 SUMMARY**

This chapter presents a thorough literature review conducted at the beginning of the study presented in this thesis. The notable studies conducted in past to optimize MR fluids, design and optimize MR dampers, mathematically model MR damper behavior, control current supplied to MR damper during operation and implement MR damper in automobiles. The chapter also presents the motivation that led the author to lay down the objectives for conducting the study presented in this thesis. The methodology adopted by the author to achieve these objectives has also been presented in this chapter.



## **CHAPTER 3**

### **EXPERIMENTAL EVALUATION AND MATHEMATICAL MODELLING OF COMMERCIAL MR DAMPER**

#### **3.1 INTRODUCTION**

In general, a damper is an energy-dissipating device. A damper in the suspension system of an automobile, dissipates the energy absorbed by the spring element when the vehicle is subjected to road undulations. The dampers improve the ride comfort and stability of the vehicle, thereby improving the passengers' safety. The damping force generated by a passive damper largely depends on its excitation velocity. Its mathematical modeling at different excitation velocities is also crucial in simulating various vibration systems, including an automotive suspension system. The MR damper adds a whole new dimension to the mathematical model of a damper due to its ability to deliver variable damping force under different current values. Several studies have been presented to capture this variable damping behavior, as discussed in Chapter 2. This chapter presents the modelling of a commercial MR damper.

#### **3.2 METHODOLOGY FOR MR DAMPER MODEL SELECTION**

The methodology adopted to experimentally evaluate and develop a mathematical model of the commercial MR damper has been depicted in Figure 3.1. The commercial MR damper, RD-8041-1, supplied by LORD Corporation US, is characterized on a damper testing machine by subjecting it to sinusoidal excitation with varying frequency and current. The damping behavior of the commercial MR damper is determined at different current values. The data obtained from the experiment on the damper testing machine is used to develop a mathematical model of the MR damper based on MFM, which is generally used to represent tire force data and the equivalent damping. As per the manufacturer's specification sheet, the commercial MR damper used in this study was built for the seat suspension system. Therefore, using the developed MFM, this MR damper is simulated on a quarter-car model with seat suspension in MATLAB. The on-off skyhook control is used to improve the ride comfort of the passenger in the simulation of a QCM with seat suspension. The

performance of the MR damper models was evaluated through the seat suspension response and the simulation time of the model subjected to random roads.

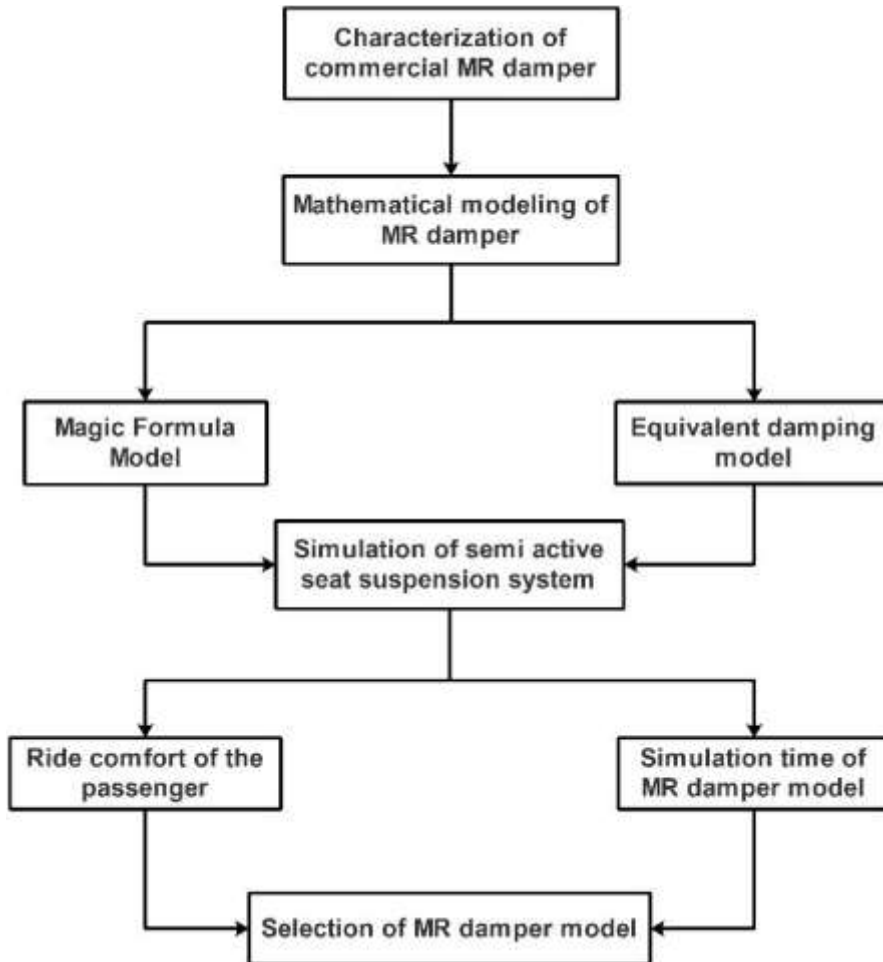


Figure 3.1 Methodology for MR damper model selection

### 3.3 EXPERIMENTAL EVALUATION OF COMMERCIAL MR DAMPER

#### 3.3.1 The commercial MR damper

The commercially available MR damper used in this study, RD-8041-1, can be seen in Figure 3.2. The RD-8041-1 is classified as a long-stroke MR damper by its manufacturer with a stroke of 74mm. It is a monotube damper with a diaphragm-type accumulator charged with Nitrogen gas at  $2.068 \times 10^6$  Pa (300 psi). A maximum current of 1A can be given to the damper continuously and 2A intermittently. The response time of the damper is within 15 milliseconds (“LORD Corporation”, 2019). The manufacturer rates the maximum testing velocity to be 0.2 m/s.

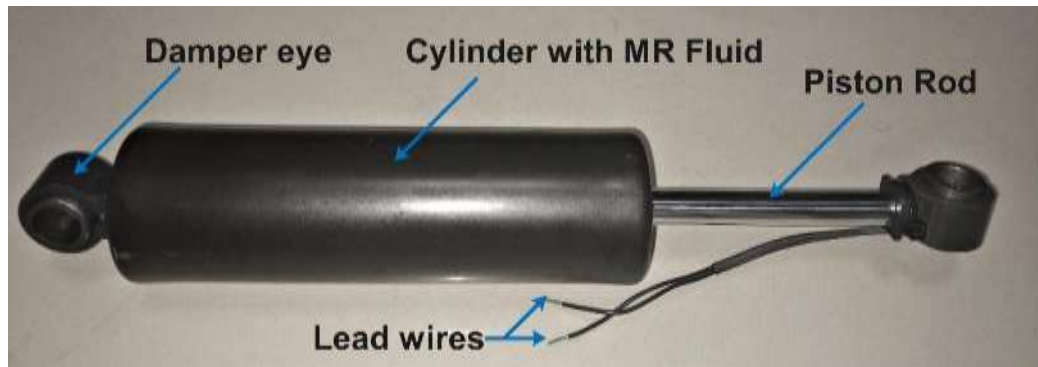


Figure 3.2 Commercial MR damper, RD-8041-1

### 3.3.2 The damper testing machine

The experimental setup employed in this study to characterize the MR damper is a hydraulically actuated damper testing machine shown in Figure 3.3. The actuator provided in this machine is supplied by a hydraulic pump capable of generating an oil flow of 65 liters/min, allowing the actuator to achieve a velocity of up to 1.2 m/s with a 150 mm ( $\pm 75$  mm) stroke. The machine is also provided with a load cell with a capacity of 20kN and a displacement sensor with measurement range of 200 mm (refer Appendix – HEICO Damper testing machine). The arrangement of the actuator, the load cell, the displacement sensor and the damper, when loaded in the machine, can be seen in Figure 3.3. The MOOG® controller commands the MOOG® servo valve on the actuator. It also works as a Data Acquisition system (DAQ) for the displacement and load sensors with a sampling rate of 1kHz. The controller can generate various actuation signals such as sinusoidal, triangular, square, saw-tooth etc. The controller is programmed using the proprietary software MOOG® Integrated Test suite to excite the damper.

The MR damper is excited sinusoidally with a fixed amplitude and varying frequency at different current values. The manufacturer specifies the MR damper at the lowest velocity of 0.05m/s and highest velocity of 0.2m/s. Moreover, the manufacturer limits the maximum continuous supply of current at 1A. Hence, the MR damper is supplied with a maximum current of 1A to prevent any damage to the electromagnetic coil. Therefore, the MR damper, in this study, is subjected to sinusoidal excitation of an amplitude of 20mm and varying frequency to obtain the piston velocity amplitudes:

0.05m/s, 0.1m/s, 0.15m/s and 0.2m/s. The experiment was repeated while supplying a direct current (DC) of 0A, 0.25A, 0.5A, 0.75A and 1A.

### **3.3.3 Discussion on results from experiments on RD-8041-1 in the damper testing machine**

During the experiments on the damper testing machine, the force and displacements are recorded at every combination of piston velocity and current. The peak velocity is first set to 0.05 m/s, and the machine is operated for ten cycles before changing peak velocity to the next increment value while supplying 0A current. The above steps are repeated for each value of the current supplied. During the transition of one peak velocity to the next, it takes approximately five cycles for the damper to operate steadily (Desai et al., 2019). Therefore, data from the sixth cycle, at each peak velocity and current value, is considered for analysis. The Force-Displacement (FD) diagrams thus obtained from the experiment on the RD-8041-1 in the damper testing machine are presented in Figure 3.4.

The positive values of force and displacement represent the extension stroke, and the negative values represent the compression stroke. Therefore, the part of the FD curve above the abscissa represents the compression stroke, and the part below the abscissa represents the extension or rebound stroke. The FD curve can be traced clockwise during excitation. The area under the FD curve represents the energy dissipated per excitation cycle. It can be seen in Figure 3.4 that at any given velocity of excitation, the energy dissipated per cycle increases with an increase in current value. The increase in damping force of the MR damper with an increase of current supplied, as a result of the MR effect, can also be seen in Figure 3.4. It is difficult to ignore the misalignment of the upper and lower part of the FD curve in Figure 3.4 when the current is supplied to the damper. This misalignment is known as the force-lag phenomenon, generally occurring during the transition from compression to rebound stroke or vice versa due to the fluid compressibility and vacuum for flow block at the active gap of MR dampers (Peng et al., 2014). The peak damping force observed at each velocity amplitude of excitation at different current values are plotted to obtain the characteristic graph of an MR damper. The characteristic graph of RD-8041-1 obtained in this study can be seen in Figure 3.5.

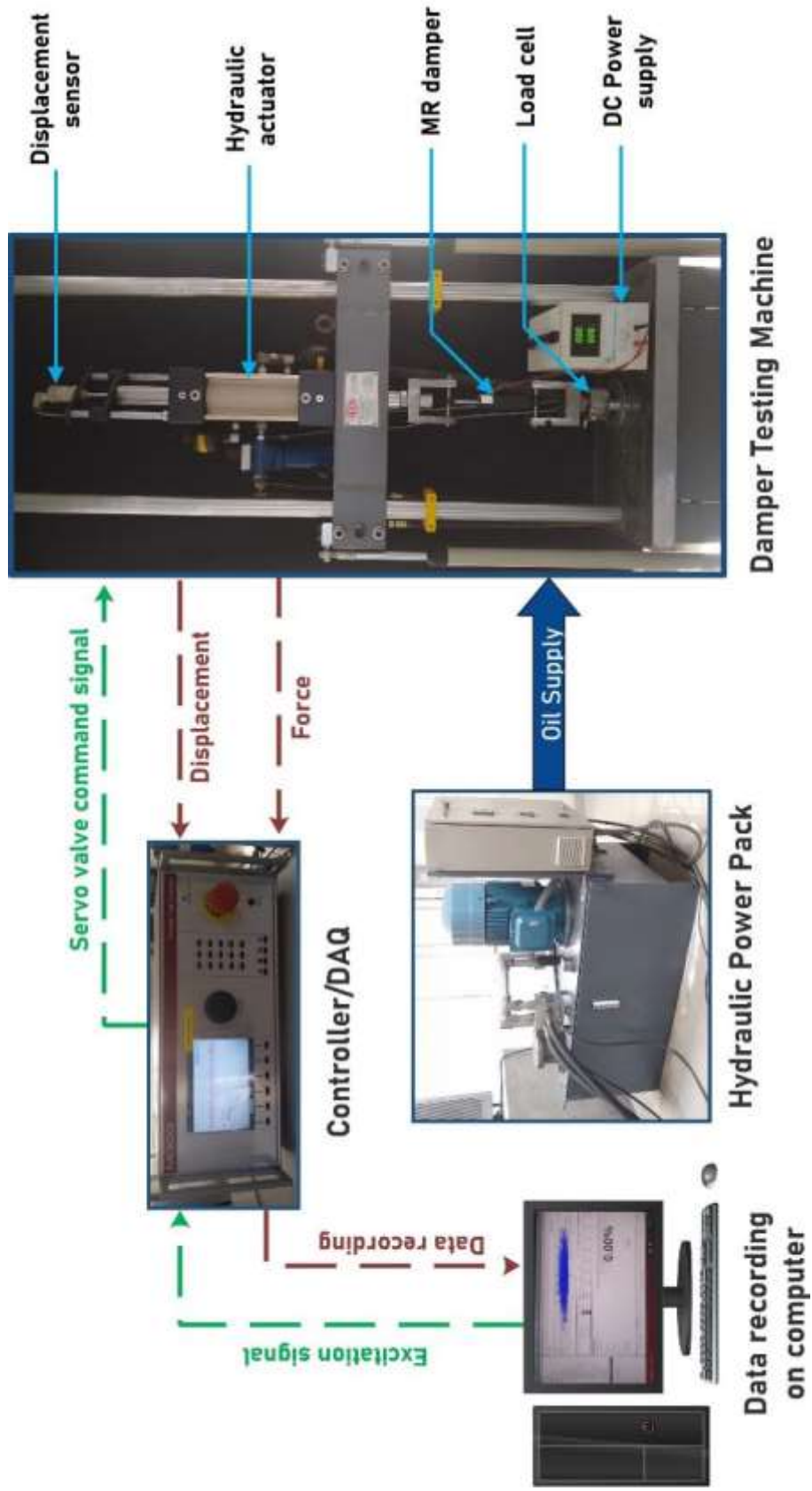
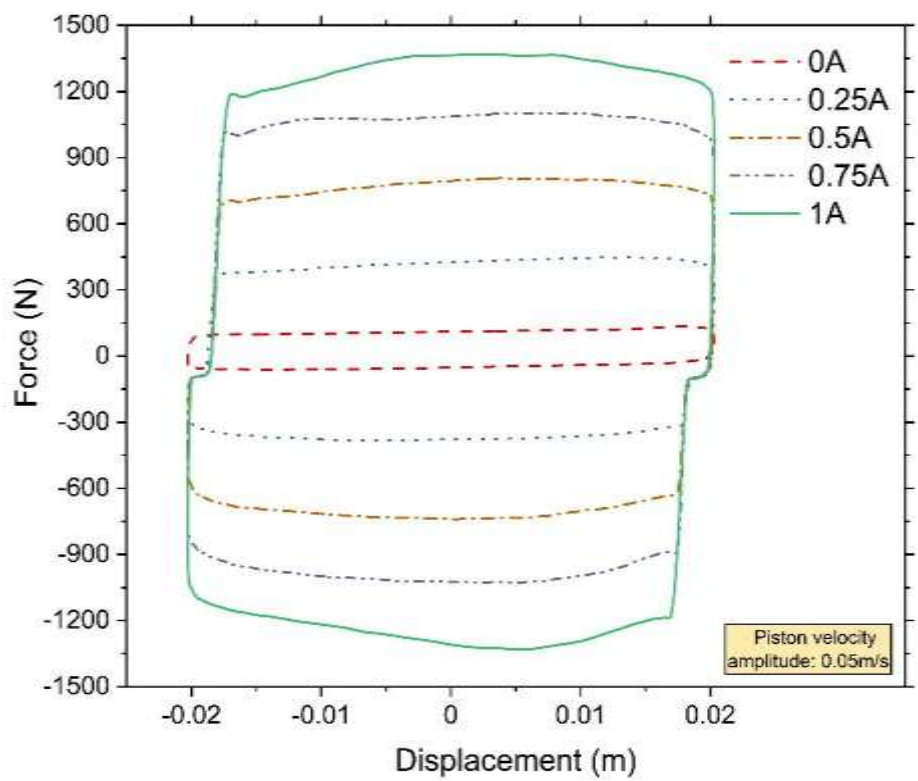
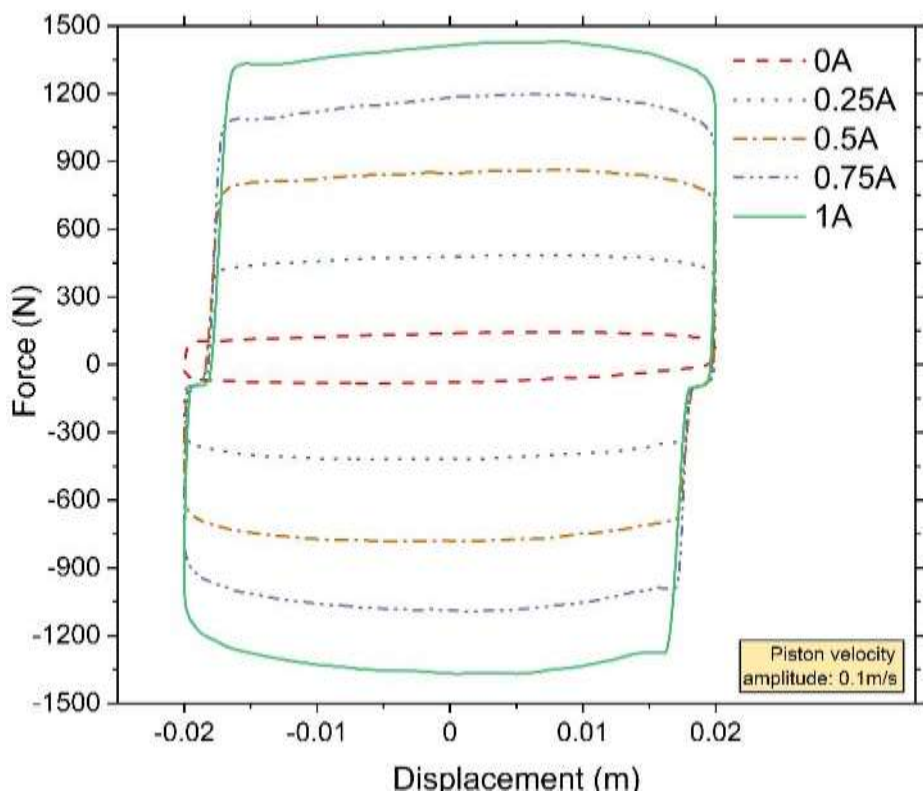


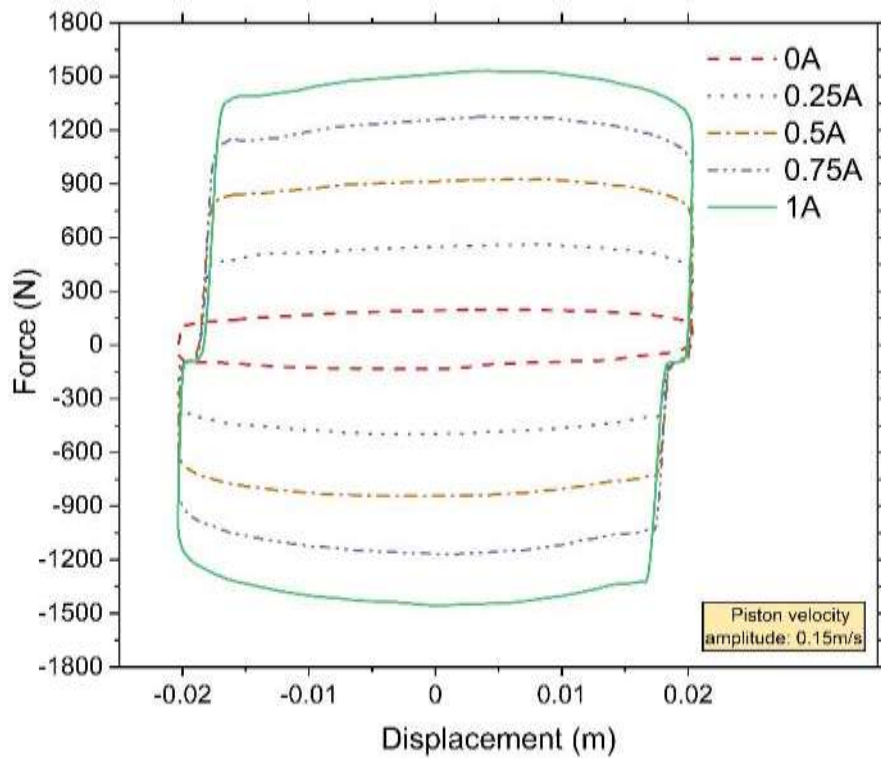
Figure 3.3 Experimental setup for MR damper characterization



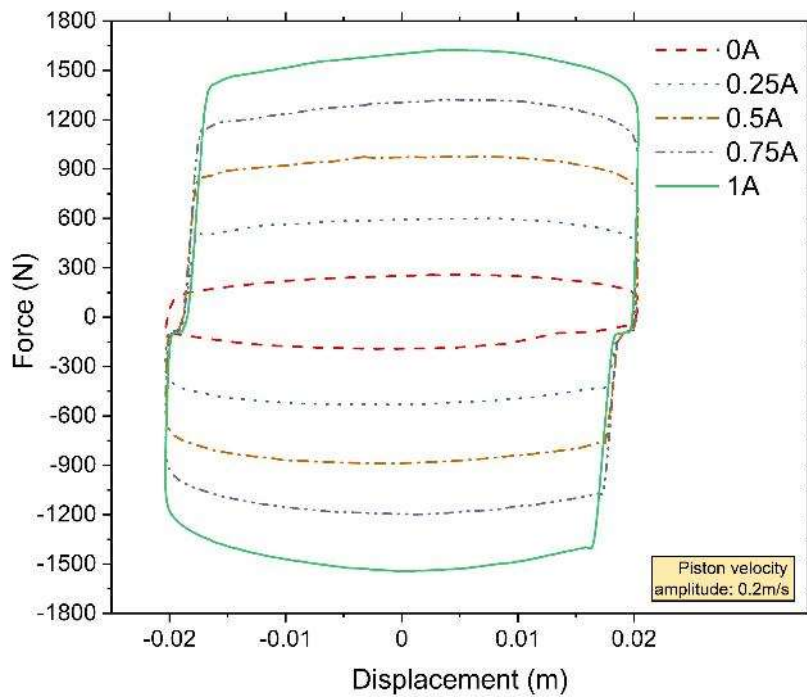
(a)



(b)



(c)



(d)

Figure 3.4 FD diagram at (a) 0.05m/s (b) 0.1m/s (c) 0.15m/s (d) 0.2m/s

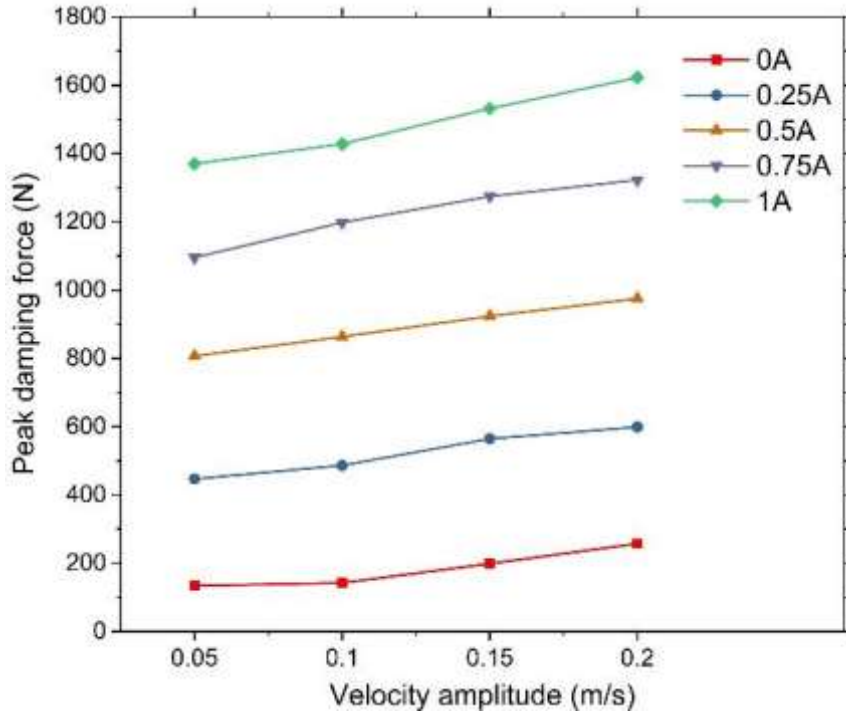


Figure 3.5 Characteristic graph of RD-8041-1

### 3.4 MATHEMATICAL MODELLING OF RD-8041-1 MR DAMPER

#### 3.4.1 Equivalent damping model (EDM)

As mentioned earlier, the area enclosed by an FD curve of a damper represents the energy dissipated by the damper per excitation cycle. The energy dissipated by the damper can be used to predict the damping force by calculating the coefficient equivalent damping coefficient given by equation 3.1 (Pang et al. 1998a)

$$F_d = C_{eq}\dot{x} \quad (3.1)$$

$$C_{eq} = \frac{E}{\pi\omega X^2} \quad (3.2)$$

Where,  $F_d$  is the damping force in N,  $C_{eq}$  is the coefficient of equivalent damping in Ns/m,  $\dot{x}$  the velocity of the damper,  $E$  is the energy dissipated by the damper in J that is measured as the area under the FD curve,  $\omega$  is the excitation or oscillation frequency, and  $X$  is the displacement amplitude of sinusoidal excitation. The damping force in the case of a passive damper is only velocity dependent; hence, equation 3.1 is sufficient to model the damping behavior of a passive damper. However, the damping



behavior of an MR damper depends on the current, apart from the velocity. An MR damper behaves as a passive damper when the current supplied is constant, which is the case during the experiments on the MR damper in the damper testing machine. Therefore, the equivalent damping coefficient of the MR damper at various velocities and currents tested is calculated using equation 3.2. The equivalent damping coefficient values thus obtained have been listed in Table 1 and plotted in Figure 3.6 as functions of velocity and current.

Table 3.1 Equivalent damping coefficients of RD-8041-1

Current (A)	Equivalent damping coefficient, $C_{eq}$ (Ns/m)			
	At 0.05m/s	At 0.1m/s	At 0.15m/s	At 0.2m/s
0	2050.81	1227.06	1193.23	1190.08
0.25	9639.63	5216.71	4050.86	3262.09
0.5	17959.49	9522.10	6894.09	5444.65
0.75	24991.29	13105.72	9416.85	7309.65
1	30842.803	15929.06	11428.61	9023.06

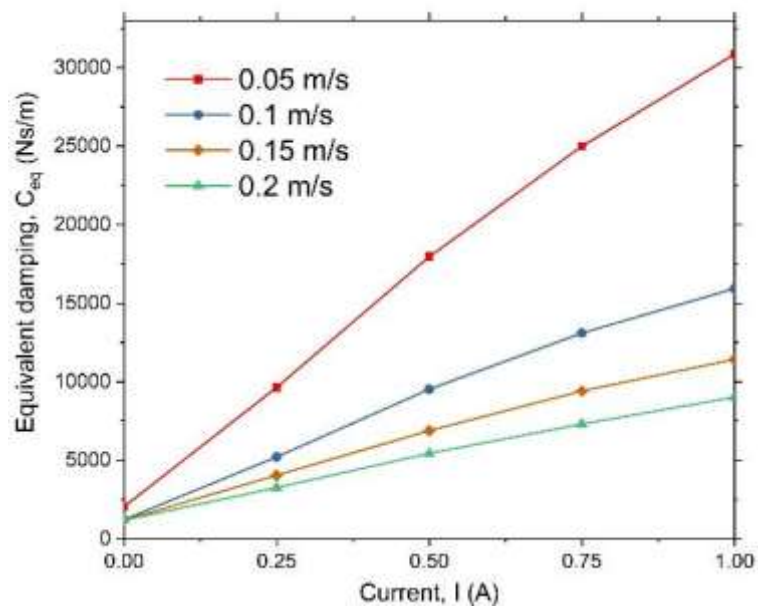


Figure 3.6 Equivalent damping of RD-8041-1

It can be observed in Figure 3.6 that the equivalent damping coefficient increases linearly with increase in current supplied at all the velocities tested. This behavior of the damping coefficient has been modeled using equation 3.3, which is hereon referred to as EDM.

$$C_{eq} = A \times I + B \quad (3.3)$$

Where  $I$  represents the current supplied to the damper,  $A$  is the slope, and  $B$  is the intercept of each curve in Figure 3.6. The values of EDM coefficients  $A$  and  $B$  are obtained by fitting the EDM to the experimental data in Figure 3.6 using the Curve Fitting Toolbox™ in MATLAB R2018b. The values of  $A$  and  $B$  thus obtained are listed in Table 3.2.

Table 3.2 Coefficient values of EDM

Velocity (m/s)	A	B
0.05	29170	2510
0.1	14920	1542
0.15	10330	1429
0.2	7885	1303

It can be further observed from Figure 3.6 and Table 3.2 that, at any given current value, the damping coefficient varies non-linearly with velocity. Therefore, the coefficients  $A$  and  $B$  are expressed as third-order polynomial functions of piston velocity, as shown in equations 3.4 and 3.5.

$$A = -11601824.12\dot{x}^3 + 5643722.74\dot{x}^2 - 54484.78\dot{x} + 65848.32 \quad (3.4)$$

$$B = -1157333.33\dot{x}^3 + 518200\dot{x}^2 - 76836.66\dot{x} + 5201 \quad (3.5)$$

The results of fitting the EDM to the experimentally obtained damping coefficient values are presented in Figure 3.7. It is clear from Figure 3.7 that the EDM predicts the experimentally obtained damping coefficients satisfactorily.

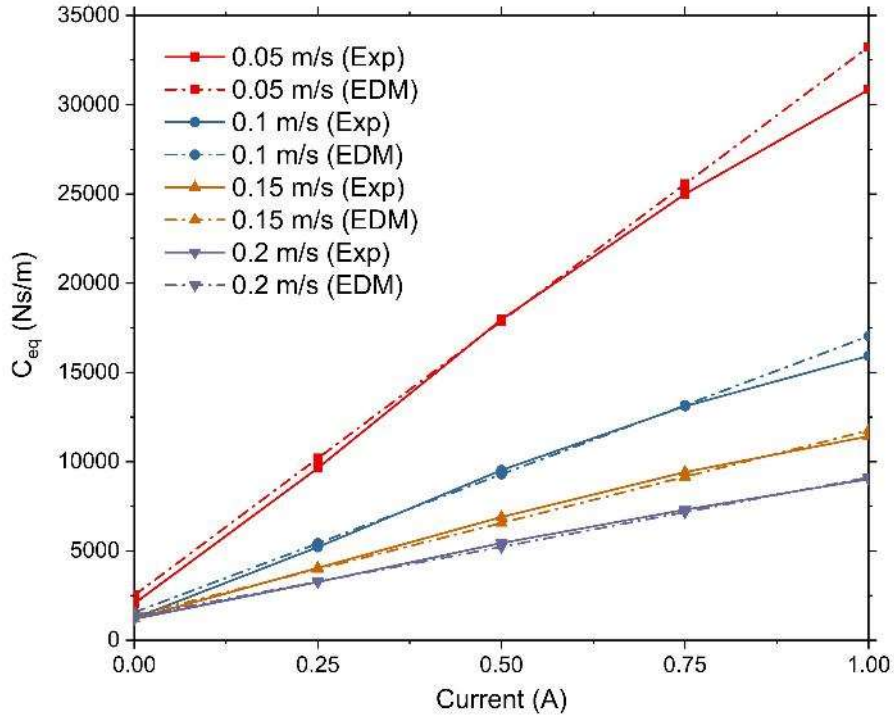


Figure 3.7 EDM curve fitting results

### 3.4.2 Magic Formula Model (MFM)

The MFM was originally presented to describe the steady state behavior of a tire, such as longitudinal forces, lateral forces and self-aligning torque in pure and combined slip conditions, by Bakker et al. (1989). Since then, the MFM has found its application in describing the damping behavior of MR dampers in the form of a non-parametric model (Zhang et al., 2020; Bui et al., 2020; Pan et al., 2018; Boada et al., 2017; Kim et al., 2011). The MFM for the MR damper is given by equation 3.6.

$$F_d = A\dot{x} + D\sin(C \arctan(B\phi)) \quad (3.6)$$

$$\phi = (1 - E)\dot{x} + (E/B) \arctan(B\dot{x}) \quad (3.7)$$

Where  $F_d$  is the damping force (N),  $\dot{x}$  is the piston velocity,  $A$ ,  $B$ ,  $C$ ,  $D$  and  $E$  are the parameters of the MFM obtained by fitting equation 3.6 to the experimental characteristic graph of an MR damper such as the one presented in Figure 3.5. The non-linear curve fitting technique with a Trust Region Reflective algorithm, available in the Optimization Toolbox™ of MATLAB R2018b, was used for this purpose. This

particular algorithm has been considered to be one of the best methods to solve non-linear problems by Conn et al. (2005) and Wang et al. (2011). The MFM coefficient values thus obtained have been listed in Table 3.3.

Table 3.3 MFM coefficients for RD-8041-1

<b>Current (A)</b>	<b>A</b>	<b>B</b>	<b>C</b>	<b>D</b>	<b>E</b>
<b>0</b>	1411.63	32.456	335.67	39.95	-155.66
<b>0.25</b>	1419.54	23.53	333.70	191.08	-300.48
<b>0.5</b>	1468.35	11.73	333.38	365.22	-937.36
<b>0.75</b>	1562.52	7.61	333.27	551.58	-3243.65
<b>1</b>	1825.52	5.57	333.28	594.74	-7743.98

It is clear from Table 3.3 that the MFM coefficients are nonlinearly dependent on the current supplied except the coefficient 'C', which maintains an average value of 333.8578 at all the current values. A second-order polynomial was found to be adequate to represent this non-linearity between the MFM coefficients and the current. Equations 3.8 to 3.11 represent the resulting polynomial equations of MFM coefficients in terms of current, and Figure 3.8 represents the result of MFM fitting to the experimental data.

$$A = 158.72I^2 - 123.29I + 1422.7 \quad (3.8)$$

$$B = 6.13I^2 - 26.2I + 33.184 \quad (3.9)$$

$$D = -58.203I^2 + 410.42I + 25.4 \quad (3.10)$$

$$E = -3090I^2 + 258.9I - 426.21 \quad (3.11)$$

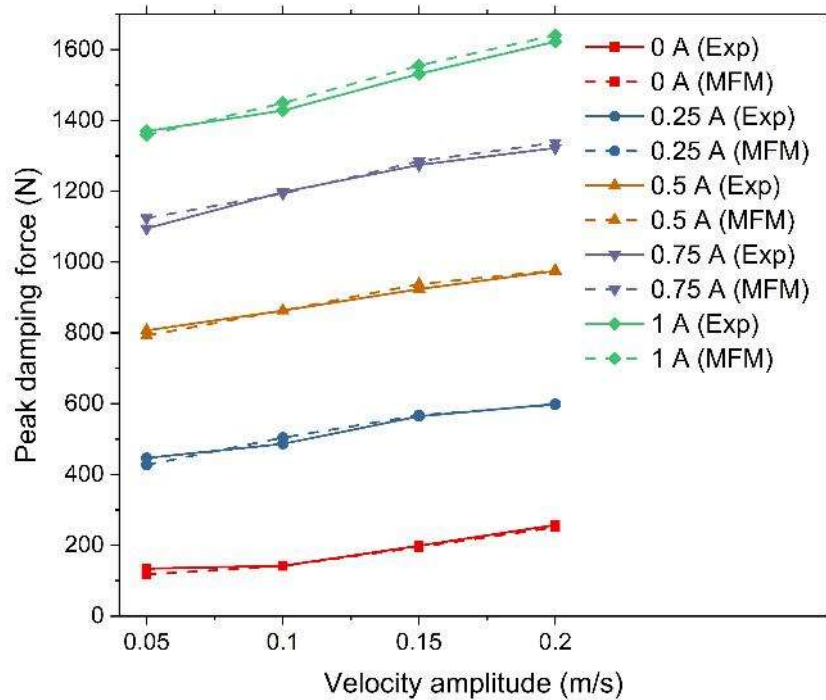


Figure 3.8 Curve fitting results of MFM

It can be observed in Figure 3.8 that the damping force predicted by the MFM is in good agreement with the experimental values. The performance and computational efficiency of the two damper models are evaluated by employing them in the simulation of a quarter-car model with seat suspension.

### 3.5 SIMULATION OF A QUARTER CAR MODEL WITH SEAT SUSPENSION

The performance of the two damper models of concern here is evaluated by employing them in the simulation of a QCM with seat suspension system featuring a MR damper. The QCM is subjected to random road vibrations and the performance of the damper models is evaluated based on the Root Mean Square (RMS) acceleration of the driver mass (TharehalliMata et al. 2019; TharehalliMata et al. 2022).

#### 3.5.1 The quarter car model with seat suspension

The MR damper, RD-8041-1, is designed for a seat suspension system, as per the manufacturer specification sheet (“LORD Corporation,” 2019). Hence, the current study has analyzed a QCM featuring a seat suspension system with an MR damper. The QCM with a seat suspension is a vertically vibrating system with four degrees of

freedom system that involves four masses,  $m_u$  - the unsprung mass (tire),  $m_s$  - sprung mass (vehicle chassis),  $m_f$  - seat frame mass,  $m_d$  - driver mass, as shown in Figure 3.9. The seat cushion is represented by a spring and a dashpot in parallel. The seat is connected to the vehicle's sprung mass using a spring and a damper in parallel, representing the seat suspension system. The damper in the seat suspension is passive in one case and MR damper in the other, represented by EDM and MFM.

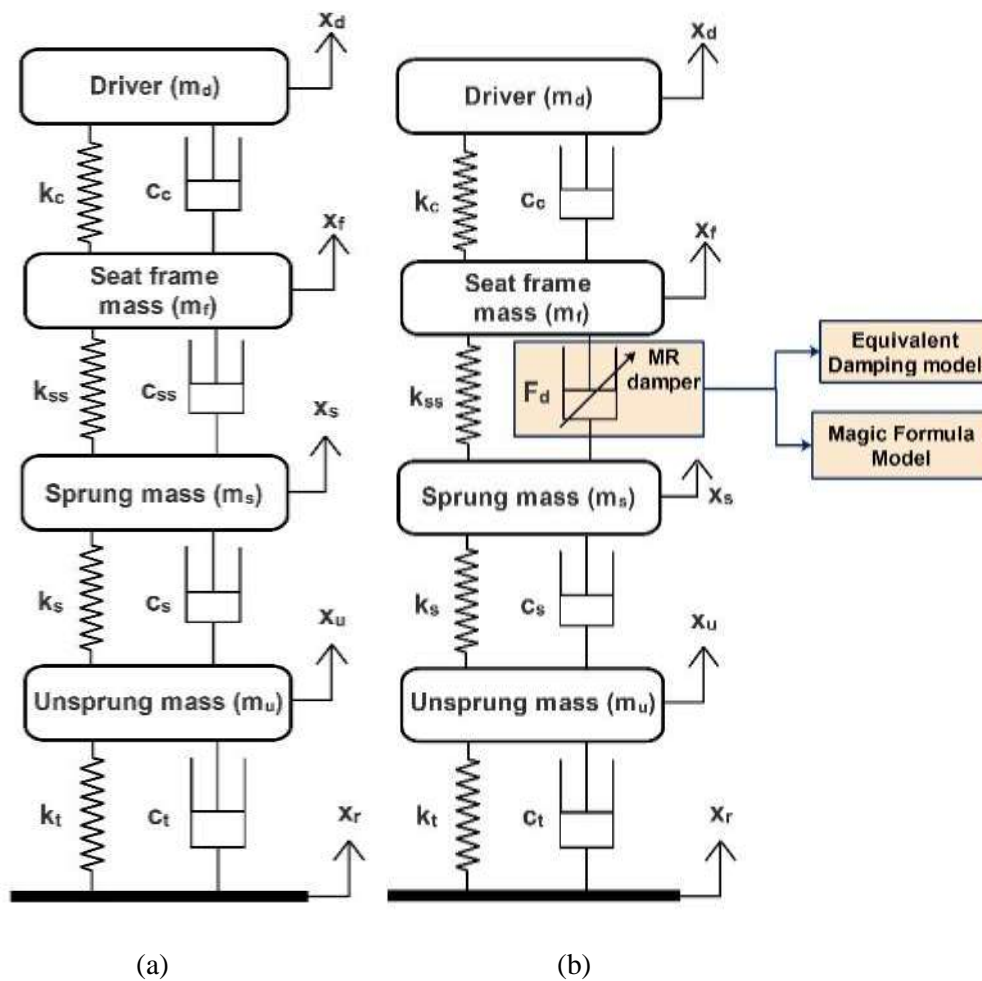


Figure 3.9 QCM with Seat suspension models (a) with passive damper (b) with MR damper

The equations of motion for the QCM shown in Figure 3.9 are given in equations 3.12 to 3.15.

*Unsprung mass:*

$$m_u \ddot{x}_u + k_t(x_u - x_r) + c_t(\dot{x}_u - \dot{x}_r) - k_s(x_s - x_u) - c_s(\dot{x}_s - \dot{x}_u) = 0 \quad (3.12)$$

*Sprung mass:*

$$m_s \ddot{x}_s + k_s(x_s - x_u) + c_s(\dot{x}_s - \dot{x}_u) - k_{ss}(x_f - x_s) - c_{ss}(\dot{x}_f - \dot{x}_s) = 0 \quad (3.13)$$

*Seat frame mass:*

$$m_f \ddot{x}_f + k_{ss}(x_f - x_s) + c_{ss}(\dot{x}_f - \dot{x}_s) - k_c(x_d - x_f) - c_c(\dot{x}_d - \dot{x}_f) = 0 \quad (3.14)$$

*Driver mass:*

$$m_d \ddot{x}_d + k_c(x_d - x_f) + c_c(\dot{x}_d - \dot{x}_f) = 0 \quad (3.15)$$

Where  $\ddot{x}$  is acceleration,  $\dot{x}$  is the velocity,  $x$  is displacement,  $m$  is mass,  $k$  is spring stiffness, and  $c$  is the damping coefficient. The subscripts  $u, s, f, d$ , and  $ss$  denote unsprung mass, sprung mass, seat frame, driver and seat suspension, respectively. The description of coefficients and their values used in equations 3.12 to 3.15 are provided in Table 3.4.

Table 3.4 Coefficients of QCM with seat suspension (Choi and Han, 2007)

<b>Coefficient</b>	<b>Description</b>	<b>Value</b>
$m_d$	Driver mass	56 kg
$m_f$	Seat frame mass	15 kg
$m_s$	Sprung mass	300 kg
$m_u$	Unsprung mass	20 kg
$k_c$	Cushion stiffness	18000 N/m
$k_{ss}$	Seat suspension stiffness	31000 N/m
$k_s$	Suspension stiffness	10000 N/m
$k_t$	Stiffness of tire	180000 N/m
$c_c$	Cushion damping coefficient	200 Ns/m
$c_{ss}$	Seat suspension damping coefficient	830 Ns/m
$c_s$	Suspension damping coefficient	2000 Ns/m

$c_t$	Tire damping coefficient	0 Ns/m
-------	--------------------------	--------

Equations 3.12 to 3.15 can be used for passive and semi-active seat suspension systems. However, the term  $c_{ss}(\dot{x}_f - \dot{x}_s)$  is replaced with  $F_d$  in case of a semiactive seat suspension system with an MR damper.

### 3.5.2 The control strategy

As described in section 1.5, the skyhook control algorithm assumes a viscous passive damper connected between the body of interest, in this case, the seat frame and a hypothetical sky. The damping coefficient of this damper is determined such that the body of interest is isolated from vertical disturbances. The on-off version of skyhook control has been adopted due to its inherent nature to eliminate the need to tune the control gain coefficient ( $C_{sky}$ ) and also because it is least affected by the response time of the MR damper (Strecker et al., 2015). The skyhook control strategy employed in the simulation of the QCM with semiactive seat suspension in this study is governed by equation 3.16.

$$F_d = \begin{cases} F_{dmax}, & \text{for } \dot{x}_f(\dot{x}_f - \dot{x}_s) \geq 0 \\ F_{dmin}, & \text{for } \dot{x}_f(\dot{x}_f - \dot{x}_s) < 0 \end{cases} \quad (3.16)$$

Where  $F_{dmax}$  is the maximum damping force delivered by the MR damper when 1A of current is supplied and  $F_{dmin}$  is the minimum damping force delivered when no current or 0A current is supplied.

### 3.5.3 The road input

The QCM in this study is subjected to random road profiles that are classified from very good to very bad depending upon the randomness of the road and measured in terms of power spectral density (PSD) by the International Standard Organization (ISO). The road profiles used in this study are governed by equation 3.17 (He et al., 2008).

$$\dot{Z}_r(t) = -2\pi un_0 Z_r(t) + \sqrt{G_q(\Omega_0)}uw(t) \quad (3.17)$$



Where  $G_q(\Omega_0)$  is coefficient of roughness,  $Z_r(t)$  is the amplitude of road irregularity,  $w(t)$  is the white noise signal,  $u$  is vehicle velocity, and  $n_0$  is the spatial frequency. The three road profiles considered for simulation in this study have been listed in Table 3.5. These three profiles were selected assuming they represent most of the real road conditions, i.e., highway, street roads and off-road trails, respectively. One of the road profiles, a medium road with a vehicle speed is 12 m/s, has been illustrated in Figure 3.10 for representation purposes. The vehicle velocity in equation 3.17 is varied from 12 m/s to 21 m/s with an increment of 3 m/s for road profiles R3, R6 and R9 in Table 3.5.

Table 3.5 Random road profiles as per ISO standards (Du et al., 2012)

<b>Road roughness <math>G_q(\Omega_0)</math> (<math>10^{-6}</math> m<sup>2</sup>/(cycle/min)) at <math>\Omega_0=0.1</math> rad/min</b>		
<b>Rating</b>	<b>Description</b>	<b>Spectral density (cm<sup>3</sup>/cycle)</b>
R3	Very good road	8
R6	Medium road	64
R9	Very poor road	512

#### **3.5.4 Discussion on results from the simulation of a quarter car model with a semiactive seat suspension system**

Considering the nature of the road input, the RMS of driver mass acceleration at various grades of roads at different vehicle velocities is used to compare the performance of the passive damper in the seat suspension and the MR damper employing the two models discussed in this chapter. The response of the driver mass acceleration with a passive damper is referred to as SS-P, and the response of the driver mass acceleration with an MR damper is referred to as SS-E when employing EDM and SS-M when employing MFM. The RMS response of the driver mass acceleration obtained during simulation has been presented in Figure 3.11.

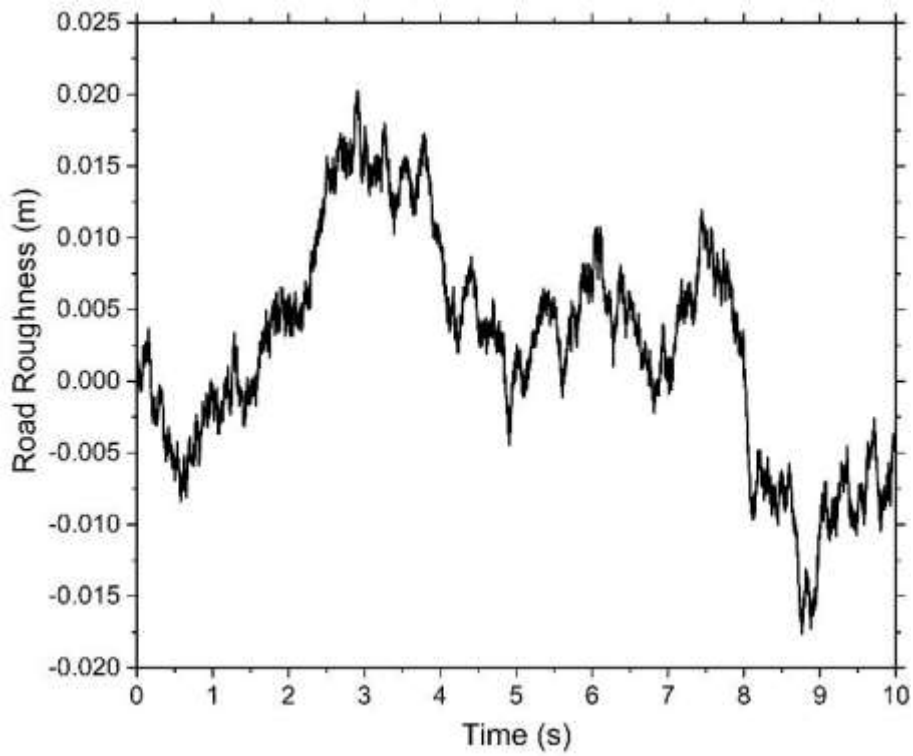
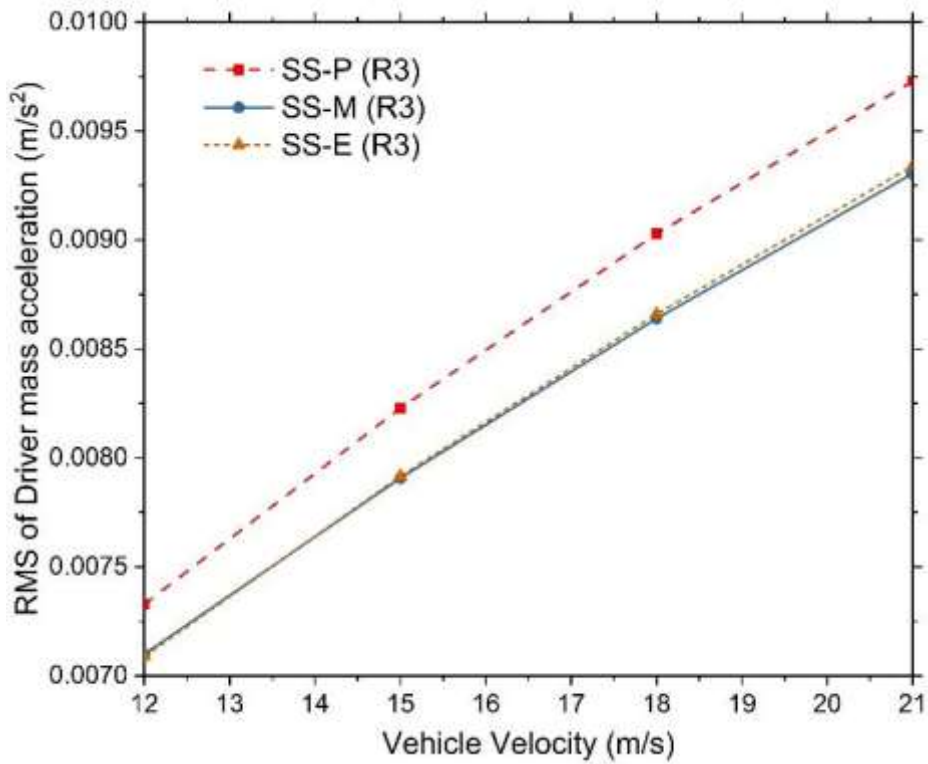
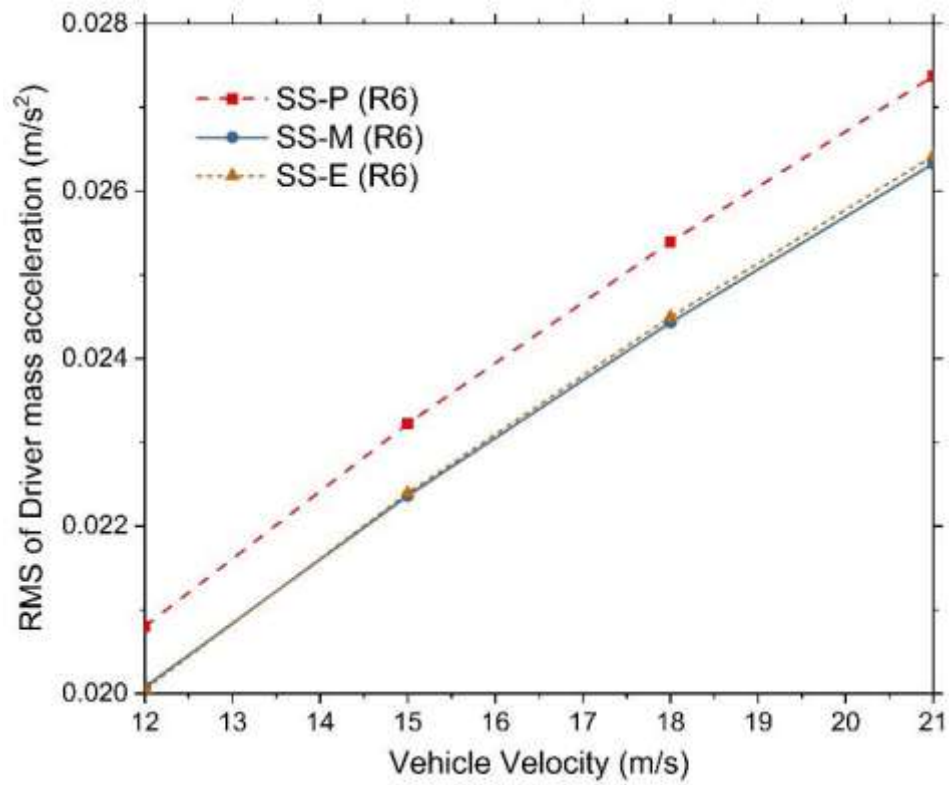


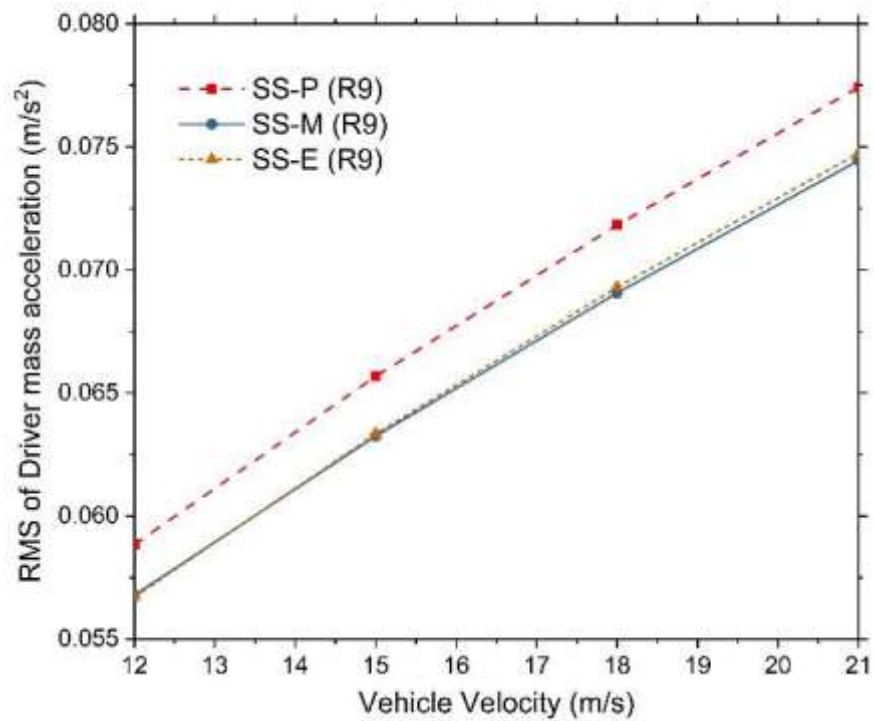
Figure 3.10 Random road profile of Medium road (R6) at 12 m/s



(a)



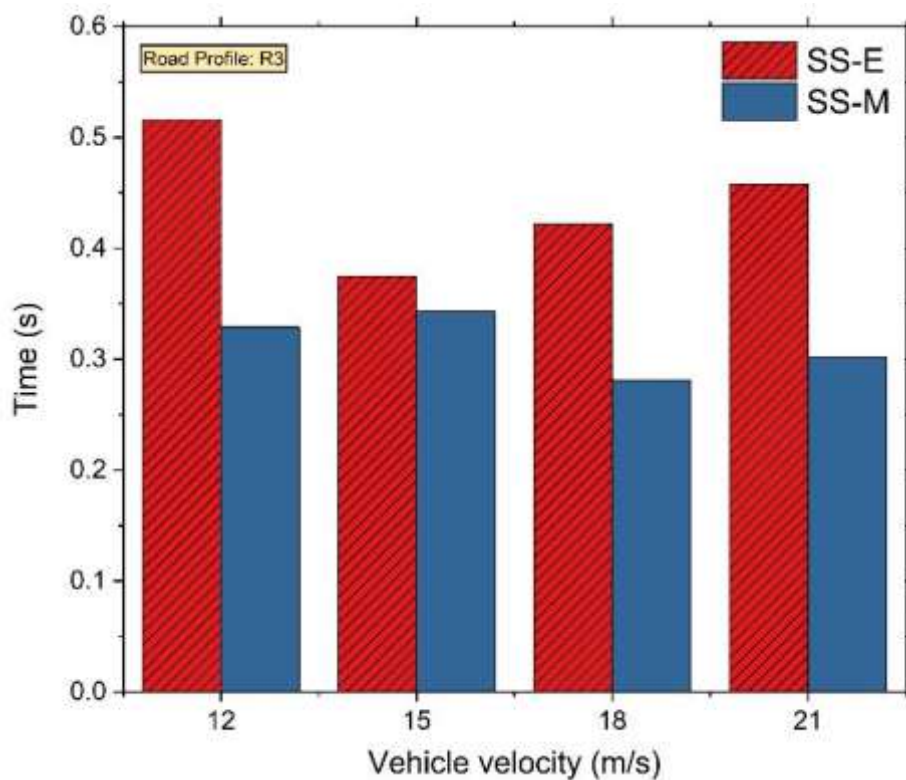
(b)



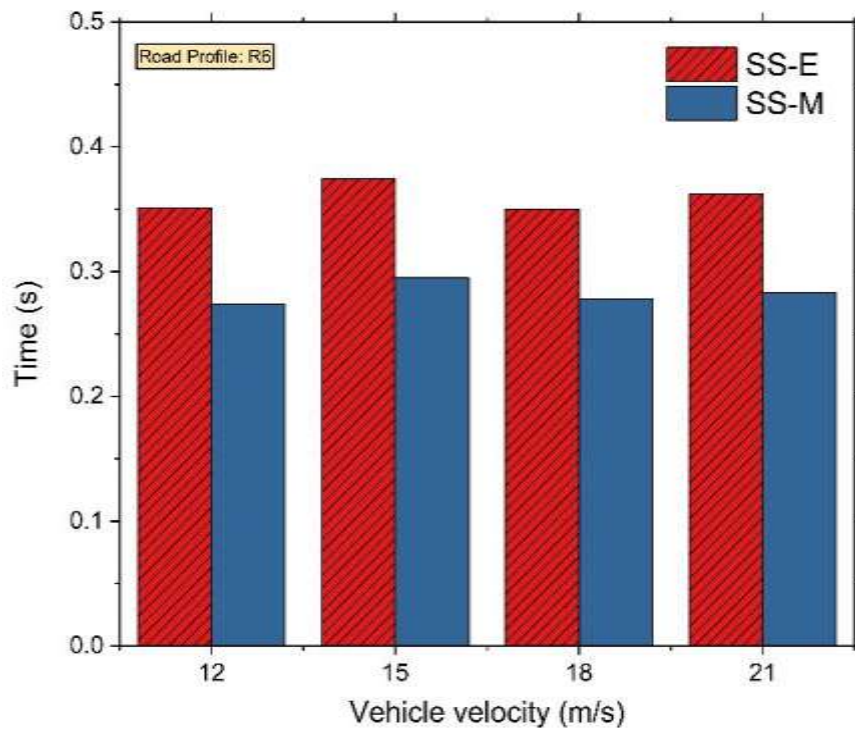
(c)

Figure 3.11 RMS of driver mass acceleration on road profile (a) R3 (b) R6 (c) R9

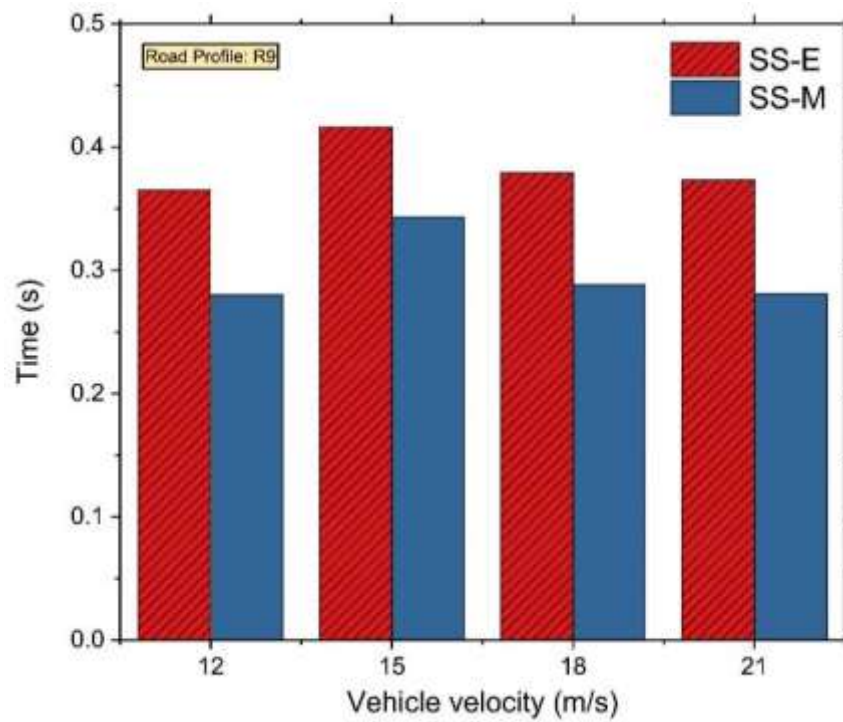
The MR damper models used in the current study are also compared based on the simulation time taken by each model for damping force evaluation. All the simulations in this study were carried out on the machine with an 8<sup>th</sup> Generation Intel core i5 quad-core x64 processor clocked at 1.6 GHz with 8 gigabytes of RAM running on Windows 10. Each QCM, SS-E and SS-M, is run as individual files in MATLAB Simulink and the run time of each file is noted using MATLAB profiles. Since SS-E and SS-M differ only by the models used for the MR damper, the difference between the simulation time of both files will be because of the MR damper models only. The QCMs were given each type of random road as input at various velocities mentioned previously. The results of comparing the simulation time of the MR damper models for various road profiles are summarized in Figure 3.12.



(a)



(b)



(c)

Figure 3.12 Simulation time of QCMs with MR damper on road profile (a) R3 (b) R6 (c) R9

It can be observed in Figure 3.11 that semiactive seat suspension with MR damper outperforms the seat suspension with passive damper irrespective of road profile grade and the forward velocity of the QCM. Moreover, the error between the RMS of driver mass response with EDM and MFM is practically non-existent. Furthermore, Figure 3.12 shows that the simulation time MFM is less than that of the EDM irrespective of the road profile and the forward velocity of the QCM, indicating that the MFM is computationally more efficient than the EDM. Although the difference between the simulation time of the two models is in the order of milliseconds, it should be noted that the reaction time of the MR damper used in this study is also in the order of milliseconds. Therefore, even such a small reduction in computational load improves the overall performance of a semiactive suspension system.

### **3.6 SUMMARY**

A commercial MR damper is characterized by sinusoidal excitation in the damper testing machine. The characterized data is used to model the damping behavior of the MR damper using two different mathematical models. One model uses the equivalent damping of the damper obtained at different currents and piston velocities, while the other uses the Magic Formula equation, commonly used in tire force calculations, to model the MR damper. Since the commercial MR damper used in this study is designed for seat suspension, the performance and computational efficiency of the two MR damper models are evaluated based on the simulation response of a quarter-car model with seat suspension subjected to random road profiles of varying grades. Considering the random nature of the road profiles, the accuracy of the two models is determined by observing the deviation in driver mass acceleration while using each of the MR damper models. The error between the RMS of driver mass response in seat suspension with MR damper represented by EDM and MFM is practically non-existent, suggesting that the MFM is as accurate as the EDM. The simulation time of the seat suspension system with MR damper represented by the MFM was less than when EDM was used, indicating higher computational efficiency of the MFM. Therefore, the computationally accurate and efficient MFM is used in the later parts of the work presented in this thesis.

## **CHAPTER 4**

### **DESIGN AND EXPERIMENTAL EVALUATION OF A COST-EFFECTIVE MONOTUBE MR DAMPER FOR APPLICATION IN PASSENGER VAN**

#### **4.1 INTRODUCTION**

The design of a hydraulic damper generally includes determining the piston orifice dimensions and the oil properties. The design of the MR damper involves the magnetic circuit design of the electromagnet used to activate the MR fluid in addition to the orifice design. A monotube MR damper is the most successful design for automobile suspension systems due to its robustness, compactness and reliability. Moreover, operating the MR fluid in flow mode is known to deliver higher controllable damping force in the case of MR dampers. Therefore, this chapter presents the hydraulic and electromagnetic circuit design of a monotube MR damper featuring a piston operating in flow mode with a floating piston-type accumulator. This chapter evaluates the developed MR damper on the damper testing machine and the test vehicle at the industrial collaborator Rambal Ltd., Chennai.

#### **4.2 METHODOLOGY TO DESIGN MR DAMPER AND EVALUATE ITS PERFORMANCE**

The methodology adopted to design and experimentally evaluate an MR damper in this chapter has been depicted in Figure 4.1. The optimal dimensions of the MR damper piston are obtained using the geometric dimension of its passive counterpart and the magnetic saturation of the MR damper piston components to maximize the magnetic flux density at the fluid flow gap. The optimized dimensions are analyzed in FEMM to determine the maximum flux density at the fluid flow gap. The damper is then characterized in the damper testing machine. The developed MR dampers are installed in the rear suspension of the test vehicle, Force Motor's – Traveller. The test vehicle with MR dampers is run over a sharp speed bump. The ride comfort and road handling of the test vehicle are evaluated using the vehicle body and wheel acceleration, respectively, while implementing the skyhook and ground hook control strategies for

supplying current to the MR dampers onboard. The obtained accelerations are compared with those obtained with stock passive dampers to evaluate the performance of the developed MR dampers on the test vehicle.

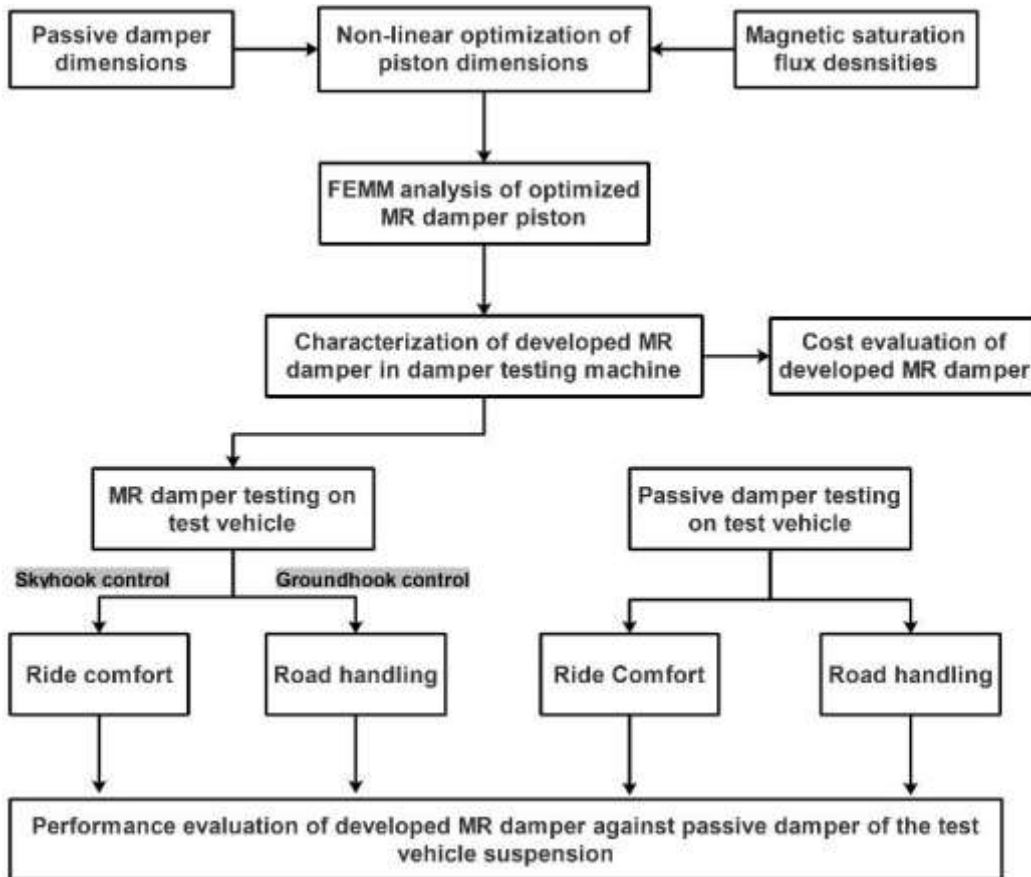


Figure 4.1 Methodology to evaluate performance of MR damper developed for passenger van

### 4.3 DESIGN OF MONOTUBE MR DAMPER

An optimized MR damper performs better than its unoptimized counterpart (Sung and Choi, 2008). In general, an optimization problem is formulated by defining an objective function governed by design variables subject to constraints. Designing an MR damper involves optimizing the critical geometrical dimensions influencing its performance to achieve desired damping forces within geometric and practical constraints (Gołdasz and Sapiński, 2015). Studies have shown that the monotube configuration of an MR damper is a desirable choice in vehicular applications due to fewer components and simplicity of operation (Dixon, 2007). Moreover, MR dampers with annular flow paths operating in flow mode have been found more suitable for



automotive applications (Gołdasz and Sapiński, 2015). The schematic of the monotube MR damper operating in flow mode with a gas-charged floating piston-type accumulator, adopted in this study, is shown in Figure 4.2.

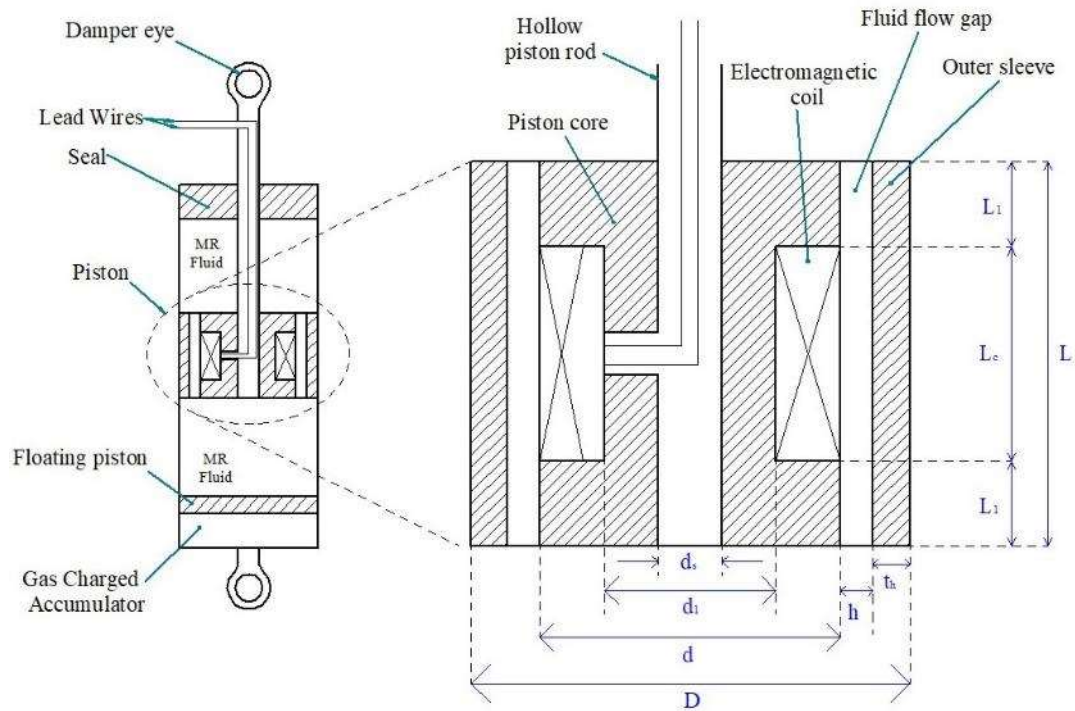


Figure 4.2 Schematic of MR damper

The MR damper illustrated in Figure 4.2 consists of a hollow piston rod accommodating the lead wires for supplying the current to the electromagnetic coil housed inside the piston. The piston core forms the path for the magnetic flux required for activating the fluid at the flow gap. The magnetic flux passes from the piston core to the outer sleeve at the top, then goes through the sleeve and moves back to the piston core at the bottom of the piston core. The magnetic flux path forms a closed circuit known as the magnetic circuit. The accumulator compensates for volume changes in the cylinder induced due to movement of the piston rod within the cylinder during operation.

The damping force delivered by the MR damper consists of two components, an uncontrollable hydraulic force arising due to the viscosity of MR fluid and the controllable component generated due to the magnetic nature of MR fluid. Hence, the design of an MR damper involves two parts; hydraulic design and magnetic circuit

design. The hydraulic design involves determining the overall piston height, overall piston diameter, and the fluid flow gap. The overall piston height is fixed to keep the stroke of the MR damper the same as its passive counterpart. The piston diameter is the same as the cylinder's inner diameter, which will carry the MR fluid, MRF-132DG, supplied by LORD Corporation, USA. The MR damper cylinder used in this study is a standard one that is in production at Rambal Ltd.

On the other hand, the fluid flow gap is also a part of magnetic circuit design. Magnetic circuit design is done to determine the dimensions, such as the fluid flow gap and piston core dimensions (flange thickness and piston core diameter at coil area), to minimize the reluctance of the magnetic circuit while the required damping capacity is achieved. In addition to a material's magnetic permeability, the area of the component's cross-section through which the flux flows also affect the magnetic reluctance. A material with higher magnetic permeability exhibits lower magnetic reluctance and vice-versa. Moreover, a larger cross-sectional area material exhibits a lower magnetic reluctance. The damping force of a monotube MR damper in flow mode is governed by equations 4.1 to 4.8 (Nguyen et al., 2009; Nguyen et al., 2014).

$$F_d = F_a + F_{vis} + F_{mr} \quad (4.1)$$

$$F_a = P_a A_s \quad (4.2)$$

$$P_0 = P_a \left( \frac{V_0}{V_0 - A_s x_p} \right)^{\gamma} \quad (4.3)$$

$$F_{vis} = \frac{12\eta Q L_t}{wh^3} \quad (4.4)$$

$$F_{mr} = \left( 2.07 + \frac{12\eta Q}{12\eta Q + 0.4 wh^2 \tau_0} \right) \frac{\tau L A_p}{h} \quad (4.5)$$

$$w = \pi (d + h) \quad (4.6)$$

$$Q = A_s \dot{x}_p \quad (4.7)$$

$$A_p = (\pi D^2/4) - (\pi d_s^2/4) - (\pi(d + 2h)^2/4) \quad (4.8)$$

Where  $F_d$  is the damping force of MR damper,  $F_a$  is the force due to the accumulator,  $F_{vis}$  is the damping force due to the viscosity of MR fluid,  $F_{mr}$  is the MR component of the damping force,  $P_a$  is the accumulator pressure,  $P_0$  is the initial pressure in the accumulator,  $A_s$  is the cross-sectional area of the piston rod,  $V_0$  is the volume of gas in the accumulator,  $\gamma$  is the isentropic expansion factor,  $x_p$  is the piston displacement,  $\eta$  is the MR fluid viscosity without magnetic field,  $Q$  is the volumetric flow,  $\dot{x}_p$  is the piston velocity,  $L_t$  is the total axial pole length and is defined as the sum of each pole length  $L_1$ ,  $d$  is the piston core diameter,  $h$  is the fluid flow gap,  $\tau$  is the shear stress of the MR fluid at its magnetic saturation,  $L$  is the total axial length of the piston,  $A_p$  is the effective piston area given by  $A_p = (\pi D^2/4) - (\pi d_s^2/4) - (\pi(d + 2h)^2/4)$ ,  $D$  is the overall piston diameter,  $d$  is the piston core diameter,  $d_s$  is the diameter of the piston rod. A dimensionless number known as dynamic range determines the damping capacity of an MR damper. It is defined as the ratio of the damping force in on-state to the damping force in off-state, i.e., the ratio of the damping force of the MR damper when no current is supplied to the damping force when the maximum possible current is supplied. The piston dimensions can be varied to achieve the desired dynamic range while keeping the magnetic flux density lower than the saturation flux density of the materials of the piston components. Figure 4.3 depicts the magnetic structure of the piston. The relationship between the coil current, the number of turns and the magnetic flux are governed by Ohm's Law, presented by equation 4.9.

$$NI = \phi S \quad (4.9)$$

Where  $\phi$  is the magnetic flux,  $N$  is the number of turns in the coil,  $I$  is current,  $S$  is the total magnetic reluctance of the magnetic circuit. It can be observed from Figure 4.2 that the geometry of the piston is symmetric about the piston rod axis. Hence, only one side of the piston is considered for the magnetic circuit. The overall reluctance of a magnetic circuit can be computed by adding the reluctance of each link from  $n_1$  to  $n_8$ .

It is clear from Figure 4.3 that  $n_2 = n_8$ ,  $n_3 = n_7$  and  $n_4 = n_6$ . Hence the total reluctance now becomes the sum of the reluctance of individual links from  $n_1$  to  $n_5$ , given by equation 4.10.

$$S = S_1 + 2S_2 + 2S_3 + 2S_4 + S_5 \quad (4.10)$$

Where  $S_1$ ,  $S_2$ ,  $S_3$ ,  $S_4$  and  $S_5$  are the reluctances of the links  $n_1$ ,  $n_2$ ,  $n_3$ ,  $n_4$  and  $n_5$ , respectively. In Figure 4.3, the piston core and the outer sleeve are made of EN1A, low-carbon steel with magnetic properties similar to AISI 1010 steel (Desai et al. 2019), readily available at Rambal Ltd.

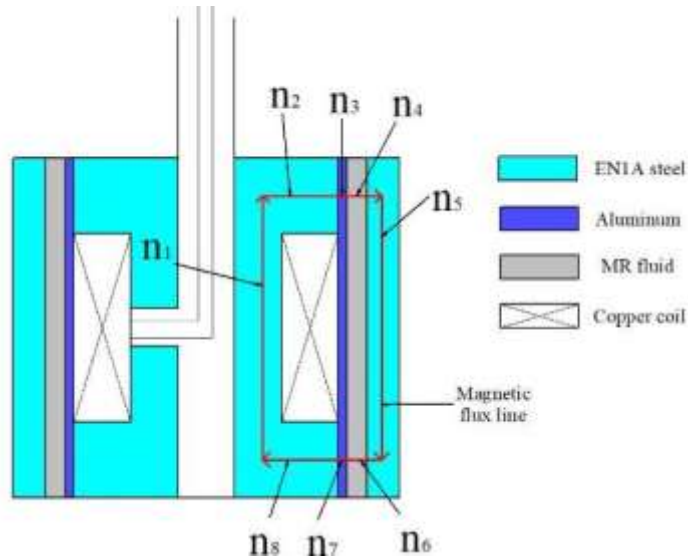


Figure 4.3 Magnetic circuit of the piston

Figure 4.3 features a new component, the inner sleeve, other than those shown in Figure 4.2. The purpose of the inner sleeve is to avoid the leakage of MR fluid through the hollow piston rod. Though the inner sleeve does not directly participate in the damper operation, it does add to the magnetic reluctance in the magnetic circuit (Desai et al., 2019). Hence the thickness of the inner sleeve is kept to a minimum of 1mm and is made of aluminum to avoid shorting of the magnetic circuit. The magnetic reluctances of the links shown in Figure 4.3 are calculated using equations 4.11 to 4.15 (Desai et al., 2019).

$$S_1 = \frac{4(2L_1 + L_c)}{\mu_0 \mu_{core} \pi d_1^2} \quad (4.11)$$

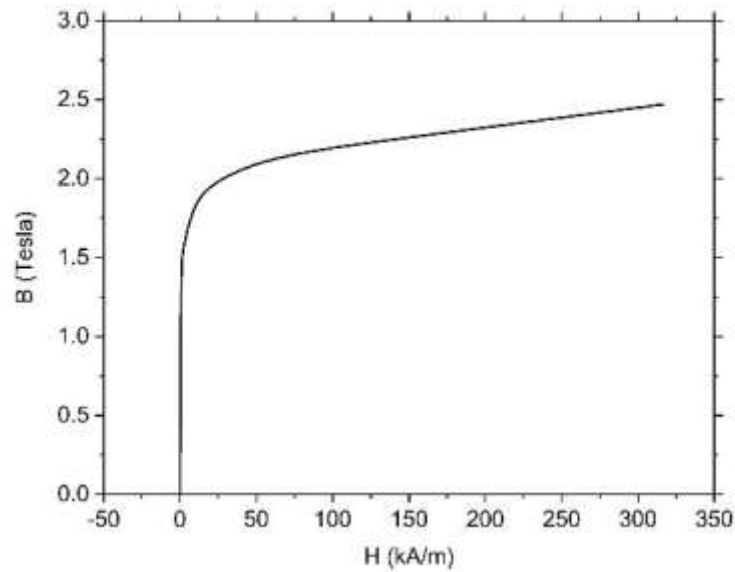
$$S_2 = \frac{\ln(d/d_1)}{\mu_0 \mu_{core} \pi (d^2 - d_1^2)} \quad (4.12)$$

$$S_3 = \frac{\ln(d/(d-2))}{\mu_0 \mu_{inner\ sleeve} \pi (d^2 - (d-2)^2)} \quad (4.13)$$

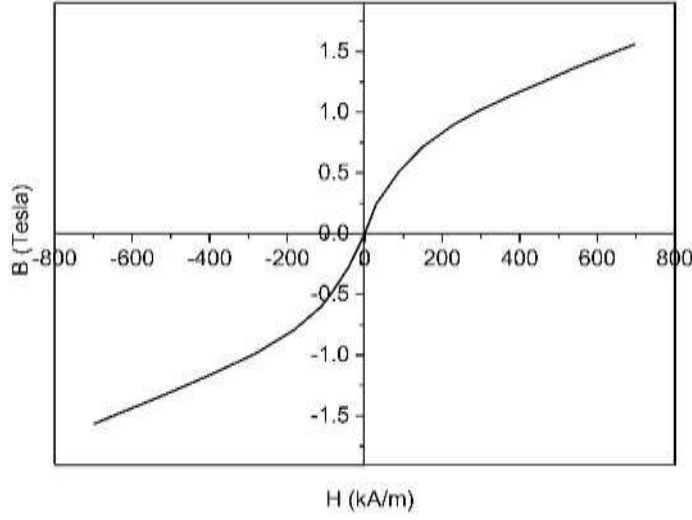
$$S_4 = \frac{\ln((d+h)/d)}{\mu_0 \mu_{MRF} \pi ((d+h)^2 - d^2)} \quad (4.14)$$

$$S_5 = \frac{4t_h}{\mu_0 \mu_{outer\ sleeve} \pi (d+2h+2t_h)^2} \quad (4.15)$$

Where,  $\mu_0$  is the permeability of free space ( $4\pi \times 10^{-7} H/m$ ),  $\mu_{core}$  is the relative permeability of the piston core material,  $\mu_{inner\ sleeve}$  is the relative permeability of the inner sleeve material (Aluminum),  $\mu_{outer\ sleeve}$  is the relative permeability of the outer sleeve material and  $\mu_{MRF}$  is the relative permeability of MRF-132DG. The permeability of a material can be obtained by taking the slope of its B-H curve, where B refers to magnetic flux density with unit Tesla (T) and H refers to magnetic field strength with unit A/m. The B-H curve of AISI 1010 steel and MRF-132DG can be seen in Figures 4.4a and 4.4b, respectively.



(a)



(b)

Figure 4.4 B-H curves of (a) AISI 1010 steel (MagWeb, 2021) (b) MRF-132DG (“LORD Corporation” 2019)

A higher magnetic flux density at the flow gap could result in a higher dynamic range of an MR damper. However, it should also be ensured that the flux density across the magnetic circuit does not exceed the saturation flux density of any material in the magnetic circuit. A flux density of 0.2T is a minimum requirement in the piston design presented in this study for a passenger van MR damper (Desai et al., 2019). The flux densities at each link shown in Figure 4.3 are given by equations 4.16 to 4.20 (Xu et al., 2013).

$$B_1 = \frac{4\phi}{\pi d_1^2} \quad (4.16)$$

$$B_2 = \frac{2\phi}{\pi(d_1 + d - 0.002)L_1} \quad (4.17)$$

$$B_3 = \frac{\phi}{\pi(d - 0.001)L_1} \quad (4.18)$$

$$B_4 = \frac{\phi}{\pi\left(\frac{2d + h}{2}\right)L_1} \quad (4.19)$$

$$B_5 = \frac{4\phi}{\pi(D^2 - (D - t_h)^2)} \quad (4.20)$$

Where  $B_1$ ,  $B_2$ ,  $B_3$ ,  $B_4$  and  $B_5$  are the flux densities of the links  $n_1$ ,  $n_2$ ,  $n_3$ ,  $n_4$  and  $n_5$ , respectively. It is clear from equation 4.1 and equation 4.20 that piston dimensions take part in both damping force generation and the reluctance of the magnetic circuit. The damping capacity of the damper needs to be maximized while keeping the magnetic flux density at the flow gap below the saturation flux densities of piston components and the MR fluid. These objectives could be achieved by altering the fundamental geometric dimensions of the piston by employing an optimization technique.

The overall piston height and diameter are fixed at 40.9 mm and 50 mm, respectively, to ensure that the outer diameter of the damper and the working stroke remains the same as the passive damper. The upper plate thickness is fixed at 2 mm to allow higher values of upper limits for rest of the components. The lower plate thickness is fixed at 4.4 mm to increase its strength to hold all the other components of piston in place firmly when the piston is assembled with piston rod. The added thickness of the lower plate also ensures that there is enough material to machine a counter sunk hole to accommodate the screw for assembling the piston. The hollow piston rod used in damper has an outer diameter of 16mm and inner diameter of 10 mm. The outer diameter of the piston rod is 12mm where the piston is attached. The flow gap is machined through wire cutting machine and the smallest diameter that can be achieved in the available wire cutting machine is 0.5mm. This can be set as the lower limit for the fluid flow gap. In the past studies, the upper limit for the fluid flow gap is generally taken as 3mm. The upper limit for diameters of all the components such as piston core, inner sleeve and outer sleeve is set as the inner diameter of the cylinder i.e., 40.9 mm and the lower limit is set at the piston rod diameter i.e., 12 mm. The upper limit of each flange is half of the total height of the piston core, 53.5 mm, and the lower limit can be set as 1 mm. Equations 4.21 and 4.22 ensure that the optimized design variables fall within the geometric restrictions of the MR damper.

$$d_1 + d + D = 40.9mm \quad (4.21)$$

$$2L_1 + L_c = 53.6mm \quad (4.22)$$

The field-dependent yield stress of the MRF-132DG used in equations 4.1 to 8 can be seen in Figure 4.5.

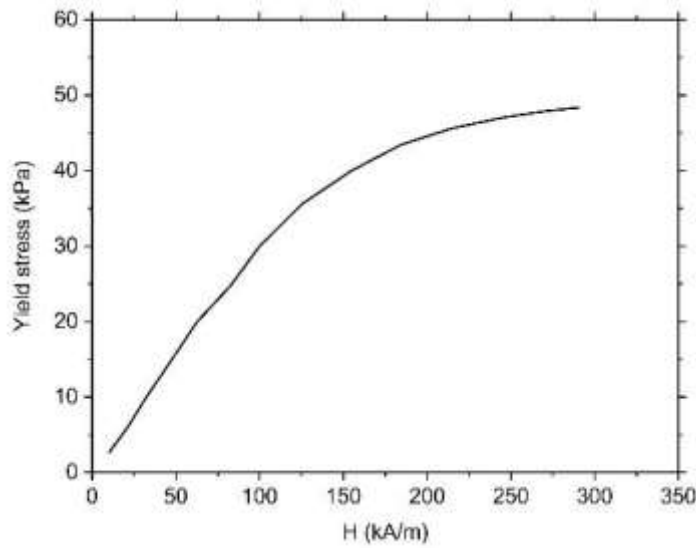


Figure 4.5 Field-dependent yield stress of MRF-132DG (“LORD Corporation”, 2019)

The saturation flux density of AISI 1010 steel is 1.25 T (Xu et al., 2013) and that of MRF 132 DG is 1.65 T (Shiao and Nguyen, 2013). Figure 4.4b shows that the magnetic field strength of the MRF-132DG corresponding to its saturation flux density is 700 kA/m. However, the yield strength of the MR fluid reaches a maximum of 48 kPa at 300 kA/m itself, as shown in Figure 4.5. The magnetic flux density corresponding to 300 kA/m in Figure 4.4b is 0.9T, which is the saturation flux density of the MR fluid in this study. The damping force generated by an MR damper is a measure of the damping capacity of that damper. The damping force of an MR damper, as seen in equation 4.1, is a non-linear function dependent on multiple variables (fundamental geometric dimensions) subjected to constraints (saturation flux density and space constraints). Hence, a non-linear minimization approach would suit for optimization of the variables. The Optimization Toolbox™ in MATLAB® R2018b can minimize a constrained non-linear multivariable function using the fmincon algorithm (Xu et al., 2013; Acharya et al., 2019; Moon et al., 2011). Table 4.1 lists the optimized



piston dimensions so acquired which have been used to fabricate the MR damper and Figure 4.6 illustrates the final piston component dimensions.

Table 4.1 Dimensions of MR damper piston

Dimension	Value (m)	Dimension	Value (m)
$d_s$	0.012	$h$	0.0005
$d_1$	0.020	$t_h$	0.00345
$d$	0.030	$L_1$	0.018
$D$	0.0409	$L_c$	0.0176

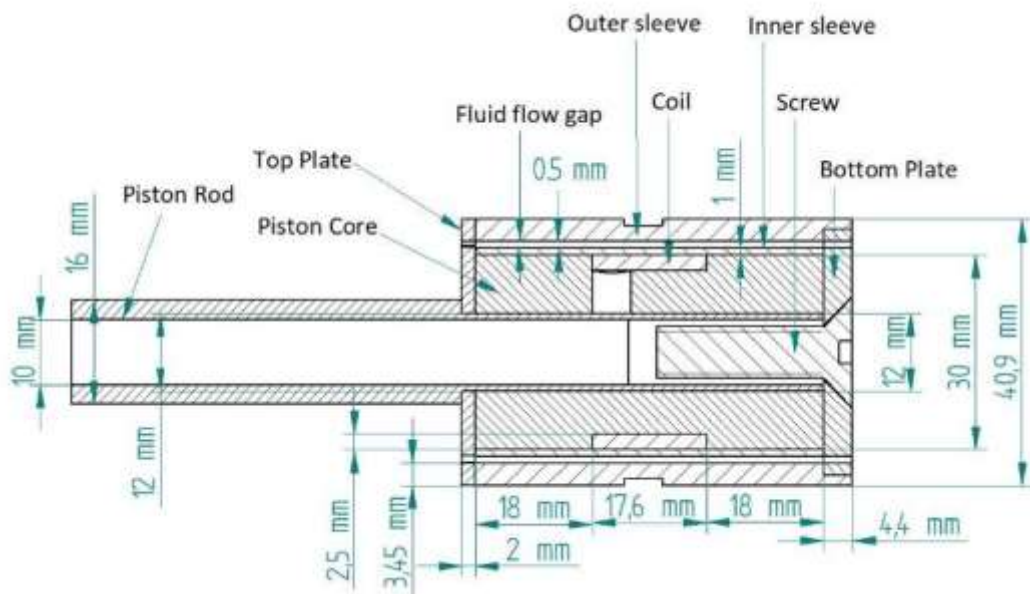


Figure 4.6 Dimensions of the MR damper piston

The magnetic flux along the magnetic circuit of the MR damper was simulated using FEMM. The results from FEMM analysis, shown in Figure 4.7, show that the magnetic flux density at the flow gap is 0.25T, which is less than the saturation flux density of the MR fluid used in this study and is also more than the desired flux density of 0.2T. The results of the FEMM analysis of the MR damper piston with optimized parameters show that the Fmincon optimization algorithm employed, has satisfied the given constraints of the MR damper piston. The FEMM analysis results also show that the magnetic flux density generated at the flow gap provides enough variation in the damping capacity of the MR damper without causing magnetic saturation of any piston components and the MR fluid. It can also be observed in Figure 4.7 that the use of

aluminum material for the top plate, bottom plate and inner sleeve restricts the magnetic flux between the piston core and the outer sleeve, thus avoiding shorting of the magnetic circuit.

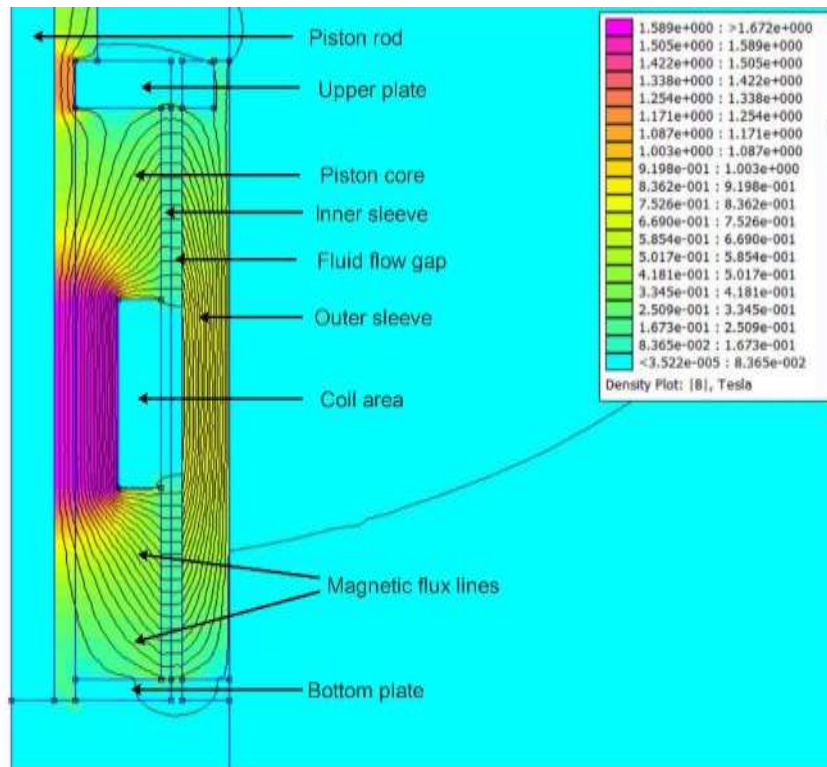
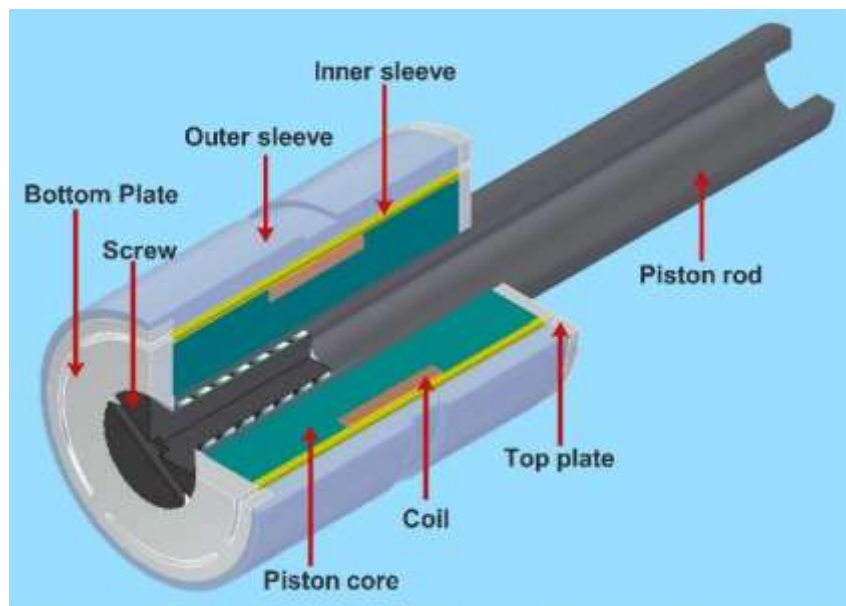


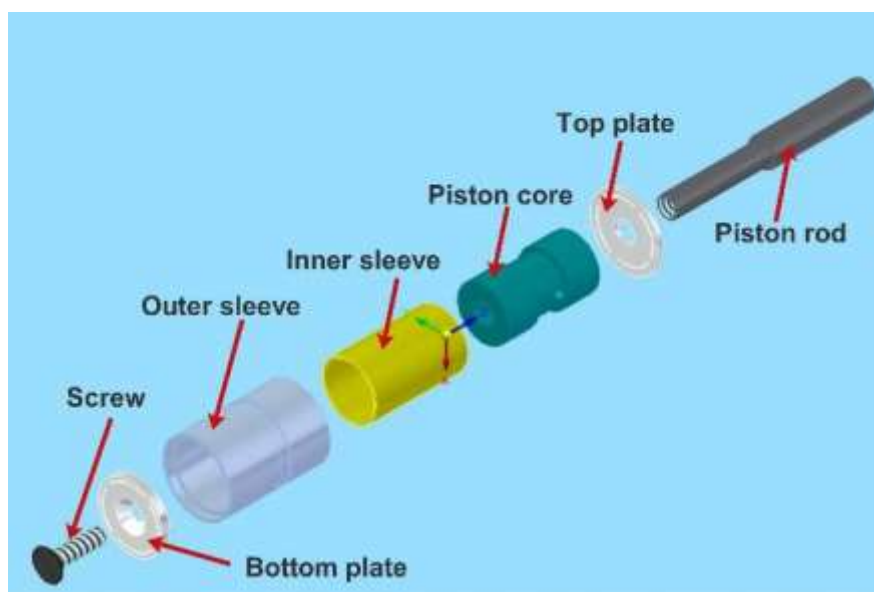
Figure 4.7 Simulation result of the magnetic circuit in FEMM

Figure 4.8a shows the quarter section of the piston assembly, Figure 4.8b shows the exploded view of the CAD model of the piston assembly, and Figure 4.8c shows the actual components fabricated. The CAD model shows two more piston assembly components, apart from the components described in Figure 4.2, the top and bottom plates. These two components and the screw at the bottom hold the complete piston assembly together on the piston rod. These two components are also made of aluminum to avoid flux leakage. The fabricated piston core is provided with slots along the circumference of both flanges. These slots accommodate the seals (O-rings) that prevent fluid leakage through the hollow piston rod. The piston core is wound with 26 AWG copper wire to make the electromagnetic coil. A total of 240 turns were completed, whose resistance was measured to be 5.6 Ohms. As per equations 4.9, 4.14 and 4.19, the flux density at the fluid flow gap reaches 0.9T at 7.2A. The maximum current rating of the 26AWG copper wire used in this study is 7A (“Hitachi Cables

America Incorporated”, 2022). A 12V battery supplies current to the MR damper. Therefore, Ohm’s Law restricts the maximum current to the electromagnetic coil to 2.14A. Hence, the MR dampers in this study are given a maximum of 2A of current throughout the study. The assembled piston with the electromagnetic coil is inserted into the cylinder and filled with MR fluid. The accumulator is charged with nitrogen gas until the damper fully extends in the unloaded condition, which is 20 bars. The fully assembled MR damper, ready for testing, is shown in Figure 4.9.



(a)



(b)



(c)

Figure 4.8 (a) CAD model of piston assembly (b) Exploded view of piston assembly (c) Fabricated parts of the piston assembly

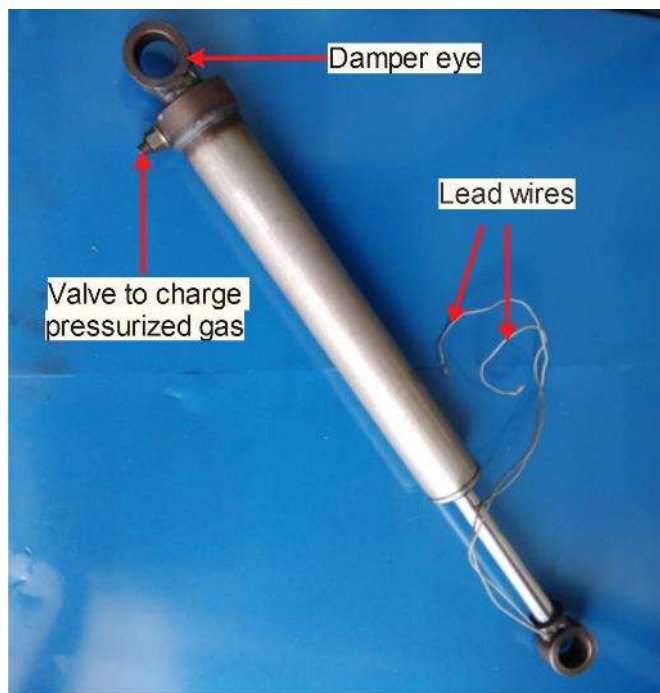


Figure 4.9 Fully assembled monotube MR damper for the test vehicle

#### 4.4 PERFORMANCE EVALUATION OF DEVELOPED MR DAMPER

##### 4.4.1 Characterization of developed MR damper on damper testing machine

The fabricated MR damper is tested on the damper testing machine available at Rambal Ltd. itself, as shown in Figure 4.10. The damper testing machine available at Rambal has a hydraulic actuator to generate the required cyclic excitations with a

loading capacity of 1 ton, 250 mm of stroke limit and controlled by a servo controller, which can generate a sinusoidal excitation signal with a peak velocity of 1m/s. A load cell with a capacity of 12 kN measures the damping force, and an integrated displacement sensor measures the damper displacement. A NI-USB-6221 data logger records the displacement and damping force during the experiments with a maximum sampling rate of 10 kHz. The data logger and the servo controller interface with the computer using LABVIEW® software.

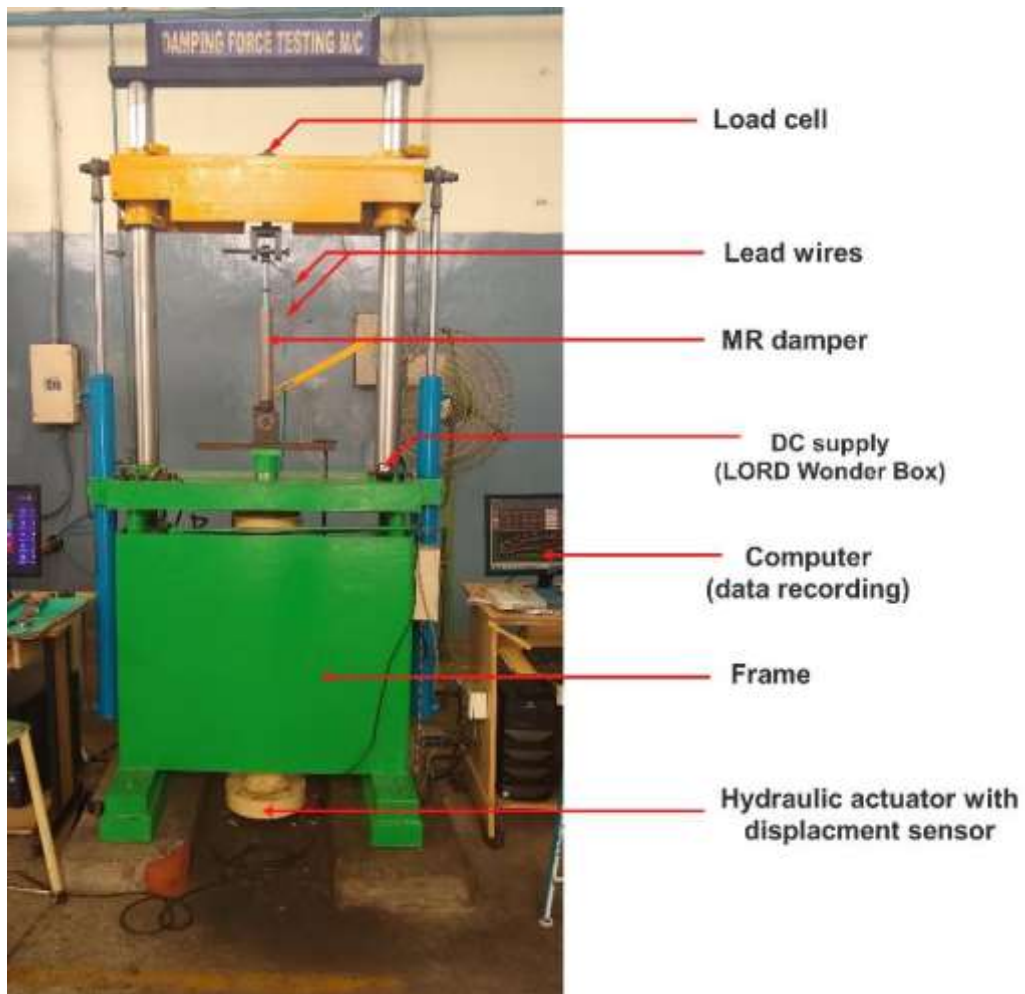
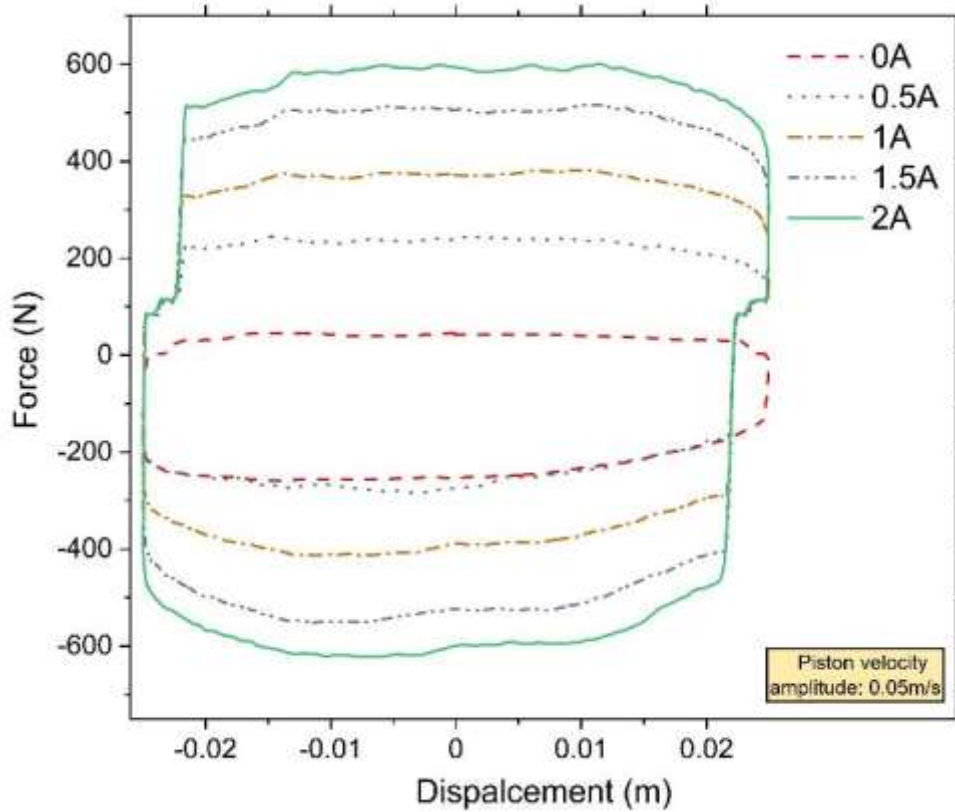


Figure 4.10 Damper testing machine from Rambal Ltd., Chennai

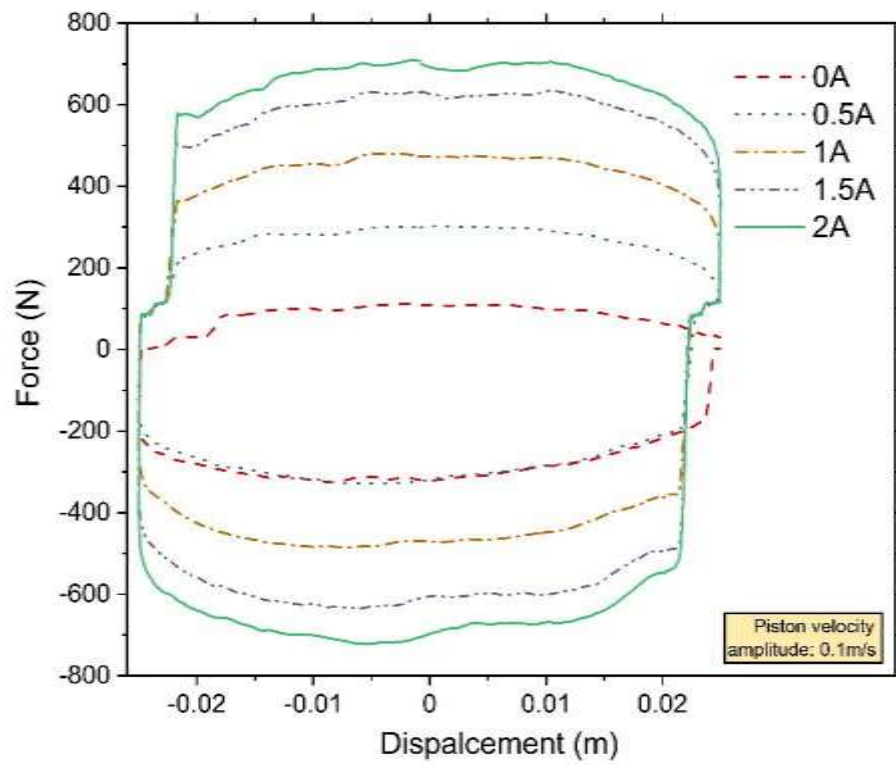
The damper is supplied with DC using the LORD Wonder Box®, which allows the user to vary the current during the experiment. During the characterization, the MR damper is subjected to sinusoidal excitation with an amplitude of 25mm. The velocity is varied from 0.05m/s to 0.4m/s by varying the frequency. The peak velocity is first set to 0.05 m/s for ten cycles, then to 0.1 m/s for ten cycles, and then so on up to 0.4



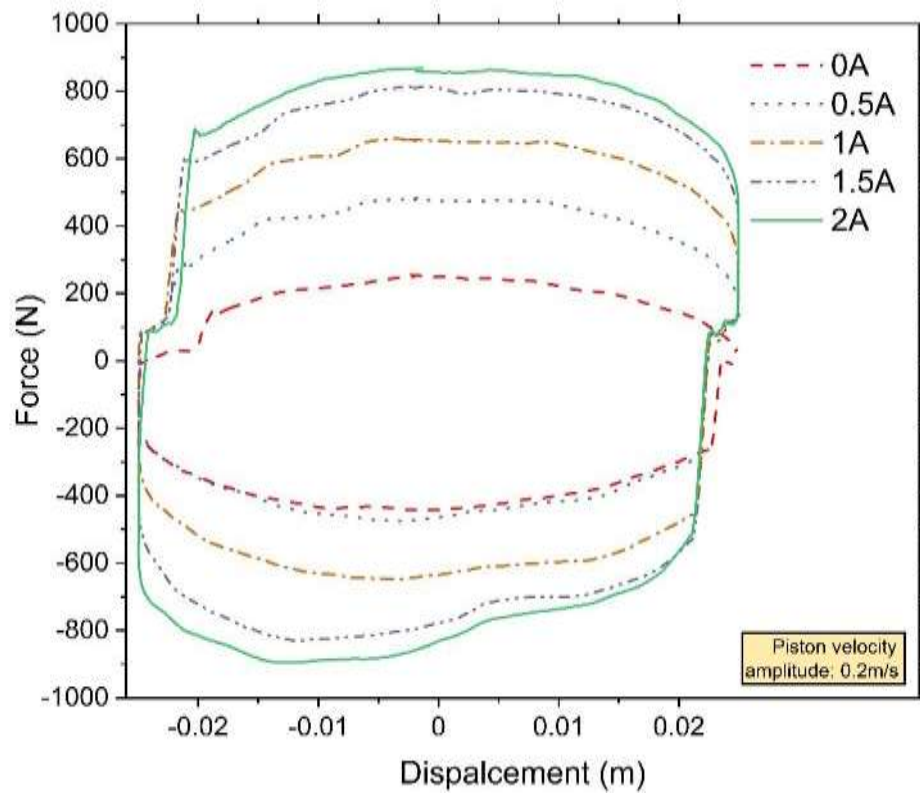
m/s while supplying 0A of current. The above steps are repeated while supplying 0.5A current, then 1A, and then so on till 2A. During the transition of one peak velocity to the next, it takes approximately five cycles for the damper to operate steadily (Desai et al., 2020). Therefore, force and displacement data from the sixth cycle, at each peak velocity and current value, considered for analysis in this study, has been presented in the form of FD diagrams in Figure. 4.11. Figure 4.12 represents the characteristic graph obtained during the experiment.



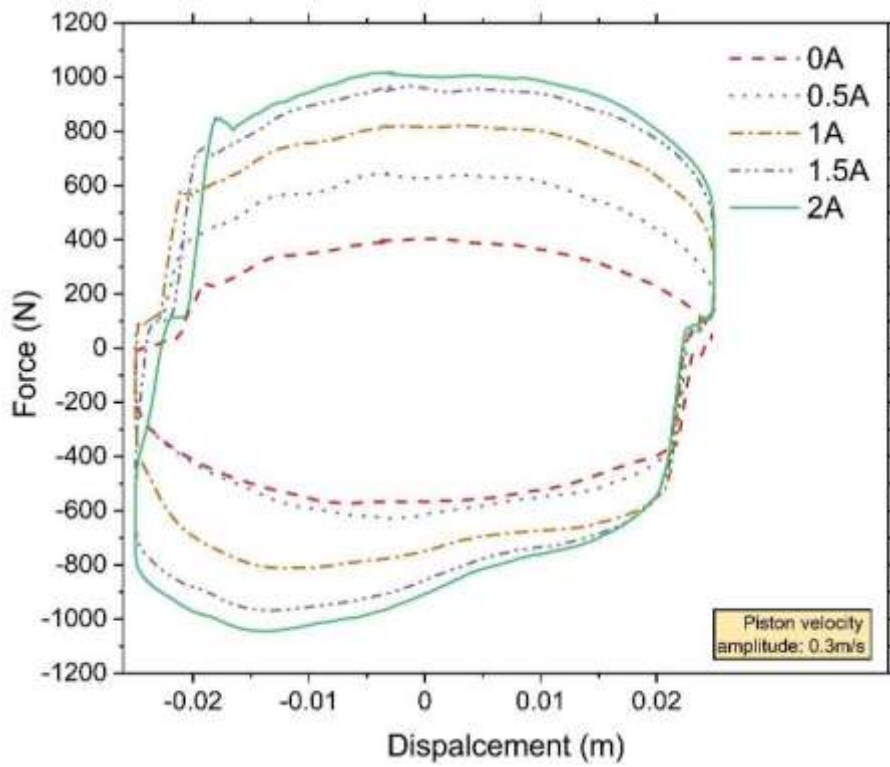
(a)



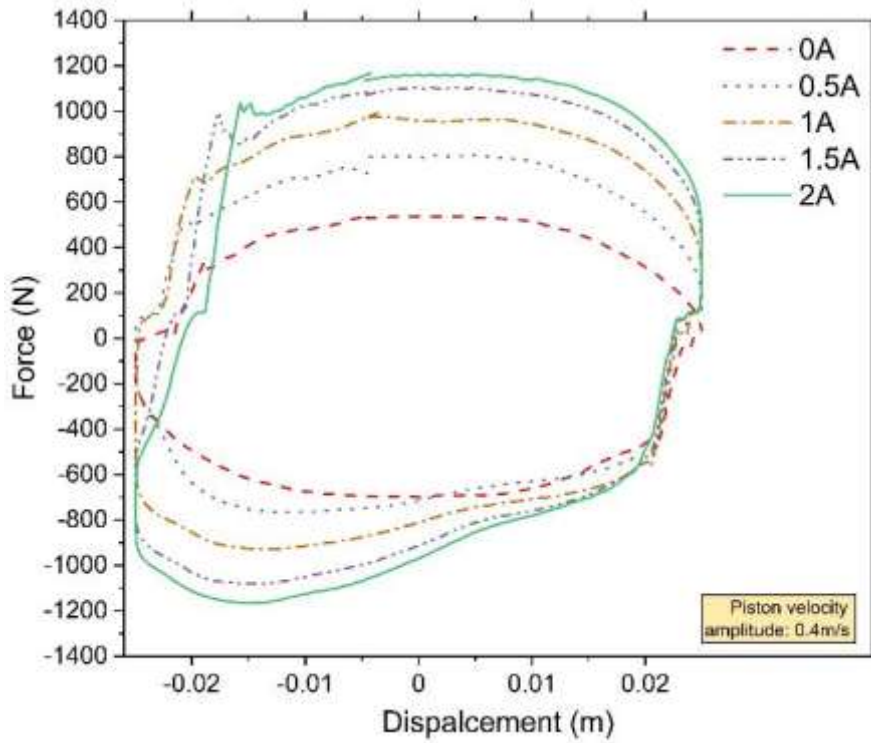
(b)



(c)



(d)



(e)

Figure 4.11 FD diagrams of developed MR damper at (a) 0.05m/s (b) 0.1m/s (c) 0.2m/s (d) 0.3m/s (e) 0.4 m/s



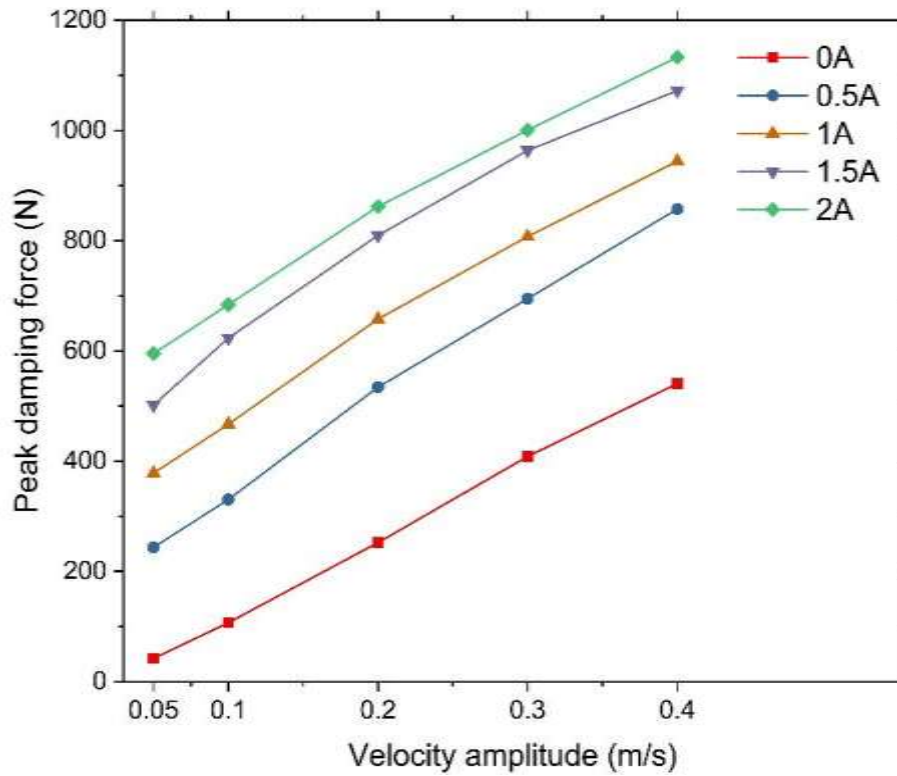


Figure 4.12 Characteristic graph of the developed MR damper

It can be observed in Figure 4.11 that the damping force of the developed MR damper increases with increasing current at all the excitation velocity amplitudes, indicating that the designed damper piston is working as desired to provide the intended MR effect. It can be observed in Figure 4.12 that the increase in damping force is minimal when the current is increased from 1.5A to 2A. Therefore, 2A is the maximum current that can be supplied to the damper. Further, the force-lag phenomenon, as discussed in section 3.3.3 of this thesis, can also be seen in Figure 4.11(a), which is pronounced more and more with an increase in excitation velocity amplitude, distorting the shape of FD curve in Figures 4.11(b) to 4.11(e). During the entire characterization experiment, no fluid leakage was observed even after its continuous operation on the damper testing machine, owing to the robustness of the piston design. The developed MR damper delivered sufficient damping force to make it feasible to be installed on the test vehicle for further testing.

#### 4.4.2 Real-time testing of developed MR damper on the test vehicle

The test vehicle used in the present study is a Force Motor's – Traveller, which was available at Rambal Ltd., as shown in Figure 4.13(a), and the right side of the rear suspension of the test vehicle with a stock passive damper is shown in Figure 4.13(b).



(a)



(b)

Figure 4.13 (a)The test vehicle (b) Rear suspension of the vehicle (right side)

It is a rear-wheel drive passenger van with rigid axles at the front and rear ends. The front suspension of the test vehicle consists of a leaf spring along with stock passive dampers, and the rear suspension consists of a combination of a half-leaf spring and bellow-type air spring on each side along with stock passive dampers. The suspension of the test vehicle is converted into a semi-active one by replacing the passive damper in Figure 4.13(b) with the developed MR damper and placing the accelerometers on the vehicle and the wheel. The purpose of the experiment on the test vehicle is to evaluate the performance of the MR damper against the stock passive damper based on the acceleration response of the vehicle body and the wheels. Therefore, one accelerometer is placed on the vehicle body and the other on the wheel. The nearest location accessible for acceleration measurement on the wheel is the axle, as evident from Figure 4.14. Hence, the acceleration data collected from the axle at the location shown in Figure 4.14 is designated as data collected at the wheel.

The accelerometer used in this experiment is a model 352C33 uniaxial accelerometer from PCB electronics. The accelerometer has a ceramic sensing element with a sensitivity of 100 mV/g and a sensing range of  $\pm 50g$  (“PCB Electronics”, 2022). The NI-9234 records the accelerometer data, and digital I/O, NI-9403, triggers the current supply to the MR damper. The NI-CDAQ-9174 communicates the accelerometer data from DAQ to the computer onboard the test vehicle and the triggers signal for the current supply to the MR damper. In this case, the MR damper's current is supplied by a 5000 mAh lithium-ion battery and amplified by a 20A DC motor controller. The laptop, DAQ, DC power source and signal amplifier are placed inside the vehicle during the experiment. the data flow schematic during the experiment can be seen in Figure 4.14.

The current supplied to the MR damper in the experiments on the test vehicle is governed by the on-off skyhook control and the ground hook control. The skyhook control, described in section 3.5.2 of this thesis, takes the form of equation 4.23.

$$F_d = \begin{cases} F_{dmax} & \text{for } \dot{x}_b(\dot{x}_b - \dot{x}_w) \geq 0 \\ F_{dmin} & \text{for } \dot{x}_b(\dot{x}_b - \dot{x}_w) < 0 \end{cases} \quad (4.23)$$

Where  $\dot{x}_b$  is the vehicle body velocity and  $\dot{x}_w$  is the velocity of the wheel,  $F_{dmax}$  is the maximum damping force obtained at 2A and  $F_{dmin}$  is the minimum damping force obtained at 0A.

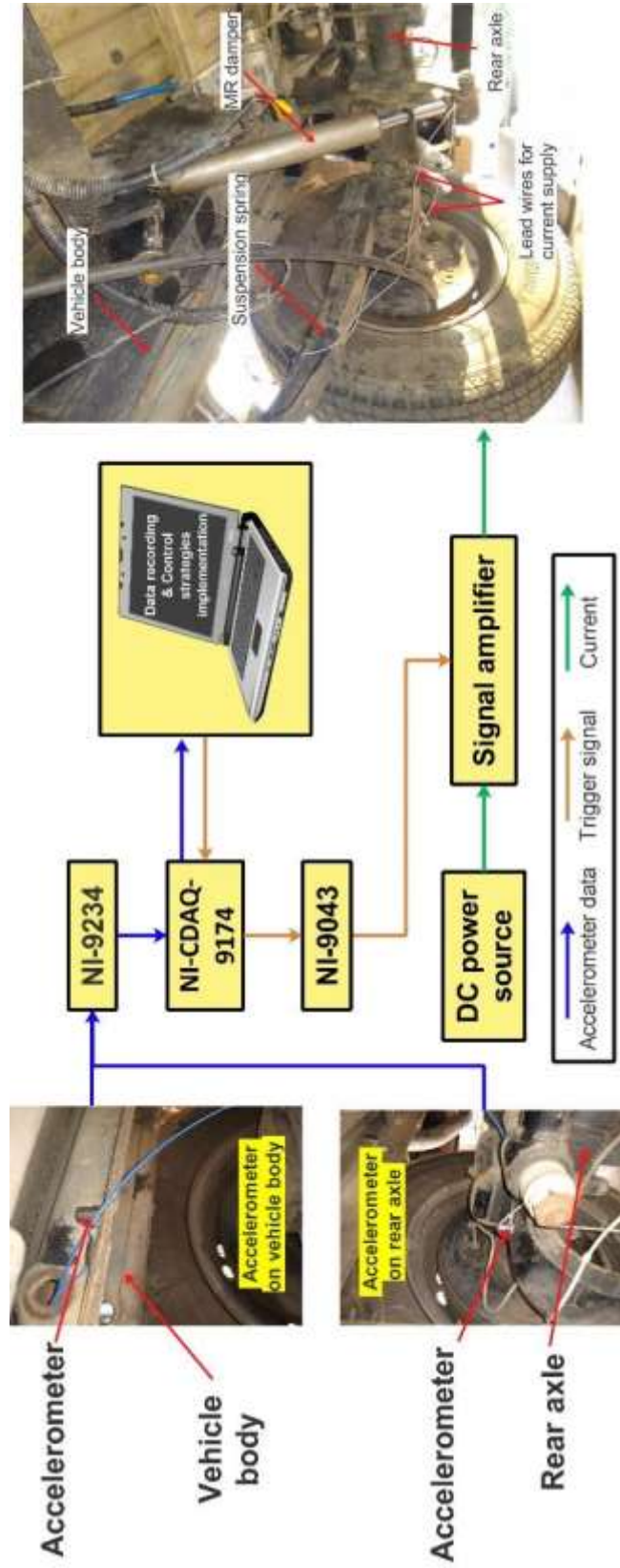


Figure 4.14 Schematic of data flow during the experiment on the test vehicle

The ground hook control logic is similar to the skyhook control logic, but the imaginary damper is assumed to be connected between the wheel (unsprung mass) and the sky. As a result, this control logic attempts to reduce the vertical acceleration of the unsprung mass. The term deciding the supply of current in the ground hook control changes to  $\dot{x}_w(\dot{x}_b - \dot{x}_w)$  as can be seen in equation 4.24.

$$F_d = \begin{cases} F_{dmax} & \text{for } \dot{x}_w(\dot{x}_b - \dot{x}_w) \geq 0 \\ F_{dmin} & \text{for } \dot{x}_w(\dot{x}_b - \dot{x}_w) < 0 \end{cases} \quad (4.24)$$

The test vehicle is run over a sharp speed bump within the premise of Rambal Ltd. The speed bump used in this study is 40 mm wide and 4mm high, as shown in the schematic in Figure 4.15. The vehicle is run at two speeds, 10 km/h and 20 km/h. It is ensured that the vehicle speed is maintained at the required speed by allowing a sufficient running distance of at least 28m before and after the speed bump.

A total of four test runs are conducted on the test vehicle. In the first test run, the test vehicle with stock damper is run over the speed bump at 10km/h and 20km/h. In the second test run, the test vehicle is fitted with MR dampers and is run over the speed bump at the same test speeds while operating the MR dampers in off-state. The third test run involves running the test vehicle with MR dampers at the same test speeds over the speed bump while implementing the skyhook control strategy. In the fourth type of test run, the vehicle with MR dampers is run over the speed bump at the same test speeds while implementing the ground hook control strategy. The acceleration data from the vehicle body and the wheel obtained from the test vehicle with stock dampers and MR dampers are compared to determine the performance of the semiactive suspension system. Since the test vehicle is run over a flat road with a single speed bump, the peak accelerations of the chassis and the wheel are considered to be the performance indices. The results obtained from this experiment on the test vehicle can be seen in Figure 4.16.

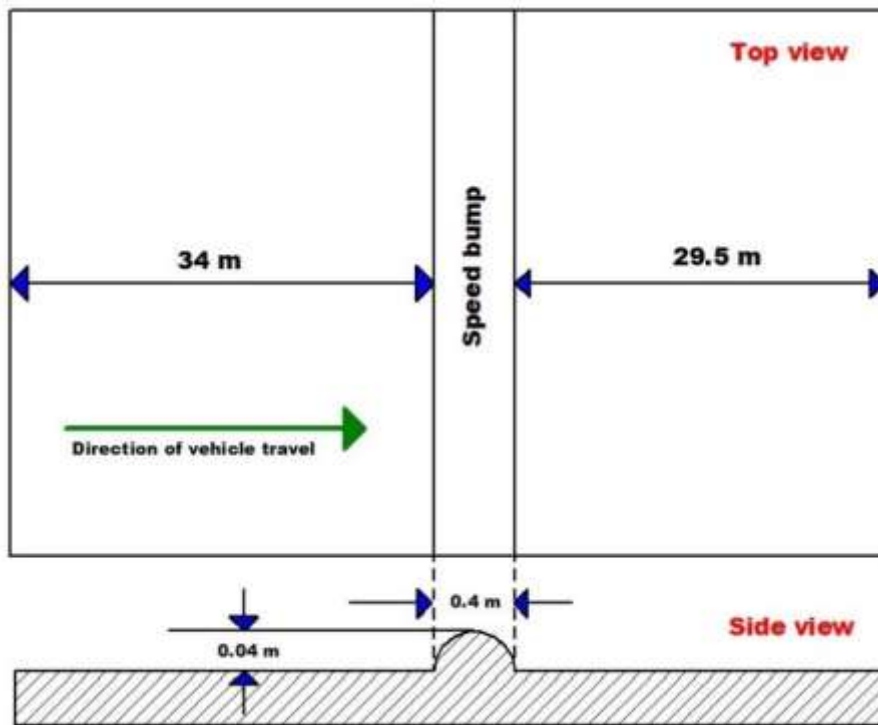
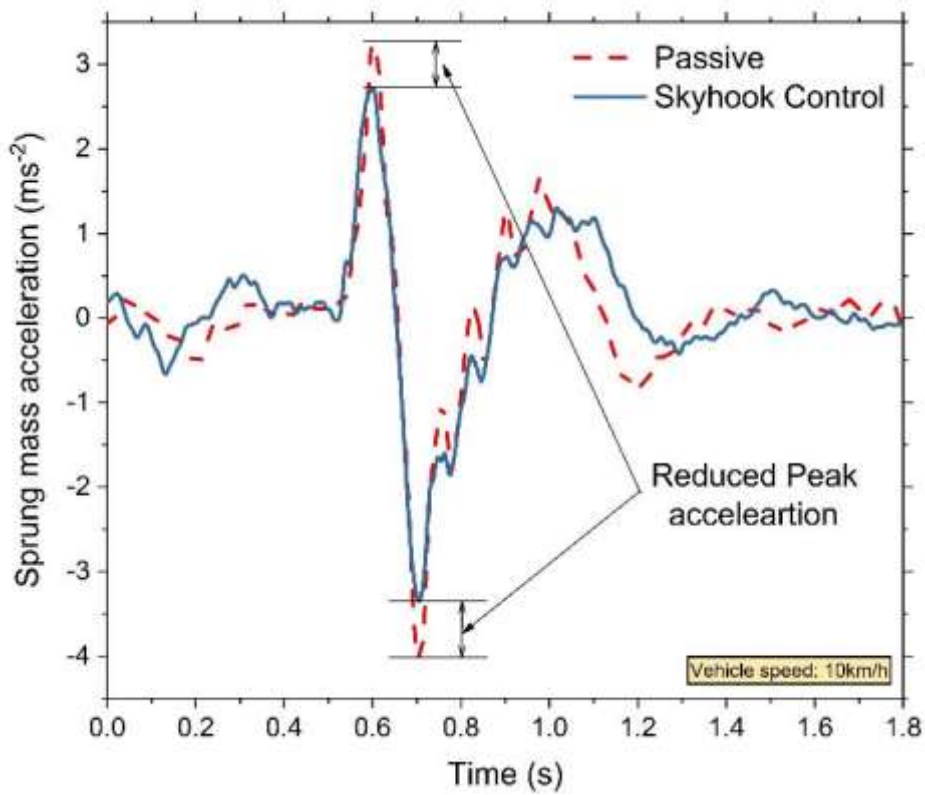
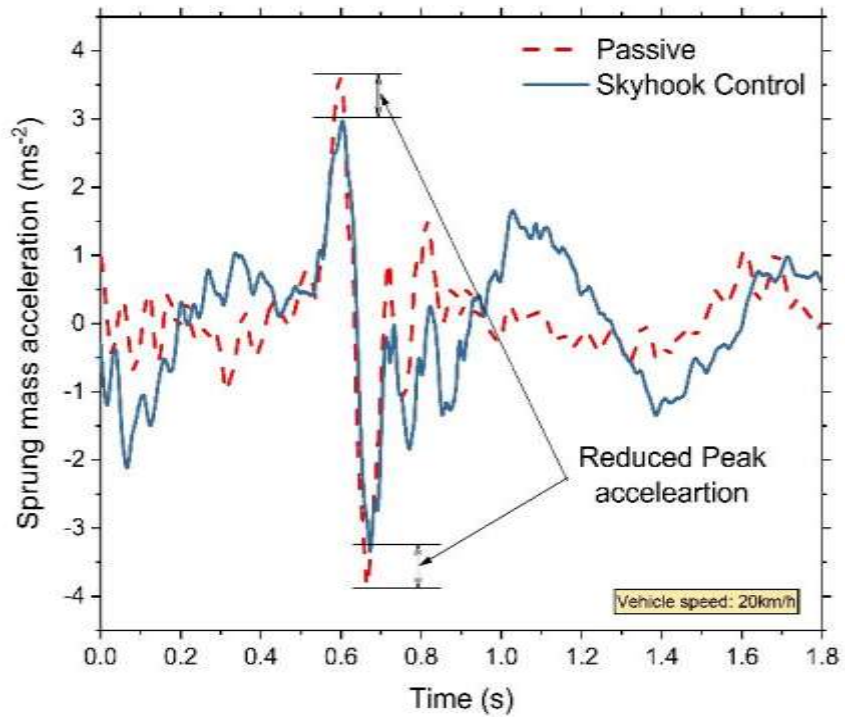


Figure 4.15 Schematic of the sharp speed bump

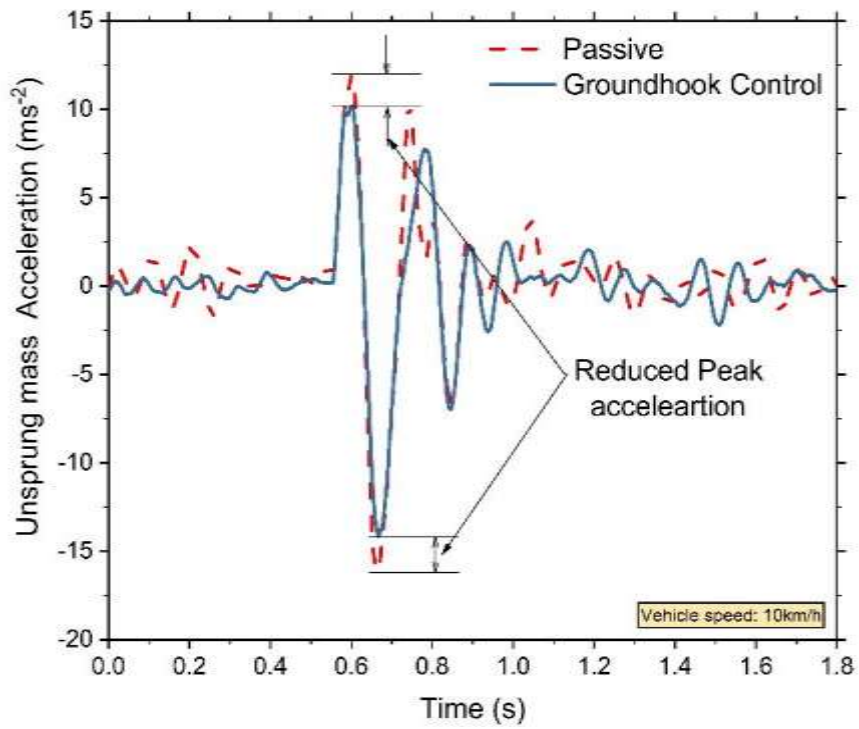


(a)



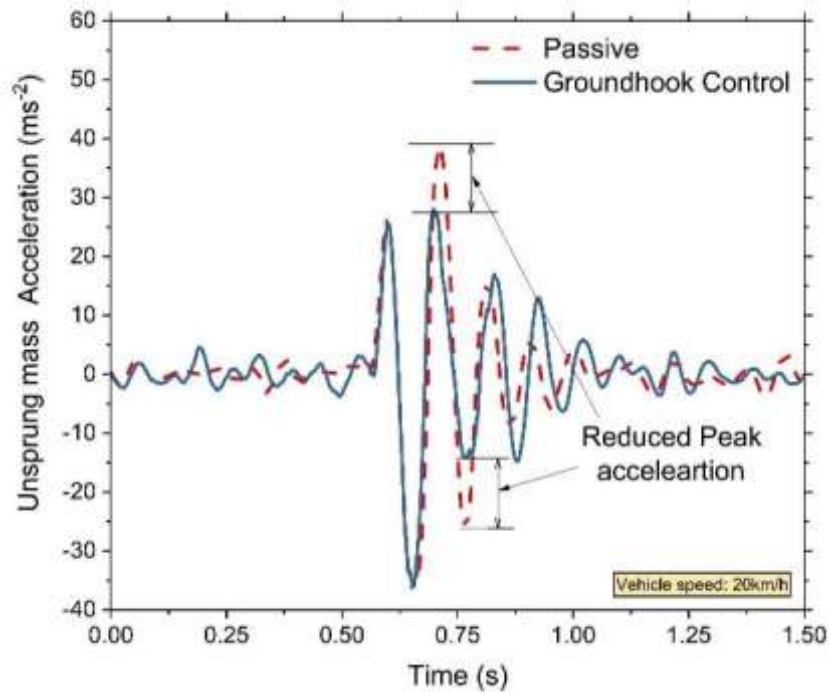
(b)

Figure 4.16 (a) Vehicle body acceleration measured at 10km/h (b) Vehicle body acceleration measured at 20km/h



(a)





(b)

Figure 4.17 (a) Wheel acceleration measured at 10km/h (b) Wheel acceleration measured at 20km/h

#### 4.5 COST EVALUATION OF DEVELOPED MR DAMPER

The cost of the MR damper developed in this study can be divided into fabrication and MR fluid costs. The materials for the damper cylinder, the piston rod and the piston components (upper plate, bottom plate, piston core, inner sleeve, outer sleeve and coil winding) were obtained from Rambal Ltd., along with testing. The damper fabrication charges are INR 20,246.19/-. The MR fluid used in the study is the LORD MRF-132DG, purchased from LORD Corporation, USA, through their reseller in India. The cost of the fluid stands at INR 1,52,714/- per liter. Approximately 250 ml of MR fluid is used in the MR damper developed under this study. Therefore, the cost of the volume of fluid used in the developed MR damper is calculated to be INR 38,178/-. The overall cost of the MR damper is calculated as the sum of fabrication cost, testing charges and the cost of MR fluid which comes to be INR 58,424/-. The MR dampers, RD-8040-1 and RD-8041-1, will cost approximately INR 2,07,172/- each in India. Moreover, these two MR dampers are designed for seat suspension systems as per the product specifications.



LORD Corporation also develops MR dampers for the primary suspension of certain vehicles (“Parker”, 2022). Although the price of those MR dampers is not readily available, it is logical to assume that they will be larger in size and damping capacity, hence will contain a larger quantity of the MR fluid than the RD-8040-1 or RD-8041-1. Therefore, it is also logical to assume that the cost of those dampers will also be higher as compared to RD-8040-1 or RD-8041-1. The MR damper developed under this study costs less than the commercial MR dampers while performing better than the stock passive dampers in improving the test vehicle's ride quality and road handling.

#### **4.6 RESULTS AND DISCUSSION**

It can be observed in Figure 4.11 that the damping force of the developed MR damper increases with increasing current at all the excitation velocity amplitudes, indicating that the designed damper piston is working as desired to provide the intended MR effect. It can be observed in Figure 4.12 that the increase in damping force is minimal when the current is increased from 1.5A to 2A. Therefore, 2A is the maximum current that can be supplied to the damper. Further, the force-lag phenomenon, as discussed in section 3.3.3 of this thesis, can also be seen in Figure 4.11(a), which is pronounced more and more with an increase in excitation velocity amplitude, visible in Figures 4.11(b) to 4.11(e). During the entire characterization experiment, no fluid leakage was observed even after continuous operation on the damper testing machine, owing to the robustness of the piston design. The developed MR damper was found to deliver sufficient damping force, as approved by Rambal Ltd., to make it feasible to be installed on the test vehicle for further testing.

The performance of the developed MR damper is compared against the stock passive damper based on the vehicle body and the wheel acceleration of the test vehicle running over a sharp speed bump at different speeds. Since the road input is a straight road with a speed bump, the vehicle body and the wheel's peak accelerations are considered the performance index. Although it is evident from Figures 4.16 and 4.17 that the MR dampers have reduced the vibrations in the vehicle body and wheel, thereby increased ride comfort and road handling, it is essential to determine the extent of

improvement. Hence, the percentage improvement in ride comfort or road handling is calculated using equation 4.25.

$$\text{Percentage Improvement} = \frac{a_{passive} - a_{MRD}}{a_{passive}} \times 100 \quad (4.25)$$

Where,  $a_{MRD}$  is the peak acceleration recorded from the vehicle with the MR damper and  $a_{passive}$  is the peak acceleration recorded from the test vehicle with stock passive dampers. The term  $a_{MRD}$  refers to the peak acceleration of vehicle body when ride comfort improvement is calculated. The same term refers to the peak acceleration of wheel when improvement in road handling is to be calculated. The percentage improvement in ride comfort and road handling has been listed in Table 4.2 and Table 4.3.

Table 4.2 Peak acceleration of sprung mass

<b>Vehicle speed (km/h)</b>	<b>With stock passive damper (m/s<sup>2</sup>)</b>	<b>With MR damper – Skyhook control (m/s<sup>2</sup>)</b>	<b>Improvement in ride comfort (%)</b>
10	3.247208	2.715114	16.2
20	3.616653	2.965367	17.6

Table 4.3 Peak acceleration of unsprung mass

<b>Vehicle speed (km/h)</b>	<b>With stock passive damper (m/s<sup>2</sup>)</b>	<b>With MR damper – Ground hook control (m/s<sup>2</sup>)</b>	<b>Improvement in road handling (%)</b>
10	11.87795	10.17621	14.32
20	38.81199	28.06268	29.3

It is evident from Figure 4.16 and Table 4.2 that the developed MR damper has successfully improved the ride comfort of the test vehicle by 16.2% at 10km/h and by 17.6% at 20km/h. The road handling of the test vehicle has also improved by 14.32% at 10km/h and 29.3% at 20km/h with the installation of the developed MR damper as evident from Figure 4.17 and Table 4.3.

#### **4.7 SUMMARY**

This chapter abridged the methodology adopted to design, characterize and implement an MR damper for application in a passenger van. The MR damper piston dimensions are optimized by considering the space limitations of a stock passive damper and the magnetization limits of the MR damper piston materials as constraints to maximize the magnetic flux density at the flow gap. The nonlinear optimization technique has been employed using the `fmincon` algorithm in the Optimization Toolbox® of MATLAB R2018b. The MR damper is fabricated using the optimized dimensions and characterized in the damper testing machine. The developed MR damper exhibited the intended MR effect, delivered sufficient controllable damping force and showed no signs of fluid leakage owing to its robust design. The MR damper was then installed in the suspension of the test vehicle. The test vehicle was run over a sharp speed bump at different speeds while implementing skyhook and ground hook control. The developed MR damper successfully improved the ride comfort and the road handling of the test vehicle while being more affordable than the commercial MR dampers currently available in the market, which was evident from the cost evaluation of the developed damper.



## **CHAPTER 5**

### **DESIGN OF COST-EFFECTIVE MR FLUID AND ITS EXPERIMENTAL EVALUATION**

#### **5.1 INTRODUCTION**

The rheological properties of the fluid used in automotive dampers, especially MR dampers, play a significant role in the damping capacity of those damper. Designing an MR fluid generally involves optimizing the proportion of the magnetic particles in the carrier fluid. It is a general practice to optimize the composition of an MR fluid based on either the rheology of the fluid or the desired damping force/desired braking torque in case of MR dampers/MR clutches and brakes, as described in section 2.2 of this thesis. The cost of the MR fluid is often ignored during its optimization. However, it can be seen in section 4.6 of this thesis that the cost of the MR fluid is the major component in the overall cost of manufacturing an MR damper. Therefore, this chapter presents a technique to optimize the composition of MR particles in the carrier fluid while considering the cost of the MR fluid synthesis.

#### **5.2 METHODOLOGY TO DESIGN AND EVALUATE PERFORMANCE OF A COST-EFFECTIVE MR FLUID**

The methodology adopted in this study to design a cost-effective MR fluid has been described in Figure 5.1, which can be divided into three stages. In the first stage, five MR fluid samples with volume fractions of 5%, 10%, 15%, 20% & 25% of total fluid volume and carbonyl iron particles sized 2.9 microns and 8.27 microns are synthesized with silicone oil as the carrier fluid (Rankin et al., 1999, Liu et al., 2016, Deep et al. 2016). The fluid samples are later characterized in a rheometer to determine their rheological properties at different levels of magnetic field strengths. The second stage involves using rheological data of MR fluid samples to estimate the damping forces generated by the developed MR damper, described in section 4.3 of this thesis, which is later used to model the damping behavior of the MR damper with each MR fluid sample. The MR damper model is employed to simulate a full car model of the

test vehicle to determine the performance of each MR fluid sample on the suspension performance.

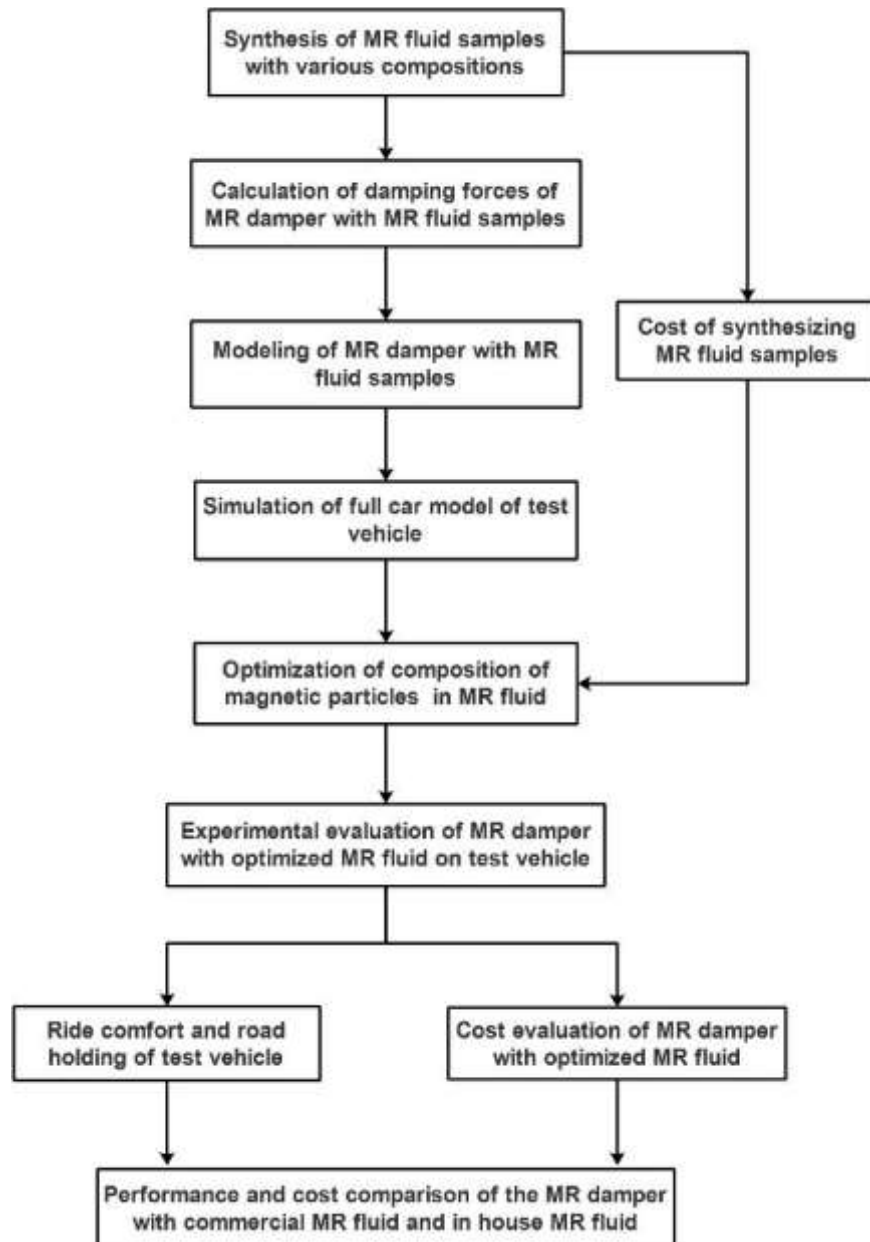


Figure 5.1 Methodology to design and evaluate performance of an MR fluid

The response of the full car model simulation, the particle size and the cost of synthesizing the MR fluid samples are then used to optimize the composition of magnetic particles in the carrier fluid. In the third stage of the study, the developed MR damper is filled with optimized MR fluid, installed on the vehicle, and tested over a sharp speed bump and a random road at Rambal. Ltd., Chennai.

## 5.3 SYNTHESIS AND CHARACTERIZATION OF MR FLUID SAMPLES

### 5.3.1 Synthesis of MR fluid samples

MR fluid samples are synthesized by mixing paramagnetic particles in a carrier fluid along with some additives for stability. The paramagnetic particles used in this study are the CIP supplied by Sigma-Aldrich, USA. Sigma-Aldrich supplies the CIP as two products with product numbers 44890 and C3518. While both CIPs have a density of 7.86 g/ml, the mean size of the particles in 44890 is 5-9 microns, and in C3518 is 3-5 microns (“Sigma Aldrich”, 2022). The shape of the particles in the CIPs considered in this study is mostly spherical and has a narrow particle size distribution. The mean diameter of the particles in 44890 is 8.97 microns, and in C3518 is 2.9 microns (Acharya et al., 2019). The carrier fluid used in this study is Silicone oil with a viscosity of 350 cSt, a density of 0.96 g/ml and a boiling point of approximately 140°C.

A total of ten MR fluid samples are prepared, five with each size of particle. The volume fraction of the particles varies from 5% to 25% with an increment of 5%. The issue of particle settling in MR fluid is the area of research that has been explored quite extensively since the invention of MR fluids. The metallic salt Aluminum Di stearate has found to not only delay the settling of particles but also improve re-dispersibility (Acharya et al., 2019; Acharya et al., 2021; Iglesias et al., 2015; Marins et al., 2019). Therefore 2% Aluminum Di stearate has been added to each fluid sample to ensure stability and re-dispersibility of the MR fluid samples (Acharya et al., 2019; Acharya et al., 2021; Aruna et al., 2022). The weight of individual components of the MR fluid required to make a sample of desired volume can be determined using equations 5.1 to 5.4. Equations 5.1 to 5.4 present the calculations for an MR fluid sample of 30 ml quantity with a 5% volume fraction of large-sized particles. The same equation can be used to calculate the weight of each component of MR fluid with the mentioned volume fractions of CIP.

$$\text{Weight of CIP} = 0.05 \times 30\text{ml} = 1.5\text{ml} \times 7.86 \text{ g/ml} = 21.22\text{g} \quad (5.1)$$

$$\text{Weight of Silicon oil} = 0.95 \times 30\text{ml} = 28.5\text{ml} \times 0.96 \text{ g/ml} = 27.36\text{g} \quad (5.2)$$

$$\text{Weight of Aluminum Di-Stearate} = 0.02 \times (21.22 + 27.36) = 0.97g \quad (5.3)$$

$$\text{Total weight of the sample} = 21.22 + 27.36 + 0.9716 = 49.55g \quad (5.4)$$

A mechanical stirrer mixes the constituents of the MRF for 8 to 12 hours prior to their testing in a rheometer ensuring uniform mixing of CIP and additives with the base fluid (Acharya et al., 2021; Kariganaur et al., 2022; Desai et al., 2020; Nagiredla et al., 2022). The nomenclature of the fluid samples is based on the particle size and volume fraction. For instance, an MR fluid sample with large-sized particles and a 15% volume fraction is named LMRF15.

### **5.3.2 Rheological characterization of MR Fluid samples**

The rheological properties of the prepared MR fluid samples are characterized at different magnetic field strengths in a rheometer with a rotating parallel plate. The rheometer used in this study is the MCR-702, a Modular Compact parallel plate Rheometer supplied by Anton Parr, Austria, as shown in Figure 5.2. The rheometer measures the shear stress of the MR fluid sample at different magnetic field strengths in a controlled shear rate mode using its proprietary software RheoCompass. The fluid samples are placed between the bottom and top plates in the rheometer. The top plate is a rotating spindle connected to an electric motor that applies the required shear rate and an integrated torque sensor to measure the shear stress of the fluid sample, which is lowered until the gap between the top plate and the bottom plate is 1 mm. The extra fluid that is squeezed out after making this adjustment is wiped off, and the yoke is loaded to complete the magnetic circuit allowing the magnetic flux to pass through the fluid sample vertically. The Magneto-Rheological Device (MRD) cell generates the required magnetic field as per the input from RheoCompass. The yoke is enveloped by a thermal jacket that maintains the temperature of the fluid, which in this study is 25<sup>0</sup>C.



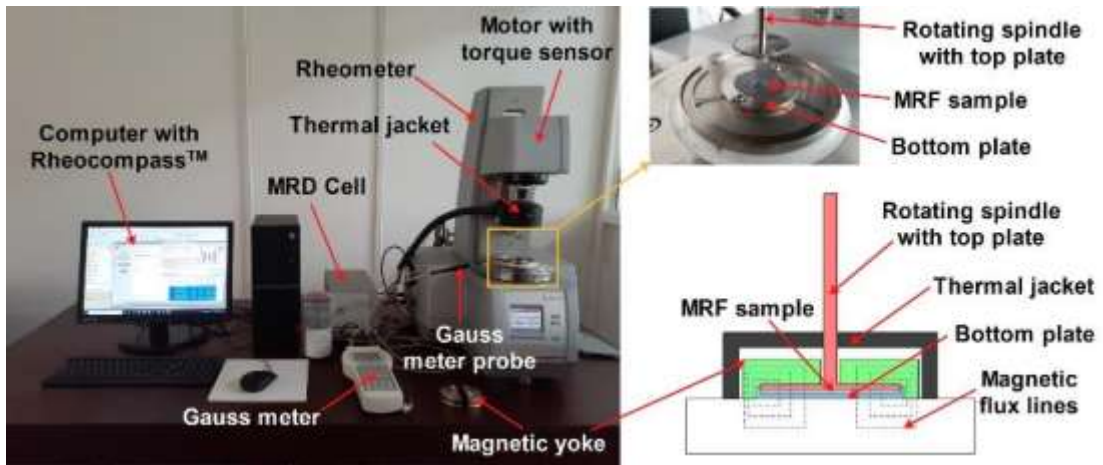
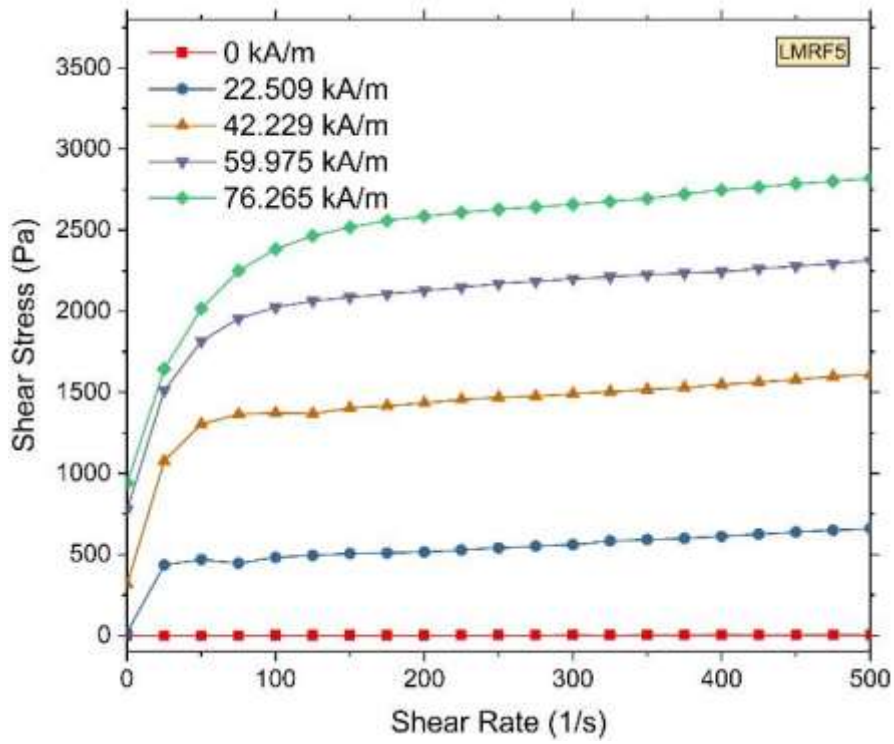


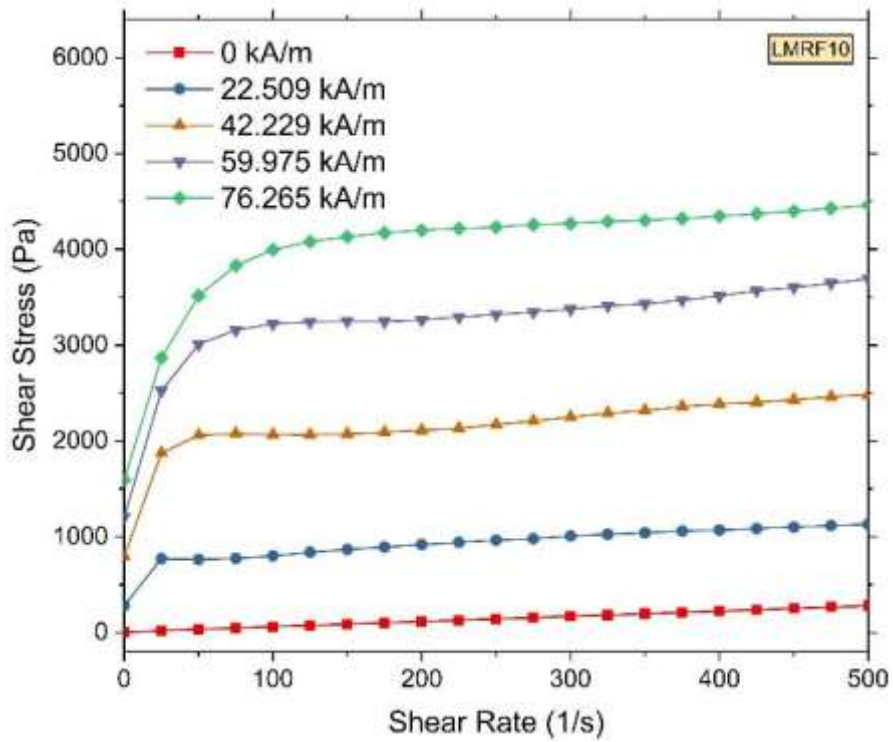
Figure 5.2 Rheometer setup for MR fluid characterization

The MRF samples are mixed in the mechanical stirrer up to the moment they are loaded in the rheometer to ensure that particle settling does not affect the readings from the rheometer. Additionally, each MR fluid sample is manually stirred well before loading it on the rheometer to ensure homogenous distribution of CIP particles in the carrier fluid. The shear rate of the top plate is linearly varied from 0 to  $500\text{s}^{-1}$ , and the obtained shear stress is recorded. The procedure is repeated by varying the current supply to the MRD cell from 0A to 2A with an increment of 0.5A. Consequently, the magnetic field strength varies from 0 kA/m to 76 kA/m with an approximate increment of 20 kA/m. The designed MR damper generates a maximum field strength of 68.5 kA/m when 2A of current is supplied to it, as observed during FEMM simulations of the developed MR damper, which is well within the maximum field strength used to test the MR fluid samples in Rheometer.

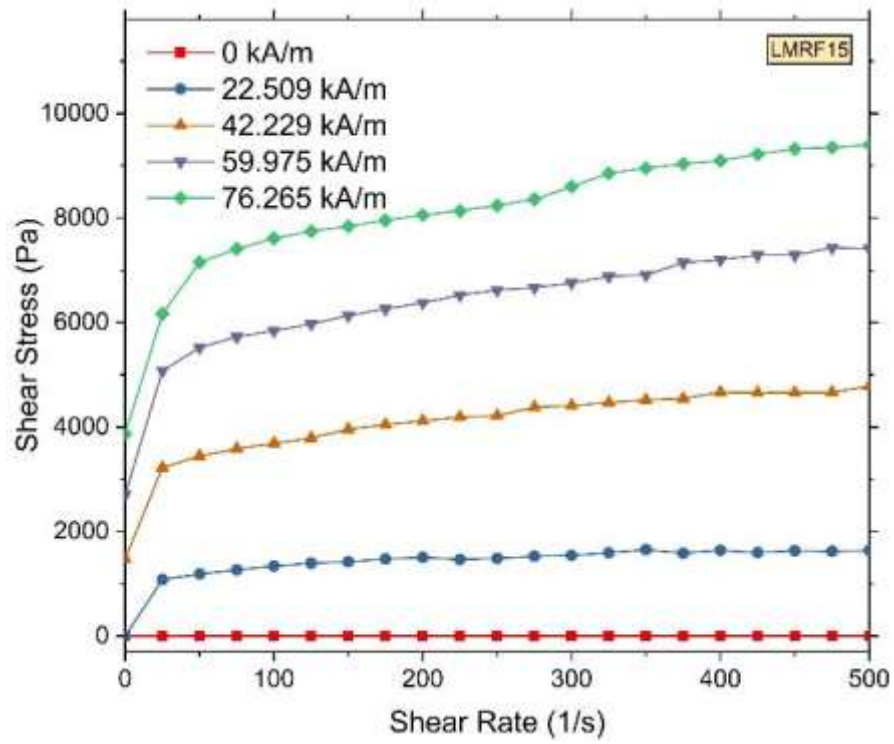
All the above mentioned steps are repeated with all the MR fluid samples. The recorded shear stress is plotted against the applied shear rate at each magnetic flux density value at the sample gap to obtain the flow curves of LMRF and SMRF samples as presented in Figure 5.3 and 5.4, respectively.



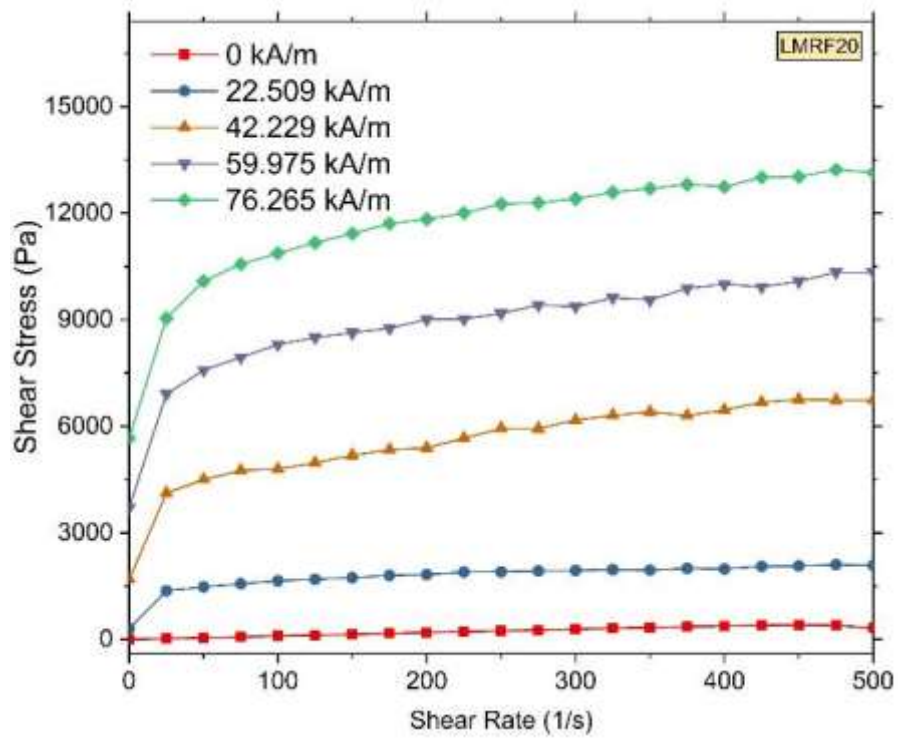
(a)



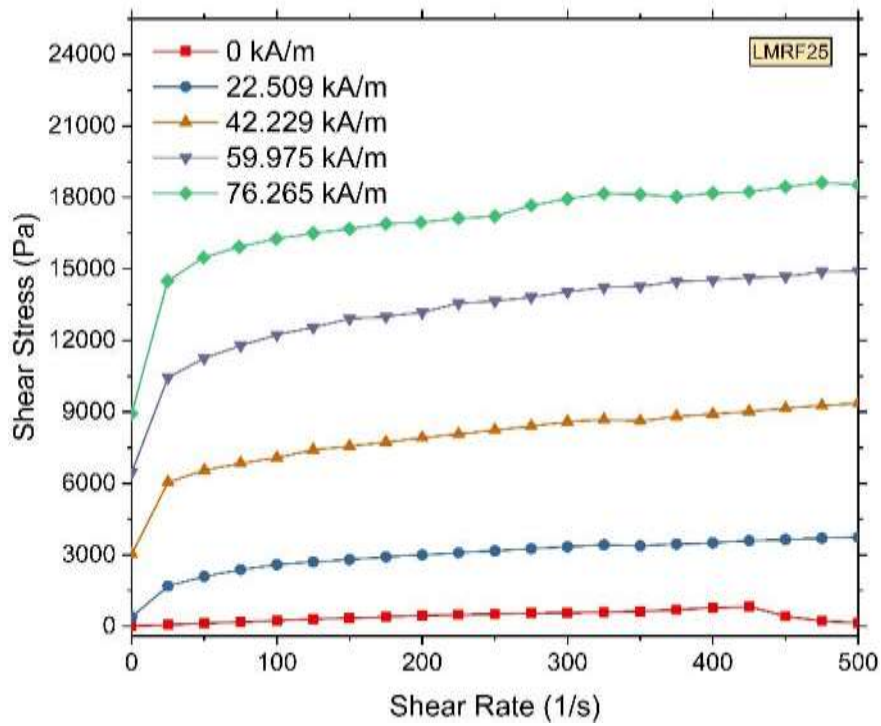
(b)



(c)

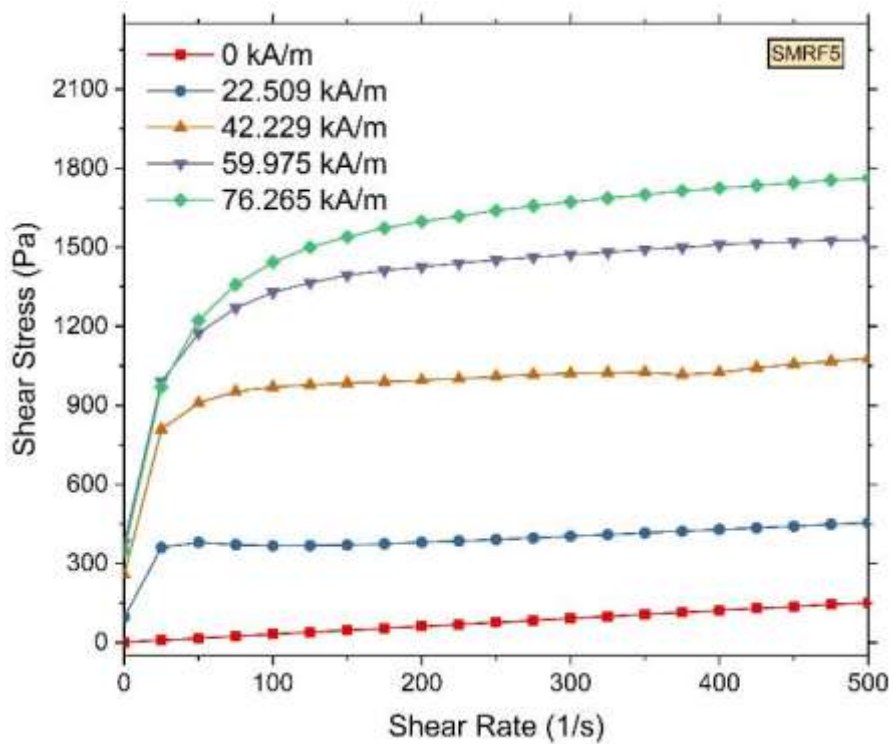


(d)

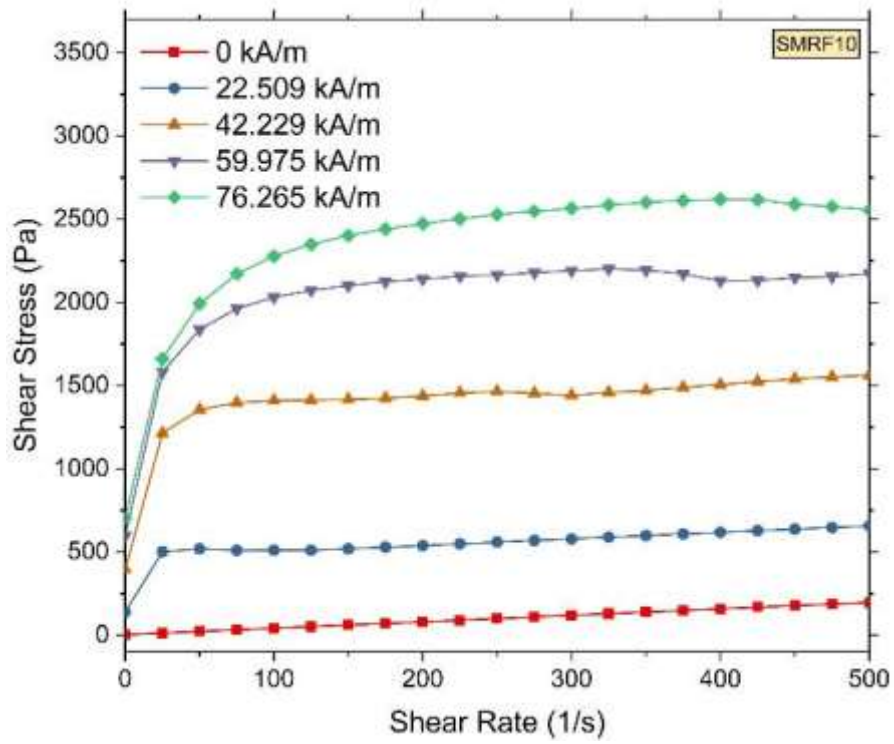


(e)

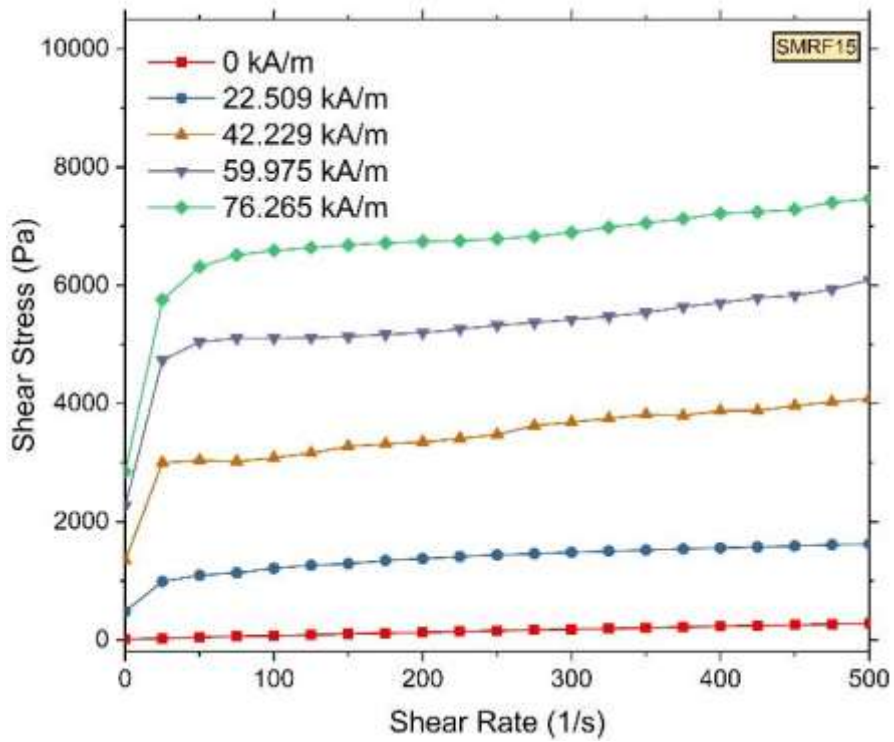
Figure 5.3 Rheological behavior of (a) LMRF5 (b) LMRF10 (c) LMRF15 (d) LMRF20 (e) LMRF25



(a)

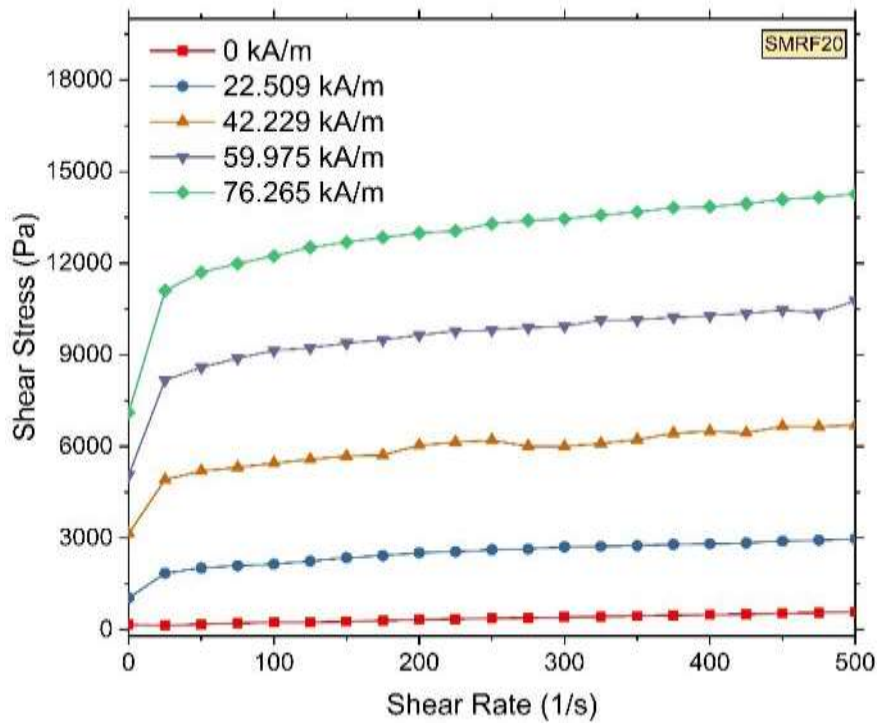


(b)

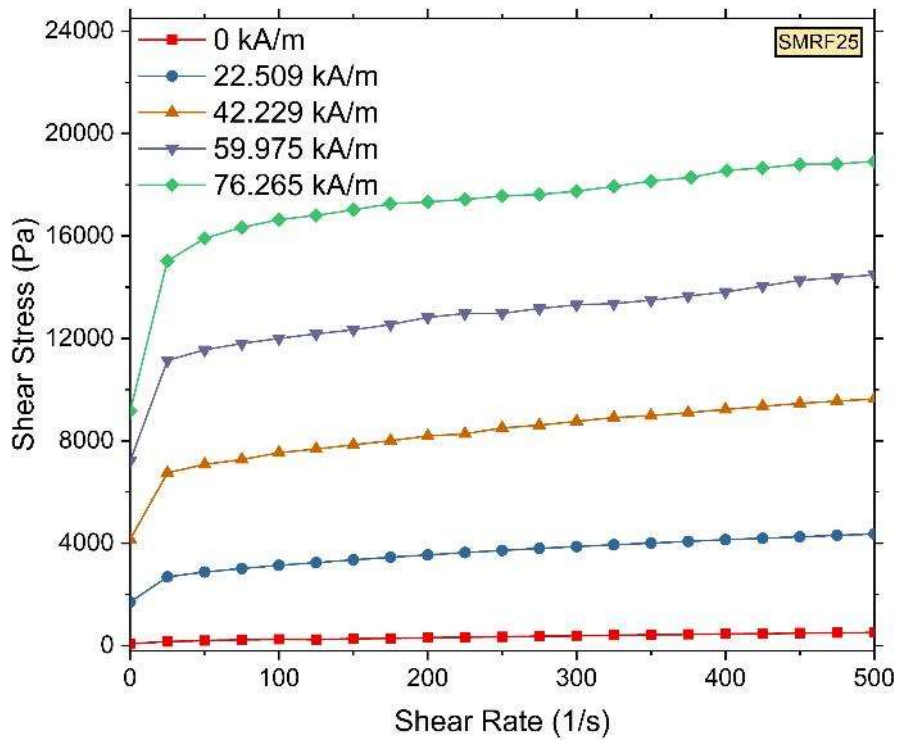


(c)





(d)



(e)

Figure 5.4 Rheological behavior of (a) SMRF5 (b) SMRF10 (c) SMRF15 (d) SMRF20 (e) SMRF25

#### 5.4 DAMPING FORCE ESTIMATION OF DEVELOPED MR DAMPER WITH MR FLUID SAMPLES

The damping force generated by the MR damper using the MR fluid samples can be estimated through equations 4.1 to 4.8, with the piston dimensions listed in Table 4.1. The shear stress,  $\tau$ , of the MR fluid in equation 4.5 is calculated for each MR fluid sample at each magnetic field strength value by modeling rheology data of the MR fluid samples, obtained in the previous section, using the Bingham model given by equation 5.5 (Zubieta et al., 2009).

$$\tau = \tau_y + \mu\dot{\gamma} \quad (5.5)$$

Where  $\tau$  is the shear stress,  $\tau_y$  is the field-dependent yield stress in Pa,  $\mu$  is the dynamic viscosity of the fluid in Pa-s and  $\dot{\gamma}$  is the shear rate in  $s^{-1}$ . The coefficients of the Bingham model  $\tau_y$  and  $\mu$  are obtained by fitting the model to the experimental data in Figures 5.3 and 5.4. The dynamic viscosity is calculated as the slope of the flow curve of an MR fluid sample at 0kA/m presented in Figures 5.3 and 5.4. It can be observed in Figures 5.3 and 5.4 that the slope of the flow curve is constant with respect to the applied magnetic field strength for a given fluid sample. The yield stress, however, is field dependent, which is, therefore, obtained by fitting equation 5.5 to the experimental rheology data in Figures 5.3 and 5.4. The Curve Fitting Toolbox™ of MATLAB R2018b has been employed for this purpose which uses a Trust-Region algorithm to determine the coefficients of the equation by reducing the error between the predicted values and the experimental values of shear stress. The coefficients of the Bingham model obtained from curve fitting have been listed in Tables 5.1 and 5.2.

Table 5.1 Coefficients of Bingham model for LMRF samples

<b>H</b> (kA/m)	<b>LMRF5</b>		<b>LMRF10</b>		<b>LMRF15</b>		<b>LMRF20</b>		<b>LMRF25</b>	
	$\tau_y$	$\mu$	$\tau_y$	$\mu$	$\tau_y$	$\mu$	$\tau_y$	$\mu$	$\tau_y$	$\mu$
0	6.86	0.5439	13.16	0.6059	21.89	0.6983	23.06	0.8343	51.94	1.797
22.509	740.7		429.2		1252		1527		2380	
42.229	1872		1317		3430		4335		6554	

59.975	3033		1995		5473		7804		11660	
76.265	4005		2416		7056		10460		15730	

Table 5.2 Coefficients of Bingham model for SMRF samples

<b>H</b> (kA/m)	<b>SMRF5</b>		<b>SMRF10</b>		<b>SMRF15</b>		<b>SMRF20</b>		<b>SMRF25</b>	
	$\tau_y$	$\mu$	$\tau_y$	$\mu$	$\tau_y$	$\mu$	$\tau_y$	$\mu$	$\tau_y$	$\mu$
0	1.29	0.3013	2.09	0.3891	19.57	0.5267	140.6	0.6552	162.5	0.7249
22.509	334		461.7		1096		1989		2831	
42.229	940.7		1356		2861		5129		6971	
59.975	1298		2022		4694		8811		11370	
76.265	1394		2282		6188		11860		15840	

The yield stress must be represented in terms of the magnetic field strength for calculating the field-dependent damping forces. Therefore, the yield stress is expressed as the second-order polynomial function of the field strength. The resulting functions are presented in equations 5.6 to 5.15.

$$\tau_y (LMRF5) = -0.0111H^2 + 49.757H - 139.19 \quad (5.6)$$

$$\tau_y (LMRF10) = -0.0867H^2 + 38.019H - 119.42 \quad (5.7)$$

$$\tau_y (LMRF15) = 0.1048H^2 + 83.758H - 220.61 \quad (5.8)$$

$$\tau_y (LMRF20) = 0.4691H^2 + 98.752H - 336.73 \quad (5.9)$$

$$\tau_y (LMRF25) = 0.8533H^2 + 138.3H - 400.89 \quad (5.10)$$

$$\tau_y (SMRF5) = -0.1387H^2 + 29.542H - 81.135 \quad (5.11)$$

$$\tau_y (SMRF10) = -0.1692H^2 + 43.113H - 140.1 \quad (5.12)$$

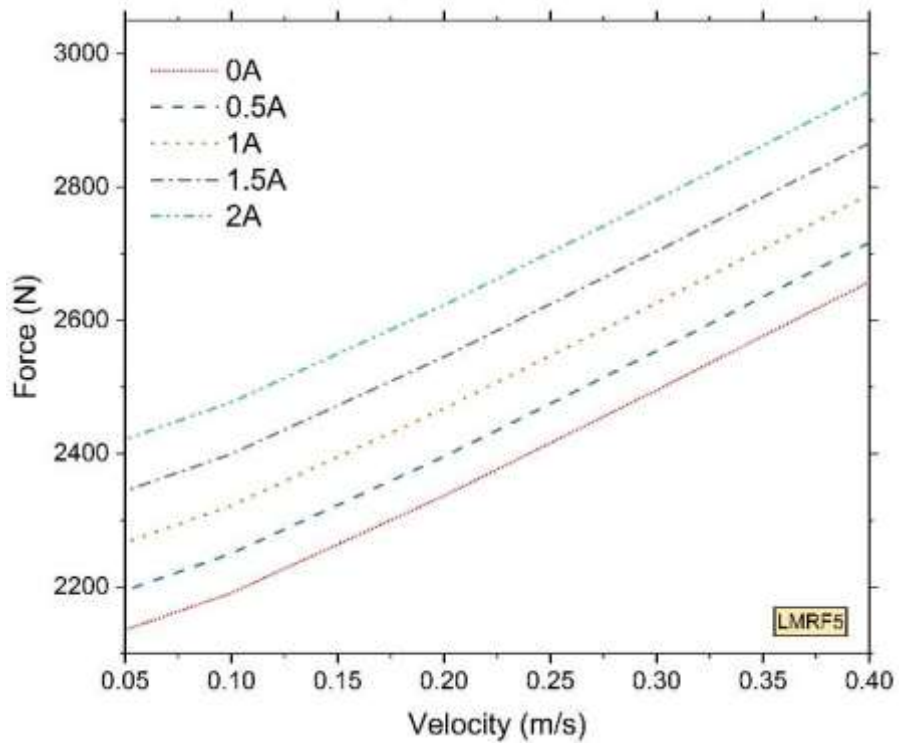


$$\tau_y (SMRF15) = -0.0072H^2 + 82.378H - 260.48 \quad (5.13)$$

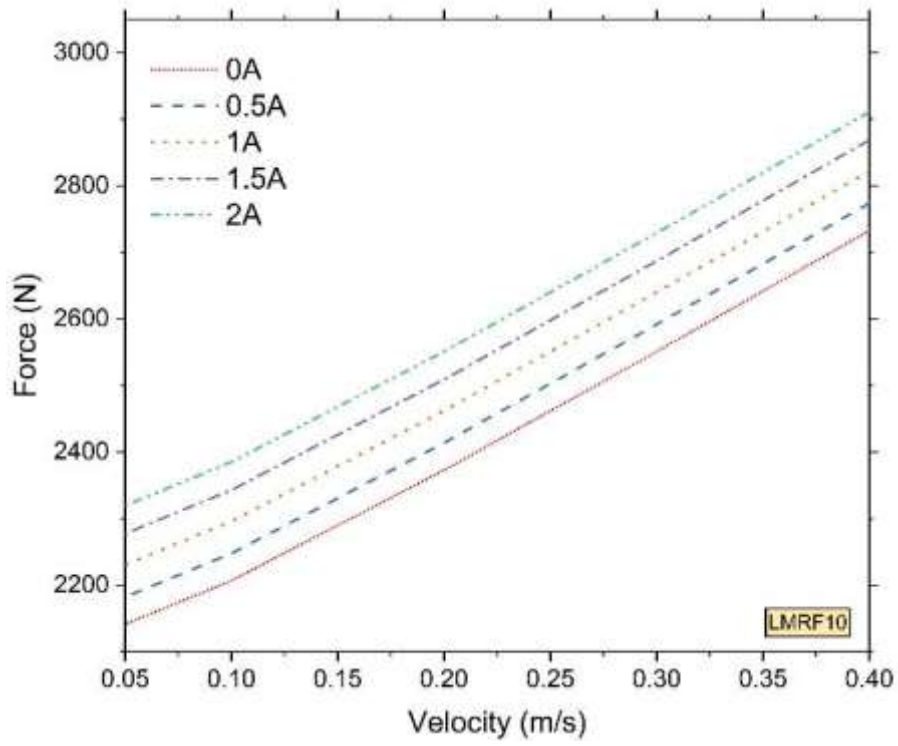
$$\tau_y (SMRF20) = 0.3621H^2 + 121.39H - 265.41 \quad (5.14)$$

$$\tau_y (SMRF25) = 0.8164H^2 + 138.87H - 157.33 \quad (5.15)$$

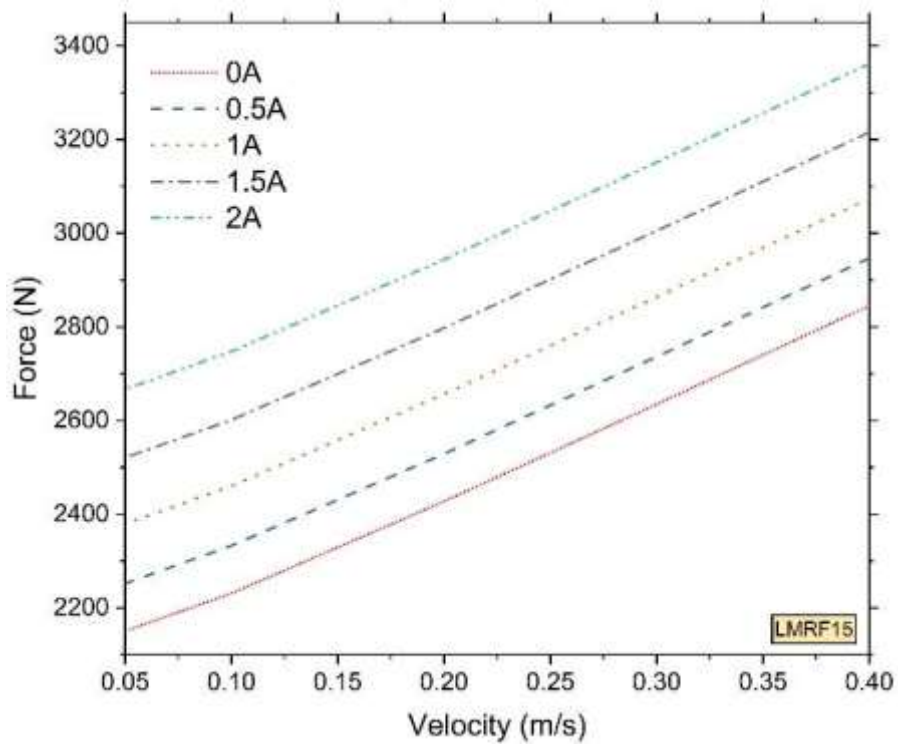
Equations 4.1 to 4.8 can now be used to estimate the damping force of the developed MR damper while employing the prepared MR fluid samples. The excitation velocity and the current values used during the experiments on the damper testing machine have been used to estimate the damping force in this chapter. The magnetic field strength generated by the electromagnetic coil at the fluid flow gap can be determined through FEMM simulations. The same is used to calculate the shear stress for a given current input to the MR damper. The resulting characteristic graphs of the developed MR damper with prepared MR fluid samples have been presented in Figures 5.5 and 5.6.



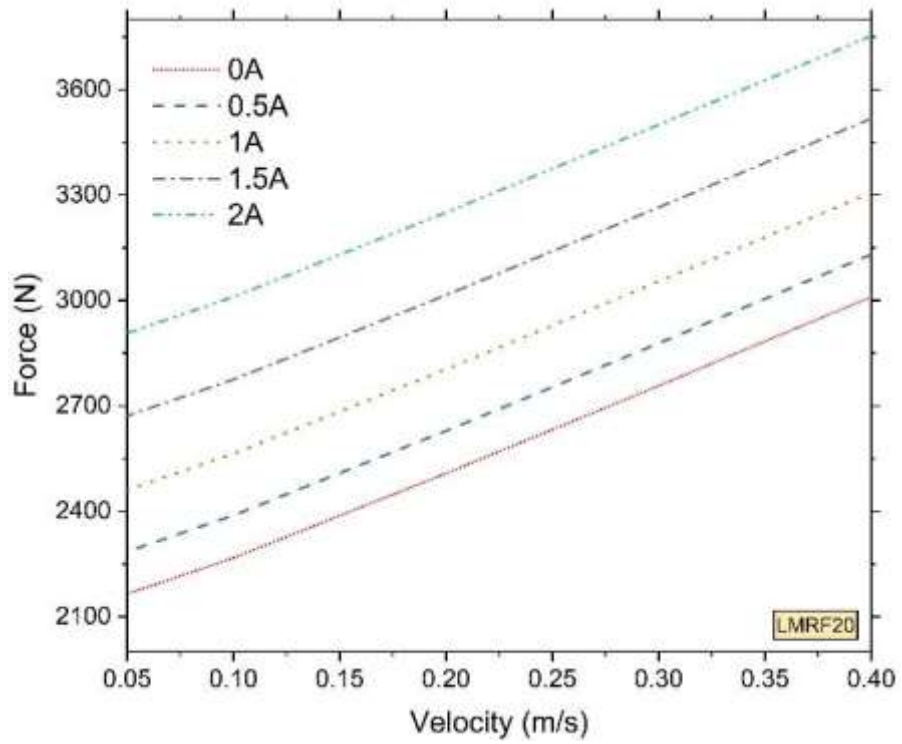
(a)



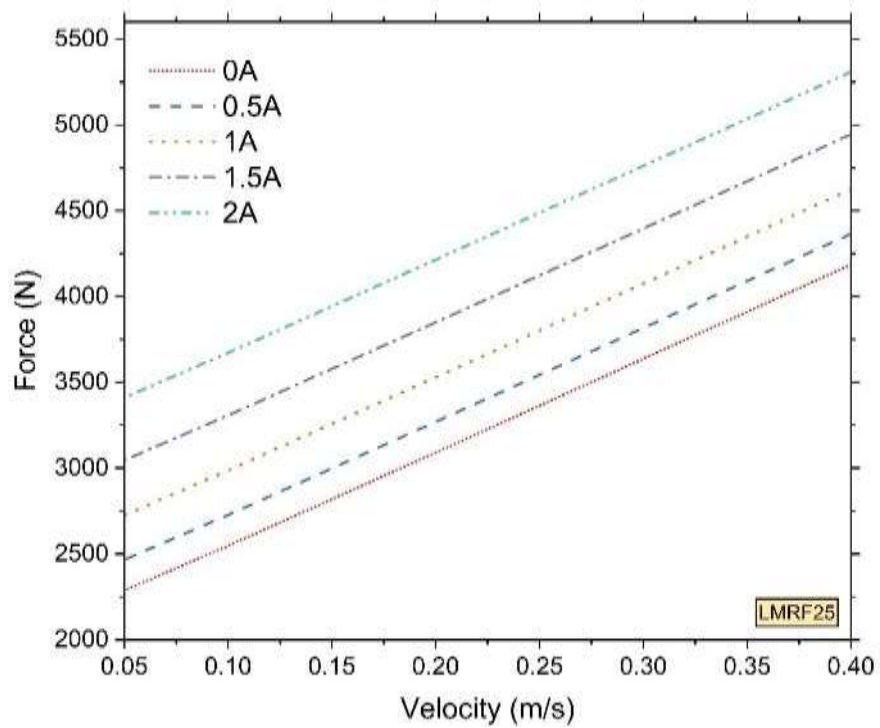
(b)



(c)

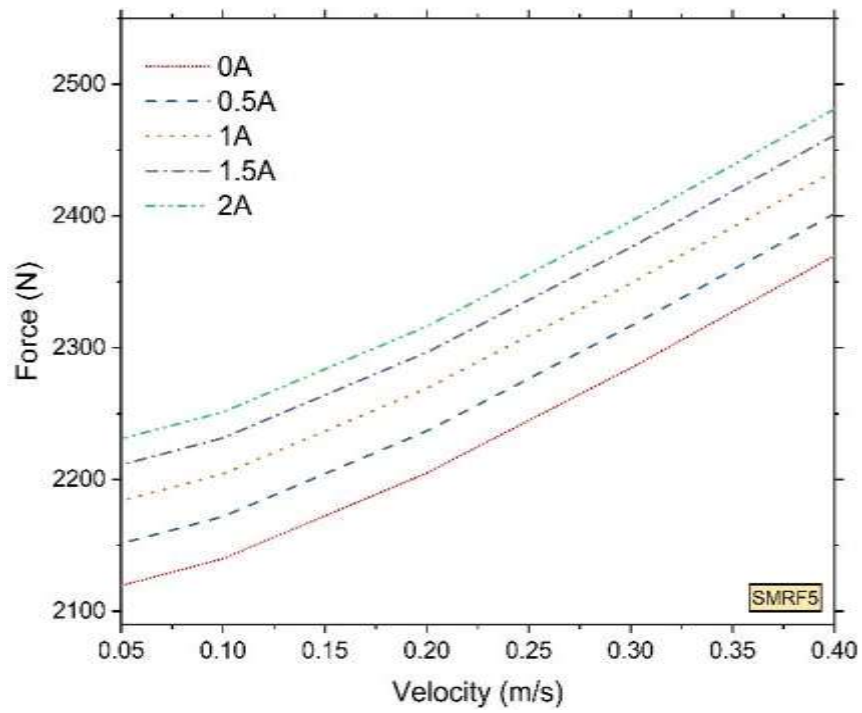


(d)

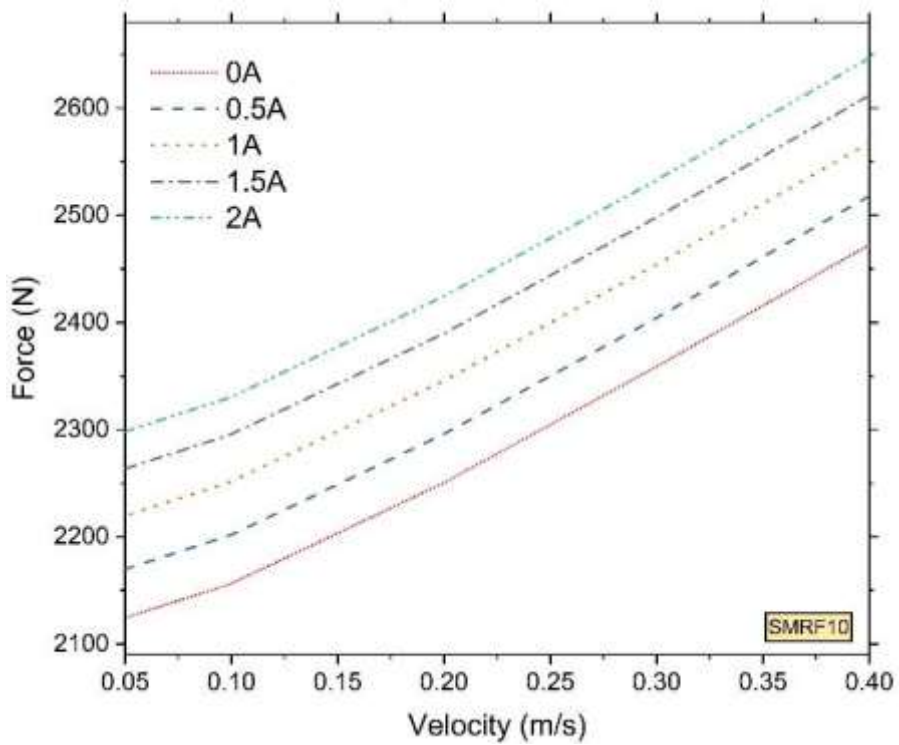


(e)

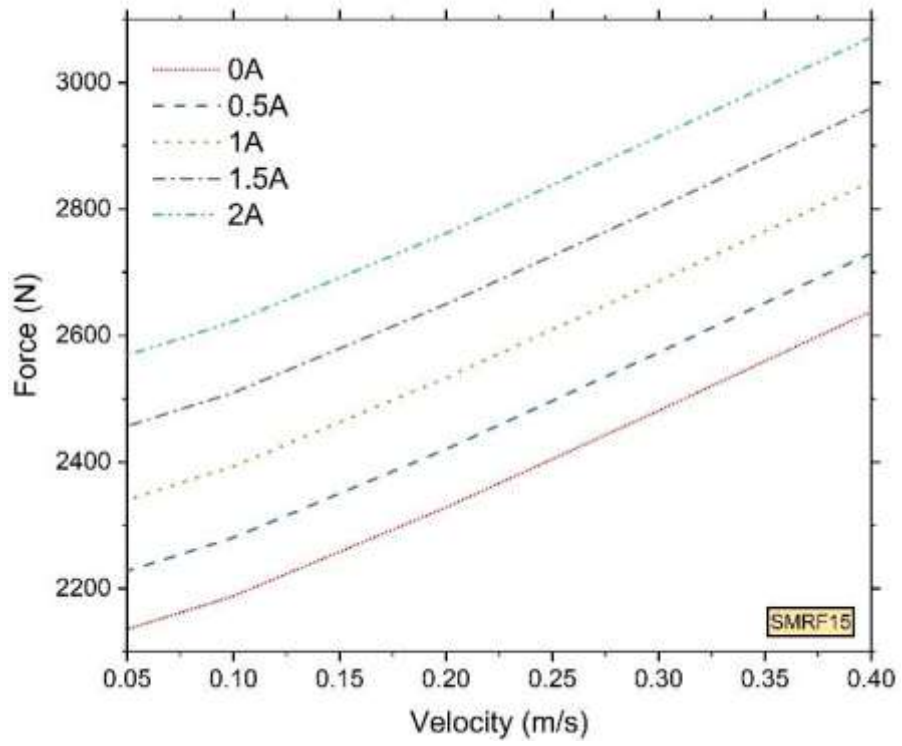
Figure 5.5 Theoretical characteristic graphs of developed MR damper with (a) LMRF5 (b) LMRF10 (c) LMRF15 (d) LMRF20 (e) LMRF25



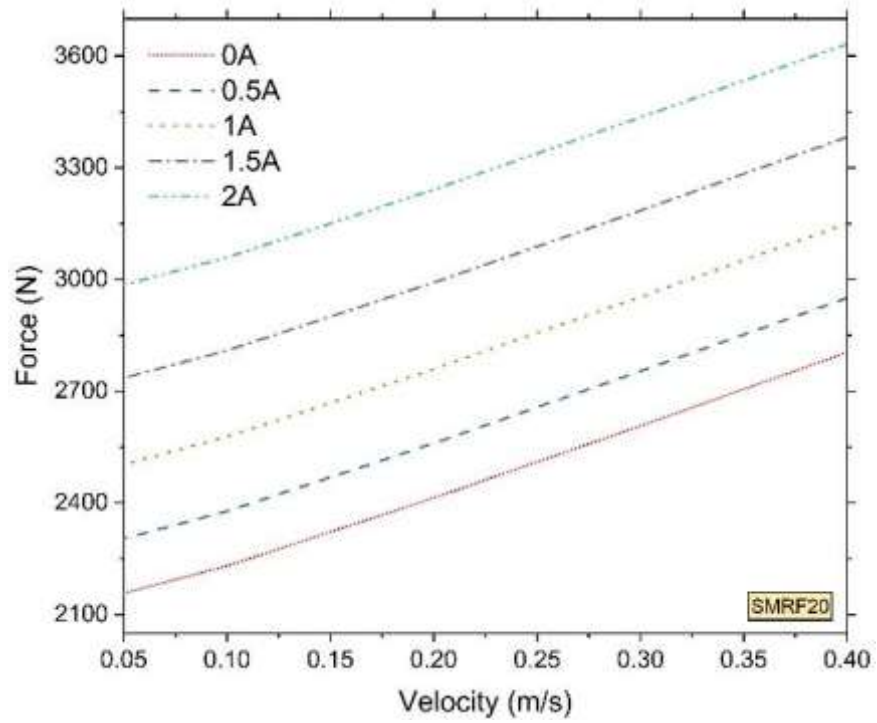
(a)



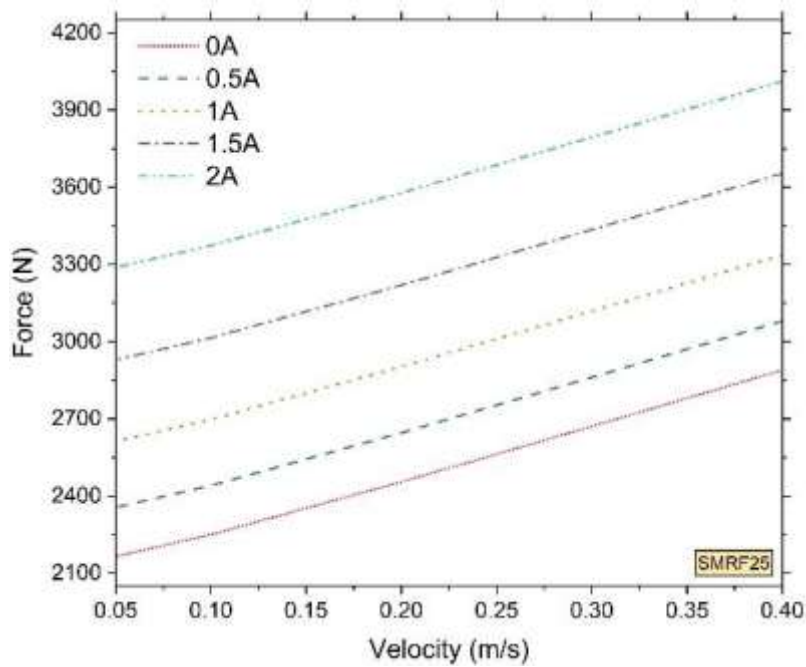
(b)



(c)



(d)



(e)

Figure 5.6 Theoretical characteristic graphs of developed MR damper with (a) SMRF5 (b) SMRF10 (c) SMRF15 (d) SMRF20 (e) SMRF25

The estimated damping forces for each MR fluid sample are modeled using the MFM, equation 3.6, for their utilization in the simulation of the full car model of the test vehicle. The response of the vehicle model in simulation is considered to optimize the volume fraction of CIP in the carrier fluid. The nonlinear curve fitting technique used in section 3.4.2 has been employed for this purpose. The resulting coefficients of MFM for each LMRF and SMRF samples have been listed in Table 5.3 and Table 5.4, respectively.

Table 5.3 MFM coefficients for MR damper with LMRF samples

MR fluid sample	Current (A)	Coefficients				
		A	B	C	D	E
LMRF5	0	1664.025	536.4095	389.1781	2059.053	76.0311
	0.5	1664.208	709.5165	389.1763	2118.517	57.8454
	1	1664.285	818.2154	389.1737	2190.787	51.2055

	1.5	1664.292	826.5632	389.1707	2268.202	51.1903
	2	1664.303	840.2332	389.1679	2345.786	50.8001
<b>LMRF10</b>	0	1854.86	782.5351	389.1774	2058.077	55.7509
	0.5	1854.777	655.6109	389.1751	2098.65	67.5234
	1	1854.653	528.8742	389.1725	2146.393	85.1688
	1.5	1854.497	426.757	389.1698	2192.741	107.444
	2	1854.443	400.0439	389.168	2234.551	115.966
<b>LMRF15</b>	0	2134.516	235.9858	389.1691	2053.551	223.065
	0.5	2132.082	80.8365	389.1542	2147.93	741.152
	1	2131.464	69.87533	389.1481	2274.533	914.951
	1.5	2131.453	69.65884	389.1436	2415.868	946.902
	2	2131.451	69.60985	389.1395	2562.033	976.287
<b>LMRF20</b>	0	2550.826	289.8167	389.1691	2053.213	216.436
	0.5	2550.882	315.1528	389.1653	2174.966	208.927
	1	2550.903	326.4851	389.1593	2350.748	206.482
	1.5	2550.926	337.1643	389.1529	2562.354	-205.43
	2	2550.968	362.3523	389.1469	2797.965	-203.44
<b>LMRF25</b>	0	5490.8310	408.3504	389.4554	2569.584	-1273.14
	0.5	5490.5201	299.7577	389.3697	2571.962	-1303.5
	1	5490.3092	258.8044	389.2149	2590.13	-1374.69
	1.5	5490.1092	201.9669	389.0149	2630.824	-1383.47
	2	5490.0090	103.9788	389.0147	3100.625	-1509.36

Table 5.4 MFM coefficients for MR damper with SMRF samples

MR fluid sample	Current (A)	Coefficients				
		A	B	C	D	E
<b>SMRF5</b>	0	913.4886	2497.024	389.1869	2074.167	-10.4298
	0.5	913.6513	4884.809	389.1856	2106.089	-4.86952
	1	913.7208	8324.194	389.1842	2138.514	-2.466
	1.5	913.7505	11755.11	389.1831	2165.815	-1.46881
	2	913.7574	12669.15	389.1823	2185.525	-1.30095
<b>SMRF10</b>	0	1189.118	12758.94	389.1858	2067.107	-1.51478
	0.5	1189.122	12854.42	389.1838	2112.559	-1.49585
	1	1189.125	12908.79	389.1817	2162.232	-1.48695
	1.5	1189.129	13280.61	389.1798	2206.337	-1.46928
	2	1189.132	13554.47	389.1784	2241.12	-1.43846
<b>SMRF15</b>	0	1612.086	13553.72	389.1813	2062.476	-1.90147
	0.5	1612.09	13588.01	389.1773	2154.579	-1.95899
	1	1612.094	13694.25	389.1729	2267.418	-2.01285
	1.5	1612.098	13706.76	389.1686	2383.963	-2.08369
	2	1612.101	13723.69	389.1647	2495.99	-2.16017
<b>SMRF20</b>	0	2005.061	13690.27	389.1791	2072.09	-2.5349
	0.5	2005.065	13678.01	389.173	2218.723	-2.65642
	1	2005.068	13645.34	389.1657	2418.392	-2.8342
	1.5	2005.071	13638.66	389.1583	2650.273	-3.01496



	2	2005.074	13488.5	389.1513	2900.236	-3.25137
<b>SMRF25</b>	0	2216.077	13460.23	389.1825	2078.024	-3.28814
	0.5	2216.078	13435.74	389.1747	2268.754	-3.47519
	1	2216.082	13429.31	389.1655	2525.877	-3.73526
	1.5	2216.087	13390.68	389.156	2842.784	-4.04472
	2	2216.087	13381.94	389.147	3201.66	-4.36222

It can be observed from Table 5.3 and Table 5.4 that the value of coefficient C does not vary either with the current or the fluid sample; therefore, it has been assumed to be constant. However, coefficient A's value remains constant with the variation of current supplied for a given fluid sample. Therefore, it can be assumed constant for a given fluid sample. The remaining coefficients have been expressed as a second-order polynomial of the current supplied. The general form of the current dependent coefficients takes the general form of the equations 5.16 to 5.18.

$$B = B_1 I^2 + B_2 I + B_3 \quad (5.16)$$

$$D = D_1 I^2 + D_2 I + D_3 \quad (5.17)$$

$$E = E_1 I^2 + E_2 I + E_3 \quad (5.18)$$

After expressing the current dependent coefficients as the third-order polynomial of current, the final coefficients of MFM have been listed in Tables 5.5 and 5.6.

Table 5.5 MFM coefficients of LMRF samples

<b>Coefficients</b>	<b>MR fluid sample</b>				
	<b>LMRF5</b>	<b>LMRF10</b>	<b>LMRF15</b>	<b>LMRF20</b>	<b>LMRF25</b>
<i>A</i>	1664.223	1854.646	2132.193	2550.901	5490.356
<i>B</i> <sub>1</sub>	-119.78	64.298	91.699	-0.2712	1.5215

$B_2$	384.5	-327.36	-252.18	33.959	-144.35
$B_3$	541.36	789.68	219.83	292.64	396.64
$C$	389.1739	389.1739	389.1739	389.1739	389.1739
$D_1$	11.824	0.3082	33.802	75.298	273.53
$D_2$	12.98	88.792	189.38	224.78	-322.88
$D_3$	2057.8	2056.8	2050.7	2050.1	2605.2
$E_1$	-12.062	0.5348	319.79	-3.5522	-36.755
$E_2$	35.547	-33.14	-982.01	13.002	-36.972
$E_3$	-74.869	-54.033	-258.14	-215.82	-1276.7

Table 5.6 MFM coefficients of SMRF samples

Coefficients	MR fluid sample				
	SMRF5	SMRF10	SMRF15	SMRF20	SMRF25
$A$	913.6737	118.125	1612.094	2005.068	2216.082
$B_1$	-844.56	192.63	-36.696	-71.381	-0.1955
$B_2$	7132	18.185	165.13	54.185	-39.936
$B_3$	2160	12764	13543	13681	13460
$C$	389.1739	389.1739	389.1739	389.1739	389.1739
$D_1$	-8.4416	-7.6874	12.444	68.249	113.16
$D_2$	73.372	103.74	194.39	281.07	337.93
$D_3$	2073.3	2065.7	2059.8	2068.5	2075.7
$E_1$	-3.4832	0.0093	-0.0157	-0.0665	-0.0887

$E_2$	11.298	0.0172	-0.0971	-0.2253	-0.3662
$E_3$	-10.18	-1.5123	-1.9029	-2.5333	-3.2819

## 5.5 OPTIMIZATION OF MAGNETIC PARTICLE COMPOSITION IN CARRIER FLUID

The MR damper models with each MR fluid sample will now be used to simulate the response of the test vehicle fitted with MR damper with each MR fluid sample. The response of the test vehicle along with the cost of synthesizing the MR fluid samples will be considered for optimization.

### 5.5.1 Simulation of full car model of the test vehicle

The performance of each MR fluid sample is evaluated based on the simulation response of the full car model of the test vehicle by using the MFM developed in the previous section of this chapter to represent the MR damper in the test vehicle model. The full car model used in this study has seven-degrees-of-freedom with MR dampers in its suspension (Nigwal et al., 2022), as shown in Figure 5.7.

It consists of a slab-shaped sprung mass with three degrees of freedom (heave, pitch and roll motions) and four masses representing four wheels at each corner of the vehicle body, each with one degree of freedom (vertical motion). The equations of motion are presented in equations 5.19 to 5.25, which are solved in MATLAB R2018b for a given road input. The road input is the R9 random road profile employed in Chapter 3, given by equation 3.17. The design of a mechanical component is carried out considering worst-case scenarios, which, in this study, is a vehicle running over very poor roads at very high speeds. Therefore, the full car model is simulated for a vehicle running at 21m/s speed over a road profile with a road roughness of  $512 e^{-6} m^3/cycle$ .

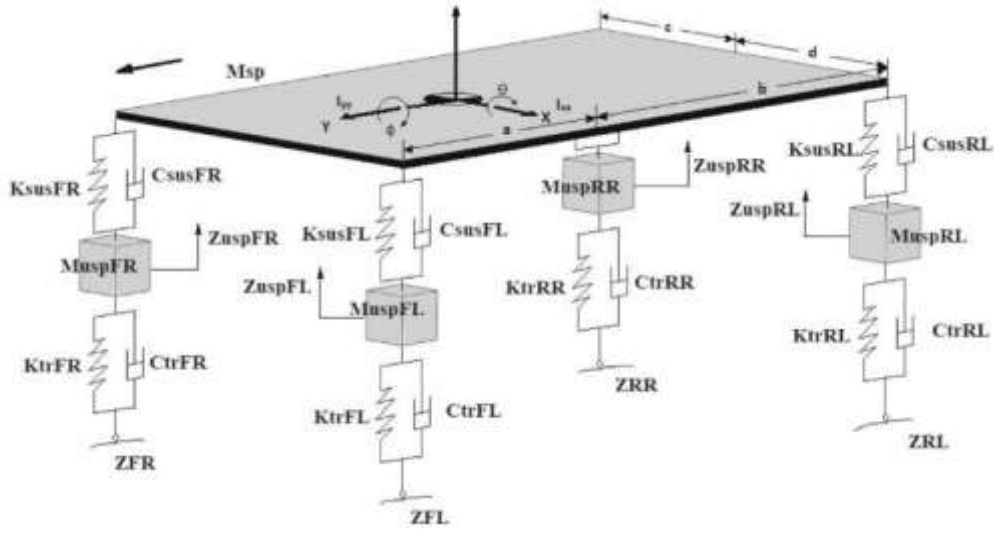


Figure 5.7 Full car model of the test vehicle (Nigwal et al., 2022)

*Sprung mass – Bounce:*

$$\begin{aligned}
 M_{Sp}\ddot{Z}_{Sp} + C_{susFL}(\dot{Z}_{Sp} - a\dot{\theta} + c\dot{\phi} - \dot{Z}_{uspFL}) + K_{susFL}(Z_{Sp} - a\theta + c\phi - \\
 Z_{uspFL}) + C_{susFR}(\dot{Z}_{Sp} - a\dot{\theta} - d\dot{\phi} - \dot{Z}_{uspFR}) + K_{susFR}(Z_{Sp} - a\theta - \\
 d\phi - Z_{uspFR}) + FD_{RL}\cos\psi + K_{susRL}(Z_{Sp} + b\theta + c\phi - Z_{uspRL}) + \\
 FD_{RR}\cos\psi + K_{susFL}(Z_{Sp} + b\theta - d\phi - Z_{uspRR}) = 0
 \end{aligned} \quad (5.19)$$

*Sprung mass - Roll:*

$$\begin{aligned}
 I_{YY}\ddot{\phi} + c[C_{susFL}(\dot{Z}_{Sp} - a\dot{\theta} + c\dot{\phi} - \dot{Z}_{uspFL}) + K_{susFL}(Z_{Sp} - a\theta + c\phi - \\
 Z_{uspFL})] - d[C_{susFR}(\dot{Z}_{Sp} - a\dot{\theta} - d\dot{\phi} - \dot{Z}_{uspFR}) - K_{susFR}(Z_{Sp} - a\theta - \\
 d\phi - Z_{uspFR})] + c[FD_{RL}\cos\psi + K_{susRL}(Z_{Sp} + b\theta + c\phi - Z_{uspRL})] - \\
 d[FD_{RR}\cos\psi - K_{susFL}(Z_{Sp} + b\theta - d\phi - Z_{uspRR})] = 0
 \end{aligned} \quad (5.20)$$

*Sprung mass – Pitch:*

$$\begin{aligned}
I_{XX}\ddot{\theta} - a[C_{susFL}(\dot{Z}_{Sp} - a\dot{\theta} + c\dot{\varphi} - \dot{Z}_{uspFL}) - K_{susFL}(Z_{Sp} - a\theta + c\varphi - \\
Z_{uspFL})] - a[C_{susFR}(\dot{Z}_{Sp} - a\dot{\theta} - d\dot{\varphi} - \dot{Z}_{uspFR}) - K_{susFR}(Z_{Sp} - a\theta - \\
d\varphi - Z_{uspFR})] + b[FD_{RL}\cos\psi + K_{susRL}(Z_{Sp} + b\theta + c\varphi - Z_{uspRL})] + \\
b[FD_{RR}\cos\psi + K_{susFL}(Z_{Sp} + b\theta - d\varphi - Z_{uspRR})] = 0
\end{aligned} \tag{5.21}$$

*Unsprung mass - Front left wheel:*

$$\begin{aligned}
M_{uspFL}\ddot{Z}_{uspFL} - C_{susFL}(\dot{Z}_{Sp} - a\dot{\theta} + c\dot{\varphi} - \dot{Z}_{uspFL}) - K_{susFL}(Z_{Sp} - a\theta + \\
c\varphi - Z_{uspFL}) + C_{tr}(\dot{Z}_{uspFL} - Z\dot{F}L) + K_{tr}(Z_{uspFL} - ZFL) = 0
\end{aligned} \tag{5.22}$$

*Unsprung mass - Front right wheel:*

$$\begin{aligned}
M_{uspFR}\ddot{Z}_{uspFR} - C_{susFR}(\dot{Z}_{Sp} - a\dot{\theta} - d\dot{\varphi} - \dot{Z}_{uspFR}) - K_{susFR}(Z_{Sp} - \\
a\theta - d\varphi - Z_{uspFR}) + C_{tr}(\dot{Z}_{uspFR} - Z\dot{F}R) + K_{tr}(Z_{uspFR} - ZFR) = 0
\end{aligned} \tag{5.23}$$

*Unsprung mass - Rear left wheel:*

$$\begin{aligned}
M_{uspRL}\ddot{Z}_{uspRL} - FD_{RL}\cos\psi - K_{susRL}(Z_{Sp} + b\theta + c\varphi - Z_{uspRL}) \\
+ C_{tr}(\dot{Z}_{uspRL} - Z\dot{R}L) + K_{tr}(Z_{uspRL} - ZRL) = 0
\end{aligned} \tag{5.24}$$

*Unsprung mass - Rear right wheel:*

$$\begin{aligned}
M_{uspRR}\ddot{Z}_{uspRR} - FD_{RR}\cos\psi - K_{susFL}(Z_{Sp} + b\theta - d\varphi - Z_{uspRR}) \\
+ C_{tr}(\dot{Z}_{uspRR} - Z\dot{R}R) + K_{tr}(Z_{uspRR} - ZRR) = 0
\end{aligned} \tag{5.25}$$

In equations 5.19 to 5.25,  $M$  stands for mass,  $I$  stands for inertia,  $C$  stands for the damping coefficient,  $K$  stands for the stiffness,  $Z$  stands for linear vertical displacement,  $FD$  stands for the MR damper force,  $\theta$  is the angular displacement about the lateral axis of the vehicle,  $\varphi$  is the angular displacement about the longitudinal axis, and  $\psi$  is the angle made by the damper axis with the horizontal which was measured to be  $58^\circ$ . A single dot above any of the coefficients represents the velocity, and a double dot represents the acceleration. The subscript ‘sp’, ‘usp’, ‘sus’, ‘tr’, ‘FL’, ‘FR’, ‘RL’

and ‘RR’ refer to the sprung mass of the vehicle, unsprung mass of the vehicle, suspension, tire, Front Left side of the vehicle, Front Right side of the vehicle, Rear Left side of the vehicle and Rear Right side of the vehicle, respectively. ZFL, ZFR, ZRL and ZRR are the road displacement inputs to the vehicle's Front Left, Front Right, Rear Left and Rear Right side, respectively. The coefficients a, b, c and d refer to the distance of the vehicle's center of gravity to the front axle, the rear axle, the right wheel and the left wheel, respectively. The values of the coefficients in equations 5.19 to 5.25 are listed in Table 5.7.

Table 5.7 Coefficient values of full car model of the test vehicle

<b>Coefficient</b>	<b>Value</b>	<b>Coefficient</b>	<b>Value</b>
$M_{Sp}$	3080 kg	$K_{tr}$	195 kN/m
$I_{YY}$	2880.44 kg-m <sup>2</sup>	$C_{tr}$	762 Ns/m
$I_{XX}$	926.567 kg-m <sup>2</sup>	$a$	0.57 m
$M_{uspFL}, M_{uspFR}, M_{uspRL}, M_{uspRR}$	107.5 kg	$b$	2.78 m
$K_{susFL}, K_{susFR}$	53 kN/m	$c$	0.95 m
$K_{susRL}, K_{susRR}$	145 kN/m	$d$	0.95 m
$C_{susFL}, C_{susFR}$	3.147 kNs/m		

Although the industrial collaborator could provide most vehicle parameters, the tire properties are found experimentally. It is evident from Figure 5.7 that the tire is modeled as a combination of a spring and a viscous damper. In this study, the tire's vertical stiffness and viscous damping are obtained by subjecting the tire to sinusoidal excitation in the damper testing machine shown in Figure 3.3. The experimental setup used for this purpose and the schematic of the tire model used in this study is shown in Figure 5.8. The tire is held between a top fixture plate and a bottom fixture plate in the damper testing machine, as shown in Figure 5.8. The top fixture plate is connected to the actuator, whereas the bottom fixture plate is connected to the load cell. The actuator is given a sinusoidal input, resulting in an FD curve, as shown in Figure 5.9. The area under the FD curve gives the energy dissipated per cycle, which can be used to calculate

the tire's damping coefficient. The tire's stiffness is obtained by measuring the slope of the linear part of the hysteresis curve.

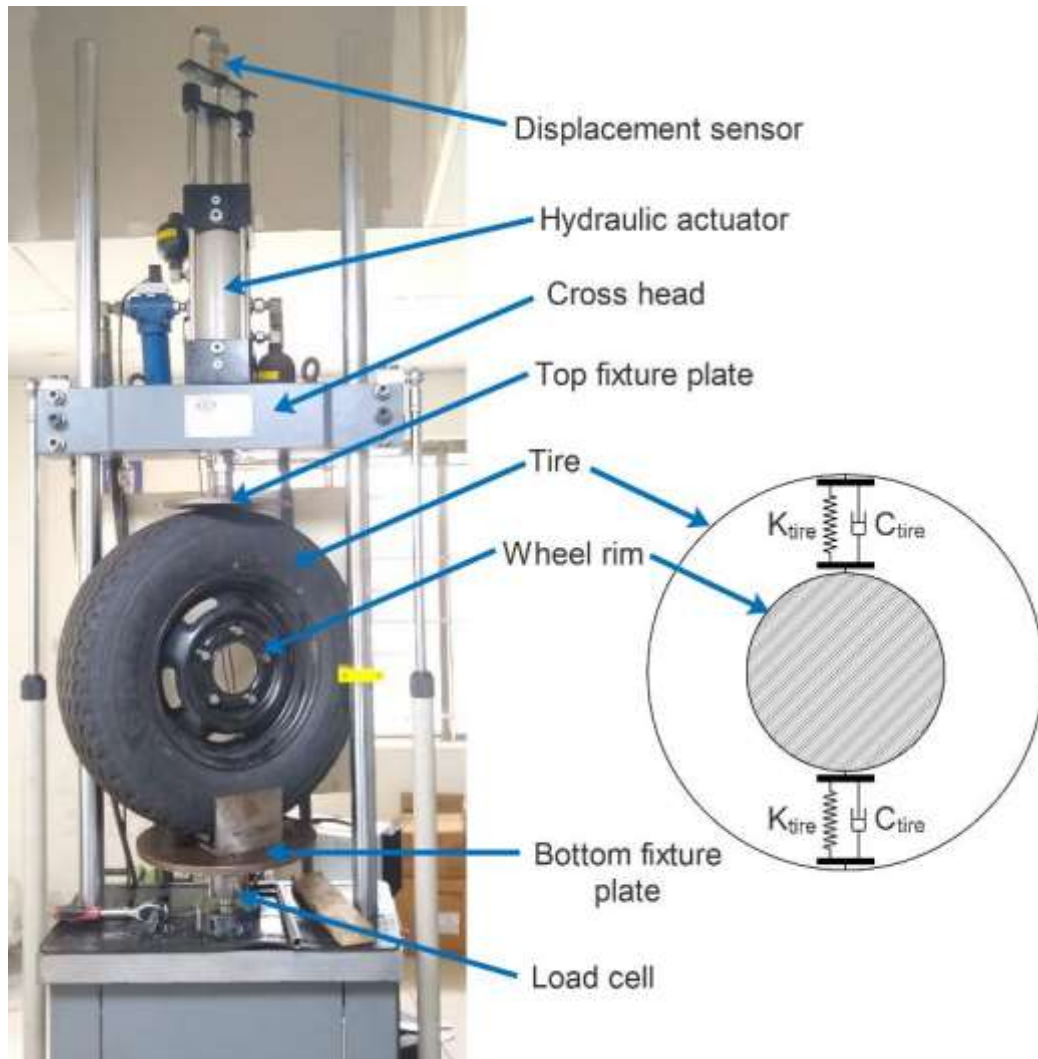


Figure 5.8 Experimental setup to determine tire properties

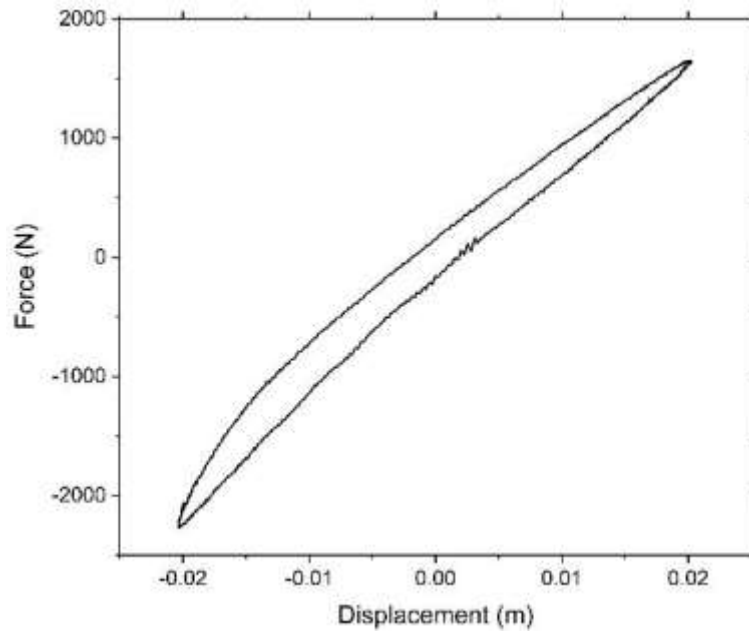
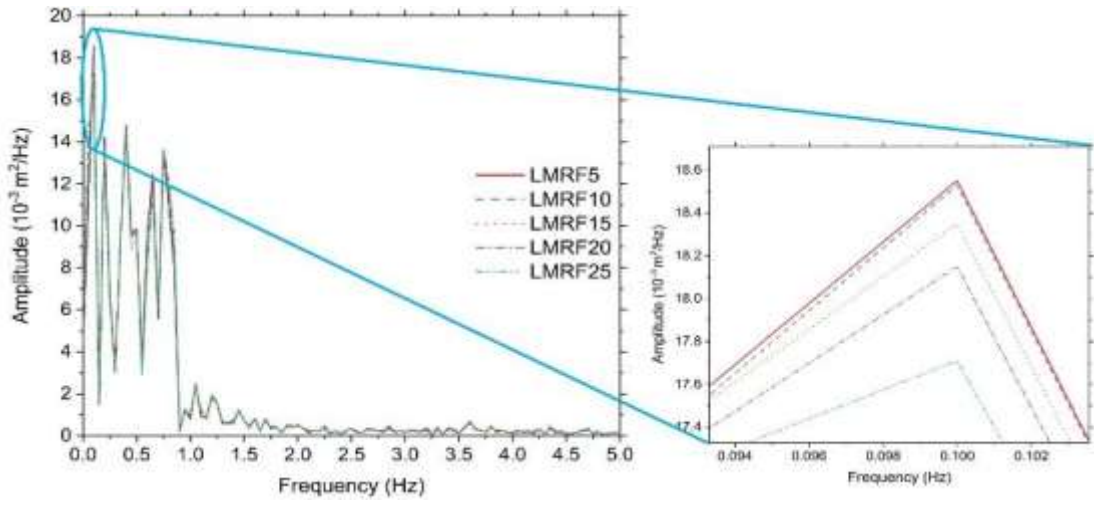


Figure 5.9 Force-Displacement diagram of tire

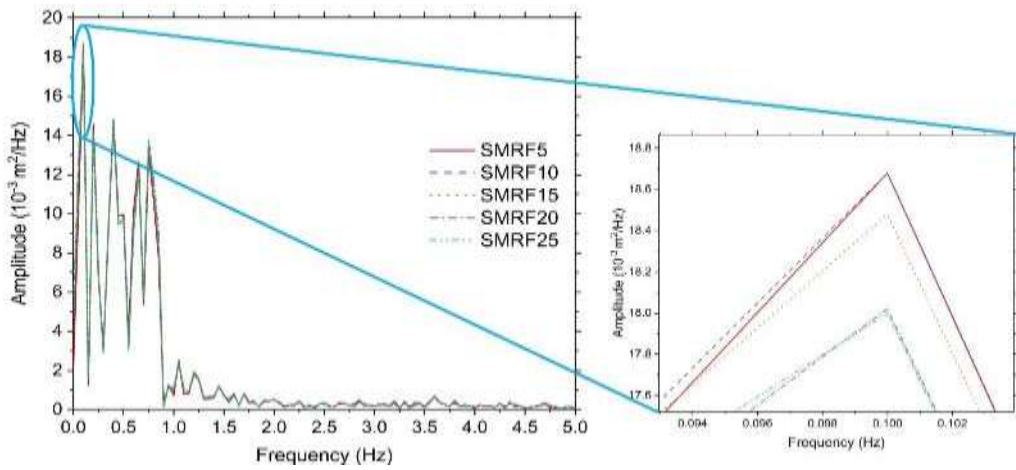
It should be noted that the stiffness and damping calculated using the FD diagram are the combined stiffness and damping of the tire above and below the wheel rim shown in Figure 5.8. Only one side of the tire will be subjected to road input during the simulation and in real-time. Therefore, the stiffness and damping of the tire on each side of the wheel rim are calculated using the theory of springs and dampers in series. The resulting values have been listed in Table 5.7.

It should be noted that the damper undergoes compression and expansion irrespective of whether the vehicle is under heave motion, roll motion or pitching motion; therefore, any of these motions can be used for comparing the performance of each MR fluid sample. The random nature of the input makes it difficult to examine the simulation results in the time domain; hence, the FFT of the simulation outputs is considered the performance index for comparison. The FFTs of the simulation results are plotted in Figure 5.10. The peak values of FFT response obtained from simulations, which will be employed in the optimization of the composition of the MR fluid, have been listed in Table 5.8.





(a)



(b)

Figure 5.10 FFT response of full car model simulation on the random road (a) LMRF samples  
(b) SMRF samples

Table 5.8 Peak FFT values of simulation response

Fluid	FFT (Disp-m <sup>2</sup> /Hz)	Fluid	FFT (Disp-m <sup>2</sup> /Hz)
LMRF5	0.0185450	SMRF5	0.0186817
LMRF10	0.0185270	SMRF10	0.0186799
LMRF15	0.0183467	SMRF15	0.0184835
LMRF20	0.0181493	SMRF20	0.0180166
LMRF25	0.0180042	SMRF25	0.0177055

### 5.5.2 Cost estimation of MR fluid samples

The cost of each MR fluid sample is calculated by adding the cost of each ingredient of the MR fluid sample, i.e., the silicone oil, the CIP and the aluminum di-stearate. The cost of the silicone oil could be found on the box itself, but the cost of the CIP and Aluminum Di-Stearate was obtained from the nearest resellers of the manufacturer, Sigma Aldrich, in India. The cost of an MR fluid sample depends on the sample quantity; therefore, the cost of one 1 liter of MR fluid has been considered for optimization, listed in Table 5.9.

Table 5.9 Cost of MR fluid samples

Fluid	Fluid cost (INR/Liter)	Fluid	Fluid cost (INR/Liter)
LMRF5	7553.7	SMRF5	18977.42
LMRF10	14775.62	SMRF10	37623.07
LMRF15	21997.54	SMRF15	56268.71
LMRF20	29219.46	SMRF20	74914.36
LMRF25	36441.38	SMRF25	93560

### 5.5.3 Optimization of MR fluid composition

It is evident from Table 5.9 that the cost of the fluid increases with an increase in the volume fraction of CIP, as it is the costliest item among all the components of MR fluid. Moreover, the cost of SMRF samples is drastically higher than that of the LMRF samples. It can be inferred from Tables 5.8 and 5.9 that a costlier MR fluid does not yield better ride comfort. Therefore, the objective function of the optimization should be to maximize the ride comfort and minimize the cost of the fluid. Such a conflicting criterion has been solved in this study using the Response Surface Optimization (RSO) technique.

The field of RSO consists of the experimental strategy for exploring the space of the independent variables, empirical statistical modeling to develop an appropriate approximating relationship between the response and the independent variables, and

optimization methods for finding the levels or values of the independent variables that produce desirable values of the responses (Myers et al., 1995). In this study, the independent variables are particle size and volume fraction. The peak values of FFT response of the test vehicle model simulation and the fluid cost are the response factors to be minimized. The relation between the independent variables and response factors is obtained by regression analysis using the MINITAB™ software. The regression model of the FFT response, with an R-Square value of 93.24%, is given by equation 5.26. The regression model for the MR fluid cost, with an R-Square value of 100%, is given by equation 5.27.

$$FFT = 0.018738 - 0.000018 \times PS + 0.000010 \times VF - 0.000002 \times VF \times VF - 0.000001 \times PS \times VF \quad (5.26)$$

$$Cost = 331.8 + 4821 \times VF - 376.4 \times VF \times PS \quad (5.27)$$

Where *PS* stands for Particle size and *VF* stands for the volume fraction of CIP in MR fluid. The optimization results obtained through RSM revealed that the LMRF25 is the optimal MR fluid with a corresponding FFT value of 0.0180042 m<sup>2</sup>/Hz and a cost price of INR 36,441.381/-.

#### **5.5.4 Performance evaluation of developed MR damper with optimized MR fluid**

The optimized in-house MR fluid, LMRF25, is filled in the developed MR damper and is experimentally evaluated on the damper testing machine and the test vehicle under the same testing conditions employed in Chapter 4. The characteristic graph and vehicle testing results have been presented in Figures 5.11 to 5.13. Rambal Ltd. had acquired a new random road test track when the MR damper with LMRF25 was ready for testing. Therefore, this test track has also been used to evaluate the performance of the developed MR damper with LMRF25. The same was not available when the MR damper with commercial MR fluid was tested. A satellite view of the random road test track can be seen in Figure 5.14.

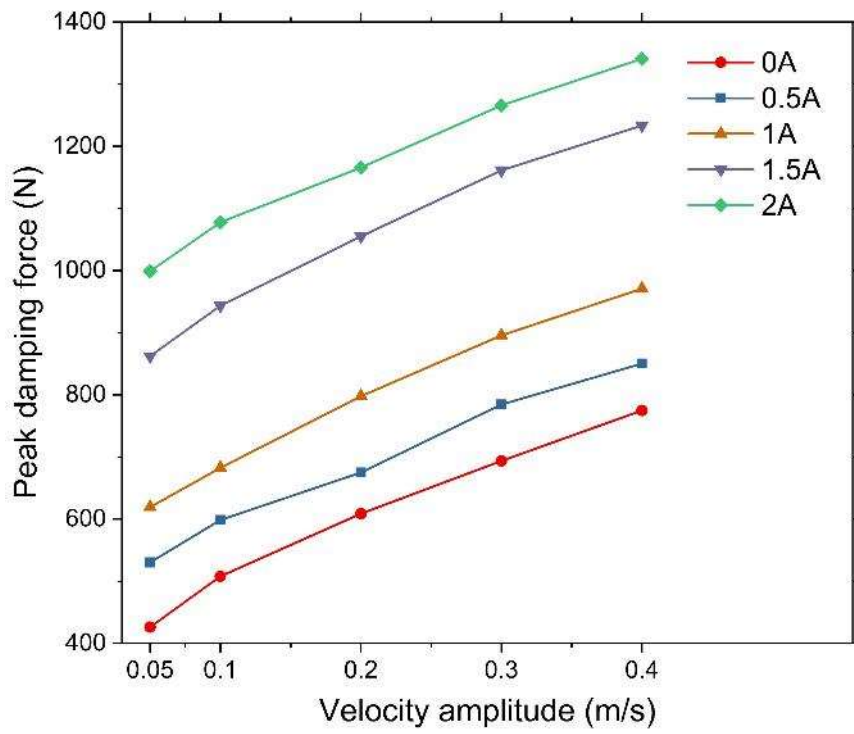
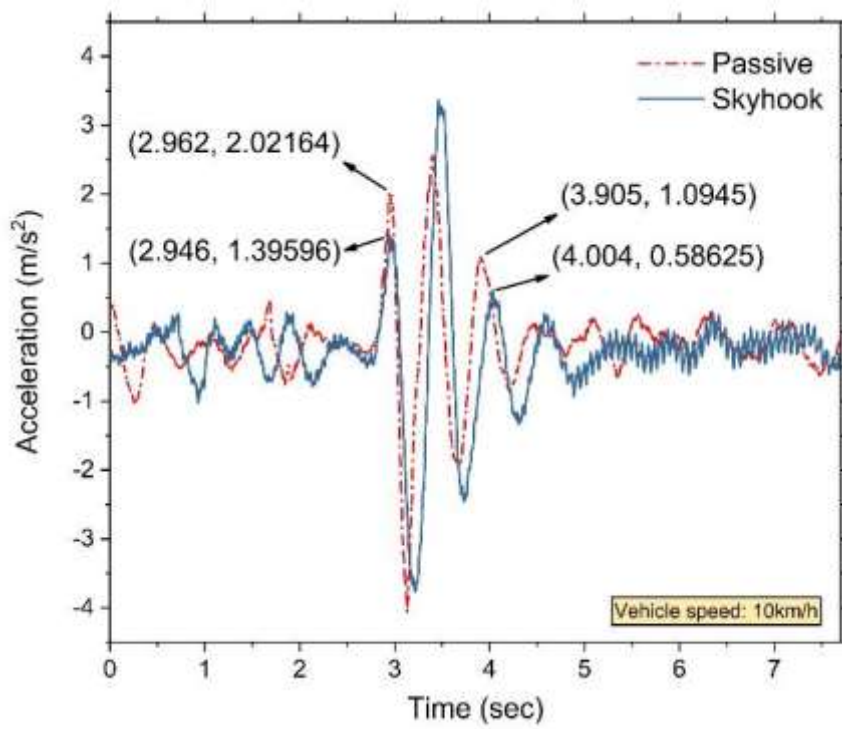
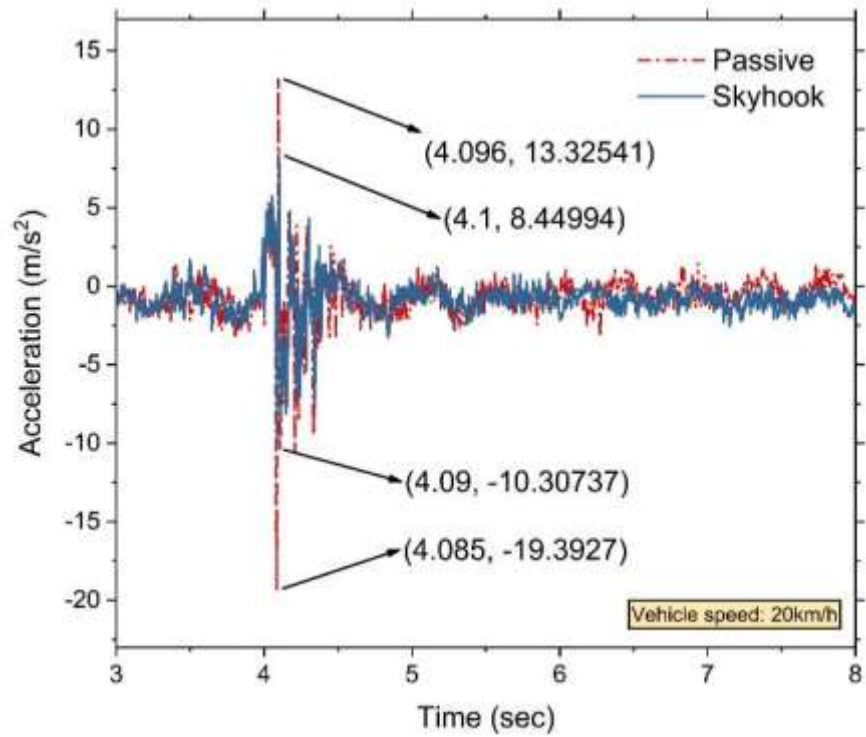


Figure 5.11 Experimental characteristic graph of developed MR damper with LMRF25

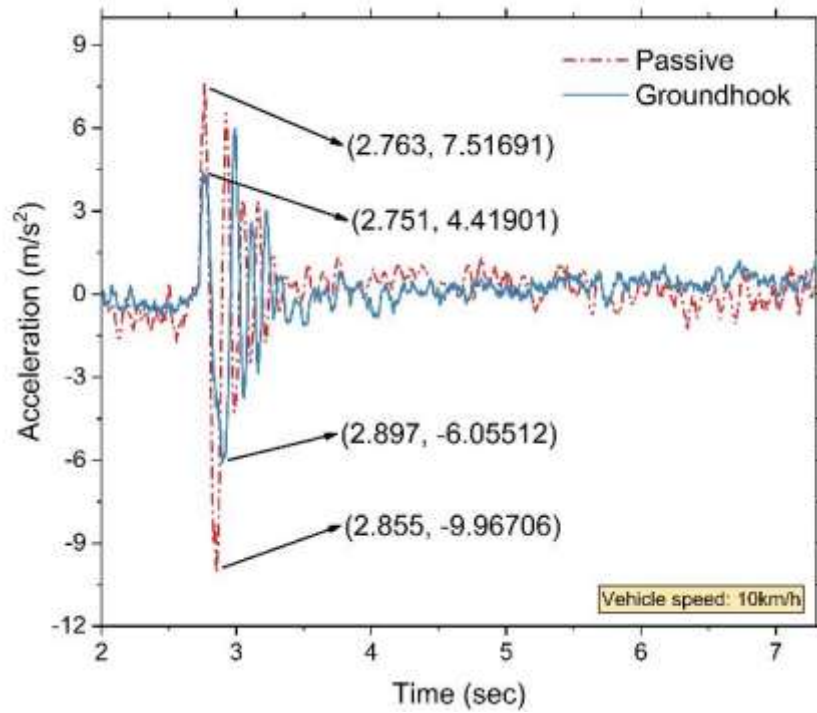


(a)

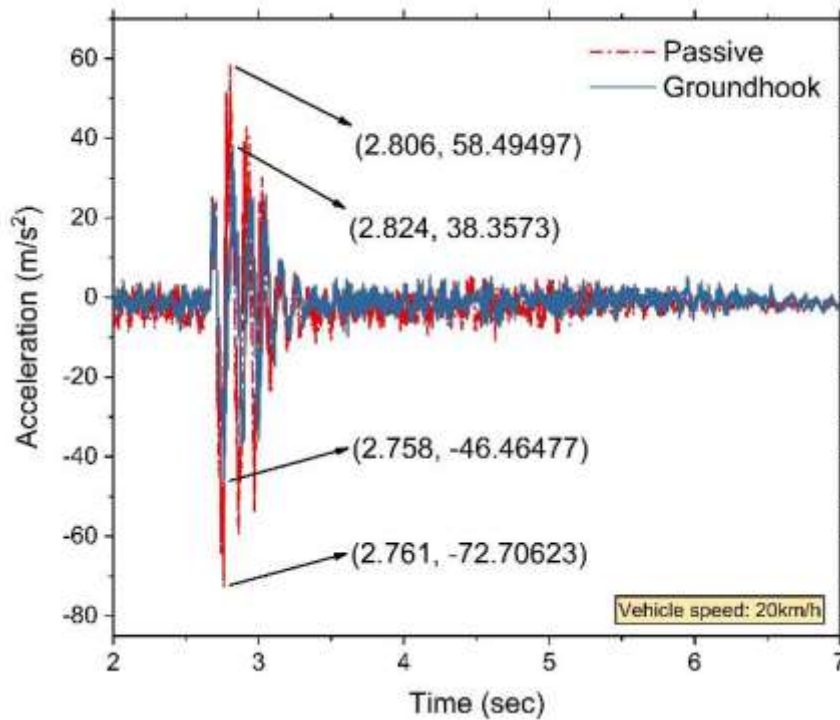


(b)

Figure 5.12 Experimental results of testing the vehicle over the sharp speed bump (a) Sprung mass acceleration at 10km/h (b) Sprung mass acceleration at 20km/h



(a)



(b)

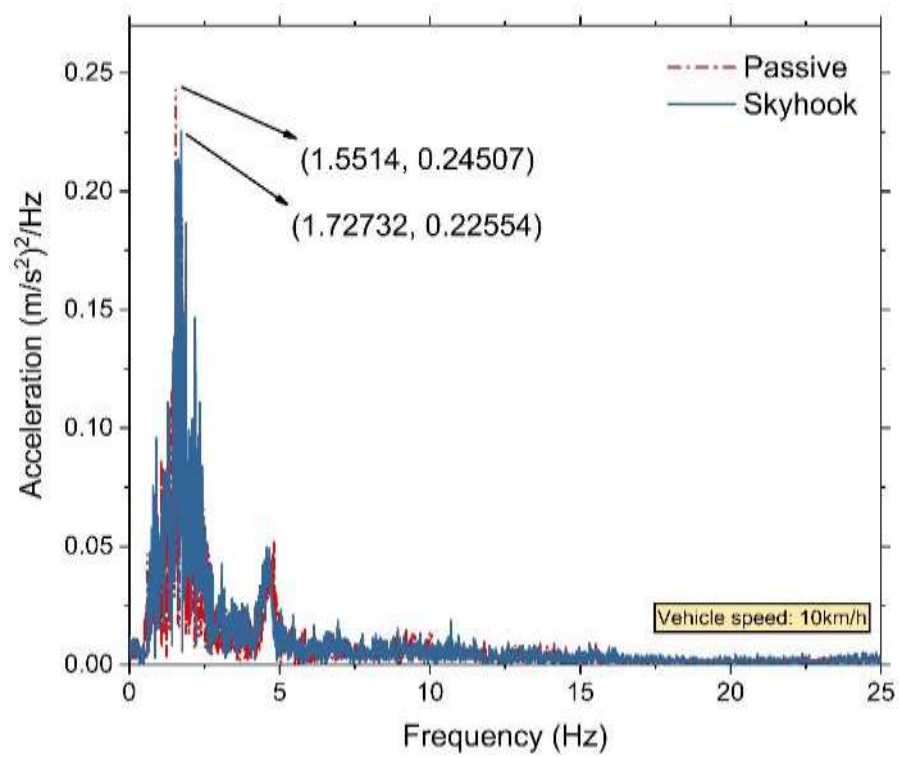
Figure 5.13 Experimental results of testing the vehicle over the sharp speed bump (a) Unsprung mass acceleration at 10km/h (b) Unsprung mass acceleration at 20km/h

The random road test track is an oval-shaped off-road track with an approximate length of 300m. The vehicle is run over the oval test track at two different speeds, 10km/h and 20km/h, and each control strategy, skyhook control and ground hook control are implemented at each vehicle speed tested. The test vehicle is also run with stock passive dampers in the suspension. The accelerations measured at the sprung mass and the unsprung mass during the experiment with MR dampers and the passive damper are compared to evaluate the performance of the developed semiactive suspension system with that of the existing passive suspension system. The results of testing the vehicle on this test track have been presented in Figures 5.15 and 5.16 in the form of FFT of vehicle body and the wheel acceleration due to random nature of the road input.

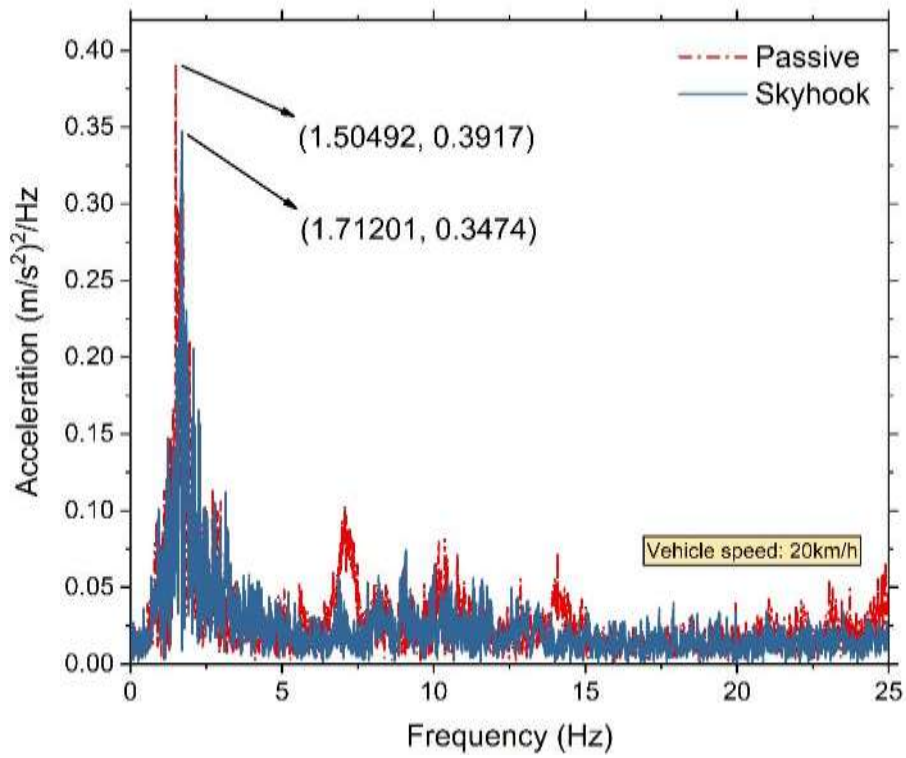




Figure 5.14 Satellite view of the random road test track at Rambal Ltd., Chennai (“Google Earth”, 2022)

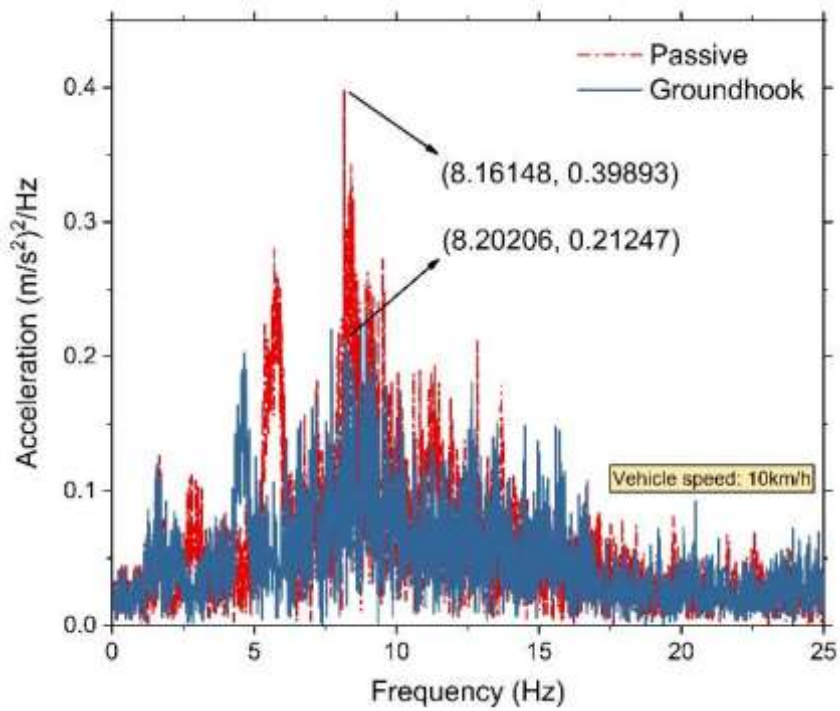


(a)



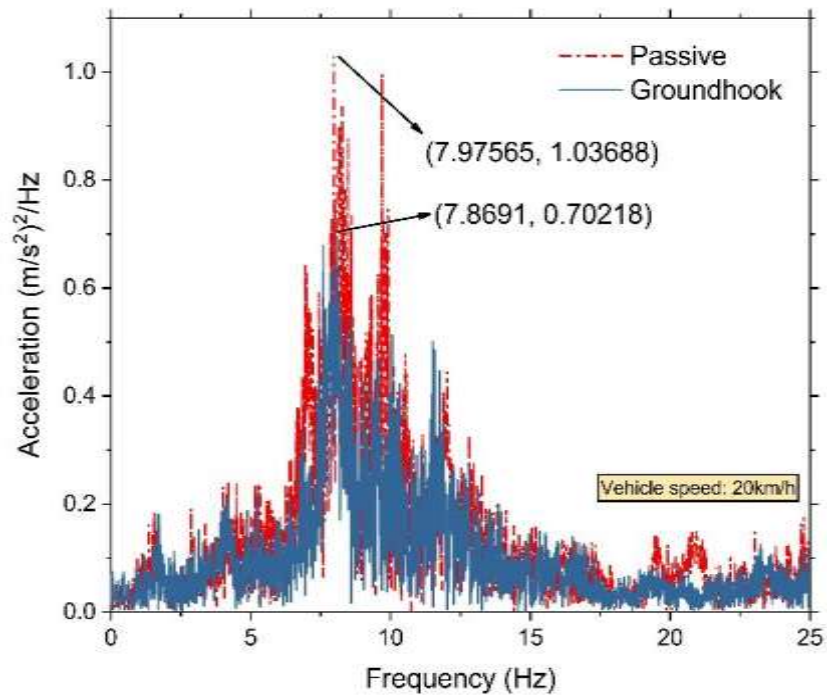
(b)

Figure 5.15 Experimental results of testing the vehicle over the random road test track (a) FFT of mass response at 10 km/h (b) FFT of sprung mass response at 20 km/h



(a)





(b)

Figure 5.16 Experimental results of testing the vehicle over the random road test track (a) FFT of unsprung mass response at 10 km/h (b) FFT of unsprung mass response at 20 km/h

## 5.6 RESULTS AND DISCUSSIONS

### 5.6.1 Performance comparison of LMRF25 and MRF-132DG using Rheometer and damper testing machine

The flow curve of LMRF25 was compared with that of the MRF-132DG at the maximum magnetic field strength of 76.265 kA/m. The LMRF25 exhibited higher shear stress than MRF-132DG, as evident in Figure 5.17, which should result in a higher damping force when used in the MR damper than when MRF-132DG is used.

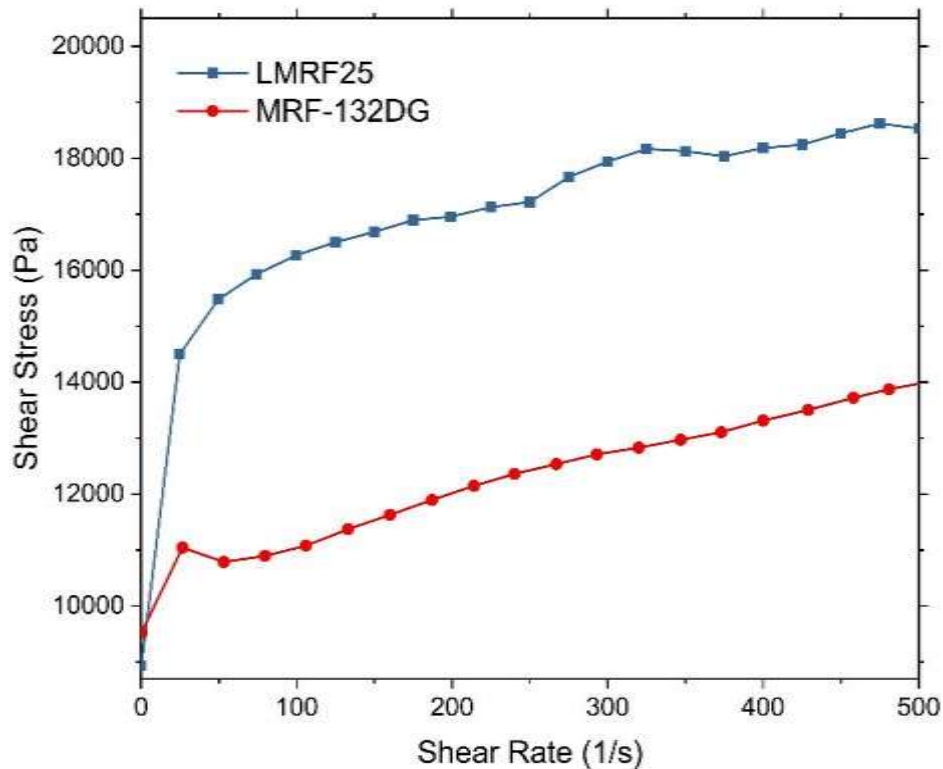


Figure 5.17 Comparison of experimental flow curves of LMRF25 and MRF-132DG

The characteristic graph of the MR damper filled with LMRF25 and MRF-132DG shown in Figures 4.12 and 5.11 have been combined and presented in Figure 5.18 for comparative analysis. It can be seen in Figure 5.18 that the MR damper with LMRF25 generates a higher damping force as compared to when MRF-132DG is used at any given velocity and current value. The off-state viscosity, i.e., viscosity measured with no supply of current, calculated at a shear rate of  $400\text{s}^{-1}$ , corresponding to peak velocity of  $0.4\text{m/s}$ , was found to be  $1949.9\text{ Pa}\cdot\text{s}$  in the case of LMRF25 which is a lot higher than  $97.862\text{ Pa}\cdot\text{s}$  as found in case of MRF-132DG. The increased off-state viscosity results in a higher off-state damping force in the case of the MR damper with LMRF25, as evident from Figure 5.18.

It can be further seen in Figure 5.18 that all the curves of the characteristic graph belonging to LMRF25 have a lower slope as compared to curves of the characteristic graph belonging to MRF-132DG, indicating a lower sensitivity of the MR damper with LMRF25. However, this shortcoming is compensated by a higher damping force delivered at each velocity tested and the current value supplied. The controllable

damping force generated by the developed MR damper with LMRF25 and MRF-132DG has been presented in Figure 5.19.

It can be inferred from Figure 5.19 that the LMRF generates almost the same amount of controllable damping force as the MRF-132DG in the developed MR damper while costing less than half of what MRF-132DG costs. The LMRF25 and the MRF-132DG have been further compared based on their performance in the MR damper installed on the test vehicle.

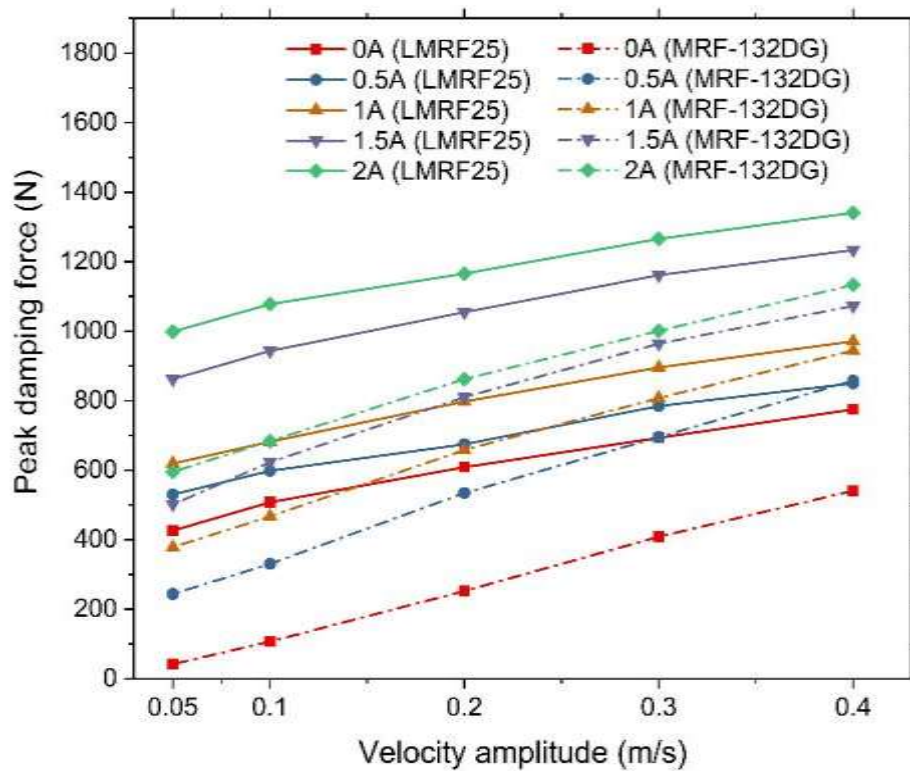


Figure 5.18 Comparison of experimental characteristic graphs with LMRF25 and MRF-132DG

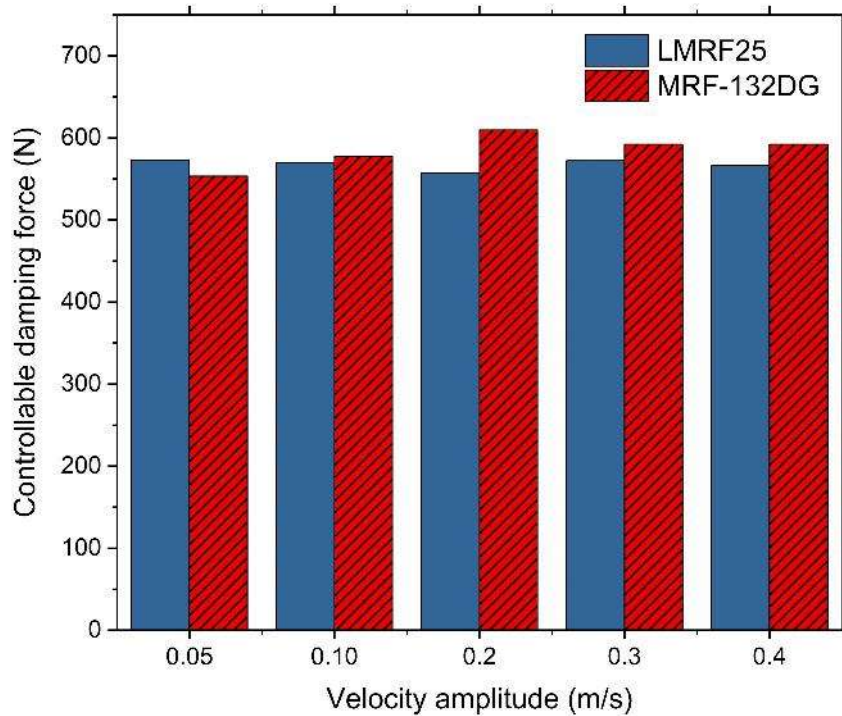


Figure 5.19 Controllable damping forces of developed MR damper with LMRF25 and with MRF-132DG

### 5.6.2 Performance evaluation of LMRF25 in the test vehicle and comparison with MRF-132DG

It can be seen in Figure 5.12 that the MR damper with LMRF25 was able to improve the ride comfort of the test vehicle when run over a sharp speed bump as compared to the passive damper. The percentage improvement in ride comfort was calculated at each vehicle speed using equation 4.25. Although the peak acceleration is not reduced, the preceding and succeeding acceleration accelerations were reduced at 10km/h by 31.7% and 43.97%, respectively, by employing an MR damper with LMRF25. The peak acceleration of the vehicle body was reduced by 36.58% at 20km/h when the MR damper with LMRF25 was used in the vehicle suspension. It can be seen in Figure 5.13 that the MR damper with LMRF25 was able to improve the road handling of the test vehicle over a sharp speed bump as compared to the passive damper. The percentage improvement in ride comfort was calculated at each vehicle speed using equation 4.25. The peak acceleration of unsprung mass reduced by 45% at 10 km/h and

34.44% at 20 km/h by employing the MR damper with LMRF25, as evident from Figure 5.13.

The test vehicle was run over an oval off-road test track to evaluate the performance of the developed MR damper on a random road. The FFT of the vehicle body and wheel response was used to compare the performance of the MR damper against the passive damper. The percentage improvement in ride comfort and road handling was calculated using equation 4.25, however in this case, the terms  $a_{passive}$  and  $a_{MRD}$  represent the peak value of the FFT response with passive damper and MR damper, respectively. The FFT response of the test vehicle with passive damper running at 10km/h, presented in Figure 5.15a, showed that the dominant frequency occurred at 1.551Hz with a peak PSD of acceleration of  $0.245(m/s^2)^2/Hz$ . Implementing the MR damper with skyhook control reduced the peak PSD acceleration to  $0.225(m/s^2)^2/Hz$  at 1.727Hz frequency. Therefore, an improvement of 8% was observed in ride comfort of the vehicle with the semiactive suspension system at 10km/h.

The test vehicle was also run at 20km/h on the test track, and the FFT of the body response showed a peak PSD of acceleration of  $0.391(m/s^2)^2/Hz$  at 1.504Hz, as presented in Figure 5.15b. The peak PSD of acceleration reduced to  $0.347(m/s^2)^2/Hz$  with a shift in the corresponding frequency to 1.712Hz when the MR damper with skyhook control was implemented. Therefore, a semiactive suspension system improved ride comfort by 11.3% at 20km/h.

The FFT of the unsprung mass response on the test track at 10km/h showed that the peak PSD of acceleration of  $0.398(m/s^2)^2/Hz$  occurs at 8.202Hz frequency with the passive damper in the vehicle suspension at 10 km/h, as shown in Figure 5.16a. Implementing the MR damper with ground hook control at this vehicle speed improved the PSD of acceleration to  $0.212(m/s^2)^2/Hz$  with the corresponding frequency shifting to 8.9Hz. The FFT of unsprung mass response at 20km/h with passive damper showed a peak PSD of  $1.036(m/s^2)^2/Hz$  at 7.975Hz, as shown in Figure 5.16b. The peak PSD was reduced to  $0.70218(m/s^2)^2/Hz$  with the implementation of the MR damper with ground hook control, and the corresponding frequency was shifted to 7.8691Hz. Therefore, the MR damper implemented on the vehicle with ground hook control improved the vehicle's handling capability by 46.3% at 10km/h and 32.8% at 20km/h.

The peak amplitude of vibrations occurring in the FFT response generally reveals the system's natural frequency. In this case, the natural frequency of the vehicle's sprung mass was found to be in the range of 1.5Hz to 1.8Hz, and that of the unsprung mass was found to be in the range of 7.8 to 8.2Hz. It can also be inferred that the use of semi-active suspension has hardly changed the natural frequency of the vehicle's sprung and unsprung mass.

The percentage improvement in ride comfort and road handling obtained in each case of MR damper with MRF-132DG and LMRF25 has been listed in Table 5.10. The cost of each fluid and the developed MR damper filled with each fluid has been listed in Table 5.11.

Table 5.10 Performance comparison of LMRF25 and MRF-132DG in the test vehicle

Vehicle speed	Percentage improvement			
	Ride comfort		Road handling	
	MRF-132DG	LMRF25	MRF-132DG	LMRF25
10km/h	16.20%	31.70%	14.32%	45%
20km/h	17.60%	36.58%	29.30%	34.44%

Table 5.11 Cost comparison of the LMRF25 and MRF-132DG

MR Fluid	Cost of Fluid (INR/liter)	Cost of MR damper (INR)
MRF-132DG	1,24,903.75/-	58,426.48/-
LMRF25	36,548.92/-	29,384.30/-

It is evident from Table 5.10 that the MR damper with LMRF25 outperforms the MR damper with MRF-132DG on the test vehicle running over a sharp speed bump at any vehicle speeds tested. It is also evident from Table 5.11 that LMRF25 costs 70.74% less than the MRF-132DG, with no compromise in rheological performance. The MR damper operating with LMRF25 costs 49.71% less than the same damper operating with MRF-132DG while improving performance.

## 5.7 SUMMARY

This chapter describes a methodology to reduce the overall cost of the developed MR damper by developing an MR fluid whose performance is not only on-par with commercial MR fluid but also more affordable.

The optimization of MR fluid involves the determination of optimal composition of the magnetic particles in the carrier fluid. Therefore, MR fluid samples with multiple compositions of CIP of two different particle sizes were prepared and characterized in the rheometer. The rheology data was used to predict the damping force generated by the MR damper developed in the previous chapter. This damping force was non-parametrically modeled using MFM for representation in the simulation of the full car model of the test vehicle. The FFT response of vehicle test model simulation was evaluated with all the MR fluid samples prepared. The particle size of CIP, the FFT response of the full car model simulation response and the cost of synthesizing the MR fluid samples were used to optimize the composition of CIP in the carrier fluid through the RSO technique. The MR fluid sample with large-sized CIP in 25% volume fraction, LMRF25, was optimal for this application.

The performance of LMRF25 was evaluated in the rheometer, on the damper testing machine and the test vehicle. The testing conditions used on the damper testing machine and the test vehicle remained the same while testing the LMRF25 as the ones used in the previous chapter while testing the MRF-132DG. The rheological study of the two fluids showed that the LMRF25 outperformed the MRF-132DG in terms of shear stress and off-state viscosity. A comparison of the characteristic graph of the MR damper with the two MR fluids revealed that the LMRF25 delivers a higher damping force than the MRF-132DG. The controllable damping force delivered by the LMRF25 was significantly closer to that delivered by the MRF-132DG. The results of the experiments on the test vehicle with the MR damper filled with LMRF25 revealed that the developed MR fluid successfully improved the ride comfort and road handling of the vehicle over the passive damper at all speeds, whether it is a sharp speed bump or a random road. The LMRF25 outperformed the MRF-132DG by improving the ride comfort and road handling of the test vehicle while being more affordable than the MRF-132DG.





## CHAPTER 6

### EXPERIMENTAL EVALUATION AND SIMULATION OF AN ACCELERATION-BASED CURRENT CONTROL STRATEGY

#### 6.1 INTRODUCTION

A current control strategy of a semiactive suspension system is a mathematical equation that determines the timing and magnitude of the current supply to the MR damper such that the performance of the suspension system is improved. Almost all semiactive control strategies implemented till date use the system component velocities, such as the sprung mass, the unsprung mass and the damper velocity, in the case of a vehicle. The velocity of the system components is measured by filtering and integrating the acceleration data from the accelerometers in the system, which increases the computational load, thereby increasing the reaction time of the semiactive suspension system. This issue has led the researchers to gain interest in acceleration-based control strategies due to their simplicity, reduced computational load and cost-effectiveness. Studies integrating the conventional control strategies with acceleration have been discussed in Chapter 2; however, the direct use of acceleration of the system in a semi-active control strategy has rarely been explored. One such control strategy has been proposed in this chapter.

The acceleration-based skyhook control (ASHC) strategy proposed in this chapter has been developed by replacing the vehicle body velocity and wheel velocity with vehicle body acceleration and wheel acceleration in the conventional velocity-based skyhook control (VSHC) given by equation 4.23. The resulting equation of the ASHC is given by equation 6.1.

$$F_d = \begin{cases} F_{dmax} & \text{for } \ddot{x}_b(\ddot{x}_b - \ddot{x}_w) \geq 0 \\ F_{dmin} & \text{for } \ddot{x}_b(\ddot{x}_b - \ddot{x}_w) < 0 \end{cases} \quad (6.1)$$

Where  $\ddot{x}_b$  is the vehicle body acceleration and  $\ddot{x}_w$  is the wheel acceleration.

## 6.2 METHODOLOGY TO EVALUATE PERFORMANCE OF ASHC AND VSHC

The methodology adopted in this chapter has been depicted in Figure 6.1. The effectiveness of the ASH is evaluated experimentally based on the response of an SDOF system with an MR damper subjected to different excitations. The computational efficiency of the proposed control strategy is based on the simulation response of the SDOF with an MR damper subjected to the same excitations used during the experiments.

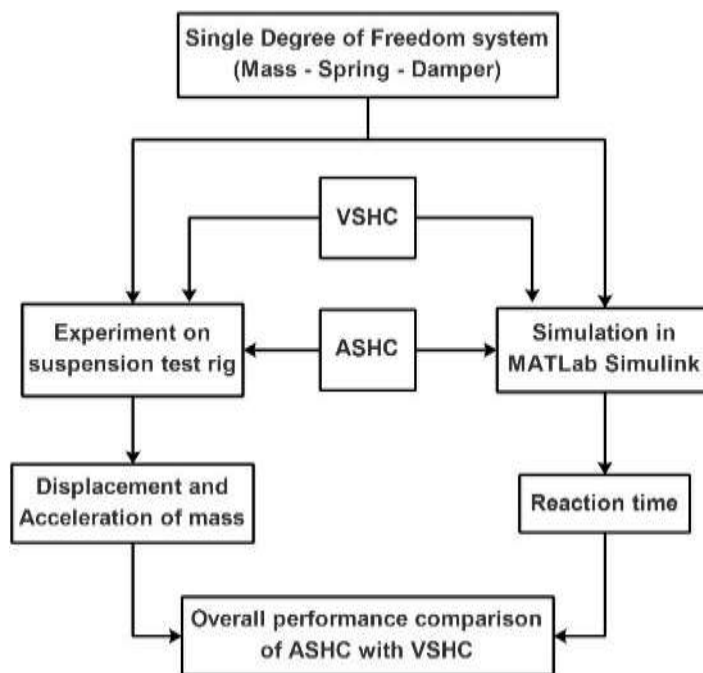


Figure 6.1 Methodology to evaluate performance of ASHC and VSHC

## 6.3 EXPERIMENTAL EVALUATION OF ACCELERATION BASED SKYHOOK CONTROL IN THE SDOF SYSTEM

The experimental set up used in this study is a suspension test rig modified to work as an SDOF (Desai et al., 2021). It consists of a mass weighing 136 kg, in the shape of a plate free to slide on the rigid frame and is provided with fixtures to mount it on a coil spring with a spring rate of 40.8 N/mm along with the MR damper. One end of the spring and damper is connected to the mass, and the other is connected to a servo-controlled double-acting hydraulic actuator, as shown in Figure 6.2. The actuator is connected to spring and damper on one end, and the other is connected to a position sensor. An LVDT, fitted on the rigid frame, records the displacement of the mass.

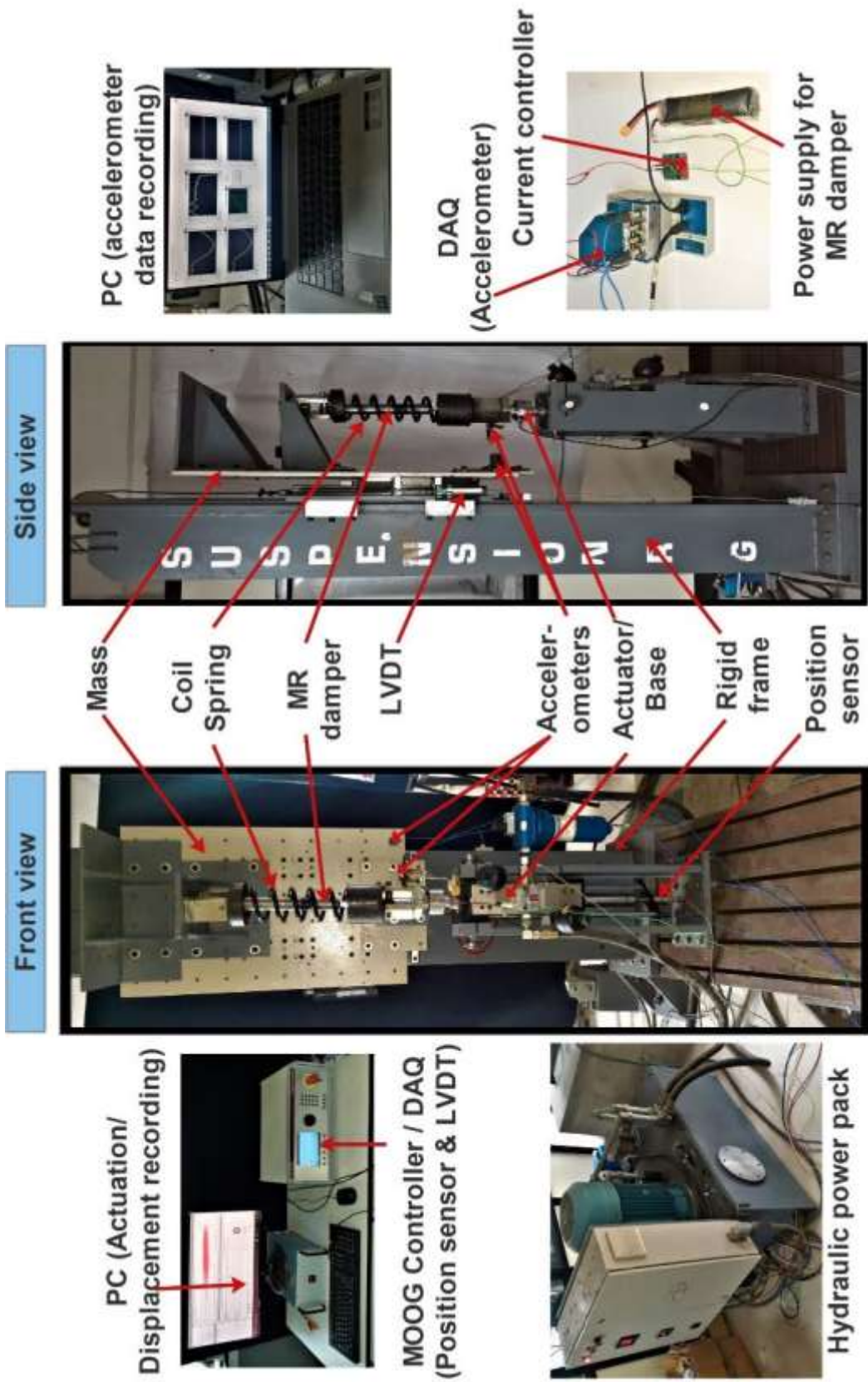


Figure 6.2 Experimental setup of SDOF with MR damper

The hydraulic actuator is supplied with an oil pressure of 210 bars with a flow rate of 65 lpm from the hydraulic power pack allowing the actuator to achieve a maximum velocity of 1.2 m/s with a maximum amplitude of 75mm (stroke 150 mm). A radiator has been provided to keep the hydraulic oil temperature within its limits during operation. The servo valve receives input commands from a MOOG® Controller that generates input signals through various continuous inputs, such as sinusoidal wave, square wave, sawtooth wave, etc., using its proprietary software. The controller also acts as data acquisition system for the displacement data from the position sensor on the actuator and LVDT on mass at a sampling rate of 1kHz. The acceleration data required for implementing the semi-active control is obtained using two accelerometers, one on the mass and another on the actuator. The accelerometers used in this study are PCB 352C3 uniaxial accelerometers, consisting of ceramic sensing elements with a sensitivity of 100 mV/g and a sensing range of  $\pm 50g$  (“PCB Electronics”, 2022). The data from these accelerometers is recorded by the NI-9234 IEPE module mounted on NI-cDAQ-9174. The LabView program processes the accelerometer data on the laptop shown in Figure 6.2 as per the control strategy implemented. The trigger signal to supply current to the MR damper from the power supply is given by digital I/O DAQ, NI-9403.

The MR damper has a fully extended length of 540mm (measured between the centers of the damper's eyes), and the free length of the coil spring is 405mm; consequently, the mass is suspended on the spring. Therefore, the mass and the spring are connected, in this setup, solely by the weight of the mass. Hence, to ensure that the mass and the spring maintain contact during the experiment, the acceleration of the mass should not exceed the acceleration due to gravity, i.e.,  $9.81 \text{ m/s}^2$ . One way of ensuring this is by keeping the acceleration of the actuator below  $9.81 \text{ m/s}^2$  under any type of excitation. The working stroke of the sliding mass is 100 mm. The SDOF is subjected to free and forced vibrations to determine the transient and continuous response of the system, respectively, while implementing the two control strategies considered for this study.

In this study, the free vibrations are induced by giving step input to the actuator. A step input can be given in two forms, i.e., upward step hereon referred to as positive

step, and downward step hereon referred to as negative step. In the case of step input, the acceleration tends to attain very high values. Therefore, to ensure the contact between the mass and spring during the step input, the positive step is executed by displacing the actuator 40mm upward from its mean position and the negative step by displacing the actuator 40mm downward from its mean position. The transient response of the mass is recorded as displacement from LVDT and acceleration from the accelerometers.

The forced vibrations are induced by subjecting the actuator to a sinusoidal input. The sinusoidal input also can be given in two forms, high frequency and low-frequency sine wave. The amplitude and frequency of the sine wave considered in this study are 30mm and 2Hz, respectively, hereon referred as Sine-1, and 10mm and 5Hz, respectively, hereon referred as Sine-2. The Sine-1 wave with 30mm amplitude ensures that the sliding mass does not exceed its working stroke of 100mm and the chosen frequency of 2Hz ensures that there is ample suspension deflection under this excitation signal. The Sine-2 input, with 10mm amplitude and 5Hz, was considered to study the effect of high frequency on the system. The spring employed in the experimental setup is held between the mass and the actuator solely due to the weight of the mass in the system. Therefore, the amplitude and frequency of forcing function should be chosen as high as possible while expecting the amplitude of mass acceleration does not  $9.81\text{m/s}^2$  so as to allow the spring to maintain contact with both the mass and the actuator during the excitation. After trial and error, this frequency was found to be 5Hz with an amplitude of 10mm. The calculated acceleration amplitude of the actuator was  $9.87\text{m/s}^2$ .

#### **6.4 SIMULATION OF SDOF WITH ASHC AND VSHC**

The computational efficiency of the ASHC is evaluated and compared against that of VSHC through the reaction time measured during the simulation of SDOF with MR damper implementing each control strategy. The methodology used in chapter 3 to determine the simulation time of MFM and EDM was employed in this chapter, too, to determine the reaction time of each control strategy. Two programs for SDOF with MR damper are simulated in MATLAB, one implementing VSHC and the other implementing ASHC. Since the two programs differ only by the control algorithm used,

the time taken by each program for execution will be a measure of the reaction time of the respective control strategy. The time taken for each program execution, under the same inputs as the ones used during the experiment, is evaluated and compared. The SDOF system is governed by its equation of motion given by:

$$m\ddot{x} + F_d + k(x - y) = 0 \quad (6.2)$$

Where  $m$  is the mass,  $\ddot{x}$  is the acceleration of the mass,  $F_d$  is the damping force of the MR damper  $k$  is the spring rate, and  $x$  &  $y$  are the displacements of the mass and the base, respectively. The damping force of the MR damper is represented by the MFM given by equation 3.6. The developed MR damper described in Chapter 4, filled with LMRF25, is used in the SDOF experimental setup, whose characteristic graph has been presented in Figure 5.10. The MFM fits the characteristic graph in Figure 5.10 using the methodology presented in section 3.4.2. The resulting MFM coefficients are listed in Table 6.1. It can be observed in Table 6.1 that coefficients A and C remain mostly constant with changes in current as compared to the remaining coefficients. Therefore, A and C can be considered independent of current in the final equation of MFM. The remaining coefficients are considered to be current dependent. However, a linear relationship between these coefficients and the current is impossible due to the nonlinear variation of damping force with increasing current at any particular velocity on the characteristic graph, as shown in Figure 5.10.

Table 6.1 MFM coefficients for the developed MR damper with LMRF25

<b>Current</b>	<b>A</b>	<b>B</b>	<b>C</b>	<b>D</b>	<b>E</b>
0A	788.7	444.55	66.38	841.92	29.08
0.5A	788.99	5983.75	66.35	1034.68	4.79
1A	789	36702.59	66.19	2308.24	2.51
1.5A	789	50114.18	66.15	4082.24	1.93
2A	789	50452.89	66.15	4470.21	1.88

Therefore, the coefficients B, D and E are represented as a third-order polynomial of current, as per equations 6.3, 6.4 and 6.5, respectively, determined using MATLAB Curve Fitting Toolbox™.

$$B = B_1 I^3 + B_2 I^2 + B_3 I + B_4 \quad (6.3)$$

$$D = D_1 I^3 + D_2 I^2 + D_3 I + D_4 \quad (6.4)$$

$$E = E_1 I^3 + E_2 I^2 + E_3 I + E_4 \quad (6.5)$$

Where  $I$ , is current to the damper,  $B_1 = -25502$ ,  $B_2 = 68588$ ,  $B_3 = -10166$ ,  $B_4 = 222.89$ ,  $D_1 = -1644.5$ ,  $D_2 = 5188.2$ ,  $D_3 = -1984$ ,  $D_4 = 860.58$ ,  $E_1 = -14.318$ ,  $E_2 = 57.292$ ,  $E_3 = -70.913$  and  $E_4 = 28.806$ . The error between the experimental and the MFM calculated force data was minimal, as seen in Figure 6.3, making the MFM suitable for simulation. The SDOF is simulated in MATLAB on the same PC described in 3.5.4.

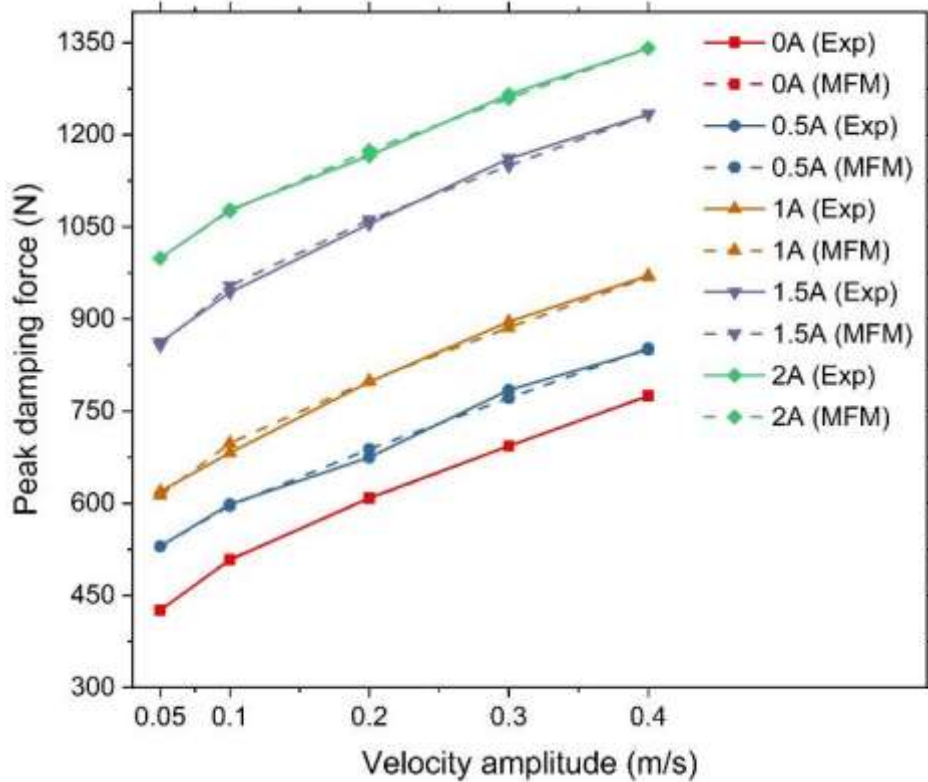


Figure 6.3 MFM fitting results for developed MR damper with LMRF25

## 6.5 RESULTS AND DISCUSSION

The transient response of SDOF under step input (either positive step or negative step) is observed in the form of displacement and acceleration of the mass in Figure 6.4. The step input theoretically requires the actuator to move from the initial position to the final position instantly, i.e., in zero time which is impossible to achieve practically due to the extreme change in momentum of the actuator piston. However, a good hydraulic system attempts to achieve this within the least time possible with as little overshoot of the input as possible. It can be observed in Figures 6.4a and 6.4c that the MOOG<sup>®</sup> controller, along with the 65 LPM hydraulic powerpack used in this study, takes merely 100 milliseconds to move the actuator from the initial position to its final position with an acceptable overshoot of only 2mm.

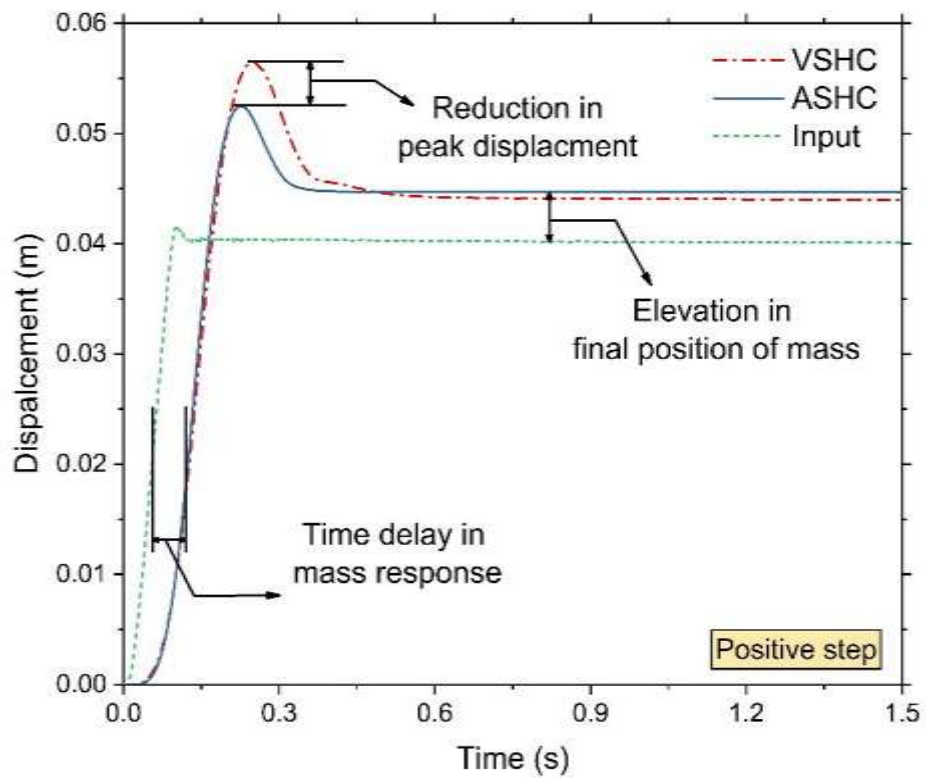
The percentage reduction in displacement and acceleration is calculated using equations 6.6 and 6.7, respectively.

$$\text{Percentage reduction in displacement} = \frac{d_{VSHC} - d_{ASHC}}{d_{VSHC}} \times 100 \quad (6.6)$$

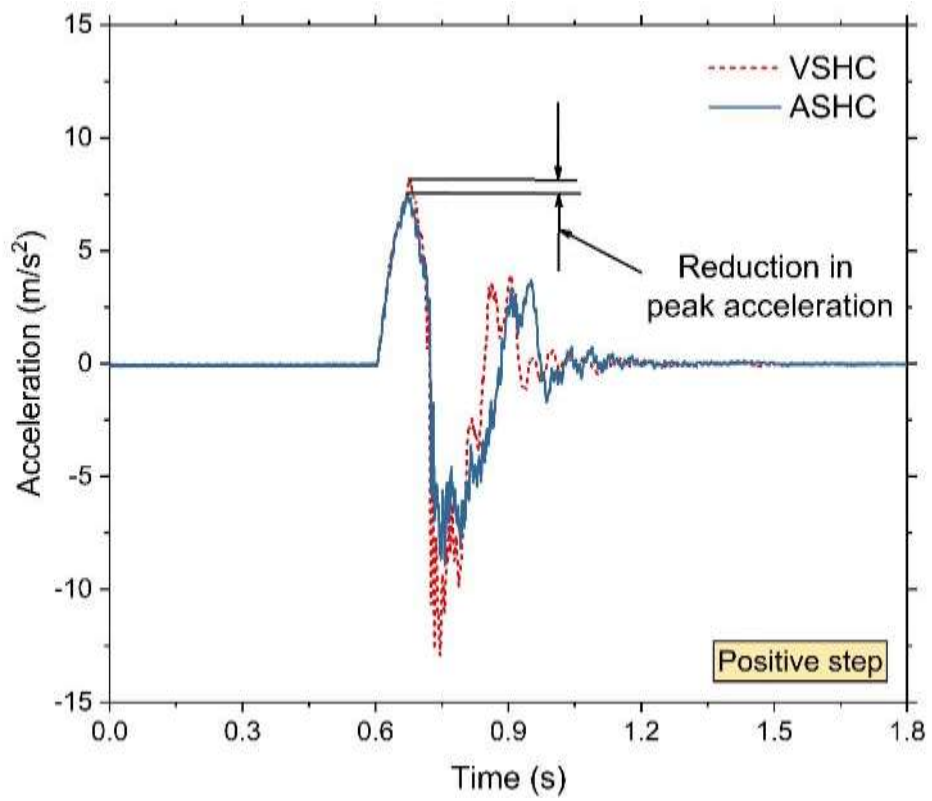
$$\text{Percentage reduction in acceleration} = \frac{a_{VSHC} - a_{ASHC}}{a_{VSHC}} \times 100 \quad (6.7)$$

Where  $d$  and  $a$  are the displacement and acceleration of the mass, in the case of positive step or negative step, they refer to the peak displacement and acceleration. In case of the response of the mass under Sine – 1 and Sine-2 input, they refer to the amplitude of displacement and acceleration. The percentage reduction in peak displacement and peak acceleration has been listed in Table 6.2

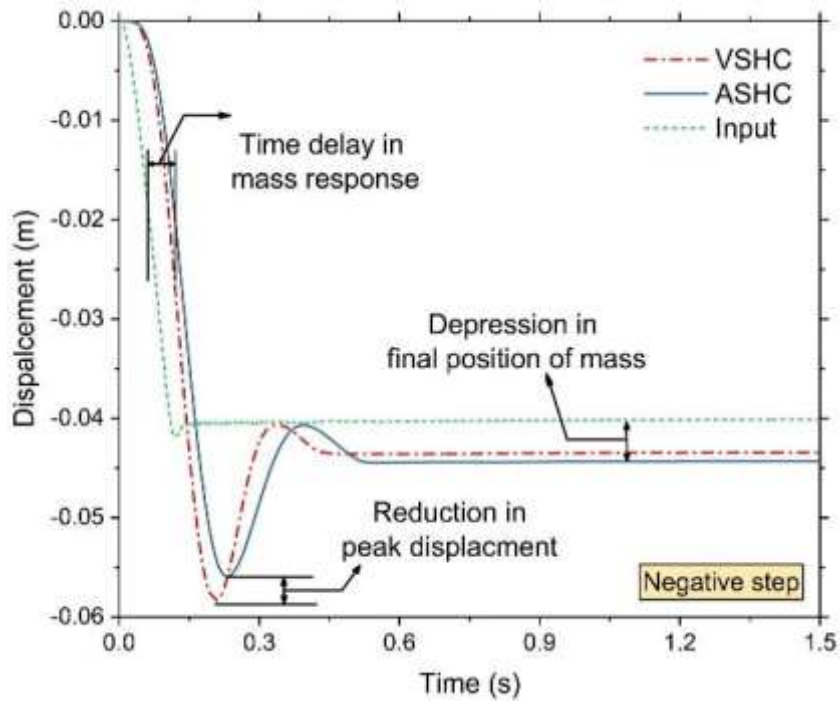




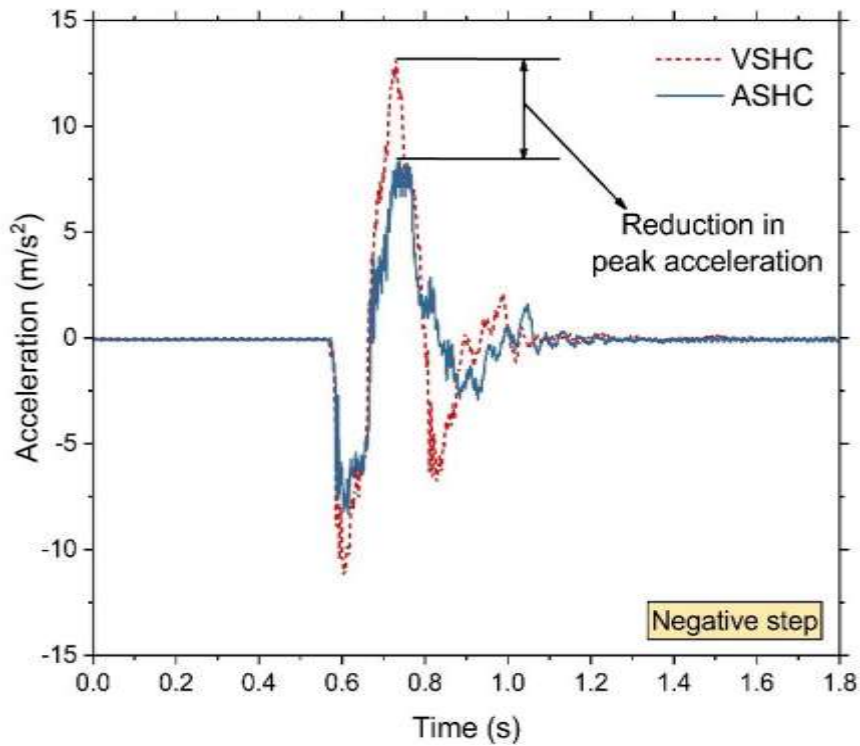
(a)



(b)



(c)



(d)

Figure 6.4 (a) Displacement of mass under positive step input (b) Acceleration of mass under positive step input (c) Displacement of mass under negative step input (d) Acceleration of mass under negative step input

Table 6.2 Improvement in peak displacement and acceleration with ASHC

Input type	Displacement response			Acceleration response		
	VSHC (m)	ASHC (m)	Percentage reduction	VSHC (m/s <sup>2</sup> )	ASHC (m/s <sup>2</sup> )	Percentage reduction
Positive step	0.036	0.032	11%	8.044	7.455	7%
Negative step	0.035	0.032	7%	11.085	8.240	25.66%

It can be observed from Figure 6.4a, Figure 6.4b and Table 6.2 that the mass's peak displacement and acceleration during the positive step were reduced by 11% and 7%, respectively, when the ASHC was implemented. During the negative step, as observed in Figure 6.4c, Figure 6.4c and Table 6.2, the reduction in peak displacement and acceleration was 7% and 25.66%, respectively, when the ASHC was implemented. The mass's settling time reduced by approximately 200 milliseconds with implementation of ASHC during positive step and by approximately 100 milliseconds during the negative step.

The sinusoidal input was used to observe the continuous response of the system with VSHC and ASHC. The response of mass as displacement and acceleration under each type of sine wave can be seen in Figure 6.5. The response of a system subjected to sinusoidal excitation will also be sinusoidal. Hence, the amplitude of mass displacement and acceleration are considered the performance indices to evaluate the effectiveness of each control strategy under this type of excitation. The percentage reduction in amplitude of mass under each type of sine wave input calculated using equations 6.6 and 6.7 has been listed in Table 6.3.

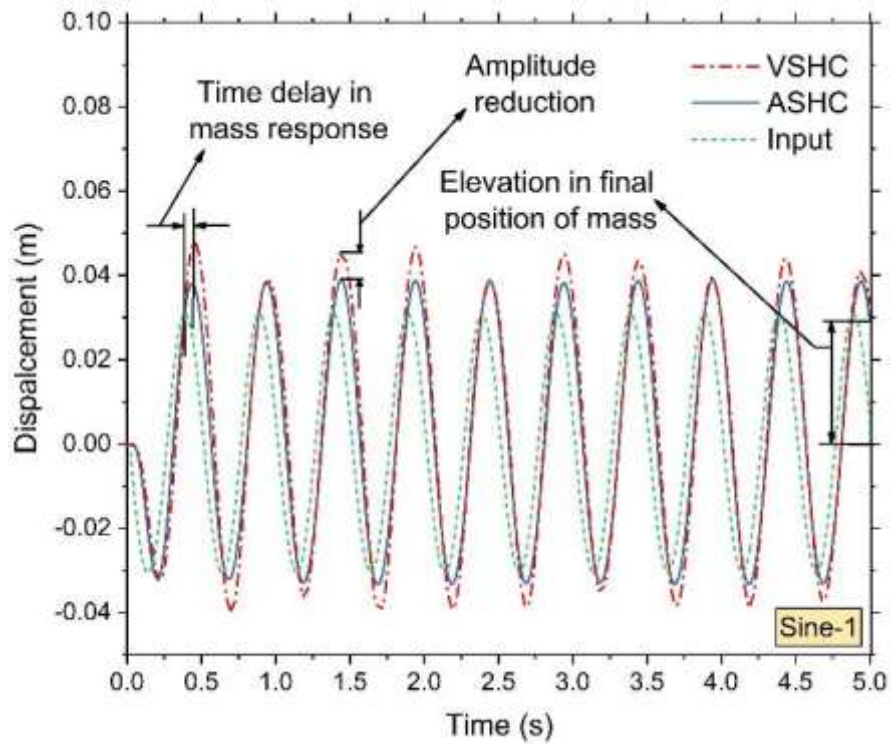
It can be observed in Figure 6.5a, Figure 6.5b and Table 6.3 that under the Sine-1 input, the amplitude of the mass displacement and acceleration reduced by 21.8% and 24.23%, respectively, when ASHC was implemented.

Table 6.3 Improvement in displacement and acceleration amplitude with ASHC

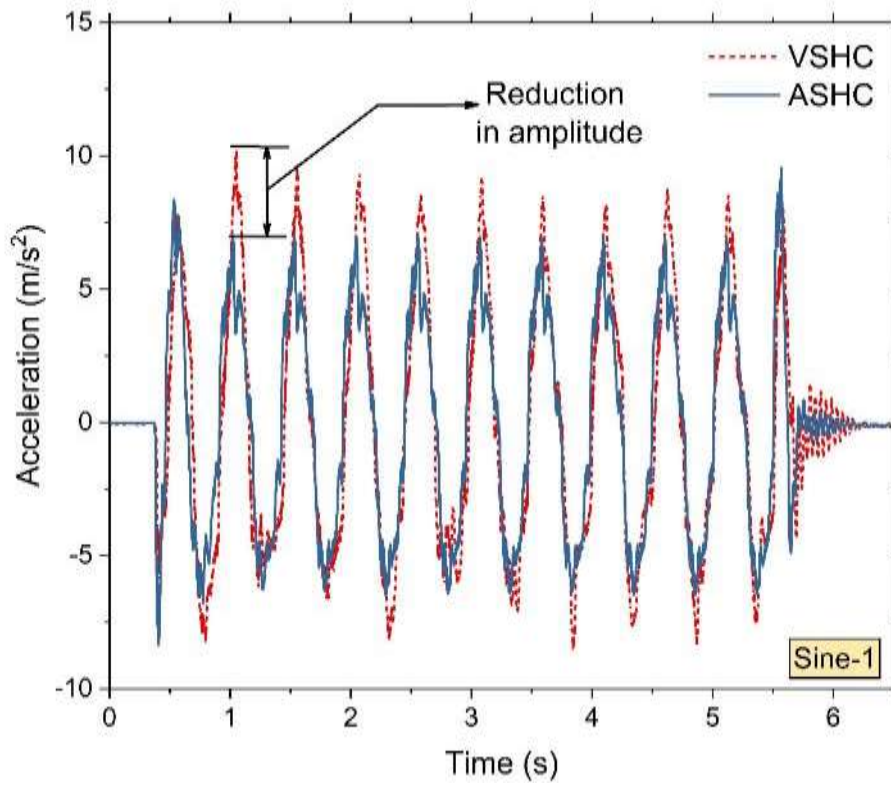
Input type	Displacement response			Acceleration response		
	VSHC (m)	ASHC (m)	Percentage reduction	VSHC (m/s <sup>2</sup> )	ASHC (m/s <sup>2</sup> )	Percentage reduction
Sine-1	0.044	0.034	21.8%	9.1046	6.898	24.23%
Sine-2	0.008	0.005	34.06%	12.759	7.672	39.86%

It is evident from Figure 6.5c, Figure 6.5d and Table 6.3 that, under Sine-2 input, the ASHC improved mass displacement by 34.06% and acceleration by 39.86%. The ASHC outperforms VSHC in transient and continuous responses of an SDOF system. Further, it can be observed, in Table 6.3, that the reduction in amplitude of mass response (either displacement or acceleration) under Sine-2 input is larger than the response under Sine-1 input, suggesting that the ASHC strategy is more effective under high-frequency excitation.

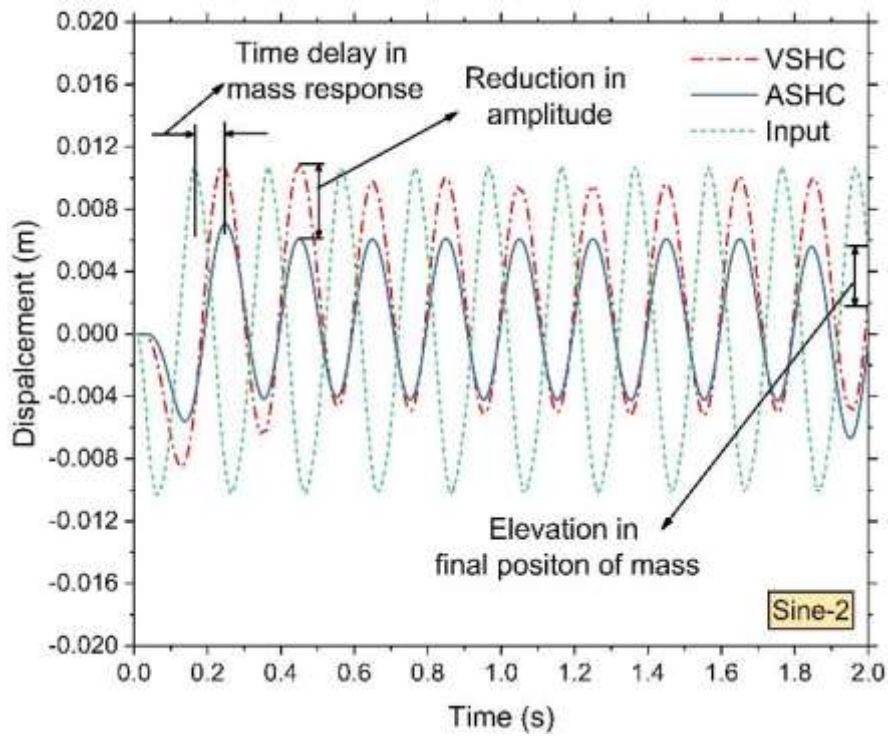
It can be observed in Figures 6.4a, 6.4c, 6.5a and 6.5c that there is a time delay of 20 to 40 milliseconds between the input and the mass response. The time delay under the Sine-1 excitation in Figure 6.5a has caused a phase shift between the input and the mass response. The phase shift increases under Sine-2 excitation to the extent that mass response becomes completely out of phase with the input, as observed in Figure 6.5c. This phenomenon occurs as result of choosing the excitation frequency close to one of the octaves of the undamped natural frequency of the SDOF system, which is calculated to be 2.8Hz. It can be rectified either by retaining the system parameters (mass and spring) or by changing the excitation frequency. The frequency of Sine-2 input was chosen such that there is sufficient suspension deflection to observe appreciable mass response and control strategy response. Although there is a phase shift between the input and the mass response, there is no phase shift between the displacement responses of the mass with ASH and with VSH in Figure 6.5. Hence it can be inferred that the phase shift between the input and the mass displacement response does not affect the performance of either of the control strategies.



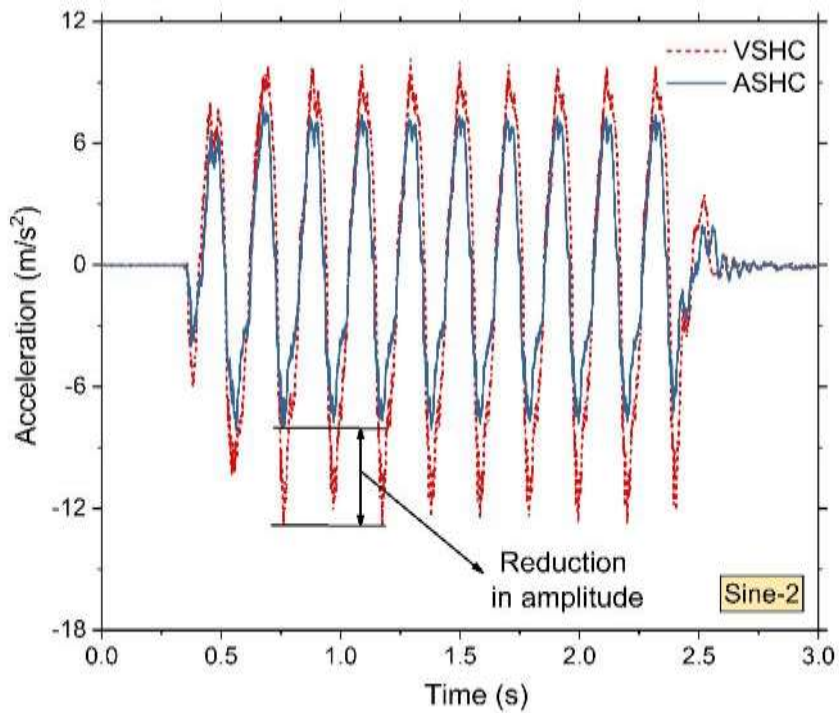
(a)



(b)



(c)



(d)

Figure 6.5 (a) Displacement of mass under Sine-1 input (b) Acceleration of mass under Sine-1 input (c) Displacement of mass under Sine-2 input (d) Acceleration of mass under Sine-2 input



It can also be observed in Figures 6.4a, 6.4c, 6.5a and 6.5c that the final position of mass is slightly higher (in case of positive step) or lower (in case of negative step) than the actuator (input). This behavior can be attributed to the friction between the piston rod and the seal, the friction between the mass and the rigid frame and also the friction due to the MR fluid itself. The friction due to MR fluid can be observed in the form of resistive force by the damper at zero velocity in Figure 5.10. It can also be inferred from Figures 6.4a, 6.4c, 6.5a and 6.5c that, since the difference between the final position of the mass with each control strategy is minimal, the effect of these frictional forces on the performance of control strategies is also minimal. The transient response of the mass can be observed once again at the end of the continuous excitation (both Sine-1 and Sine-2) in Figures 6.5b and 6.5d.

A comparison of the reaction time of the two control strategies, shown in Figure 6.6, reveals an improved reaction time of the semiactive suspension system with the implementation of ASHC compared to that of VSHC.

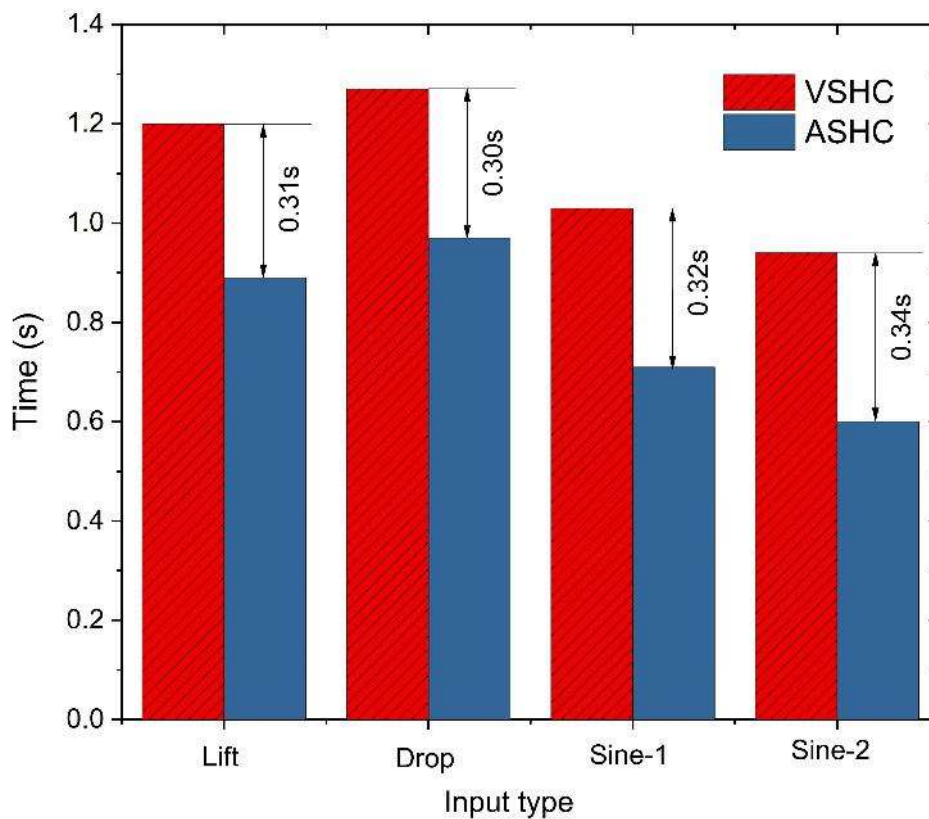


Figure 6.6 Reaction time of ASHC and VSHC

The improvement in the reaction time of the control strategy is in the order of a hundred milliseconds. However, because MR dampers have their reaction time also in milliseconds (“LORD Corporation”, 2022), improvement in the reaction time of the control strategy affects the overall performance of the semi-active suspension system.

## **6.6 SUMMARY**

This chapter proposes an ASHC to improve computational efficiency without compromising performance. The proposed control strategy is experimentally evaluated and simulated using an experimental setup of an SDOF system with an MR damper under different types of inputs. The performance of the proposed control strategy is compared with its conventional counterpart both experimentally and through simulation. The experimental setup of the SDOF is subjected to an upward step and a downward step to study its transient response. The peak mass displacement and acceleration are considered performance indices. The experimental setup of the SDOF is subjected to two types of sinusoidal waves, one with high frequency-low amplitude and the other with low frequency and high amplitude, to study its continuous response. The mass displacement and acceleration amplitude were considered the performance indices in this case. The ASHC outperformed the VSHC under each type of excitation by delivering lower mass displacement and acceleration. The simulation of SDOF with MR damper implementing ASHC and VSHC was also carried out under the same excitations used in the experiment to evaluate the reaction time of each control strategy. The ASHC also outperformed the VSHC in simulation by improving the reaction by at least 300ms. Although the improvement is very small, the overall reaction time of the semiactive suspension system will improve, considering the reaction time of the MR dampers is also in the range of a hundredth of a second.



## CHAPTER 7

### SUMMARY AND CONCLUSIONS

#### 7.1 SUMMARY

The research work presented in this thesis develops a cost-effective monotube MR damper and experimentally evaluates its performance in the laboratory and on the test vehicle in real time. An automobile MR damper is developed, and its performance is evaluated in the damper testing machine and the test vehicle while implementing current control strategies to improve ride comfort and road handling. An MR fluid is designed considering the cost of the synthesis, and the performance of the optimized fluid is compared against a commercial MR fluid based on the results from the rheometer, the damper testing machine and the test vehicle suspension response. An acceleration-based current control strategy is also proposed, whose performance is evaluated based on the response of an SDOF system experimentally and through simulation. The significant contributions of this dissertation research are as follows:

##### 7.1.1 Experimental evaluation and mathematical modelling of commercial MR damper

A commercial MR damper, RD-8041-1, manufactured by LORD Corporation, USA, is experimentally evaluated on the damper testing machine by subjecting it to sinusoidal excitation. The amplitude and frequency of the sinusoidal excitation were decided based on the specifications supplied by the manufacturer. The excitation amplitude is fixed at 20mm, and the frequency is varied to achieve velocity amplitude varying from 0.05m/s to 0.2m/s. The procedure is repeated while varying the current supplied to the MR damper from 0A to 1A. The damping behavior of the MR damper is presented in the form of a characteristic graph using the force and velocity data obtained during the experiment on the damper testing machine. The MR damper delivered a damping force that is both current and velocity dependent. The damping behavior of the MR damper was modeled using an MFM. The MFM was previously employed for this purpose; however, it was assumed that all its coefficients are current dependent. The research work presented in this thesis rather attempts to determine the

current dependent coefficients through a curve fitting technique to improve the computational efficiency of the model without compromising its accuracy to represent the damping behavior of the damper. The accuracy and computational efficiency of the MFM are compared with an existing model, EDM, based on the response of a QCM with a semi-active seat suspension system. The QCM is subjected to random road input with profiles ranging from an off-road to a highway pavement with a varying forward velocity.

### **7.1.2 Design and experimental evaluation of a cost-effective monotube MR damper for application in passenger van**

An MR damper is designed for application in the Force Motor's – Traveller test vehicle. The flow mode of operation of the MR fluid and a floating piston-type accumulator were found to be suitable for this application. The MR damper is designed by optimizing the piston dimensions to maximize the magnetic flux generated at the fluid flow gap while fulfilling the spatial requirements of the existing stock passive damper and the magnetization limits of the piston component materials and the MR fluid. The optimization is carried out using the `fmincon` algorithm in the Optimization Toolbox™ of MATLAB R2018b. The resulting dimensions are used to fabricate the damper and evaluate its performance on the damper testing machine. The MR damper is further evaluated in real-time by installing it on the test vehicle while implementing on-off skyhook and ground hook control. The test vehicle is run over a sharp speedbump at speeds of 10km/h and 20km/h. The peak acceleration of the vehicle body and the wheel is used as a performance index to determine improvement in ride comfort and road handling of the test vehicle with the developed MR damper as compared to passive damper.

### **7.1.3 Design of cost-effective MR fluid and its experimental evaluation**

The cost evaluation of the developed MR damper also revealed that the cost of MR fluid forms the largest portion of the overall cost of an MR damper. Therefore, the MR damper cost can be further reduced by reducing the cost of MR fluid without compromising the fluid performance. Designing an MR fluid generally involves optimizing the volume fraction of the magnetic particles to be mixed in the carrier fluid.

In this study, ten samples of MR fluids are prepared using CIP of two different sizes and five different volume fractions of CIP in the silicon oil carrier fluid. The rheological properties of each MR fluid sample are studied by obtaining their flow curves under different magnetic field strengths in a rotational parallel plate-type rheometer. The rheological properties of each MR fluid sample are used to predict the damping force generated by them in the developed MR damper. The predicted damping force is then modeled using the MFM to represent the damping behavior of the developed MR damper with each MR Fluid sample in the simulation of the full car model of the test vehicle subjected to a very bad random road profile. The peak value of the FFT of the simulation response of the full car model of the test vehicle is considered the performance index for each MR fluid sample. The cost of each MR fluid sample is also evaluated. The issue of improving ride comfort and minimizing the cost of the MR fluid are two conflicting criteria that have been solved as an optimization problem by employing the RSM technique, in this study. The performance of the optimal MR fluid is compared with the commercial MR fluid, MRF-132DG, using the rheometer, in the damper testing machine and the test vehicle.

#### **7.1.4 Experimental evaluation and simulation of ASHC**

An ASHC was also proposed in this research work to improve the reaction time of the semiactive system without compromising the performance of the semiactive control strategy. The ASHC and the existing VSHC are evaluated based on the experimental and simulation response of an SDOF system with an MR damper. The effectiveness of the ASHC is determined by subjecting the SDOF experimental setup to step and sinusoidal input. The step input examines the system's transient response, and the sinusoidal input examines the continuous response of the SDOF. The peak mass displacement and acceleration are used as the performance index under step input. The amplitude of the displacement and acceleration is used as the performance index under sinusoidal excitation. The computational efficiency of the ASHC is compared against VSHC by simulating the SDOF system in MATLAB under the same excitations used in the experiment.

## 7.2 CONCLUSIONS

The significant conclusions drawn from the research work, summarized in the previous section, are as follows:

- The RMS acceleration of the passenger mass, obtained during simulation of QCM with semiactive seat suspension, plotted against the forward vehicle speeds on different road profiles revealed that the semiactive suspension system could improve the ride comfort of the passengers as compared to the stock passive dampers.
- The response of QCM with MFM was very similar to the one with EDM, indicating that the MFM is as accurate as the existing EDM.
- The comparison of execution time of the MATLAB programs of QCM with MFM and EDM revealed that the MFM was faster than EDM by 50 to 100ms. Although the improvement in computational time may be minimal, it should be noted that the reaction time of this damper is also in milliseconds. A minimal improvement in the reaction time of the damper could improve the overall performance of the semiactive system.
- The MR damper developed in collaboration with Rambal Ltd. delivered desirable damping force with no signs of leakage or other issues, indicating the robustness of the design and fabrication methodology.
- The developed MR damper is successfully able to improve the ride comfort and road handling of the test vehicle over a sharp speed bump as compared to the passive damper at the tested vehicle speeds.
- The calculated cost of developing the said MR damper indicated its cost effectiveness compared to the commercial MR damper available in the Indian automobile market, even after employing commercial MR fluid in the developed MR damper.
- The rheological performance analysis of the synthesized MR fluid samples on the rheometer revealed increasing field dependent yields stress with increasing volume fraction of CIP in the sample.

- The cost analysis of MR fluid samples revealed increasing cost with increasing volume fraction of the CIP as it is the costliest item that goes into making of MR fluids.
- Simulated response of the test vehicle model featuring the developed MR damper functioning with the synthesized MR fluid samples revealed increasing ride comfort with increasing volume fraction of CIP indicating increasing ride comfort with increasing cost of the MR fluid.
- The developed MR fluid, optimized while taking cost of synthesis into consideration, costs 70.74% less than the commercial MR fluid, MRF-132DG.
- The optimized MR fluid, LMRF25 exhibits higher field dependent yield stress than the MRF-132DG under the influence of magnetic flux of same field strength, as observed in Rheometer.
- The developed MR damper with LMRF25 delivers a higher damping force than with the MRF-132DG.
- The semiactive suspension system of the test vehicle featuring LMRF25 provided higher ride comfort and road handling than the one featuring MRF-132DG over the test tracks and vehicle speeds employed in the study.
- The experimental evaluation of a SDOF with MR damper revealed that the proposed ASHC was successful in improving its transient and continuous response as compared to the conventional VSHC.
- The simulation of the SDOF with MR damper featuring ASHC was found to be at least 300ms faster than the conventional VSHC. indicating it would improve the overall performance of the semi-active suspension system.

### **7.3 SCOPE OF FUTURE WORK**

In the present work, a commercial MR damper was characterized and mathematically modeled. A monotube MR damper featuring a flow mode piston was designed and tested on the damper testing machine and the test vehicle. A cost-effective MR fluid was also optimized, whose performance was compared with the commercial MR fluid using the rheometer, damper testing machine and test vehicle. A computationally efficient acceleration-based current control strategy was also presented in this research work. The study can be further extended as follows:

- The cost of the piston component materials can be used as a design variable during the optimization stage rather than at the end of fabrication.
- A multi-coil MR damper piston can also be proposed to improve the damper's controllable force without affecting the working stroke of the vehicle suspension.
- The test vehicle can be run on test tracks with potholes and bumps to determine the rolling and pitching performance of the suspension with the prototype MR damper.
- The advantage of an acceleration based control strategy can be effectively quantified by experimentally determining its reaction time.
- Reliability tests and thermal performance evaluation of the MR dampers and MR fluids can also be taken up in the future.

## REFERENCES

- Acharya, S., Saini, T. R. S., and Kumar, H. (2019). "Determination of optimal magnetorheological fluid particle loading and size for shear mode monotube damper." *J. Brazilian Soc. Mech. Sci. Eng.*, 41(10), 1–15.
- Acharya, S., Saini, T. R. S., Sundaram, V., and Kumar, H. (2021). "Selection of optimal composition of MR fluid for a brake designed using MOGA optimization coupled with magnetic FEA analysis." *J. Intell. Mater. Syst. Struct.*, 32(16), 1831–1854.
- Ahmadian, M., and Gravatt, J. (2004). "A comparative analysis of passive twin tube and skyhook MRF dampers for motorcycle front suspensions." *Smart Struct. Mater. 2004 Damping Isol.*, 5386, 238.
- Ahmadian, M., and Simon, D. E. (2003). "An analytical and experimental evaluation of magneto rheological suspensions for heavy trucks." *Veh. Syst. Dyn.*, 37(SUPPL.), 38–49.
- Ai, H. X., Wang, D. H., and Liao, W. H. (2006). "Design and modeling of a magnetorheological valve with both annular and radial flow paths." *J. Intell. Mater. Syst. Struct.*, 17(4), 327–334.
- Aruna, M. N., Rahman, M. R., Joladarashi, S., kumara, H., Meena, S. S., Sarkar, D., and Umesh, C. K. (2022). "A study on magnetorheological and sedimentation properties of soft magnetic Fe58Ni42 particles." *J. Magn. Magn. Mater.*, 563(April), 169934.
- Ashtiani, M., Hashemabadi, S. H., and Ghaffari, A. (2015). "A review on the magnetorheological fluid preparation and stabilization." *J. Magn. Magn. Mater.*, 374, 711–715.
- Atray, V. S., and Roschke, P. N. (2003). "Design, fabrication, testing, and fuzzy modeling of a large magnetorheological damper for vibration control in a railcar." *Proc. IEEE/ASME Jt. Railr. Conf.*, 223–229.
- Atray, V. S., and Roschke, P. N. (2004). "Neuro-fuzzy control of railcar vibrations

using semiactive dampers.” *Comput. Civ. Infrastruct. Eng.*, 19(2), 81–92.

Aydar, G., Wang, X., and Gordaninejad, F. (2010). “A novel two-way-controllable magneto-rheological fluid damper.” *Smart Mater. Struct.*, 19(6).

Bai, X. X., Wang, D. H., and Fu, H. (2013). “Principle, modeling, and testing of an annular-radial-duct magnetorheological damper.” *Sensors Actuators, A Phys.*, 201, 302–309.

Bakker, E., Nyborg, L., and Pacejka, H. B. (1987). “Tyre Modelling for Use in Vehicle Dynamics Studies.”

Bakker, E., Pacejka, H. B., and Lidner, L. (1989). “A New Tire Model with an Application in Vehicle Dynamics Studies.” *SAE Int.*, 890087.

Boada, M. J. L., Boada, B. L., and Diaz, V. (2017). “A novel frequency dependent model based on trigonometric functions for a magnetorheological damper.” *Meccanica*, 52(11–12), 2567–2581.

Bui, Q., Nguyen, Q. H., Bai, X. ‘Frank,’ and Mai, D. (2020). “A new hysteresis model for magneto–rheological dampers based on Magic Formula.” *Proc. Inst. Mech. Eng. Part C J. Mech. Eng. Sci.*, 1–15.

Burton, S. A., Makris, N., Konstantopoulos, I., and Antsaklis, P. J. (1996). “Modeling the Response of ER Damper: Phenomenology and Emulation.” *J. Eng. Mech.*, 122(9), 897–906.

Canudas-de-Wit, C. (1998). “Comments on ‘A new model for control of systems with friction.’” *IEEE Trans. Automat. Contr.*, 43(8), 1189–1190.

Cao, M., Wang, K. W., and Lee, K. Y. (2008). “Scalable and invertible PMNN model for MagnetoRheological fluid dampers.” *JVC/Journal Vib. Control*, 14(5), 731–751.

Carlson, J. D., and Weiss, K. D. (1995). “Magnetorheological Materials Based on Alloy Particles.” United States.

Chandiramani, N. K., and Motra, G. B. (2013). “Lateral-torsional response control of MR damper connected buildings.” *ASME Int. Mech. Eng. Congr. Expo. Proc.*, 4 B.



- Chang, C.-C., and Zhou, L. (2002). “Neural Network Emulation of Inverse Dynamics for a Magnetorheological Damper.” *J. Struct. Eng.*, 128(2), 231–239.
- Chang, C. C., and Roschke, P. (1998). “Neural network modeling of a magnetorheological damper.” *J. Intell. Mater. Syst. Struct.*, 9(9), 755–764.
- Chiriac, H., and Stoian, G. (2010). “Influence of particle size distributions on magnetorheological fluid performances.” *J. Phys. Conf. Ser.*, 200(SECTION 7).
- Choi, S. B., and Han, Y. M. (2007). “Vibration control of electrorheological seat suspension with human-body model using sliding mode control.” *J. Sound Vib.*, 303(1–2), 391–404.
- Choi, S. B., Lee, S. K., and Park, Y. P. (2001). “A hysteresis model for the field-dependent damping force of a magnetorheological damper.” *J. Sound Vib.*, 245(2), 375–383.
- Choi, S. B., Song, H. J., Lee, H. H., Lim, S. C., Kim, J. H., and Choi, H. J. (2003). “Vibration control of a passenger vehicle featuring magnetorheological engine mounts.” *Int. J. Veh. Des.*, 33(1–3), 2–16.
- Chooi, W. W., and Olutunde Oyadiji, S. (2009a). “Mathematical modeling, analysis, and design of magnetorheological (MR) dampers.” *J. Vib. Acoust. Trans. ASME*, 131(6), 0610021–06100210.
- Chooi, W. W., and Olutunde Oyadiji, S. (2009b). “Experimental testing and validation of a magnetorheological (MR) damper model.” *J. Vib. Acoust. Trans. ASME*, 131(6), 0610031–06100310.
- Chooi, W. W., and Oyadiji, S. O. (2008). “Design, modelling and testing of magnetorheological (MR) dampers using analytical flow solutions.” *Comput. Struct.*, 86(3–5), 473–482.
- Conn, A. R., Scheinberg, K., and Vicente, L. N. (2005). *INTRODUCTION TO DERIVATIVE-FREE OPTIMIZATION*. Soc. Ind. Appl. Math. Philadelphia.
- Deep, G., Rajora, V., and Singh, I. (2016). “Synthesis and Sedimentation analysis of Magnetorheological Fluids.” *Adv. Simul. Exp. Tech. Mech. Eng.*, 253–257.

- Desai, R. M., Jamadar, M. e. H., Kumar, H., and Joladarashi, S. (2021). “Performance Evaluation of a Single Sensor Control Scheme Using a Twin-Tube MR Damper Based Semi-active Suspension.” *J. Vib. Eng. Technol.*, 9(6), 1193–1210.
- Desai, R. M., Jamadar, M. E. H., Kumar, H., Joladarashi, S., and Raja Sekaran, S. C. (2019). “Design and experimental characterization of a twin-tube MR damper for a passenger van.” *J. Brazilian Soc. Mech. Sci. Eng.*, 41(8).
- Dixon, J. C. (2007). *The shock absorber handbook (Second Edition)*.
- Dixon, J. C. (2009). *Suspension Geometry and Computation*. Wiltshire: John Wiley & Sons Ltd.
- Dominguez, A., Sedaghati, R., and Stiharu, I. (2004). “Modelling the hysteresis phenomenon of magnetorheological dampers.” *Smart Mater. Struct.*, 13(6), 1351–1361.
- Dominguez, A., Sedaghati, R., and Stiharu, I. (2006a). “A new dynamic hysteresis model for magnetorheological dampers.” *Smart Mater. Struct.*, 15(5), 1179–1189.
- Dominguez, A., Sedaghati, R., and Stiharu, I. (2006b). “Semi-active vibration control of adaptive structures using magnetorheological dampers.” *AIAA J.*, 44(7), 1563–1571.
- Dominguez, A., Sedaghati, R., and Stiharu, I. (2008). “Modeling and application of MR dampers in semi-adaptive structures.” *Comput. Struct.*, 86(3–5), 407–415.
- Du, H., Lam, J., and Zhang, N. (2006). “Modelling of a magneto-rheological damper by evolving radial basis function networks.” *Eng. Appl. Artif. Intell.*, 19(8), 869–881.
- Du, H., Li, W., and Zhang, N. (2012). “Integrated seat and suspension control for a quarter car with driver model.” *IEEE Trans. Veh. Technol.*, 61(9), 3893–3908.
- Du, X., Yu, M., Fu, J., and Huang, C. (2020). “Experimental study on shock control of a vehicle semi-active suspension with magneto-rheological damper.” *Smart Mater. Struct.*, 29(7), 074002.
- Dyke, S. J., Spencer, B. F., Sain, M. K., and Carlson, J. D. (1996). “Modeling and control of magnetorheological dampers for seismic response reduction.” *Smart Mater. Struct.*, 5(5), 565–575.

- Gamota, D. R., and Filisko, F. E. (2010). “Dynamic mechanical studies of electrorheological materials : Moderate frequencies.” 399(1991).
- Gavin, H., Hoagg, J., and Dobossy, M. (2001). “Optimal Design for Magnetorheological Dampers.” *Proc. U.S.-Japan Work. Smart Struct. Improv. Seism. Perform. Urban Reg.*, (August), 225–236.
- Genç, S., and Phulé, P. P. (2002). “Rheological properties of magnetorheological fluids.” *Smart Mater. Struct.*, 11(1), 140–146.
- Ginder, J. M., Davis, L. C., and Elie, L. D. (1996). “Rheology Of Magnetorheological Fluids: Models And Measurements.” *Int. J. Mod. Phys. B*, 10(23n24), 3293–3303.
- Gołdasz, J., and Sapiński, B. (2015). “Configurations of MR Dampers.” *Insight into Magnetorheol. Shock Absorbers*, Cham: Springer International Publishing, 25–49.
- Goncalves, F. D. (2005). “Characterizing the Behavior of Magnetorheological Fluids at High Velocities and High Shear Rates.” Virginia Polytechnic Institute and State University, Blacksburg, Virginia.
- Goncalves, F. D., Ahmadian, M., and Carlson, J. D. (2006). “Investigating the magnetorheological effect at high flow velocities.” *Smart Mater. Struct.*, 15(1), 75–85.
- “Google Earth.” (2022). .
- Gurubasavaraju, T. M., Kumar, H., and Arun, M. (2017a). “Evaluation of optimal parameters of MR fluids for damper application using particle swarm and response surface optimisation.” *J. Brazilian Soc. Mech. Sci. Eng.*, 39(9), 3683–3694.
- Gurubasavaraju, T. M., Kumar, H., and Arun, M. (2017b). “Optimisation of monotube magnetorheological damper under shear mode.” *J. Brazilian Soc. Mech. Sci. Eng.*, 39(6), 2225–2240.
- He, L., Qin, G., Zhang, Y., and Chen, L. (2008). “Non-stationary random vibration analysis of vehicle with fractional damping.” *Proc. - Int. Conf. Intell. Comput. Technol. Autom. ICICTA 2008*, 2, 150–157.
- “Hitachi Cables America Incorporated.” (2022). <[https://www.hca.hitachicable.com/products/hca/faq/data/Current-Carrying-Capacity\\_Jan2012.pdf](https://www.hca.hitachicable.com/products/hca/faq/data/Current-Carrying-Capacity_Jan2012.pdf)> (Dec. 21,

2022).

Hong, K. S., Sohn, H. C., and Hedrick, J. K. (2002). “Modified skyhook control of semi-active suspensions: A new model, gain scheduling, and hardware-in-the-loop tuning.” *J. Dyn. Syst. Meas. Control. Trans. ASME*, 124(1), 158–167.

Hong, S. R., John, S., Wereley, N. M., Choi, Y. T., and Choi, S. B. (2008). “A unifying perspective on the quasi-steady analysis of magnetorheological dampers.” *J. Intell. Mater. Syst. Struct.*, 19(8), 959–976.

Hu, G., Liu, F., Xie, Z., and Xu, M. (2016). “Design, Analysis, and Experimental Evaluation of a Double Coil Magnetorheological Fluid Damper.” *Shock Vib.*, 2016.

Hu, W., and Wereley, N. M. (2008). “Hybrid magnetorheological fluid-elastomeric lag dampers for helicopter stability augmentation.” *Smart Mater. Struct.*, 17(4).

Ierardi, R. F., and Bombard, A. J. F. (2009). “Off-state viscosity and yield stress optimization of magneto-rheological fluids: A mixture design of experiments approach.” *J. Phys. Conf. Ser.*, 149, 012037.

Iglesias, G. R., Roldán, A., Reyes, L., Rodríguez-Arco, L., and Durán, J. D. G. (2015). “Stability behavior of composite magnetorheological fluids by an induction method.” *J. Intell. Mater. Syst. Struct.*, 26(14), 1836–1843.

Ikhouane, F., and Dyke, S. J. (2007). “Modeling and identification of a shear mode magnetorheological damper.” *Smart Mater. Struct.*, 16(3), 605–616.

Jazar, R. N. (2014). *Vehicle Dynamics*. Springer, New York, NY: Springer New York.

Jiménez, R., and Álvarez-Icaza, L. (2005). “LuGre friction model for a magnetorheological damper.” *Struct. Control Heal. Monit.*, 12(1), 91–116.

Jiménez, R., and Alvarez, L. (2002). “Real time identification of structures with magnetorheological dampers.” *Proc. IEEE Conf. Decis. Control*, 1, 1017–1022.

Kamath, G. M., and Wereley, N. M. (1997). “A nonlinear viscoelastic - plastic model for electrorheological fluids.” *Smart Mater. Struct.*, 6(3), 351–359.

Kamath, G. M., Wereley, N. M., and Jolly, M. R. (1999). “Characterization of

- Magnetorheological Helicopter Lag Dampers.” *J. Am. Helicopter Soc.*, 44(3), 234–248.
- Kamath, G. M., and Werely, N. M. (1997). “Nonlinear Viscoelastic-Plastic Mechanisms-Based Model of an Electrorheological Damper.” *J. Guid. Control. Dyn.*, 20(6), 1125–1132.
- Karnopp, D., Crosby, M. J., and Harwood, R. A. (1974). “Vibration Control Using Semi-Active Force Generators.” *J. Eng. Ind.*, 96(2), 619.
- Kasprzyk, J., Krauze, P., Budzan, S., and Rzepecki, J. (2017). “Vibration control in semi-active suspension of the experimental off-road vehicle using information about suspension deflection.” *Arch. Control Sci.*, 27(2), 251–261.
- Kim, B., and Roschke, P. N. (1999). “Linearization of magnetorheological behaviour using a neural network.” *Proc. 1999 Am. Control Conf. (Cat. No. 99CH36251)*, IEEE, 4501–4505 vol.6.
- Kim, H. S., and Roschke, P. N. (2006). “Fuzzy control of base-isolation system using multi-objective genetic algorithm.” *Comput. Civ. Infrastruct. Eng.*, 21(6), 436–449.
- Kim, K. J., Lee, C. W., and Koo, J. H. (2008). “Design and modeling of semi-active squeeze film dampers using magneto-rheological fluids.” *Smart Mater. Struct.*, 17(3).
- Kim, Y., Choi, S., Lee, J., Yoo, W., and Sohn, J. (2011). “Damper modeling for dynamic simulation of a large bus with MR damper.” *Int. J. Automot. Technol.*, 12(4), 521–527.
- Kopylov, S., Chen, Z. B., and Abdelkareem, M. A. A. (2020). “Acceleration based ground-hook control of an electromagnetic regenerative tuned mass damper for automotive application.” *Alexandria Eng. J.*, 59(6), 4933–4946.
- Kordonsky, W. (1993). “Elements and Devices Based on Magnetorheological Effect.” *J. Intell. Mater. Syst. Struct.*, 4(1), 65–69.
- Krauze, P., and Kasprzyk, J. (2014). “Vibration control for an experimental off-road vehicle using magnetorheological dampers.” *Vibroengineering Procedia*, 306–312.
- Krauze, P., Kasprzyk, J., Kozyra, A., and Rzepecki, J. (2018). “Experimental analysis of vibration control algorithms applied for an off-road vehicle with magnetorheological

dampers.” *J. Low Freq. Noise Vib. Act. Control*, 37(3), 619–639.

Krauze, P., Kasprzyk, J., and Rzepecki, J. (2019). “Experimental attenuation and evaluation of whole body vibration for an off-road vehicle with magnetorheological dampers.” *J. Low Freq. Noise Vib. Act. Control*, 38(2), 852–870.

Krishna, H., Kumar, H., and Gangadharan, K. (2017). “Optimization of Magneto-Rheological Damper for Maximizing Magnetic Flux Density in the Fluid Flow Gap Through FEA and GA Approaches.” *J. Inst. Eng. Ser. C*, 98(4), 533–539.

Kumar Kariganaur, A., Kumar, H., and Arun, M. (2022). “Effect of temperature on sedimentation stability and flow characteristics of magnetorheological fluids with damper as the performance analyser.” *J. Magn. Magn. Mater.*, 555(April), 169342.

Kwok, N. M., Ha, Q. P., Nguyen, T. H., Li, J., and Samali, B. (2006). “A novel hysteretic model for magnetorheological fluid dampers and parameter identification using particle swarm optimization.” *Sensors Actuators, A Phys.*, 132(2), 441–451.

Lam, A. H. F., and Liao, W. H. (2003). “Semi-active control of automotive suspension systems with magneto-rheological dampers.” *Int. J. Veh. Des.*, 33(1–3), 50–75.

Lau, Y., and Wei, L. (2006). “Pressurized magnetorheological fluid dampers.” United States Patent Application Publication.

Lee, D. Y., Choi, Y. T., and Wereley, N. M. (2002). “Performance analysis of ER/MR impact damper systems using Herschel-Bulkley model.” *J. Intell. Mater. Syst. Struct.*, 13(7–8), 525–531.

Li, W. H., Yao, G. Z., Chen, G., Yeo, S. H., and Yap, F. F. (2000). “Testing and steady state modeling of a linear MR damper under sinusoidal loading.” *Smart Mater. Struct.*, 9(1), 95–102.

Li, X., and Li, H. (2004). “Progress of studies on control strategies of magnetorheological dampers for structures.” *J. Disaster Prev. Mitig.*, 24, 335–342.

Lischinsky, P., Canudas-de-Wit, C., and Morel, G. (1999). “Friction Compensation for an Industrial Hydraulic Robot.” *IEEE Control Syst.*, 19(1), 25–32.

Liu, X., Chen, Q., Liu, H., Wang, Z., and Zhao, H. (2016). “Squeeze-strengthening

effect of silicone oil-based magnetorheological fluid.” *J. Wuhan Univ. Technol. Mater. Sci. Ed.*, 31(3), 523–527.

“LORD Corporation.” (n.d.). <<https://www.shoplordmr.com/mr-products/rd-8040-1-mr-damper-short-stroke>> (Nov. 23, 2019).

“LORD Corporation.” (2019). <[https://lordfulfillment.com/pdf/44/DS7015\\_MRF-132DGMRFluid.pdf](https://lordfulfillment.com/pdf/44/DS7015_MRF-132DGMRFluid.pdf)> (Apr. 9, 2022).

Lv, H., Zhang, S., Sun, Q., Chen, R., and Zhang, W. J. (2021). “The Dynamic Models, Control Strategies and Applications for Magnetorheological Damping Systems: A Systematic Review.” *J. Vib. Eng. Technol.*, 9(1), 131–147.

Ma, X. Q., Rakheja, S., and Su, C. Y. (2006). “Relative assessments of current dependent models for magneto-rheological fluid dampers.” *Proc. 2006 IEEE Int. Conf. Networking, Sens. Control. ICNSC’06*, 510–515.

Ma, X. Q., Rakheja, S., and Su, C. Y. (2007). “Development and relative assessments of models for characterizing the current dependent hysteresis properties of magnetorheological fluid dampers.” *J. Intell. Mater. Syst. Struct.*, 18(5), 487–502.

Ma, X. Q., Wang, E. R., Rakheja, S., and Su, C. Y. (2002). “Modeling hysteretic characteristics of MR-fluid damper and model validation.” *Proc. IEEE Conf. Decis. Control*, 2(December), 1675–1680.

Madhavrao Desai, R., Acharya, S., Jamadar, M. E. H., Kumar, H., Joladarashi, S., and Sekaran, S. R. (2020). “Synthesis of magnetorheological fluid and its application in a twin-tube valve mode automotive damper.” *Proc. Inst. Mech. Eng. Part L J. Mater. Des. Appl.*, 234(7), 1001–1016.

MagWeb. (2021). *SMAG Handbook Properties of soft magnetic materials*. Texas, USA.

Makowski, M., and Knap, L. (2018). “Investigation of an off-road vehicle equipped with magnetorheological dampers.” *Adv. Mech. Eng.*, 10(5), 1–11.

Mangal, S. K., and Kumar, A. (2015). “Geometric parameter optimization of magnetorheological damper using design of experiment technique.” *Int. J. Mech. Mater. Eng.*,

10(1), 4.

Mangal, S. K., and Sharma, V. (2017). “Multi-parameter optimization of magnetorheological fluid with high on-state yield stress and viscosity.” *J. Brazilian Soc. Mech. Sci. Eng.*, 39(10), 4191–4206.

Marathe, S., Hatwalane, S., Thorat, S., and Dhokane, N. (2011). “A Review of half-car model vibration system using Magneto rheological Dampers.” *Int. J. Curr. Eng. Technol.*, 4(4), 400–404.

Marins, J. A., Plachý, T., and Kuzhir, P. (2019). “Iron–sepiolite magnetorheological fluids with improved performances.” *J. Rheol. (N. Y. N. Y.)*, 63(1), 125–139.

Moon, S. J., Huh, Y. C., Jung, H. J., Jang, D. D., and Lee, H. J. (2011). “Sub-optimal design procedure of valve-mode magnetorheological fluid dampers for structural control.” *KSCCE J. Civ. Eng.*, 15(5), 867–873.

Morales, A. L., Nieto, A. J., Chicharro, J. M., and Pintado, P. (2018). “A semi-active vehicle suspension based on pneumatic springs and magnetorheological dampers.” *JVC/Journal Vib. Control*, 24(4), 808–821.

Myers, R. H., Montgomery, D. C., and Anderson-Cook, C. M. (1995). *Response surface methodology: process and product optimization using designed experiments*. New Jersey, USA: Wiley and Sons Inc.

Nagiredla, S., Joladarashi, S., and Kumar, H. (2022). “Rheological Properties of the In-house Prepared Magneto-rheological Fluid in the Pre-yield Region.” *Int. J. Eng. Trans. B Appl.*, 35(11), 2238–2246.

Negash, B. A., You, W., Lee, J., Lee, C., and Lee, K. (2021). “Semi-active control of a nonlinear quarter-car model of hyperloop capsule vehicle with Skyhook and Mixed Skyhook-Acceleration Driven Damper controller.” *Adv. Mech. Eng.*, 13(2), 1–14.

Nguyen, Q.-H., Choi, S.-B., and Wereley, N. M. (2008). “Optimal design of magnetorheological valves via a finite element method considering control energy and a time constant.” *Smart Mater. Struct.*, 17(2), 025024.

Nguyen, Q. H., and Choi, S. B. (2009). “Optimal design of a vehicle



magnetorheological damper considering the damping force and dynamic range.” *Smart Mater. Struct.*, 18(1).

Nguyen, Q. H., Choi, S. B., Lee, Y. S., and Han, M. S. (2009). “An analytical method for optimal design of MR valve structures.” *Smart Mater. Struct.*, 18(9).

Nguyen, Q. H., Han, Y. M., Choi, S. B., and Wereley, N. M. (2007). “Geometry optimization of MR valves constrained in a specific volume using the finite element method.” *Smart Mater. Struct.*, 16(6), 2242–2252.

Nguyen, Q. H., Nguyen, N. D., and Choi, S. B. (2014). “Optimal design and performance evaluation of a flow-mode MR damper for front-loaded washing machines.” *Asia Pacific J. Comput. Eng.*, 1(1), 1–14.

Nigwal, D., Pasi, D. K., and Chouksey, M. (2022). “Effect of nonlinear conical springs on the vibration characteristics of seven degree-of-freedom car model using MATLAB/Simscape.” *Int. J. Dyn. Control*.

Oh, H. U. (2004). “Experimental demonstration of an improved magneto-rheological fluid damper for suppression of vibration of a space flexible structure.” *Smart Mater. Struct.*, 13(5), 1238–1244.

Oh, H. U., and Onoda, J. (2002). “An experimental study of a semiactive magneto-rheological fluid variable damper for vibration suppression of truss structures.” *Smart Mater. Struct.*, 11(1), 156–162.

Pan, W., Yan, Z., Lou, J., and Zhu, S. (2018). “Research on MRD Parametric Model Based on Magic Formula.” *Shock Vib.*, 2018.

Pandian, S., Mahendran, M., Rajesh, S., and Chokkalingam, R. (2022). “Effect of magnetic field on the viscous behaviour of iron particles suspended silicone additive based magnetorheological fluids.” *Indian J. Phys.*, 96(8), 2303–2311.

Pang, L., Kamath, G. M., and Wereley, N. M. (1998a). “Dynamic characterization and analysis of magnetorheological damper behavior.” L. P. Davis, ed., 284–302.

Pang, L., Kamath, G., and Wereley, N. (1998b). “Analysis and testing of a linear stroke magnetorheological damper.” *39th AIAA/ASME/ASCE/AHS/ASC Struct. Struct. Dyn.*

*Mater. Conf. Exhib.*, Reston, Virginia: American Institute of Aeronautics and Astronautics, 2841–2856.

“Parker.” (n.d.). <<https://www.parker.com/us/en/divisions/noise-vibration-and-harshness-division/solutions/semi-active-suspensions.html>> (Apr. 9, 2022).

“PCB Electronics.” (2022). <<https://www.pcb.com/products?m=352C33>> (Apr. 20, 2022).

Peng, G. R., Li, W. H., Du, H., Deng, H. X., and Alici, G. (2014). “Modelling and identifying the parameters of a magneto-rheological damper with a force-lag phenomenon.” *Appl. Math. Model.*, 38(15–16), 3763–3773.

Peng, Y., Yu, M., Du, X., and Fu, J. (2017). “An experimental study of vehicle suspension semi-active control with skyhook controller and magneto-rheological dampers.” (1), 7427–7429.

Phillips, R. W. (1969). *Engineering applications of fluids with a variable yield stress. Theol. Today*, ProQuest Dissertations Publishing.

Pohoryles, D. A., and Duffour, P. (2015). “Adaptive control of structures under dynamic excitation using magnetorheological dampers: An improved clipped-optimal control algorithm.” *JVC/Journal Vib. Control*, 21(13), 2569–2582.

Rabinow, J. (1948). “The Magnetic Fluid Clutch.” *Trans. Am. Inst. Electr. Eng.*, 67, 1308–1315.

Rahman, M., Ong, Z. C., Julai, S., Ferdaus, M. M., and Ahamed, R. (2017). “A review of advances in magnetorheological dampers: their design optimization and applications.” *J. Zhejiang Univ. A*, 18(12), 991–1010.

Rankin, P. J., Horvath, A. T., and Klingenberg, D. J. (1999). “Magnetorheology in viscoplastic media.” *Rheol. Acta*, 38(5), 471–477.

Reimpell, J., Stoll, H., Betzler, J. (2001). *The automotive Chassis- Engineering Principles*. London: Butterworth-Heinemann 2001.

Rossi, A., Orsini, F., Scorza, A., Botta, F., Belfiore, N. P., and Sciuto, S. A. (2018). “A review on parametric dynamic models of magnetorheological dampers and their

characterization methods.” *Actuators*, 7(2), 16.

Saini, R. S. T., Chandramohan, S., Sujatha, S., and Kumar, H. (2021). “Design of bypass rotary vane magnetorheological damper for prosthetic knee application.” *J. Intell. Mater. Syst. Struct.*, 32(9), 931–942.

Saini, R. S. T., Kumar, H., and Chandramohan, S. (2020). “Optimal design of inverted rotary MR brake with waveform boundary using a novel combined magnetostatic approach.” *Smart Mater. Struct.*, 29(10).

Sakai, C., Ohmori, H., and Sano, A. (2003). “Modeling of MR Damper with Hysteresis for Adaptive Vibration Control.” *Proc. IEEE Conf. Decis. Control*, 4(December), 3840–3845.

Sam, Y. M., Osman, J. H. S., and Ghani, M. R. A. (2004). “A class of proportional-integral sliding mode control with application to active suspension system.” *Syst. Control Lett.*, 51(3–4), 217–223.

Sarkar, C., and Hirani, H. (2015). “Effect of Particle Size on Shear Stress of Magnetorheological Fluids.” *Smart Sci.*, 3(2), 65–73.

Sassi, S., Cherif, K., Mezghani, L., Thomas, M., and Kotrane, A. (2005). “An innovative magnetorheological damper for automotive suspension: From design to experimental characterization.” *Smart Mater. Struct.*, 14(4), 811–822.

Savaresi, S. M., and Spelta, C. (2007). “Mixed sky-hook and ADD: Approaching the filtering limits of a semi-active suspension.” *J. Dyn. Syst. Meas. Control. Trans. ASME*, 129(4), 382–392.

Schurter, K. C., and Roschke, P. N. (2000). “Fuzzy modeling of a magnetorheological damper using ANFIS.” *IEEE Int. Conf. Fuzzy Syst.*, 1, 122–127.

Schurter, K. C., and Roschke, P. N. (2001a). “Neuro-fuzzy control of structures using acceleration feedback.” *Smart Mater. Struct.*, 10(4), 770–779.

Schurter, K. C., and Roschke, P. N. (2001b). “Neuro-fuzzy control of structures using magnetorheological dampers.” *Proc. Am. Control Conf.*, 2, 1097–1102.

Search, H., Journals, C., Contact, A., Iopscience, M., Mater, S., and Address, I. P.

- (2003). “Experimental analysis of magnetorheological dampers for.” 703.
- Shiao, Y., and Nguyen, Q. A. (2013). “Development of a multi-pole magnetorheological brake.” *Smart Mater. Struct.*, 22(6).
- Shulman, Z. P., Kordonskii, V. I., Prokhorov, I. V., Demchuk, S. A., and Shchekinova, K. (1987). “DEVICES FOR THE DIAGNOSIS OF TRANSFER PROCESSES IN MAGNETORHEOLOGICAL SUSPENSIONS.” *Heat Transf. Res.*, 19(5).
- Shulman, Z. P., Kordonsky, V. I., Zaltsgendler, E. A., Prokhorov, I. V., Khusid, B. M., and Demchuk, S. A. (1986). “Structure, physical properties and dynamics of magnetorheological suspensions.” *Int. J. Multiph. Flow*, 12(6), 935–955.
- “Sigma Aldrich.” (2022).  
 <<https://www.sigmaaldrich.com/IN/en/product/sigma/c3518>> (Dec. 5, 2022).
- Sims, N. D., Holmes, N. J., and Stanway, R. (2004). “A unified modelling and model updating procedure for electrorheological and magnetorheological vibration dampers.” *Smart Mater. Struct.*, 13(1), 100–121.
- Sims, N. D., Peel, D. J., Stanway, R., Johnson, A. R., and Bullough, W. A. (2000). “The electrorheological long-stroke damper: a new modelling technique with experimental validation.” *J. Sound Vib.*, 229(2), 207–227.
- Singh, H. J., and Wereley, N. M. (2014). “Optimal control of gun recoil in direct fire using magnetorheological absorbers.” *Smart Mater. Struct.*, 23(5).
- Snyder, R. A., Kamath, G. M., and Wereley, N. M. (2001). “Characterization and analysis of magnetorheological damper behavior under sinusoidal loading.” *AIAA J.*, 39(7), 1240–1253.
- Soliman, A. M. A., and Kaldas, M. M. S. (2021). “Semi-active suspension systems from research to mass-market – A review.” *J. Low Freq. Noise Vib. Act. Control*, 40(2), 1005–1023.
- Song, X., Ahmadian, M., and Southward, S. (2008). “Adaptive skyhook control for magneto-rheological suspension systems.” *2007 Proc. ASME Int. Des. Eng. Tech. Conf. Comput. Inf. Eng. Conf. DETC2007*, 3 PART B, 1169–1178.

- Song, X., Ahmadian, M., and Southward, S. C. (2005a). "Modeling magnetorheological dampers with application of nonparametric approach." *J. Intell. Mater. Syst. Struct.*, 16(5), 421–432.
- Song, X., Ahmadian, M., Southward, S., and Miller, L. (2007). "Parametric study of nonlinear adaptive control algorithm with magneto-rheological suspension systems." *Commun. Nonlinear Sci. Numer. Simul.*, 12(4), 584–607.
- Song, X., Ahmadian, M., Southward, S., and Miller, L. R. (2005b). "An adaptive semiactive control algorithm for magnetorheological suspension systems." *J. Vib. Acoust. Trans. ASME*, 127(5), 493–502.
- Spencer, B. F., Dyke, S. J., Sain, M. K., and Carlson, J. D. (1997). "Phenomenological Model for Magnetorheological Dampers." *J. Eng. Mech.*, 123(3), 230–238.
- Strecker, Z., Mazurek, I., Roupec, J., and Klapka, M. (2015). "Influence of MR damper response time on semiactive suspension control efficiency." *Meccanica*, 50(8), 1949–1959.
- Sung, K. G., and Choi, S. B. (2008). "Effect of an electromagnetically optimized magnetorheological damper on vehicle suspension control performance." *Proc. Inst. Mech. Eng. Part D J. Automob. Eng.*, 222(12), 2307–2319.
- Taghirad, H. D., and Esmailzadeh, E. (1998). "Automobile Passenger Comfort Assured Through LQG/LQR Active Suspension." *J. Vib. Control*, 4(5), 603–618.
- Tak, R. S. S., Kumar, H., Chandramohan, S., and Srinivasan, S. (2019). "Design of twin-rod flow mode magneto rheological damper for prosthetic knee application." *AIP Conf. Proc.*, 2200(December).
- Terasawa, T., Sakai, C., Ohmori, H., and Sano, A. (2004). "Adaptive identification of MR damper for vibration control." *Proc. IEEE Conf. Decis. Control*, 3, 2297–2303.
- Tharehalli Mata, G., Kumar, H., and Mahalingam, A. (2019). "Performance analysis of a semi-active suspension system using coupled CFD-FEA based non-parametric modeling of low capacity shear mode monotube MR damper." *Proc. Inst. Mech. Eng. Part D J. Automob. Eng.*, 233(5), 1214–1231.

- TharehalliMata, G., Krishna, H., and Keshav, M. (2022). “Characterization of magnetorheological fluid having elongated ferrous particles and its implementation in MR damper for three-wheeler passenger vehicle.” *Proc. Inst. Mech. Eng. Part D J. Automob. Eng.*
- Wang, Y., Yang, C., & Yagola, A. G. (2011). *Optimization and Regularization for Computational Inverse Problems and Applications. Optim. Regul. Comput. Inverse Probl. Appl.*, (Y. Wang, C. Yang, and A. G. Yagola, eds.), Berlin, Heidelberg: Springer Berlin Heidelberg.
- Wang, D. H., and Liao, W. H. (2005). “Modeling and control of magnetorheological fluid dampers using neural networks.” *Smart Mater. Struct.*, 14(1), 111–126.
- Wang, D. H., and Liao, W. H. (2011). “Magnetorheological fluid dampers: A review of parametric modelling.” *Smart Mater. Struct.*, 20(2).
- Wang, E. R., Ma, X. Q., Rakhela, S., and Su, C. Y. (2003). “Modelling the hysteretic characteristics of a magnetorheological fluid damper.” *Proc. Inst. Mech. Eng. Part D J. Automob. Eng.*, 217(7), 537–550.
- Wang, K., Dong, X., Li, J., Shi, K., and Li, K. (2019). “Effects of Silicone Oil Viscosity and Carbonyl Iron Particle Weight Fraction and Size on Yield Stress for Magnetorheological Grease Based on a New Preparation Technique.” *Materials (Basel)*, 12(11), 1778.
- Wang, L. X., and Kamath, H. (2006). “Modelling hysteretic behaviour in magnetorheological fluids and dampers using phase-transition theory.” *Smart Mater. Struct.*, 15(6), 1725–1733.
- Wang, X., Chang, C. C., and Du, F. (2002). “Achieving a more robust neural network model for control of a MR damper by signal sensitivity analysis.” *Neural Comput. Appl.*, 10(4), 330–338.
- Wang, X., and Gordaninejad, F. (2000). “Field-controllable electro- and magnetorheological fluid dampers in flow mode using Herschel-Bulkley theory.” *Smart Struct. Mater. Damping Isol.*, T. T. Hyde, ed., 232–243.

- Wereley, N. M., Kamath, G. M., and Madhavan, V. (1999). "Hysteresis Modeling of Semi-Active Magnetorheological Helicopter Dampers." *J. Intell. Mater. Syst. Struct.*, 10(8), 624–633.
- Wereley, N. M., and Pang, L. (1998). "Nondimensional analysis of semi-active electrorheological and magnetorheological dampers using approximate parallel plate models." *Smart Mater. Struct.*, 7(5), 732–743.
- Wereley, N. M., Pang, L., and Kamath, G. M. (1998). "Idealized Hysteresis Modeling of Electrorheological and Magnetorheological Dampers." *J. Intell. Mater. Syst. Struct.*, 9(8), 642–649.
- Wilson, N. L., Wereley, N. M., Hu, W., and Hiemenz, G. J. (2013). "Analysis of a magnetorheological damper incorporating temperature dependence." *Int. J. Veh. Des.*, 63(2/3), 137.
- Xu, Z.-D., Sha, L.-F., Zhang, X.-C., and Ye, H.-H. (2013). "Design, performance test and analysis on magnetorheological damper for earthquake mitigation." *Struct. Control Heal. Monit.*, 20(6), 956–970.
- Xu, Z. D., and Guo, Y. Q. (2006). "Fuzzy control method for earthquake mitigation structures with magnetorheological dampers." *J. Intell. Mater. Syst. Struct.*, 17(10), 871–881.
- Yang, G., Spencer, B. F., Carlson, J. D., and Sain, M. K. (2002). "Large-scale MR fluid dampers: Modeling and dynamic performance considerations." *Eng. Struct.*, 24(3), 309–323.
- Yang, G., Spencer, B. F., Jung, H.-J., and Carlson, J. D. (2004). "Dynamic Modeling of Large-Scale Magnetorheological Damper Systems for Civil Engineering Applications." *J. Eng. Mech.*, 130(9), 1107–1114.
- Yu, Y., Li, Y., and Li, J. (2015). "Nonparametric modeling of magnetorheological elastomer base isolator based on artificial neural network optimized by ant colony algorithm." *J. Intell. Mater. Syst. Struct.*, 26(14), 1789–1798.
- Yuan, X., Tian, T., Ling, H., Qiu, T., and He, H. (2019). "A Review on Structural

- Development of Magnetorheological Fluid Damper.” *Shock Vib.*, 2019.
- Zareh, S. H., Matbou, F., and Khayyat, A. A. A. (2015). “Experiment of new laboratory prototyped magneto-rheological dampers on a light commercial vehicle using neuro-fuzzy algorithm.” *JVC/Journal Vib. Control*, 21(15), 3007–3019.
- Zhang, L., Qiqi, P., Fuquan, P., Xiaohan, G., Binqin, L., Yichao, H., Yintao, W., and Yongchang, D. (2020). “Suspension Control Applications of Magnetorheological Damper Magic Formula Model.” *China Mech. Eng.*, 31(14), 1659–1665.
- Zhang, W. J., Ouyang, P. R., and Sun, Z. H. (2010). “A novel hybridization design principle for intelligent mechatronics systems.” *Abstr. Int. Conf. Adv. mechatronics Towar. Evol. fusion IT mechatronics ICAM*, 2010.5(0), 67–74.
- Zheng, J., Li, Z., Koo, J., and Wang, J. (2014a). “Magnetic circuit design and multiphysics analysis of a novel MR damper for applications under high velocity.” *Adv. Mech. Eng.*, 2014.
- Zheng, L., Duan, X., Deng, Z., and Li, Y. (2014b). “Multi-objective optimal design of magnetorheological engine mount based on an improved non-dominated sorting genetic algorithm.” *Act. Passiv. Smart Struct. Integr. Syst. 2014*, 9057, 90572N.
- Zhu, X., Jing, X., and Cheng, L. (2012). “Magnetorheological fluid dampers: A review on structure design and analysis.” *J. Intell. Mater. Syst. Struct.*, 23(8), 839–873.
- Zubieta, M., Eceolaza, S., Elejabarrieta, M. J., and Bou-Ali, M. M. (2009). “Magnetorheological fluids: Characterization and modeling of magnetization.” *Smart Mater. Struct.*, 18(9), 0–6.



## APPENDIX

### Specifications of instruments and equipment used

#### LORD MR damper RD-8040-1 and RD-8041-1



LORD MR damper

Parameter	Specification	
	RD-8040-1	RD-8041-1
Stroke, mm (in)	55 (2.17)	74 (2.91)
Extended Length, mm (in)	208 (8.2)	248 (9.76)
Body Diameter, mm (in)	42.1 (1.66) max	42.1 (1.66) max
Shaft Diameter, mm (in)	10 (0.39)	10 (0.39)
Tensile Strength, N (lbf)	8896 (2000) max	8896 (2000) max
Damper Forces, N (lbf)		
5 cm/sec @ 1 A	>2447 (>550)	>2447 (>550)
20 cm/sec @ 0 A	<667 (<150)	<667 (<150)
Operating Temperature, °C (°F)	71 (160) max	71 (160) max
Input Current, Amp		
Continuous for 30 seconds	1 max	1 max
Intermittent	2 max	2 max
Input Voltage, Volt	12 DC	12 DC
Resistance, ohms		
@ ambient temperature	5	5
@ 71°C (160°F)	7	7

## LORD Wonder Box®



LORD Wonder Box®

Parameter	Specification
Overall Dimensions (LxWxH), mm (in)	63.5 x 27.9 x 88.9 (2.5 x 1.1 x 3.5)
Input Receptacle	1 mm, Female
Pulse Width Modulation (PWM) Frequency, kHz	30
Output Current, Amp	2 max

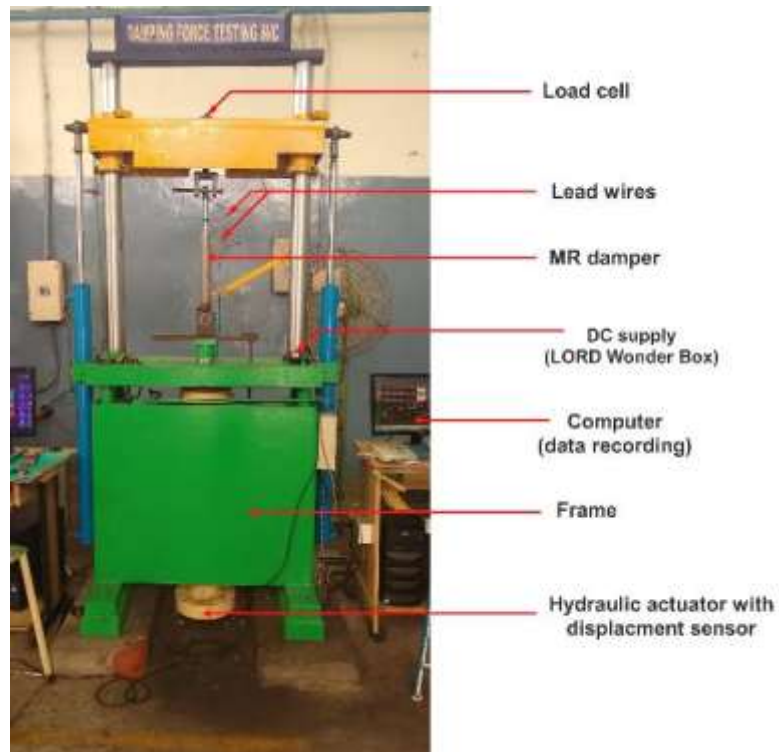
## LORD MR Fluid: MRF-132DG



LORD MRF-132DG

Parameter	Specification
Appearance	Dark Gray Liquid
Viscosity, Calculated as slope 800-1200 sec-1,Pa-s @ 40°C (104°F)	0.112 ± 0.02
Density, g/cm <sup>3</sup> (lb/gal)	2.95-3.15 (24.6-26.3)
Solids Content by Weight, %	80.98
Flash Point, °C (°F)	>150 (>302)
Operating Temperature, °C (°F)	-40 to +130 (-40 to +266)

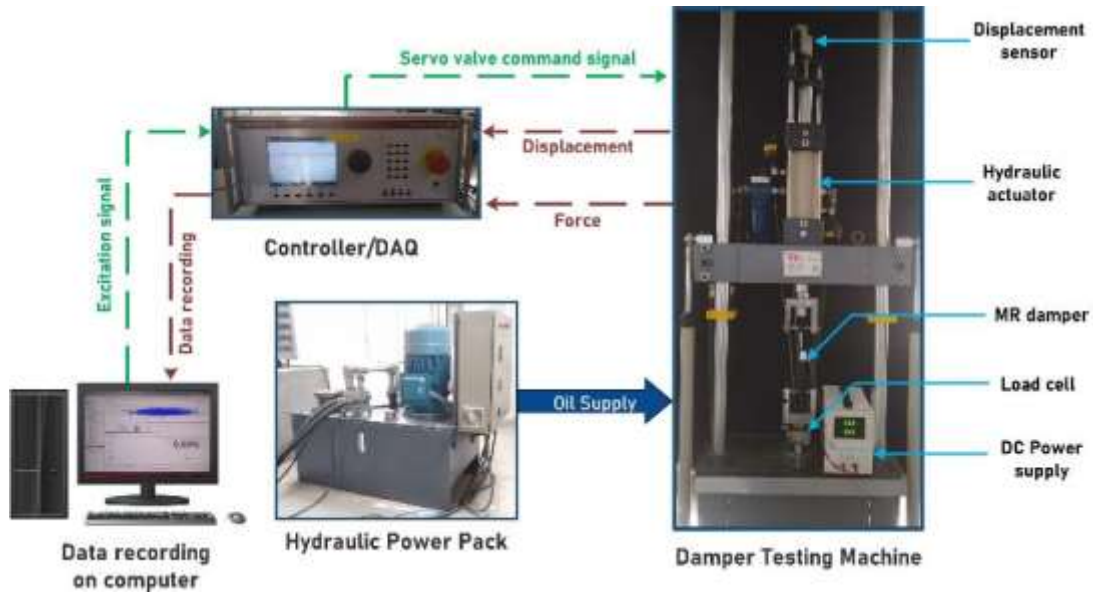
### Damper testing machine at Rambal Ltd., Chennai



Damper testing machine at Rambal Ltd.

Parameter	Specification
Capacity of hydraulic actuator	1 ton (1000 kg) or 9.81 kN
Maximum stroke of actuator	250 mm
Maximum velocity of actuator	1 m/s
Force transducer capacity (Interface make)	1200 kg or 11.77 kN
Sampling rate	10,000 samples per second
Resolution of position sensor	0.0001 mm

## HEICO damper testing machine at NITK



Damper testing machine at NITK

### i. Hydraulic power pack



Hydraulic power pack

Parameter	Specification
Flow of the pump	64 LPM
Max. Operating Pressure	210 bars
Oil tank capacity	200 liters

**ii. Hydraulic actuator**



Hydraulic actuator

Parameter	Specification
Type	Double acting double ended
Capacity	+/- 20 kN
Stroke	150 mm (+/- 75 mm)
Max. working pressure	210 bars
Max. sustained velocity	0.8 m/s
Peak velocity	1.2 m/s
Servo valve	63 LPM
Pressure line filter	180 LPM with 3 microns filtration
Accumulator (2 No.)	0.36 liter capacity

- The movement of the actuator is facilitated by a servo valve fitted with a manifold block to the actuator, which receives its command from the operating computer.
- The servo valve in this actuator, made by MOOG, is a throttle valve designed for 4-way applications with a rated pressure drop of 1000 Psi (70 kg/cm<sup>2</sup>) and a flow rate rating of 63LPM. The output stage is a closed center four-way sliding spool.

**iii. Load Cell**



Load cell

Parameter	Specification
Capacity	+/- 30 kN
Resolution	0.001 kN
Full scale output	2 mV/V
Excitation Voltage	10 Volts DC
Non-linearity	< +/- 0.15 % FSO
Safe overload	150 %
Operating temperature	0 to +60 deg. C
Accuracy	0.5% of indicated value as per ISO7500-1

**iv. Position / Displacement sensor**



Position sensor

Parameter	Specification
Range	200 mm
Make	Gefran/Balluff
Full scale output	10 volts
Repeatability	<0.01 mm
Pressure withstand	Up to 600 bars
Excitation voltage	24 volts DC
Sampling rate	2 kHz
Operating temperature	-30 to +75 °C

v. **MOOG® Controller/DAQ**



MOOG® Controller

- The controlling unit of the MOOG® controller employed in this machine is capable of generating cyclic excitation of four types - Sine, Triangular, Square and ramp wave
- It consists of 4 control channels – Load, Displacement, External channel strain 1 and strain 2, each with a high-speed 32-bit data acquisition sampling rate of 6 kHz.
- It has auto PID operation with auto zeroing, auto-tuning, auto-calibration and auto-adjustment featured servo operation. The digital signal processing (DSP) servo controller with a closed-loop update rate of 10 kHz.
- The controller also has a dedicated signal conditioning unit that processes the signal from various transducers to make the data acceptable to the DAQ.
- The dedicated servo control valve allows the servo valve to operate through an automatic PID controller in load or displacement mode.
- The controller/DAQ is operated using proprietary software installed on a dedicated computer with Intel i5 processor with 4 GB RAM and 500 GB HDD
- The proprietary software also allows plotting the transducer data while operating the machine making it user-friendly software.

## The DC Power supply



DC power supply (Scientific Instrument – PSD3005)

Parameter	Specification
Make	Scientific
Model	PSD 3005
DC output	0 to 30V / 5A
Settling resolution	V: 10 mV, I : 5 mA
Load Regulation	$\leq \pm(0.05\% + 10 \text{ mV})$
Input Supply	230 AC $\pm 10\%$ / 50-60 Hz
Internal resistance	$\leq 10$ milliOhms

### Features:

- Built-in over-heat and over-voltage protection
- Constant current and voltage operation
- Digital display with adjustable current limiter
- Over-load and short circuit protection
- Lightweight and compact



## The test vehicle



Force Motor's – Traveller (3350) at Rambal Ltd.

Parameter	Specification
Wheelbase	3350 mm
Overall length	5615 mm
Overall width	1900 mm
Overall height	2250 mm
Ground clearance	200 mm
Max. Permissible GVW	3965 kg
Frame type	Monocoque construction
Front Suspension	Spring Semi elliptical, hydraulic shock absorbers and anti-roll bar
Rear Suspension	Spring Semi elliptical, hydraulic shock absorbers and (anti-roll bar - optional)
Wheel size	215/75R15
Tire type	Radial with Tube/Tubeless (4+1)

## Accelerometer



Uniaxial accelerometer - PCB352C33

Parameter	Specification
Sensitivity	$\pm 100$ mV/g
Range	$\pm 50$ g
Frequency	0.5 to 10kHz
Resonance frequency	Greater than or equal to 50 kHz
Temperature Range	-54 to 93 °C
Cable Length	5m

## DAQs used in real-time testing

### i. NIcDAQ-9174



NIcDAQ-9174

Parameter	Specification
Input FIFO size	127 samples per slot
Timing accuracy	50 ppm of sample rate
Timing resolution	12.5 ns
Resolution (Timers and counters)	32 bits
No. of slots for modules	4 slots

ii. NI-9234



NI-9234

Parameter	Specification
IEPE channels	4-channel sound and vibration input
Resolution	24-bit resolution
Operational Range	$\pm 5$ V, 0 to 20mA Input range
Connectivity type	BNC connectivity only
Sampling rate	51.2 kS/s

**iii. NI-9403 and TTL Digital Input/Output Module**



NI 9403 with DSUB 32 Channel TTL Digital Input/Output Module

Parameter	Specification
Module type	5V, TTL digital I/O
No. of input-output channels	32 - Channel
Speed of operation	7 $\mu$ S
Isolation	60 VDC, CAT I
Operational Temperature	-40 °C to 70 °C
Operating Acceleration	5 g vibration, 50 g shock

**iv. Laptop for data recording**



Lenovo - IdeaPad S340

<b>Parameter</b>	<b>Specification</b>
Processor	8th Gen Intel® Core™ i7
Operating System	Operating System
Memory (RAM)	8 GB
Storage (ROM)	512 GB M.2 PCIe SSD
Dimensions (W x D x H)	358mm x 245mm x 17.9-19.4mm

### Rheometer

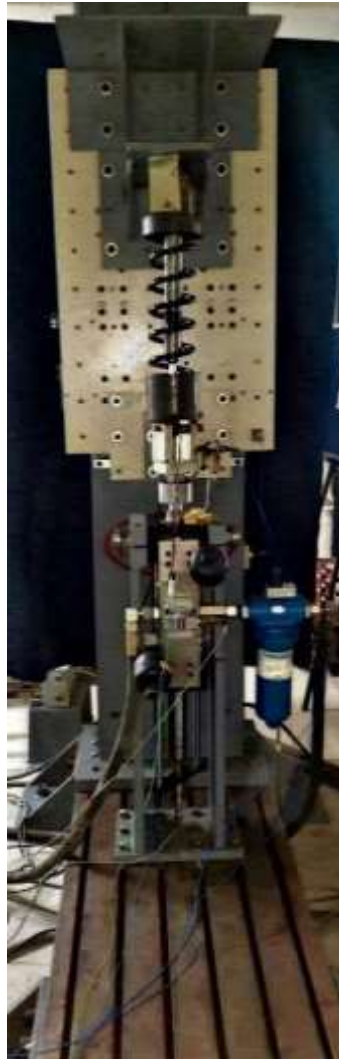


Anton Paar Rheometer MCR 702

<b>Parameter</b>	<b>Specification</b>
Minimum torque, rotation	1 nN-m
Maximum torque, rotation	230 mN-m
Minimum torque, oscillation	0.5 nN-m
Maximum angular frequency	628 rad/s
Normal force range	0.005 to 50 N

Maximum temperature range	-160 to +1000 °C
Pressure range	up to 1000 bar
Software	RheoCompass™ Professional Running under Microsoft Windows 7/8/8.1/10 (64bit versions only) - Recommended hardware: Intel i5, 2.67 GHz or higher, 8 GB RAM or more, SSD with 240 GB or more
Magnetorheological Device Cell	Magnetic Flux density up to 1 Tesla Temperature range - 0 to 170°C
Hood with Peltier Heating/Cooling	Temperature range: -40 to 200 °C
Compressor	230/50 V/Hz, 55 l/min, OILFREE Motor Power: 0.55 kW Output (5 bar): 55l/min max. Pressure: 8 bar Tank Volume: 10 l Weight: 59 kg Dimensions: 510x530x515 mm
Peltier Temperature Control Device	Temperature range: -5 to 200 °C
Power Supply Magneto Cell	230V HCP 14-12500,12.5,1 mA
Tesla meter	1 Tesla

### Suspension test rig (SDOF system)



Suspension test rig

#### i. Base Frame

Parameter	Specification
Length of the frame	1500 mm
Width of the frame	1000 mm
Working height of the frame	500 mm
T slots size	M16
Vertical loading capacity	30 kN
Number of T-slots	4

**ii. Vertical Frame**

<b>Parameter</b>	<b>Specification</b>
The base of the frame	600 mm
Length of the frame	400 mm
Height of the frame	3000 mm
Main carriage adjustment	1500 mm
Front plate of the carriage	Matrix of 100x100xM12
Travel of slide carriage (linear bearing)	100 mm

**iii. Frame to mount the dampers**

<b>Parameter</b>	<b>Specification</b>
Capacity	20 kN
Horizontal clearance	400 mm
Vertical clearance (adjustable)	200-1000 mm

**iv. LVDT**

<b>Parameter</b>	<b>Specification</b>
Make	Gefran
Stroke	100 mm ( $\pm 50$ mm)
Max displacement speed	10 m/s
Tip	Stainless steel with M2.5 thread
Temperature range	-30 °C to 100 °C

**MATLAB Software**

<b>Parameter</b>	<b>Specification</b>
Name of the software	MATLAB/SIMULINK
Version	R2018b, R2019a, R2019b, R2020b
Licensed to	NITK
Company	MathWorks



**FEMM Software**

<b>Parameter</b>	<b>Specification</b>
Name of the software	Finite Element Method Magnetics
Version	4.2 (Current version)
Licensed to	Open-Source Software

**LabVIEW Software**

<b>Parameter</b>	<b>Specification</b>
Name of the software	LabVIEW
Version	2014, 2017
Licensed to	NITK
Company	National Instruments



## LIST OF PUBLICATIONS

### INTERNATIONAL JOURNALS

1. **Mohibb-e-Hussain Jamadar**, Rangaraj M. D., Radhe Shyam T. S., Hemantha Kumar, Sharnappa J. (2021), “Dynamic analysis of a quarter car model with semi-active seat suspension using a novel model for Magneto-Rheological (MR) damper”, *Journal of Vibration Engineering & Technologies, Springer Publications (Impact Factor: 2.33, SCIE indexed)* <https://doi.org/10.1007/s42417-020-00218-1>
2. **Mohibb-e-Hussain Jamadar**, Pinjala Devikiran, Rangaraj M. D., Hemantha Kumar, Sharnappa J. “Real-time testing and thermal characterization of a cost-effective Magneto-Rheological (MR) damper for four-wheeler application”, *Journal of the Brazilian Society of Mechanical Sciences and Engineering, Springer Publications (Impact Factor: 2.361, SCIE indexed)* <https://doi.org/10.1007/s40430-023-04035-x>
3. **Mohibb-e-Hussain Jamadar**, Pinjala Devikiran, Hemantha Kumar, Sharnappa J., “Experimental and analytical evaluation of an acceleration-based control strategy for semiactive vehicle suspension system with Magneto-Rheological (MR) damper” *SAE International Journal of Passenger Vehicle System (Scopus and ESCI indexed, SAE International)* <https://doi.org/10.4271/15-16-03-0015>
4. **Mohibb-e-Hussain Jamadar**, Pinjala Devikiran, Hemantha Kumar, Sharnappa J., “Optimization and experimental analysis of a cost-effective Magneto-Rheological (MR) fluid for application in semi-active suspension of a passenger van” – *Proceedings Institution of Mechanical Engineers, Part D: Journal of Automobile Engineering, SAGE Publications (Impact Factor: 1.828, SCIE Indexed)* <https://doi.org/10.1177/09544070231184510>

### ***INTERNATIONAL CONFERENCES***

- **Mohibb-e-Hussain Jamadar**, Rangaraj M. D., Hemantha Kumar, Sharnappa J (2019). “Analyzing quarter car model with Magneto-Rheological damper using equivalent damping and Magic formula models”, *International Mechanical Engineering Congress (IMEC) 2019* (National Institute of Technology, Tiruchirapalli, Tamil Nadu - 29<sup>th</sup> Nov 2019 to 1<sup>st</sup> Dec 2019).
- **Mohibb-e-Hussain Jamadar**, Rangaraj M. D., Hemantha Kumar, Sharnappa J (2019). “Parametric Study of Magic Formula Model for Magneto-Rheological (MR) Damper”, *International Congress on Computational Mechanics and Simulation (ICCMS) 2019* (Indian Institute of Technology, Mandi, Himachal Pradesh – 11<sup>th</sup> Dec 2019 to 16<sup>th</sup> Dec 2019).

## BIODATA

**Name** : MOHIBB E HUSSAIN JAMADAR  
**Date of Birth** : 11-05-1993  
**Mobile No.** : +91 6362930399  
**Email** : [mhussain.jamadar093@gmail.com](mailto:mhussain.jamadar093@gmail.com)  
**Address** : H. No. 1688/A, S/o Moula Ali Jamadar,  
Near Peti Boudi Masjid, Jamiya Masjid  
Road, Vijayapura, Karnataka – 586101



### QUALIFICATION:

Degree	Board/Institute	Year	Percentage/CGPA
Ph. D. (Coursework)	NITK, Surathkal	2018	7.25/10
M. Tech. (Design Engineering)	VTU, Belagavi	2016	74.225%
B. E. (Mechanical Engineering)	VTU, Belagavi	2014	77.66%

### EXPERIENCE:

Sl. No.	Company/Institute	Designation	From	To
1	NITK, Surathkal	Junior Research Fellow (JRF)	June 2017	August 2019

**Journal Publications:** 4

**Conference Publication:** 2